

**Quantification of Tissue Perfusion using  
Contrast-Enhanced Ultrasound: Toward Robust Exam  
Comparison**

by

**Maxime Doury**

from the Laboratoire d'Imagerie Biomédicale

Submitted to the Université Pierre et Marie Curie (Paris VI)  
in partial fulfillment of the requirements for the degree of

**Doctor of Physics**

**September 2017**

**© Maxime Doury, 2017.**

This work is licensed under the Creative Commons Attribution-NonCommercial 4.0 License. To view a copy  
of this license, visit <http://creativecommons.org/licenses/by-nc/4.0> or send a letter to Creative  
Commons 543 Howard Street, 5th Floor, San Francisco, California, 94105, USA.

Author .....  
Laboratoire d'Imagerie Biomédicale  
September 29, 2017

Certified by .....  
Frédérique Frouin  
IMIV, Inserm, Paris Sud  
Thesis Supervisor

Certified by .....  
Alain de Cesare  
LIB, CNRS, UPMC  
Thesis Supervisor

Accepted by .....  
William M. Deen  
Chairman, Department Committee on Graduate Students



# **Quantification of Tissue Perfusion using Contrast-Enhanced Ultrasound: Toward Robust Exam Comparison**

by

Maxime Doury

Submitted to the Université Pierre et Marie Curie (Paris VI)  
on September 29, 2017, in partial fulfillment of the  
requirements for the degree of  
Doctor of Physics

## **Abstract**

In this thesis, I discuss the application and development of methods for the automated discovery of motifs in sequential data. These data include DNA sequences, protein sequences, and real-valued sequential data such as protein structures and timeseries of arbitrary dimension. As more genomes are sequenced and annotated, the need for automated, computational methods for analyzing biological data is increasing rapidly. In broad terms, the goal of this thesis is to treat sequential data sets as unknown languages and to develop tools for interpreting an understanding these languages.

The first chapter of this thesis is an introduction to the fundamentals of motif discovery, which establishes a common mode of thought and vocabulary for the subsequent chapters. One of the central themes of this work is the use of grammatical models, which are more commonly associated with the field of computational linguistics. In the second chapter, I use grammatical models to design novel antimicrobial peptides (AmPs). AmPs are small proteins used by the innate immune system to combat bacterial infection in multicellular eukaryotes. There is mounting evidence that these peptides are less susceptible to bacterial resistance than traditional antibiotics and may form the basis for a novel class of therapeutics. In this thesis, I described the rational design of novel AmPs that show limited homology to naturally-occurring proteins but have strong bacteriostatic activity against several species of bacteria, including *Staphylococcus aureus* and *Bacillus anthracis*. These peptides were designed using a linguistic model of natural AmPs by treating the amino acid sequences of natural AmPs as a formal language and building a set of regular grammars to describe this language. This set of grammars was used to create novel, unnatural AmP sequences that conform to the formal syntax of natural antimicrobial peptides but populate a previously unexplored region of protein sequence space.

The third chapter describes a novel, GEneric MOTif DIscovery Algorithm (Gemoda) for sequential data. Gemoda can be applied to any dataset with a sequential character, including both categorical and real-valued data. As I show, Gemoda deterministically discovers motifs that are maximal in composition and length. As well, the algorithm allows any choice of similarity metric for finding motifs. These motifs are representation-agnostic: they can be represented using regular expressions, position weight matrices, or any other model for

sequential data. I demonstrate a number of applications of the algorithm, including the discovery of motifs in amino acids and DNA sequences, and the discovery of conserved protein sub-structures.

The final chapter is devoted to a series of smaller projects, employing tools and methods indirectly related to motif discovery in sequential data. I describe the construction of a software tool, Biogrep that is designed to match large pattern sets against large biosequence databases in a *parallel* fashion. This makes biogrep well-suited to annotating sets of sequences using biologically significant patterns. In addition, I show that the BLOSUM series of amino acid substitution matrices, which are commonly used in motif discovery and sequence alignment problems, have changed drastically over time. The fidelity of amino acid sequence alignment and motif discovery tools depends strongly on the target frequencies implied by these underlying matrices. Thus, these results suggest that further optimization of these matrices is possible.

The final chapter also contains two projects wherein I apply statistical motif discovery tools instead of grammatical tools. In the first of these two, I develop three different physiochemical representations for a set of roughly 700 HIV-I protease substrates and use these representations for sequence classification and annotation. In the second of these two projects, I develop a simple statistical method for parsing out the phenotypic contribution of a single mutation from libraries of functional diversity that contain a multitude of mutations and varied phenotypes. I show that this new method successfully elucidates the effects of single nucleotide polymorphisms on the strength of a promoter placed upstream of a reporter gene.

The central theme, present throughout this work, is the development and application of novel approaches to finding motifs in sequential data. The work on the design of AmPs is very applied and relies heavily on existing literature. In contrast, the work on Gemoda is the greatest contribution of this thesis and contains many new ideas.

Thesis Supervisor: Frédérique Frouin  
Title: IMIV, Inserm, Paris Sud

Thesis Supervisor: Alain de Cesare  
Title: LIB, CNRS, UPMC

## Acknowledgments

I am indebted to many people who both directly and indirectly contributed to this thesis. First, I would like to thank those collaborators who directly contributed. Most of all, I'm grateful for the help and friendship of Mark Styczynski. Mark was my collaborator on all matters computational for the past four years — his influence is evident throughout this document. I'm also grateful for my collaboration with Christopher Loose, who performed many of the experiments on antimicrobial peptides described in Chapter ???. Finally, I would like to thank Isidore Rigoutsos, who straddled the line between collaborator and advisor. Isidore taught me an attention to detail and a penchant for the UNIX command line and vi editor.

Most importantly, I am indebted to Greg Stephanopoulos, my advisor, whose guidance and support was unwavering these past six years. Greg is the perpetual optimist — always positive in the face of my many failures along the way. He also gave me the freedom to pursue projects of my own choosing, which contributed greatly to my academic independence, if not the selection of wise projects.

I am much obliged to my thesis committee members: my advisor Greg, Isidore, Bill Green, and Bob Berwick. My committee was always flexible in scheduling and judicious in their application of both carrots and sticks.

There are numerous people who contributed indirectly to this thesis. First among these is my intelligent, lovely, and vivacious wife Kathryn Miller-Jensen. Next, my parents Carl and Julie, my sister Heather, and my in-laws, Ron, Joyce, Suzanne, Jeff, and Mindi. Finally, there are innumerable friends who contributed and to whom I am greatly appreciative including Michael Raab, Joel Moxley, Bill Schmitt, Vipin Guptda, and Jatin Misra.



# Contents

<b>Cover page</b>	<b>i</b>
<b>Abstract</b>	<b>iii</b>
<b>Acknowledgments</b>	<b>v</b>
<b>1 Introduction</b>	<b>1</b>
1.1 Cancer and tumor microenvironment . . . . .	1
1.2 Perfusion imaging . . . . .	3
1.3 Aims and outline . . . . .	6
1.3.1 Context . . . . .	6
1.3.2 Aims . . . . .	6
1.3.3 Outline . . . . .	6
<b>I Quantification of perfusion: state of the art</b>	<b>9</b>
<b>2 Quantification of perfusion exams: A review</b>	<b>13</b>
2.1 Semi-quantitative methods . . . . .	14
2.1.1 Generalities . . . . .	14
2.1.2 Nuclear medicine . . . . .	14
2.1.3 X-rays . . . . .	15
2.1.4 Magnetic resonance . . . . .	16
2.1.5 Ultrasound . . . . .	19
2.2 Deconvolution methods . . . . .	34

2.2.1	Generalities . . . . .	34
2.2.2	Nuclear medicine . . . . .	38
2.2.3	X-rays . . . . .	39
2.2.4	Magnetic resonance . . . . .	43
2.2.5	Ultrasound . . . . .	48
2.3	Compartmental models . . . . .	51
2.3.1	Generalities . . . . .	51
2.3.2	Nuclear medicine . . . . .	52
2.3.3	X-rays . . . . .	57
2.3.4	Magnetic resonance . . . . .	58
2.3.5	Ultrasound . . . . .	62
2.4	Discussion . . . . .	62

## **II Reproducibility of the existing methods and the relations between them**

<b>3 Quantification of tumor perfusion using DCE-US: impact of mathematical modeling</b>	<b>97</b>
3.1 Abstract . . . . .	97
3.2 Introduction . . . . .	98
3.3 Materials . . . . .	99
3.3.1 Animals . . . . .	99
3.3.2 Image acquisition . . . . .	100
3.3.3 Data pre-processing . . . . .	100
3.4 Methods . . . . .	101
3.4.1 Quantification of tumor perfusion . . . . .	101
3.4.2 Data analysis . . . . .	105
3.5 Results . . . . .	106
3.5.1 Model comparison through quality of fit criteria . . . . .	106
3.5.2 Model comparison through coefficients of variation . . . . .	107

3.6	Discussion . . . . .	108
3.7	Conclusion . . . . .	111
3.8	Acknowledgments . . . . .	112
<b>4</b>	<b>Relations between perfusion parameters: theoretical and experimental considerations</b>	<b>115</b>
4.1	Introduction . . . . .	115
4.2	Theory . . . . .	115
4.3	Data Analysis . . . . .	116
4.4	Results . . . . .	116
4.5	Discussion . . . . .	118
4.6	Conclusion . . . . .	119
<b>III</b>	<b>Proposition and assessment of a new quantification method</b>	<b>127</b>
<b>5</b>	<b>Regularized Linear Resolution of a One-Compartment Model to Improve the Reproducibility of Perfusion Parameters in CEUS</b>	<b>131</b>
5.1	Abstract . . . . .	131
5.2	Introduction . . . . .	132
5.3	Materials . . . . .	133
5.3.1	Animals . . . . .	133
5.3.2	Image acquisition . . . . .	133
5.4	Methods . . . . .	134
5.4.1	Data pre-processing . . . . .	134
5.4.2	Definition of the four models . . . . .	135
5.4.3	Data analysis . . . . .	137
5.5	Results . . . . .	138
5.6	Discussion . . . . .	140
5.7	Conclusion . . . . .	141

<b>6 Impact of Recirculation in Dynamic Contrast-Enhanced Ultrasound: a Simulation Study</b>	<b>143</b>
6.1 Abstract . . . . .	143
6.2 Introduction . . . . .	144
6.3 Theory . . . . .	146
6.3.1 One-compartment vascular model . . . . .	146
6.3.2 Simplified recirculation model . . . . .	146
6.3.3 Noise model . . . . .	148
6.3.4 Perfusion quantification methods . . . . .	148
6.4 Experimental design . . . . .	150
6.4.1 Simulations . . . . .	150
6.4.2 Data analysis . . . . .	151
6.5 Results . . . . .	152
6.5.1 Model $M_1$ . . . . .	152
6.5.2 Model $M_2$ . . . . .	152
6.5.3 Model $M_3$ . . . . .	157
6.5.4 Model $M_4$ . . . . .	157
6.5.5 Model $M_5$ . . . . .	157
6.5.6 Model $M_6$ . . . . .	158
6.6 Discussion . . . . .	158
6.7 Conclusion . . . . .	161
<b>7 Error Sources Affecting Relative Quantification of CEUS</b>	<b>165</b>
7.1 Introduction . . . . .	165
7.2 Theory . . . . .	166
7.2.1 Simulation models . . . . .	166
7.2.2 Quantification models . . . . .	167
7.3 Materials and Methods . . . . .	172
7.3.1 Simulations of CEUS data . . . . .	172
7.3.2 Data analysis . . . . .	175

7.4	Results . . . . .	176
7.5	Discussion . . . . .	196
7.6	Conclusion . . . . .	198
	<b>Abbreviations and reference data</b>	<b>207</b>



# List of Figures

3-1 Illustration of the data pre-processing steps. Left: The contours of the tumor and its necrotic core have been overlaid on a contrast enhanced image (in ochre color). The perfused tumor area was divided into 4 radial layers and 8 angular sectors. A reference tissue region (in green color) and a renal cortex region (in blue color) were also delineated. Right: Mean kinetics associated with the non-necrotic part of the tumor, the reference tissue, and the renal cortex. . . . .	101
3-2 Automated detection of the AIF: parametric maps $TTP$ and $PE$ inside the artery region; segmentation results and associated AIF with: (a) $rPE^* = 50\%$ and $\Delta TTP^* = 3$ s (in green color); (b) $rPE^* = 70\%$ and $\Delta TTP^* = 2.5$ s (in blue color). . . . .	103
3-3 Comparison of the volume-based and flow-based parameters obtained for the four test-retest exams ( $R_1$ , $R_2$ , $R_3$ , and $R_4$ ) of the mouse $m_1$ : linear regressions between (a) $rV_{RT}$ and $AUC$ , (b) $rV_{RT}$ and $V$ , (c) $rV_{RT}$ and $rAUC$ , (d) $rV_{RT}$ and $rV_{AIF}$ , (e) $rF_{RT}$ and $WIR$ , (f) $rF_{RT}$ and $F$ , (g) $rF_{RT}$ and $rWIR$ , (h) $rF_{RT}$ and $rF_{AIF}$ . . . . .	108

- 3-4 Boxplot showing the coefficients of variation of blood volume parameters (left) and blood flow parameters (right) estimated with the **aLN**, **rLN**, **aAIFd**, **rAIFd**, and **rRTd** models. For each box, the bold line represents the median value, the bottom and top lines the first and third quartiles. Dotted lines extend to the most extreme data points which are less than 1.5 times the interquartile range. Outlier points are displayed with empty circles. Two groups of parameters were built (horizontal lines below the parameter names) such that there were no significant intra-group differences while there were statistically significant inter-group differences (marked by \*). . . . . 109
- 4-1 (a-b) Median (of 16 values) coefficient of determination ( $R^2$ ) of the least-squares linear regression between pairs of parameters  $\theta_i$ ,  $\theta_j$  computed for the 32 sub-regions of one exam: (a) parameters derived from the **aLN** approach; (b) volume ( $AUC$ ,  $V$  and  $rV_{RT}$ ), flow ( $WIR$ ,  $F$  and  $rF_{RT}$ ) and time delay ( $\Delta_T$ ,  $d_t$  and  $D_{RT}$ ) parameters respectively computed with **aLN**, **aAIFd** and **RTd** models. (c-d) Coefficients of determination ( $R^2$ ) of the least-squares linear regression computed when pooling the 512 sub-regions together: (c)  $R^2$  between pairs of volume parameters computed with **aLN**, **aAIFd**, **rLN**, **rAIFd** and **RTd** models, (d)  $R^2$  between pairs of flow parameters computed with **aLN**, **aAIFd**, **rLN**, **rAIFd** and **RTd** models. . . . . 120
- 5-1 Illustration of the data pre-processing steps. Left: The contours of the perfused tumor area have been overlaid on a contrast-enhanced image (in blue color). This area was automatically divided into 4 radial layers and 8 angular sectors as shown by the spiderweb patterns. A RT region (in orange color) was also delineated. Right: Mean TICs associated with the perfused area of the tumor, and the RT. . . . . 134
- 5-2 Boxplot showing the CV of blood volume (left) and blood flow (right) estimated with the **LN**, **rLN**, **rLin**, and **rLinReg** models. . . . . 139



- 6-5 Bull's-eyes of the median estimation errors obtained by the rLN model at the intermediate noise level. From left to right: errors corresponding to tissue blood volume, tissue blood flow, time delay. From top to bottom:  $M_3$  without recirculation,  $M_3$  with recirculation,  $M_4$  without recirculation,  $M_4$  with recirculation. . . . . 155
- 6-6 Bull's-eyes of the median estimation errors obtained by the rLin and rReg models at the intermediate noise level. From left to right: errors corresponding to tissue blood volume, tissue blood flow, time delay, rate constant in tissue regions, rate constant in the reference tissue deduced from the different estimations inside tissue regions. From top to bottom:  $M_5$  without recirculation,  $M_5$  with recirculation,  $M_6$  without recirculation,  $M_6$  with recirculation. 156
- 7-1 Absolute perfusion parameters used for simulation with the OVC model, i.e. tissue blood volume,  $V_T$  and  $V_R$ , tissue blood flow,  $F_T$  and  $F_R$ , tissue rate constant,  $k_T$  and  $k_R$ , and time delay,  $D_T$  and  $D_R$ . Bullseye view of the parameters in the 32 tumor regions. The bottom disks represent the parameters used to simulated the reference tissue region, the center disk being the original value used for all experiments. The other disks are, from left to right, the half, two third, three half, and double of the original value, used to study the influence of the reference tissue. . . . . 172
- 7-2 Time-intensity curves inside of each of the 32 tumor regions (top grid), and in the reference tissue (bottom), simulated using the OVC. Each plot shows the simulated noiseless curve (orange line) in the region, i.e.  $\sigma = 0$ , as well as the curve with simulated multiplicative noise (blue dots), i.e.  $\sigma = 0.25$ . . . 173
- 7-3 Relative perfusion parameters used for simulation varying the number of tumor regions  $N_T$  from 1 (left) to 32 (right), i.e. relative tissue blood volume,  $rV$ , relative tissue blood flow,  $rF$ , tissue rate constant,  $k_T$ . . . . . 175
- 7-4 Correspondance of the regions between bullseye (left) and grid (right) representation. . . . . 176

7-5	Median (large symbols) and first and third quartiles (small symbols) of the relative estimation error for the relative blood volume ( $rV$ ) estimated using the <b>rLin</b> (yellow diamonds) and <b>rReg</b> (purple squares) models, as a function of the noise level. . . . .	177
7-6	Median (large symbols) and first and third quartiles (small symbols) of the relative estimation error for the relative blood flow ( $rF$ ) estimated using the <b>rLin</b> (yellow diamonds) and <b>rReg</b> (purple squares) models, as a function of the noise level. . . . .	178
7-7	Median (large symbols) and first and third quartiles (small symbols) of the relative estimation error for the rate constant in the tumor ( $k_T$ ) estimated using the <b>rLin</b> (yellow diamonds) and <b>rReg</b> (purple squares) models, as a function of the noise level. . . . .	179
7-8	Median (large symbols) and first and third quartiles (small symbols) of the relative estimation error for the rate constant in the reference tissue ( $k_R$ ) estimated using the <b>rLin</b> (yellow diamonds) and <b>rReg</b> (purple squares) models, as a function of the noise level. . . . .	180
7-9	Median (large symbols) and first and third quartiles (small symbols) of the relative estimation error for the relative blood volume ( $rV$ ) estimated using the <b>rLin</b> (yellow diamonds) and <b>rReg</b> (purple squares) models, as a function of the exam duration. . . . .	181
7-10	Median (large symbols) and first and third quartiles (small symbols) of the relative estimation error for the relative blood flow ( $rF$ ) estimated using the <b>rLin</b> (yellow diamonds) and <b>rReg</b> (purple squares) models, as a function of the exam duration. . . . .	181
7-11	Median (large symbols) and first and third quartiles (small symbols) of the relative estimation error for the rate constant in the tumor ( $k_T$ ) estimated using the <b>rLin</b> (yellow diamonds) and <b>rReg</b> (purple squares) models, as a function of the exam duration. . . . .	182

7-12	Median (large symbols) and first and third quartiles (small symbols) of the relative estimation error for the rate constant in the reference tissue ( $k_R$ ) estimated using the <b>rLin</b> (yellow diamonds) and <b>rReg</b> (purple squares) models, as a function of the exam duration. . . . .	183
7-13	Median (large symbols) and first and third quartiles (small symbols) of the relative estimation error for the relative tissue blood volume ( $rV$ ) estimated using the <b>rLin</b> (yellow diamonds) and <b>rReg</b> (purple squares) models, depending on the sampling period used for simulation. . . . .	184
7-14	Median (large symbols) and first and third quartiles (small symbols) of the relative estimation error for the relative tissue blood flow ( $rF$ ) estimated using the <b>rLin</b> (yellow diamonds) and <b>rReg</b> (purple squares) models, depending on the sampling period used for simulation. . . . .	185
7-15	Median (large symbols) and first and third quartiles (small symbols) of the relative estimation error for the rate constant in the tumor ( $k_T$ ) estimated using the <b>rLin</b> (yellow diamonds) and <b>rReg</b> (purple squares) models, depending on the sampling period used for simulation. . . . .	185
7-16	Median (large symbols) and first and third quartiles (small symbols) of the relative estimation error for the rate constant in the reference tissue ( $k_R$ ) estimated using the <b>rLin</b> (yellow diamonds) and <b>rReg</b> (purple squares) models, depending on the sampling period used for simulation. . . . .	186
7-17	Bullseyes of the median relative estimation error for the relative tissue blood volume ( $rV$ ) estimated using the <b>rLin</b> (top) and <b>rReg</b> (bottom) models depending on the characteristics of the reference tissue used for simulation. . . .	188
7-18	Bullseyes of the median relative estimation error for the relative tissue blood flow ( $rF$ ) estimated using the <b>rLin</b> (top) and <b>rReg</b> (bottom) models depending on the characteristics of the reference tissue used for simulation. . . .	189
7-19	Bullseyes of the median relative estimation error for the rate constant in the tumor ( $k_T$ ) estimated using the <b>rLin</b> (top) and <b>rReg</b> (bottom) models depending on the characteristics of the reference tissue used for simulation. . . .	190

7-20 Bullseyes of the median relative estimation error for the rate constant in the reference tissue ( $k_R$ ) estimated using the <b>rLin</b> (top) and <b>rReg</b> (bottom) models depending on the characteristics of the reference tissue used for simulation.	191
7-21 Bullseyes of the median value and the standard deviation of the relative estimation error for the relative tissue blood volume ( $rV$ ) estimated using the <b>rLin</b> (top) and <b>rReg</b> (bottom) models depending on the number of regions $N_T$	192
7-22 Bullseyes of the median value and the standard deviation of the relative estimation error for the relative tissue blood flow ( $rF$ ) estimated using the <b>rLin</b> (top) and <b>rReg</b> (bottom) models depending on the number of regions $N_T$	193
7-23 Bullseyes of the median value and the standard deviation of the relative estimation error for the rate constant in the tumor ( $k_T$ ) estimated using the <b>rLin</b> (top) and <b>rReg</b> (bottom) models depending on the number of regions $N_T$	194
7-24 Bullseyes of the median value and the standard deviation of the relative estimation error for the rate constant in the reference tissue ( $k_R$ ) estimated using the <b>rLin</b> (top) and <b>rReg</b> (bottom) models depending on the number of regions $N_T$	195



# List of Tables

3.1	Synthesis of the different models tested. The first three models propose absolute quantification. The last five models propose relative quantification. . .	102
3.2	Median [first-third quartiles] values of $NMRSE$ and $FMI$ (in %) obtained for the different models. $N$ is the number of sub-regions where $FMI < 90\%$ . Significant differences between <b>aLN</b> and any other model are indicated by *. In addition, significant differences between <b>aAIF</b> (resp. <b>rRT</b> ) and <b>aAIFd</b> (resp. <b>rRTd</b> ) are indicated by <sup>†</sup> (resp. <sup>‡</sup> ). The symbol <sup>◦</sup> indicates that comparisons were not reported due to the high number of missing data. . . . .	106
3.3	Mean $\pm$ standard deviation of the parameters estimated with the <b>aAIFd</b> and <b>rAIFd</b> models, using two different sets of cut-offs to generate the AIF functions. . . . .	107
3.4	Mean $\pm$ standard deviation of the volume, flow and delay parameters estimated in the different sub-regions of the tumor, for the four test-retest exams, after multiple imputation of missing values due to poor fit quality. Values of $WIR$ and $F$ are multiplied by 1000. . . . .	113
3.5	Mean $\pm$ standard deviation of the coefficients of variation (CV), expressed in percentage, of volume and flow parameters estimated for each sub-region after multiple imputation of missing values due to poor fit quality. CV were not computed for time delays, since their values can be either positive or negative. . . . .	113
4.1	Analytic expressions of perfusion parameters using the <b>aLN</b> model, $WOR$ being the absolute value of the maximum negative slope. . . . .	116

4.2	Analytic expressions of perfusion parameters using a one-compartment model <b>(aAIFd)</b> and assuming three different shapes of AIF: impulse function ( $\delta$ ), rectangle function of width $a$ and height $1/a$ , $rect_a(t)$ , and general case $C_A(t)$ . In the first two cases, $K$ stands for the injected concentration. In the general case, $MTT_{C_A}$ stands for the mean transit time of $C_A(t)$ . . . . .	117
4.3	Analytic expressions of the relative perfusion parameters using a relative one-compartment model ( <b>rAIFd</b> ) and assuming three different shapes of AIF: impulse function ( $\delta$ ), rectangle function of width $a$ and height $1/a$ , $rect_a(t)$ , and general case $C_A(t)$ . In the first two cases, $K$ stands for the injected concentration. . . . .	117
5.1	Median values of <i>FMI</i> obtained for the four models and number of sub-regions $N_{rem}$ , out of 512, for which $FMI < 90\%$ . . . . .	138
5.2	p-values obtained in the post-hoc analysis of the Friedman test. Significant results ( $p < 0.05$ ) in bold. . . . .	139
6.1	Analytic expressions of perfusion parameters using a one-compartment model and assuming two different shapes of AIF: rectangle function of width $a$ and height $1/a$ , $rect_a(t)$ , and general case $C_A(t)$ . In the first case, $K$ stands for the injected concentration. . . . .	163

# **Chapter 1**

## **Introduction**

This thesis addresses the quantification of tumor perfusion using contrast-enhanced ultrasound imaging. In this chapter, we present the biological and technical context that motivated this thesis.

### **1.1 Cancer and tumor microenvironment**

A tumor is a neoplasm composed of mutated cells undergoing abnormal growth. All tumors are not cancers, in particular benign tumors are not cancers, they are not invasive and usually not life-threatening. Cancer is in fact synonym of malignant tumor.

In 2000, Hanahan and Weinberg [1] proposed the first generation of cancer hallmarks, i.e. six acquired traits that differentiate cancerous cells from benign tumors and normal tissues:

1. Cancerous cells are able to generate their own mitogenic growth signals, and do not rely on the growth signals from the surrounding environment.
2. Cancerous cells are insensitive to the anti-growth signals originating from the surrounding environment.
3. Cancerous cells are immune to apoptotic signals, emitted by the environment, and controlling the death of malfunctioning cells.

4. The number of replication cancerous cells can achieve is unlimited.
5. After cancerous cells reached a point where further proliferation is limited by the supply in oxygen and nutrients, they switch to a angiogenic state that triggers the construction of a supplying vascular network, allowing rapid cell proliferation despite its chaotic structure.
6. When nutrients and space become limiting growth factors, cancerous cells are able to migrate and invade surrounding tissues where nutrients and space are not limiting factors to create new cancerous cell colonies known as metastases.

Later, in [2011](#), Hanahan and Weinberg [2] proposed a second generation of cancer hallmarks that include the six acquired traits presented in the previous paragraph, but they add four more hallmarks:

1. Cancerous cells are able to modify their metabolism to most effectively support tumor proliferation.
2. Cancerous cells are resistant to immunological destruction by lymphocytes and macrophages.
3. Cancerous cells exhibit unstable genomes favoring genetic mutations, that often result in an accelerated tumor progression.
4. Immune cells fighting the proliferation of cancer cells cause tissue inflammation, which can contribute to the acquired traits presented in their first study.

**Treatment of cancer** The three major treatments of cancer are surgery, radiotherapy, and chemotherapy.

Surgery aims at removing the whole tumor, however this procedure is highly invasive. Radiotherapy consists in the irradiation of the tumor by strong doses of X-rays, damaging cancerous cells, but also the surrounding tissues. These two techniques are only applicable to localized solid tumors, and some cancerous cells can remain after the treatment.

If the cancer has spread throughout the body, chemotherapy is often used to eliminate remaining and migrating cells after removal of the primary tumor by means of surgery or radiotherapy. Chemotherapy relies on the injection of a cytotoxic agent, which main purpose

is to eradicate the remaining cancerous cells. Cytotoxic agents however, are not specific of cancerous cells and are globally toxic for the patient, limiting the injected doses. Moreover, cancerous cells are highly prone to mutations and can develop a resistance to the cytotoxic agent.

Recently, anti-angiogenic treatments were proposed to disrupt or to limit the development of new vascular structures providing the tumor with the oxygen and nutrients necessary for cell division, therefore limiting further growth of the tumor. These treatments were shown to normalize the chaotic neovascularization in tumors, allowing a more efficient delivery of cytotoxic therapies inside the tumor. However, since many pathways regulating angiogenesis exist, cancerous cells can bypass the targeted pathway and activate another one, making the tumor resistant to the anti-angiogenic treatment.

**Cancer monitoring** Surgery, radiotherapy, and chemotherapy directly target cancerous cells, and an efficient treatment should have a direct impact on the size of the tumor. Therefore, morphological criteria were proposed to assess tumor response to therapy. The classical RECIST and WHO criteria are base on the changes in tumor diameter, and give an indication on the evolution of the disease, i.e. stable, regressive, or progressive.

Oppositely, anti-angiogenic treatments do not target cancerous cells, but rather the neovascularization of the tumor. They do not have a direct impact on the size of the tumor, especially the early stages of the treatment. Therefore, classical morphological criteria fail to reveal the efficiency of such treatments. Quantification of tumor angiogenesis and of the response to anti-angiogenic treatments requires the development of functional criteria assessing the microvascularization of tumor tissues. Microvascularization can be observed *in vivo* using functional imaging, and in particular through perfusion imaging.

## 1.2 Perfusion imaging

Perfusion imaging is a branch of medical imaging that focuses on the visualization and characterization of tissue vascularization. A tracer is injected in the vascular network of the patient, either as a bolus or as an infusion, and the passage of the tracer in the tissue is observed

using one of the various imaging modalities presented below.

**Nuclear medicine** Nuclear medicine regroups imaging modalities using radioactive tracers. Scintigraphy uses gamma-emitting tracers and a single gamma camera, yielding projections images of the tracer concentration. Single-photon emission computed tomography (SPECT) uses the same tracers as scintigraphy, but uses a rotating pair of gamma cameras to create three-dimensional images of the tracer concentration. Positron emission tomography (PET) uses a positron-emitting tracer, and coincident detection of the two gamma rays resulting from the annihilation of the positron emitted during the fission of the radioactive isotope.

Radioactive tracers are usually attached to a biologically active molecule, forming a radioligand that binds to a specific type of tissue, allowing the determination of the localization and density of specific binding sites.

**Magnetic resonance (MR)** As the name suggests, magnetic resonance imaging is based on nuclear magnetic resonance that exploits the ability of certain atoms to absorb and emit radio frequencies when placed in an external magnetic field. Typically, the imaged nucleids are protons present in tissues composed of water molecules. In this case, magnetic resonance images are formed by measuring the spin-lattice (T1) and spin-spin (T2) relaxation times of the protons inside the studied tissue.

Magnetic resonance contrast agents are usually paramagnetic substances that shorten the T1 relaxation time of the protons inside the observed tissues, for instance Gadolinium chelates are widely used. Most Gadolinium-based contrast agents diffuse from the blood pool to the interstitial space through the capillary surface, however intravascular contrast agents were also developed for magnetic resonance imaging.

**X-ray computed tomography (CT)** X-ray computed tomography uses a combination of multiple planar X-ray measurements with varying angles to produce three-dimensional images. The images give information about the ability of the tissue to absorb X-rays, also known as the radiodensity of the tissue.

The contrast agents used for X-ray computed tomography are usually iodinated compounds that were chosen for their high radiodensity, resulting in a strong absorption of the X-ray beams used for image formation. But also for their intravascular characteristics, that allow specific imaging of the vascular network when the injection is performed intravenously.

**Contrast-enhanced ultrasound (CEUS)** Ultrasound images are formed by sending sequences of ultrasound pulses inside the tissue using a transducer, the ultrasound pulses are reflected by scatterers in the tissue, and the reflected pulses are then recorded by the transducer. The recorded signals are finally processed to retrieve the time of flight of the echo, determining the location of the scatterer in the image, as well as the strength of the echo, determining the image intensity associated to the scatterer.

Coated gas-filled microbubbles are used as ultrasound contrast agents for their ability to oscillate asymmetrically when exposed to acoustic waves, but also for their size that makes them resonate in the ultrasound frequency domain. Their size being nearly the same as a red blood cell, it also ensures they can go everywhere in the vascular system, from the largest arteries to the smallest capillaries, but do not leak in the interstitial space. Microbubbles exhibit a strong and specific non-linear response to ultrasounds, and this non-linearity is exploited by ultrasound scanners using specific background-cancelling sequences to produce contrast-specific images.

Microbubbles can be disrupted using ultrasound pulses with high mechanical indices. This phenomenon allows a type of acquisition specific of contrast-enhanced ultrasound. Indeed, after a continuous infusion of microbubbles reached its steady-state, a series of disruptive pulses is sent, then the refillment of the microbubbles in the tissue is observed in real-time using a low mechanical contrast-specific sequence to ensure minimum destruction of the microbubbles.

## 1.3 Aims and outline

### 1.3.1 Context

This thesis was financed by the *Fondation pour la Recherche Médicale* (FRM) through grant DBS2013I128436. The project aims at developing a multiparametric tumor tissue classification tool, based on multiple ultrasound imaging modalities, including quantitative ultrasound, elastosonography, and contrast-enhanced ultrasound, in order to develop a tumor growth and treatment response prediction model. The first step of this project is therefore the accurate estimation of parameters from ultrasound data to train the tissue classification tool.

### 1.3.2 Aims

Reliable quantification of tumor perfusion is a challenging yet necessary task to establish cancer diagnosis and monitor tumors undergoing therapy. Contrast-enhanced imaging is a great tool to assess perfusion, however quantitative exam comparison remains difficult because of the poor reproducibility of the acquisitions. Moreover, most of the perfusion quantification methods are developed to estimate parameters at a global scale, therefore either hiding the local variations in tissue perfusion or not accounting for the relations between the local estimates. This thesis aims at making the estimation of perfusion parameters robust to inter-exam changes, in order to enable exam comparison while revealing the spatial heterogeneity of the tissue vascular function. Our study primarily focuses on contrast-enhanced ultrasound data, however the use of the proposed quantification methods to other perfusion imaging modalities could be investigated.

### 1.3.3 Outline

**Part I - Quantification of perfusion: state of the art** Chapter 2 presents the state of the art methods for the quantification of perfusion. Quantification approaches are classified according to whether they are semi-quantitative, based on deconvolution, or based on compartmental models. Major studies from the litterature were reviewed, however the study is

far from being exhaustive.

**Part II - Reproducibility of the existing methods and the relations between them** Chapter 3 studies the impact of mathematical modeling on the reproducibility of perfusion parameters through preclinical test-retest experiments. This study revealed the sensitivity of absolute semi-quantitative parameters to inter-exam variations in experimental or physiological conditions. It also showed the superiority of of normalized parameters, and more precisely of the reference tissue model, in terms of reproducibility. Chapter 4 extends the work from Chapter 3 by first establishing theoretically and then verifying experimentally the relations between the parameters of the various models. The existence of these relations shows the ability of semi-quantitative parameters to reveal relative variations of the vascular function.

**Part III - Proposition and assessemnt of a new quantification method** Chapter 5 first presents a new regularized linear estimation method for the reference tissue model, and compares its parameters to those obtained using the classical linear estimation method in terms of reproducibility. This study proves the superior robustness of the regularized estimates to inter-exam variations. Then Chapter 6 compares the robustness of the two models to contrast-agent recirculation through simulation experiments. And Chapter 7 studies the accuracy and the precision of the models when varying intrinsic characteristics of the data, e.g. exam duration, noise level, or quantification strategies, e.g. reference tissue, number of regions.

## Bibliography

- [1] Douglas Hanahan and Robert A Weinberg. The Hallmarks of Cancer. *Cell*, 100(1):57–70, January 2000. [1](#)
- [2] Douglas Hanahan and Robert A Weinberg. Hallmarks of cancer: the next generation. *Cell*, 144(5):646–674, March 2011. [2](#)

## **Part I**

# **Quantification of perfusion: state of the art**



# Foreword

In the first part of this thesis, we reviewed the methodological developments of perfusion quantification methods. Various modalities were historically used to assess perfusion, from the most invasive requiring catheterization for blood sampling to the most advanced in-vivo imaging techniques, however they all require injecting a tracer to monitor its concentration throughout the experiment. Quantification of perfusion consists in the estimation of parameters characterizing the physiology of the tissue under investigation, in particular regarding the distribution of blood or the exchanges between blood and tissue.

Chapter 2 addresses the three main quantification approaches used to characterize perfusion exams, i.e. semi-quantitative, deconvolution, and compartmental. The semi-quantitative approaches are the most intuitive, they derive perfusion parameters directly from the tracer concentration curves, from which physiological parameters can be derived. Deconvolution approaches consider the tissue as a black-box system fed by an arterial input, and estimate the tissue response to an instantaneous injection making few assumptions on the underlying physiology and tracer characteristics. Deconvolutions result in impulse responses with unknown shapes, from which perfusion parameters are usually derived. Compartmental models can be viewed as explicit deconvolution, where the shape of the impulse response is known and parameterized by physiologically relevant parameters.

The methods are presented by imaging modalities, however methodological transfers between modalities was common and was emphasized when a clear continuity was observed. The evolution of a technique is presented chronologically when possible to reveal the incremental development of the methods.



# Chapter 2

## Quantification of perfusion exams: A review

Generally speaking, quantification of perfusion consists in deriving parameters from blood flow measurements, regardless of the method used for the measure. This topic has been on the table, and continuously evolving, long before perfusion imaging existed. Indeed, G.N. Stewart introduced indicator dilution theory, starting with the founding paper published in the Journal of Physiology in 1897 [137]. W.F. Hamilton went further, corrected the approximations made by Stewart. Even before Stewart and Hamilton, hemodynamics of the heart had been studied through indirect measurements and reported in German language by Volkmann [157] and Vierordt [155] in the 1850s, and later through direct measurements by Stolnikow [138] and Tigerstedt [148].

This chapter fundamentally aims to review the various methods used to quantify perfusion exams acquired using one of the imaging modality briefly presented in Chapter 1. Realistically, this review of perfusion quantification techniques cannot be close to comprehensive, instead it tackles the subject from the three angles mentioned thereafter, and emphasis the major landmarks of the perfusion quantification landscape.

Section 2.1 presents semi-quantitative methods, extracting parameters directly either from raw or noise-filtered enhancement curves. Then Section 2.2 presents deconvolution-based quantification methods, estimating the vascular transfer function in the tissue of interest by means of blind or regularized deconvolution. Finally, compartmental models ac-

counting for the various interactions of the contrast agent with the tissue are presented in Section 2.3.

## 2.1 Semi-quantitative methods

### 2.1.1 Generalities

Semi-quantitative methods are probably among the most intuitive as they extract perfusion-related parameters directly from raw, interpolated, or noise-filtered enhancement curves. They are however not directly related to any physiological function and are prone to changes in experimental or physiological conditions. They are therefore often used as relative indicators of perfusion and contrast agent transit time [102], allowing intra-exam comparisons.

Examples of semi-quantitative parameters include the peak enhancement [39, 110, 111, 119], the time to peak enhancement [32, 39, 111], maximum upslope gradient, also known as wash-in rate [39, 110], the area under the enhancement curve [32], but also perfusion parameters based on indicator dilution theory based on the previously cited parameters [15, 61, 76, 100, 102, 103, 117, 118].

### 2.1.2 Nuclear medicine

Semi-quantitative parameters have been used to differentiate stenosed from healthy kidney in scintigraphy exams, i.e. a nuclear medicine technique using a gamma camera, following bolus injection of  $[^{99m}Tc]DTPA$ .

For instance, Hilson et al. and later Peters et al. both proposed an enhancement-based perfusion index, which is commonly defined as the ratio of the tissue blood flow to the cardiac output. On the one hand, Hilson et al. defined the perfusion index as the ratio of the area under the arterial curve to the area under the renal curve, both curves are integrated up to the arterial peak [61]. On the other hand, Peters et al. defined the perfusion index as the ratio of the maximum upslope of the renal curve normalized for the injected quantity to the maximum upslope of the integrated arterial curve normalized for the area under the arterial enhancement curve, and multiplied by a constant converting the gamma camera into a unit

of activity [117, 118].

Nally et al. reported significant differences in the wash-in rate, curve width at 75% of the peak enhancement, and maximum enhancement in normal and stenosed kidney in a canine model [110].

### 2.1.3 X-rays

Derived from the work of Peters et al., semi-quantitative parameters were also proposed by Miles et al. in 1991 to quantify renal cortical and medullary perfusion in X-ray computed tomography with bolus injection of Iodine [100, 102]. The proposed perfusion index was defined as the ratio of the maximum slope in the tissue curve and the peak enhancement of the arterial curve. The method was successively used to quantify perfusion in the pancreas [104], solitary pulmonary nodules [176], lymphoma masses [36], lung adenocarcinoma [140], and more generally to study tumor angiogenesis [101, 140].

Miles et al. also adapted the method to account for both arterial and venous perfusion of the liver, using the splenic enhancement as venous input because the portal vein was not present in the image [103]. Arterial perfusion was calculated using the maximum slope before peak splenic enhancement, while venous perfusion was calculated using the maximum slope after peak splenic enhancement.

In 1995 Blomley et al. proposed the liver subtraction method to quantify liver perfusion [15]. Instead of estimating the upslope in the late liver enhancement curve, they first subtracted the splenic enhancement curve multiplied by the ratio of arterial to splenic arterial perfusion, i.e. the ratio of the maximum slope in the early liver enhancement curve to the maximum slope in the spleen. The maximum slope of the corrected enhancement curve is then used to calculate portal perfusion. In this study, the time and value of peak enhancement were obtained using a gamma variate fit, allowing a finer estimation of these parameters. Whenever possible the authors used the enhancement curve in the portal vein instead of the splenic vein. Authors demonstrated the use of portal perfusion in one patient with metastatic livers, as well as in four patients with cirrhotic livers. Facing the small number of cases in the previous study, a collaborating group extended the application of the method in cirrhotic livers with more cases [151]. They estimated arterial and portal per-

fusion in a group of twenty patients with viral-induced cirrhosis and in fourteen controls. While arterial perfusion did not differ between groups, they found a significant reduction in portal perfusion among patients compared to controls, and a strong correlation between portal perfusion and the prothrombin ratio which is an indicator of hepatic parenchymal damage.

Inspired by the work of Miles et al., the method was adapted by Koenig et al. in 1998 to quantify perfusion in the brain in order to detect and assess cerebral ischemia in acute stroke [76]. While arterial enhancement could be estimated from small vessels present in the image, it was not used due to peak attenuation by partial volume effects. Instead, the peak venous enhancement in the superior sagittal sinus was used. The authors reported relatively small approximation error, with slightly flattened enhancement curves, explained by the short transit time of the contrast agent in brain tissues. The cerebral blood flow, commonly noted CBF, is the equivalent of the perfusion index in brain tissues. The authors defined it as the ratio of the maximum slope of the tissue enhancement curve to the peak enhancement in the superior sagittal sinus. The fractional cerebral blood volume, commonly noted CBV, was defined as the ratio of the peak tissue enhancement to the peak enhancement in the superior sagittal sinus. In a following study [73], the authors assess the linearity, the spatial resolution, and the sensitivity to noise of CBF through simulations and phantom study, and investigated the relative CBF estimated using large hemispherically mirrored regions of interest using follow-up CT and MR data. They reported a systematic underestimation of CBF correlated with the cardiac output of the patient, a good linearity of relative CBF, and recommend using the relative parameter as a predictor of the reversibility of an ischemic stroke.

## 2.1.4 Magnetic resonance

Following the methodological developments of Gadolinium-DTPA complex (Gd-DTPA) by Brasch et al. [19], Weinmann et al. [162], and Wesbey et al. [163] in 1984 supported by qualitative visual analysis, various applications of the technique emerged in the field of oncology.

Quantification attempts started with the work of Felix et al. [44] in 1985 using Gd-DTPA enhanced images acquired 5 minutes after injection of the contrast agent. Results were compared with pre-contrast MR images obtained using various acquisition sequences and X-ray

computed tomography imaging with injection of a iodinated contrast agent. They obtained accurate contours of brain tumor and necrosis with no significant enhancement in the region exhibiting peritumoral edema. They also attempted to differentiate the various types of tumor included in their study based on the contrast index before and after injection of Gd-DTPA. The index is defined as the ratio of signal intensity in the tumor tissue to the signal intensity in normal brain tissue. It is the first semi-quantitative parameter used for Gd-DTPA enhanced MRI.

Revel et al. [129] assessed the difference in signal intensity between the pre-contrast and 25-minute post-contrast images acquired in the largest section of subcutaneous human breast tumors implanted in mice. Signal intensity in the tissue were normalized by the signal intensity in a corn-oil phantom visible in every image. Limited by the temporal resolution of their acquisition, authors do not comment on the temporal evolution of signal intensity, despite intermediate acquisitions performed respectively 5 and 15 minutes after Gd-DTPA injection.

Pettersson et al. [119] performed repeated acquisitions of multiple MR sequences in rabbits subcutaneously implanted with a Vx2 tumor model, and additional induced hemorrhage in surrounding muscle tissue. Temporal evolution of enhancement is assessed more finely than in previous studies, acquiring an image every 2.5 minutes for the first 10 minutes after injection of Gd-DTPA and then every 5 minutes for the following 20 minutes. This allowed the authors to observe that no substantial enhancement occurred in abnormal tissues after 10 minutes, however they only reported on variations of peak signal intensity.

In 1989, Erlemann et al. [39] investigated dynamic contrast-enhanced MRI using a T1-weighted spin-echo sequence every 20 seconds following bolus injection of Gd-DTPA as a tool to differentiate tumors from healthy tissue in musculoskeletal lesions. Their primary result was an increase in contrast-to-noise ratio between tumor and muscle compared to T2-weighted images, and a decrease in contrast-to-noise ratio between tumor and bone marrow or fatty tissue compared to non-enhanced T1-weighted images. Additionally, they estimated the baseline signal intensity, the maximum signal intensity, and the time-lapse between the start of the injection and the point of maximum signal intensity. Using these estimates, the defined the signal intensity ratio as the percentage of increase over the baseline signal in-

tensity, as well as the relative enhancement slope. They observed an increase of the signal intensity ratios and relative enhancement slope in malignant tumors compared to benign tumors, the latter showing smaller overlap between malignant and benign groups. Enhancement slope enabled malignancy prediction with an accuracy of 79.7% using a cutoff value of 30%/min. They also reported lower peak intensity ratios and wash-in rates in areas with necrosis or peritumoral edema.

Wilke et al. [166] investigated the use of contrast-enhanced magnetic-resonance imaging for the quantification of myocardial perfusion in a canine study, and compared the estimated parameters to the blood flow obtained using radiolabelled microspheres. A bolus of Gd-DTPA was injected during Turbo-FLASH acquisition, and a six circular regions of interest were delineated in the myocardium, as well as one region of interest in each ventricular cavity, yielding a total of nine regional time-intensity curves. All the time-intensity curves were fitted with a gamma-variate curve to both correct for recirculation, and limit the impact of extravascular diffusion, using only the samples occurring before the curves decreases to 70% of its peak value. The mean transit time of each curve was calculated numerically, and the correlation of its inverse, of the time of peak intensity, as well as the initial slope (defined as the ratio of the peak intensity to the time of peak intensity) with absolute myocardial blood flow estimates from radiolabelled microspheres were investigated. Good correlations with the ground truth ( $r \geq 0.89$ ) were reported for the three semi-quantitative parameters cited above.

Verstraete et al. [154] also reported on the ability to differentiate benign from malignant musculoskeletal lesions, using imaging and quantification techniques similar to those used by Erlemann et al. [39]. Despite the higher temporal resolution of 2.41 seconds possible in their study, their findings are likewise nuanced because of the overlap of parameters between highly vascularized benign lesions and the malignant ones.

Baur et al. [13] reported higher signal intensity ratios after injection of Gd-DTPA in patients with intermediate-grade and high-grade diffuse malignant bone marrow infiltration in the spine compared to healthy patients. Nonetheless, they were unable to detect low-grade lesions using this technique, and reported large variabilities in all patient groups.

### 2.1.5 Ultrasound

The current section addresses the semi-quantitative methods used to quantify perfusion using ultrasound. Refer to Section 1.2 for more information on contrast-enhanced ultrasound as a perfusion imaging modality, including the nature of the contrast-agent, the image formation processes, as well as the various injection techniques. Methods assessing perfusion using bolus injection are first presented, followed by methods specific to continuous infusion injection.

As a foreword to this section, indicator dilution theory as first formalized by Stewart [137] and later by Hamilton et al. [56] is valid under the condition that the mass of contrast-agent is conserved through the time of the acquisition. Since 1979, it is known that a portion of the intravenously injected microbubbles are filtrated through the lungs [22, 98], i.e. before their first pass in the tissue of interest. Moreover, a portion of the following passes is filtered by the Kupffer cells in the liver [71, 172]. Additionally, Lampakis and Averkiou [84] confirmed that imaging using a high mechanical index disrupts a non-negligible number of microbubbles, and demonstrated that most of the microbubbles disrupted during imaging at a low mechanical-index are actually naturally disrupted. The mass conservation condition is therefore usually not respected in contrast-enhanced ultrasound, even in first-pass studies. Semi-quantitative methods based on indicator dilution theory were nonetheless extensively used to quantify perfusion in contrast-enhanced ultrasound exams.

#### Bolus injection

##### *Model-free quantification methods*

From an historical standpoint, Bommer et al. [18] were the first to report indicator-dilution curves using contrast-enhanced ultrasound data in an abstract published in The American Journal of Cardiology in 1978. Authors used a photometer to quantify the evolution of signal intensity, as visualized on the screen of the monitor. The enhancement resulted from the venous injection of a bolus of microbubbles, obtained by microcavitations through rapid injection of dextrose in water. The indicator-dilution curves were quantified in terms of time from peak enhancement to 50% decay, and to 90% decay. The latter was found correlated to

the cardiac-output, and enabled the differentiation of patients with low and normal cardiac index. In the same issue of *The American Journal of Cardiology*, the same group applied the same technique to produce indicator-dilution curves in another cardiac study [31]. They used the ultrasound images themselves to identify patients with intracardiac shunts, but also the mean clearance time of the indicator-dilution curves to identify patients with tricuspid regurgitation, and severe congestive failure.

At the same period, Hagler et al. [55] presented early data of videodensitometry data for the quantification of left-to-right shunts using echographic acquisitions with direct injection of a bolus of ultrasound contrast-agent (i.e. indocyanine green dye) in the left ventricle. They estimated the ratio of left-to-right shunt, which they defined as the ratio of the area under the curve in the right ventricle to the area under the curve in the left ventricle, and showed an strong correlation of echographic measurements with both indicator-dilution and dye measurements. Meltzer et al. [97] extended this work and investigated the relevance of a mono-exponential model to fit the wash-out curve, as suggested by indicator-dilution theory. This was assessed by fitting a linear model to the log-transformed time-density wash-out curve, exhibiting excellent correlation with experimental data. They therefore concluded on the relevance of the log wash-out slope, and established its relation to the contrast agent disappearance rate.

Following the early work of Armstrong et al. [4] and Tei et al. [142], Ten Cate et al. [143] investigated the use of contrast-enhanced echography for the assessment of myocardial perfusion following intracoronary injection of a bolus injection of microbubbles in a canine study with varying coronary artery flow (using a hydraulic occluder) to simulate ischemia, and with injection of Dipyridamole to dilate the coronary bed and therefore simulate hyperemia. The microbubbles in this study were investigated in a previous study of the same group, ensuring they were small enough to circulate through capillaries without getting trapped [43]. Semi-quantitative functional parameters were extracted from log-compressed time-intensity curves, i.e. the half wash-in time, half wash-out time (ignoring the recirculation by fitting a mono-exponential model), peak intensity time and value, and total curve duration. They found significant changes in total curve duration, and in half wash-in and wash-out times, for both ischemia and hyperemia in comparison with control measure-

ments. Interobserver and intraobserver variability, as well as injection reproducibility was assessed for the half wash-out time, with respective correlation coefficients of 0.98, 0.86, and 0.78. In addition, the relative systolic wall thickening was also estimated, and while it correlated well with the coronary artery flow measured by an electromagnetic flowmeter placed directly on the artery, no correlation was found with the ultrasound half wash-out time.

A few years later, Vandenberg et al. [153] performed a similar canine study with induced ischemia and hyperemia, intending to predict myocardial blood flow from semi-quantitative parameters derived from contrast-enhanced ultrasound time-intensity curves. In addition to peak intensity time and value, they investigated the use of the wash-in rate. Peak intensity value and wash-in rate were found correlated to myocardial blood flow, however correlations were moderate ( $r = 0.67$  and  $0.51$  respectively). However, the relative changes of the wash-in rate exhibited a stronger correlation ( $r = 0.77$ ) with the relative changes of the myocardial blood flow, i.e. with induced ischemia and hyperemia.

In a clinical study, Ten Cate et al. [144] estimated the total curve duration, the area under the curve, and the half wash-out time from time-intensity curves obtained in the ventricular septum from end-diastolic images. They performed multiple regression analysis between the parameters extracted from contrast-enhanced ultrasound data to angiographic parameters, i.e. the percentage of coronary area stenosis, and the minimal lumen area, derived from data acquired using the protocol described in [165]. Authors reported relations of various natures between the above-mentioned parameters, i.e. linear, inverse, exponential, and logarithmic. In particular, the strongest correlation was found between the area under the curve and the percentage of coronary area stenosis (exponential relation). Additionally, while all correlation were found significant, this couple of parameters was the only one with a strong correlation ( $r \geq 0.8$ ). Noting the discrepancies between the pre-clinical and the clinical results, the authors suggest they found their sources in modifications of the experimental setup, i.e. the injection method or the nature of the ultrasound contrast agent.

In 1990, Bleeker et al. [14] evaluated the stability, size, and ultrasonic properties of multiple ultrasound contrast agents, and investigated the feasibility of blood flow estimation through in vitro experiments. Their findings were in favor of the Albunex contrast agent, which were the only microbubbles exhibiting sufficiently longlasting stability (i.e. in size and number)

when exposed to ultrasound waves. In addition, a linear relation between the concentration of microbubbles and both backscatter coefficient (i.e. reflected power) and attenuation coefficient (i.e. transmitted power) was reported for low concentrations. They also found strong linear relations between the ultrasonic properties of the contrast agent and the flow estimated using an indicator-dilution theory. They emphasize the questionability of using grey-levels from ultrasound images to characterize blood flow, and instead recommend using attenuation based on transmission techniques, or backscattering after proper correction of signal attenuation. In vitro experiments showed strong relations between the ultrasonic properties of Albunex contrast agent and the flow estimated using indicator-dilution theory.

A somehow similar in vitro study was conducted a few years later by Heidenreich et al. [60], however the proposed quantification model makes use of an input function as a reference instead of the injected quantity used by Bleeker et al. [14], and extends the indicator-dilution model to estimate the tissue blood volume and mean transit time, in addition to the tissue blood flow. The model is based on the estimation of the area under the curve and mean transit time for both input and studied tissues. The ratio of the area under the curve in the studied tissue to the input yields the tissue blood volume, the system mean transit time is approximated as twice the difference in mean transit times, and the tissue blood flow was classically defined as the ratio of tissue blood volume to system mean transit time. In vitro calibration data revealed the log-compressed nature of the data in the experimental system, allowing linearization of the video intensity for low to moderate concentrations, and therefore conversion to volumetric concentration of microbubbles. Excellent agreement was found between measured and estimated flow rates, using 39 measurements at low concentration. Authors report on the difficulty to find a pure blood pool in the ultrasound imaging plane, but also to image both tissue and input with sufficient sensitivity and without saturation artifacts respectively because of the limited dynamic range of commercial ultrasound scanners. Additionally they comment on the simplicity of the model which allows to alleviate the signal attenuation artifacts which are often non-negligible in-vivo, and on the impossibility to ensure conservation of the contrast agent quantity and properties throughout the acquisition.

Aronson et al. [5], from the same research group, later assessed the model described

above in-vivo, in an attempt to quantify kidney perfusion in a canine study. A total of 58 bolus injections of microbubbles with varying concentrations (23 for aortic measurements, and 35 for cortical measurements), and 93 bolus injections with modulated blood flow (57 reduction, 10 increase, and 26 controls), were performed in 9 dogs. Blood flow was controlled by means of a renal artery occluder for flow reduction, and dopamine or fenoldopam infusion for flow increase. A major limitation of this study lies in the fact that renal and aortic data did not originate from the same injection, as a different dose of contrast-agents was used to extract the time-intensity curves in the two regions of interest. Additionally, the injected doses were adjusted empirically in order to obtain complete opacification of the region of interest, without reaching the signal saturation threshold. Direct measurements of blood flow were performed using an electromagnetic flowmeter, for comparison with the value estimated using contrast-enhanced ultrasound. The major findings of this study are the evidence of a strong correlation between the injected concentration and the pixel intensity, for both cortical and aortic measurements, and strong correlation of the estimated blood flow with in-situ flow measurements with a tendency to overestimate blood flow. Authors discuss the various pitfalls of contrast-enhanced ultrasound that could influence the accuracy of the method, including possible changes in blood volume in the modulated flow experiments, signal attenuation, and electronic thresholding. They finally conclude on the inability to perform absolute quantification of blood flow with the existing apparatus, stating that the major requirements lie in increased linearity and dynamic range.

Schwarz et al. [133] investigated the use of the wash-out rate from log-transformed time-intensity curves following bolus injection, as well as the ratio of the wash-out rates from two bolus injections with varying flow rates. Time-intensity curves were obtained using various backscatter intensity techniques, i.e. radio frequency, video intensity, pulsed wave Doppler, and intravascular Doppler. Authors obtained strong correlations of the wash-out rate with the in vitro flow rate, however they reported different slopes in two chambers with varying mixing volume. The relative wash-out rate not only exhibited excellent correlations with the relative flow rate, it also yielded a good agreement of the slopes obtained in the two mixing chambers. These results suggest the independence of the relative wash-out rate to the mixing volume, and the ability of this parameter to accurately characterize changes in blood flow.

Wiencek et al. [164] investigated the various steps necessary to achieve accurate quantification of contrast echocardiography using indicator-dilution theory. The proposed approach relies on the knowledge of an arterial input function, i.e. the time-intensity curve in a pure blood pool like the aortic root or in the left ventricle, in order to relax the need for standardized injection and physiological conditions. Authors acknowledge the difficulty of estimating the input function using a single injection, and suggest performing two separate injections to avoid saturation and non-linearities caused by high contrast-agent concentrations. They emphasize the necessity for a consistent and confined range of microbubble size, as the intensity of the signal backscattered by a single bubble is non-linearly proportional to the diameter of the bubble. The importance of conservation of contrast-agent quantity and properties throughout the acquisition of the ultrasound images was outlined, and the impact of hydrostatic pressure and gas saturation level of the solution as reported in the literature was investigated. The choice of the representation of the time-intensity curves, i.e. video intensity, log-transformed intensity, or concentration from calibration data, and its impact on the estimated parameters were discussed. A possible explanation for undetected changes when using peak height as an indicator of blood flow was proposed, authors related it to signal saturation and illustrate this phenomenon in simple cases where the changes in blood flow are caused by a change in blood volume only or in transit time only. Additionally, electronic issues resulting from signal acquisition, signal processing, and electronic thresholding were discussed. Physiological factors like tissue-dependant hematocrit were also investigated. Finally, methods which showed promising results in preliminary studies at the time of the review (i.e. 1993) were reported, including various alternative imaging schemes (e.g. acoustic velocity, radiofrequency data, second harmonic imaging).

### ***Model-based quantification methods***

In 1989, Kaul et al. [66] proposed a first-order gamma variate model to quantify blood flow using consecutive contrast-enhanced echocardiography acquisitions in an open-chest canine study with varying blood flow. They compared their results in the myocardium and in the coronary bed with the transmural myocardial blood flow measured using radiolabelled microspheres, and to direct coronary flow measurements obtained by an electromagnetic

flowmeter. They studied the influence of the injection site by performing their experiments in two groups of eight dogs. In the first group, dogs were injected a bolus of microbubbles in the circumflex artery, while in the second group they were injected in the left main coronary. Authors reported a good correlation of both myocardial and coronary blood flow measurements with the parameter of the gamma variate which influences the curve width,  $\alpha$ , for both groups (mean  $r = 0.81$  and  $0.96$  respectively), but a poor correlation of the peak intensity (mean  $r = 0.63$  and  $0.39$  respectively). Pooling estimates from the eight dogs did not affect the correlation with  $\alpha$  for the first group ( $r = 0.80$ ), however for the second group, pooling data considerably dropped the correlation ( $r = 0.23$ ). Scattered plots reveal the varying slopes obtained in the different dogs, emphasizing the impact of the injection site. Indeed, when injecting in the left main coronary the contrast agent is dispersed through the coronary tree, making quantification of myocardial blood flow intrinsically relative. Authors suggested that absolute quantification of myocardial blood flow may be possible, injecting closer to the branches of the coronary tree, but were well aware that the proposed semi-quantitative parameters are not absolute themselves.

Tiemann et al. [145] investigated the ability of harmonic power Doppler imaging to yield quantitative perfusion parameters, as this modality inherently destroys microbubble to produce contrast-specific images [146], through in vitro experiments, and ex vivo experiments in a porcine heart. They compared the time-intensity curves obtained from harmonic power Doppler, and the time-concentration curves of ICG measured with an extravascular densitometer, to direct flow measurements from a calibrated ultrasonic flowmeter. Authors fitted a log-normal model to the experimental curves, since this model has been commonly used to fit indicator-dilution curves [139, 169], and was later applied in cardiology studies [10, 90]. The area under the curve and the mean transit time of the fitted model were estimated for both modalities. While the area under the curve expectedly correlated with the injected quantity of ultrasound contrast agent, the inverse of the mean transit time obtained using microbubbles and ICG measurements exhibited very strong correlation to the direct flow measurements in both in vitro and ex vivo setups. However, the mean transit time obtained with harmonic power Doppler time concentration curves was slightly lower than with ICG densitometry, especially for high flow rates. While most studies used electromag-

netic flowmeters as ground truth, this one used an ultrasonic transit-time flowmeter. The presence of ultrasonic microbubbles could therefore influence the ground truth flow measurement, and possibly affect the correlation between ultrasonic measurements, however measurements were in agreement with densitometric ICG measurements which alleviates the suspicion.

In 2000, Postert et al. [121] proposed an empirical model for the quantification of cerebral perfusion time-intensity curves following intravenous injection of a bolus of microbubbles, imaged through the acoustic temporal bone window using phase-inversion harmonic ultrasound imaging, contrast burst imaging, and time variance imaging for comparison. The model accounts for the baseline-intensity and for the maximum change in intensity, i.e. the peak-intensity minus the baseline-intensity. Moreover, the wash-in of the bolus is modeled by a logistic curve with adjustable steepness and delay, despite authors describe it as step function, and the destruction of microbubbles is modeled by an exponential decay. However, none of the model parameters is directly related to the physiology or to physical measurements. Authors used the peak-intensity, as well as the time to peak-intensity extracted parameters from the modeled time-intensity curves as semi-quantitative parameters to compare the values obtained using the three modalities of contrast-enhanced ultrasound cited above, and in four regions of interest of nine healthy patients. The study concludes by stating the higher sensitivity of contrast burst imaging and time variance imaging compared to phase-inversion harmonic imaging.

However, three years later, a study by Eyding et al. [40] to which Postert collaborated, investigated the 90% peak width as an additional parameters to characterize time-intensity curves from phase-inversion harmonic imaging fitted with this model. Semi-quantitative parameters were evaluated in five regions of interest of the established ipsilateral view, i.e. imaging only the hemisphere on the probe side, using an imaging depth of 100 mm, and nine regions of interest using the novel bilateral view, i.e. allowing simultaneous imaging of both hemispheres with a single probe, using an imaging depth of 150 mm, of fourteen healthy patients. Consecutive transtemporal acquisitions following intravenous injection of two different ultrasound contrast agents were performed in each view of each patient, with twenty minute intervals, with for comparison purposes. The authors reported the sensitivity of

peak-intensity to depth, and the ability to differentiate arteries using either time parameter.

In a following study [80], the same group performed another transtemporal contrast-enhanced ultrasound study using the bilateral approach with a single bolus injection in twenty healthy patients. A total of fourteen regions of interest was delineated in both hemispheres, yielding as many time-intensity curves, from which were estimated the same three semi-quantitative parameters after fitting the empirical model described above. Peak intensity was once again excluded from further analysis because of the strong variations among patients. Because of the small amount of corresponding regions in the study, only descriptive data is presented in the form of aligned boxplots, as if all patients exhibited the same median value. The authors recommended the use of the time parameters, in particular the time to peak intensity, as estimated with the bilateral protocol. They believe it could be a relevant indicator to help characterize lesions in patients with acute strokes, provided that one of the hemispheres is unaffected and can be used as a reference.

In 2006, members of the Institut Gustave Roussy, also known as IGR, filed a patent application for quantification approach developed specifically for contrast-enhanced ultrasound [38]. The formulation of the mathematical model is empirical, and is inspired from the model first proposed by Eyding et al. [40], replacing both the numerator and the denominator terms by sigmoid functions. A long list of semi-quantitative parameters that can be derived from the fitted model for vascularization and tumoral angiogenesis detection are listed by the authors, i.e. peak-intensity time and value, wash-in time, mean transit time, area under the curve, wash-in rate, area under the wash-in, and under the wash-out.

The group later used the patented model in an early attempt to assess the efficacy of a disruptive anti-angiogenic treatment [88]. The group assessed tumor vasculature through the peak-intensity time and value, as well as the full-width at half maximum, in four groups of ten mice, respectively imaged at both 5 and 15 minutes, one hour, six hours, and twenty-four hours after treatment injection, and compared the post-treatment contrast-enhanced ultrasound results to pre-treatment results, but also to power Doppler and histology findings. They reported a progressive decrease in peak-intensity value reaching its minimum six hours after injection of the anti-angiogenic treatment, and opposite effects in time to peak-intensity and in the full-width at half maximum.

In 2003, Mischi et al. [108] proposed the local density random walk model for characterization of tissue perfusion in contrast-enhanced ultrasound with bolus injection of microbubbles. The model, first proposed by Sheppard and Savage [134] characterizes the dilution process through a mono-dimensional approximation of the vascular network, i.e. vessels are considered as straight tubes with constant flows, and a Brownian motion of the contrast-agent following bolus injection is assumed. A novel estimation method based on a two-phase multiple linear regression is proposed, alleviating the need for initialization and assumptions on the nature of the time-intensity curve. They also proposed a correction for the systematic negative estimation bias in the area under the curve, that was shown proportional to the noise level through simulations. From the fitted time-intensity curve, the area under the curve and the mean transit time are extracted. Then flow and volume parameters are derived using the injected quantity of contrast-agent and indicator-dilution theory. They tested their model in vitro, and compared the flow estimated with contrast-enhanced ultrasound with the direct flow measurements of an electromagnetic flowmeter. The fitted curves were strongly to the experimental data ( $r^2 > 0.95$ ), and so were the four estimated and measured flow values ( $r^2 > 0.99$ ). However the number of tested flow rates is only four, which seems small for in vitro experiments.

In 2004, Mischi et al. [105] presented a method to quantify blood volume using the flow and mean transit time estimated in two time-intensity curves derived from contrast-enhanced ultrasound bolus acquisitions, i.e. respectively acquired upstream and downstream of the volume of interest. The expression of blood volume is derived from indicator-dilution theory, and is expressed as the product of the difference in mean transit times with the blood flow. The local density random walk model and the first passage time model were fitted to time-intensity curves to estimate the mean transit time and the flow, and the blood volumes and mean transit times estimated using the two models were then compared through both in vitro and in vivo clinical experiments. These two models were described by Walley and Sheppard [158] and Wise [170], the main difference between them being that the second only accounts for the first passage of the indicator through the sampling site. They were compared by Bogaard et al. [17] in conductivity and thermodilution curves, but this comparison had never been performed for time-intensity curves derived from contrast-enhanced ultrasound

data. Note that the flow was estimated as the ratio of the injected dose to the area under the fitted curve following to indicator-dilution equations presented by Stewart [137] and Hamilton [56]. The authors reported a good agreement between the true and estimated values obtained in the in vitro experiments despite some discrepancies, especially for high blood volumes, and a good agreement between the two models for the clinical data in the absence of ground truth.

In 2008, Mischi et al. [107] established the relation of the commonly-used gamma variate model to indicator-dilution theory using a one-dimensional multi-compartmental approximation of the vascular network. They first gave a physical interpretation, that consists in seeing a blood vessel as a cascade of equal mixing chambers, each compartment having a constant flow, and an exponential impulse responses which time constant is the ratio of the compartment blood flow to the compartment blood volume. They also gave a stochastic interpretation, that models the dilution impulse response a given distance from the injection site, assuming a poisson distribution of the number of individual particle wash-out to the next compartment. Then they revealed the inverse relation between the parameters of the two interpretations, yielding an expression of the tissue impulse response as a function of the wash-out rate and the mean transit time which respects indicator-dilution theorems in the case an ideal Dirac injection. They finally established the relation of the gamma variate model with the local density random walk model using the previously presented physical interpretation. Based on the previously presented methodology [105], the authors were able to estimate the volume of dilution between two measurements of the same bolus, i.e. before and after the passage of the bolus in the volume to be estimated. They performed in vitro experiments with bolus injection, and compared the ability of the two models to estimate the dilution volume in a varying flow setup. Their in vitro findings were compared to those obtained in vivo, through a cardiac clinical study including twenty patients. Time-intensity curves in the left and right ventricle of the heart were derived from contrast-enhanced ultrasound acquisitions following bolus injection of microbubbles in an antecubital vein, using the same imaging apparatus and injection protocol than in vitro. They reported that both models were able to accurately fit both in vitro and in vivo time-intensity curves, and reported on the sensitivity of the local density random walk to initialization. In vitro, the

volume estimations were almost perfectly correlated to the real values using either model, and in good agreement in terms of absolute values, despite the underestimation in the largest volume case. In vivo, because no ground truth was available, they reported on the differences in the estimates of the two models against the mean estimated value through a Bland-Altman plot, and showed a mean difference of 63.1 mL with a standard deviation of 69.7 mL, representing 11.1% of the overall mean estimated volume.

In 2011, Kuenen et al. [83] proposed a modified local density random walk model to reveal diffusion instead of perfusion, motivated by the assumption that this process better reflects tumor angiogenesis. They observed that one of the parameters of the local density random walk model is related to the diffusion coefficient, but that it cannot be interpreted locally in-vivo because of its dependance on the distance from the injection site. They therefore proposed the replacement of the global boundary condition assuming a Dirac bolus injection, which time and distance are needed, by a local boundary condition assuming a normally distributed spatial concentration profile at the time immediately preceding the passage of the bolus at the sampling location. Replacing the old global boundary condition by the new local one yields a new expression of the local density random walk model, from which a local diffusion-related parameter  $\kappa$  can be derived, defined as the ratio of the diffusive time to the squared convective time. The accuracy of the method was investigated by fitting the model to synthetic time-intensity curves simulated using the convective diffusion equation. The model was able to fit the simulated curves accurately, and  $\kappa$  was estimated with a mean relative error of 4.33%. However, when considering curves with recirculation and therefore fitting the model on cropped curves, the authors reported a higher mean relative error of 10.15%. Clinical relevance of the method was assessed in a preliminary study including five datasets from four patients with confirmed prostatectomy. Parametric maps of  $\kappa$  were compared to histology-based tissue classification, i.e. based on the level of cell differentiation. In all patients, authors were able to discriminate cancerous from healthy tissue, i.e. cancerous regions were associated with high  $\kappa$  values. The tissue classification power of both classical semi-quantitative parameters and the parameters of the proposed model was investigated. Optimal threshold values used for classification were estimated through histogram analysis. The authors acknowledge that the proposed diffusion-related parameter,

$\kappa$ , was not the most sensitive investigated parameter, however it was the only one with both sensitivity and specificity above 80%. It also exhibited the highest area under the receiver operating characteristic curve with a value of 0.909.

In an attempt to monitor the microvascularity of colorectal metastasis in the liver of patients undergoing anti-cancer treatment, Averkiou et al. [6] investigated the use of the wash-in time ratio, defined as the ratio of the wash-in time in the metastasis to the wash-in time in normal liver parenchyma. They proposed an empirical model based on the error function to estimate the wash-in time of respiratory-gated time-intensity curves in metastatic and normal tissues obtained by contrast-enhanced ultrasonography. The function under investigation is a time-delayed error function, member of the sigmoid family, with varying rise time and maximum intensity, fitted to the wash-in of the time-intensity curve. Authors stated the rise time parameter is linearly related to the wash-in time. They performed a reproducibility study in five untreated patients with a total of twelve acquisitions, with varying injected quantity and/or injection duration of contrast-agent from one acquisition to another. While the wash-in time in the metastatic tissue exhibited variations up to 30%, the wash-in rate was more reproducible exhibiting an average deviation of 9%, with a maximum of 16%, confirming the expected normalization effect. The ability of the wash-in time ratio to assess treatment efficiency was investigated in a longitudinal study, performed in seven patients undergoing a combination of cytotoxic and antiangiogenic treatments. Major findings include the ability to discriminate good from bad responders to therapy, the ground truth responder classification being assessed by experts using conventional criteria. Indeed, four out of five good responders exhibited a significant rise of the wash-in time ratio after the first therapy cycle, revealing the early normalization of the lesion microvascularity, and the mean increase in wash-in time ratio among the good responders at the end of the treatment was 75%.

### Infusion injection

In 1998, Wei et al. [160] proposed an explicit model to quantify myocardial perfusion. For this method, microbubbles were injected as a continuous infusion. When the micro-bubble concentration reached a steady state, high mechanical index ultrasound pulses were used to

disrupt microbubbles in the myocardium with increasing pulsing interval. This technique is known as intermittent imaging. The video intensity, which was assumed proportional to the concentration in microbubbles, was plotted as a function of the pulsing interval. Then an exponential function with plateau value  $A$  and rate constant  $\beta$  was fitted. Assuming a constant beam elevation, Wei et al. [160] demonstrated that blood flow  $F$  was proportional to the slope at the origin, i.e.  $A\beta$ . The authors validated their approach *in vitro*, but also *ex vivo* and *in vivo* in a canine study. The method was later validated for perfusion quantification of the kidney, estimating both cortical and medullary blood flow in another canine study [161].

The development of power pulse inversion imaging by Simpson and Burns [136] in 1997, allowing real-time imaging of low microbubble concentration at low mechanical index [147]. Tiemann et al. [147] in 1999 and Masugata et al. [95] in 2001 demonstrated the use of power pulse inversion to image the replenishment of tissue following a single series of microbubble-disrupting pulses in real-time. Both study also reveal that the model proposed by Wei et al. could be used to accurately fit real-time replenishment curves.

In 2001, Schlosser et al. [132] applied the same model to quantify renal perfusion, and compared the estimated parameters according to the acquisition sequence, i.e. power pulse inversion [136] vs. pulse inversion [21]. The authors disclosed highly different perfusion parameter values according to the acquisition scheme, which yielded significantly different values of both parameters. However, they were able to distinguish large arteries in the renal hilum from smaller arteries in the renal cortex, using either of the schemes, and either of the parameters.

In 2003, Krix et al. [78] presented a hyperbolic model to quantify perfusion using either intermittent or real-time imaging, relying on physiological considerations, and accounting for the distribution of blood velocities in the tissue. The model assumes a spherical distribution of blood vessel directions with varying blood velocity. This assumption yields an initial linear increase of the concentration until the vessels perpendicular to the imaging plane with the highest velocity are fully refilled. After the initial linear increase in signal intensity, the fully filled vessels do not contribute to signal increase anymore. This yields a non-linear increase until only the vessels with the lowest velocity remain to be fully filled. Finally, all the vessels present in the imaging plane are fully filled and a plateau intensity is reached.

Authors describe an iterative method to estimate the instant of maximum and mean velocity. They state the slope of the replenishment curve observed at these times can be used to evaluate the maximum blood velocity in the region of interest, assuming the width of the ultrasound beam is known. The influence on the width of the blood velocity distribution is visually described. The method was evaluated in a murine study with continuous infusion and intermittent imaging, followed by a bolus injection and intermittent imaging as well [79].

Potdevin et al. [122] investigated the misfit of the exponential model to refill curves and proposed the use of the error function instead. They introduced a time-delay parameter in their model in order to better reflect experimental data. They also investigated the impact of observing multiple blood velocities in the region of interest, as well as the effect of the point spread function of the imaging system through a simulation study and concluded that replenishment curves contain more information than just mean transit time. For instance they were able to reveal the presence of abnormal vascular structures, such as shunting, i.e. direct flow from the arterial system to the venous system without passing through the capillary bed. In a latter study, they proposed an adaptation of the model to quantify local replenishment curves in tissues with complex vascular structures. Replenishment curves are first normalized according to the estimated depth-dependent pixel intensity in a pixel containing only blood. The model accounts for the specific angles, lengths, and velocities of the various vascular structures in the studied tissue [123]. They also used their model as a tissue classifier tool, determining tissue type as the predefined vascular model that best fitted the enhancement curve in the least squares sense. However, applying the simpler exponential model with the average tissue mean transit time on normalized data yielded accurate tissue classification maps, suggesting that the major factor differentiating the replenishment curves of the various tissue types is actually mean transit time. The additional information could be used to characterize vascular properties more finely. In spite, while there is no physical evidence why the exponential model should fit replenishment curves, it remains a good approximation and allows accurate differentiation among tissue types. This is especially true when applied to noisy replenishment curves.

Arditi et al. [3] introduced a new formalism for the quantification of real-time destruction-

replenishment acquisitions using a low mechanical index. The authors emphasize the importance of linearizing ultrasound data according to the type and settings of the imaging equipment, as opposed to grey levels intensities directly extracted from the log-compressed images visible on the monitor. More importantly, they present a perfusion model accounting for the variety in blood flow velocity and direction, assuming a model accurately describing the distribution of transit times is known (e.g. log-normal distribution). The method achieves a better description of the S-shaped replenishment curves that can be observed.

In 2009, Quaia et al. [124] proposed a model reflecting the drag (related to flow) and diffusion (not related to flow) of microbubbles in blood, and accounting for the variety of blood velocities and directions. This variety is modeled as the sum of a variable number of piecewise linear replenishment curves. The model was validated through in vitro experiments using a dialysis cartridge with tubular capillaries, and in vivo experiments in the renal cortex of 12 healthy volunteers, separated in two age groups. While it achieved a significantly better fit than the exponential model using a Wilcoxon signed-rank test, whether the proposed model was using two, three, or four different tracts, the differences in the mean squared error remained extremely small and exhibited non-negligible overlap. Furthermore, while the authors report a significant difference in the initial replenishment slope among the two age groups using the proposed model, based a Mann-Whitney U-test, they do not report on the slope differences obtained using the exponential model, nor on the apparent concordance of the plateau values obtained using the two models.

## 2.2 Deconvolution methods

### 2.2.1 Generalities

Deconvolution-based methods are model-free approaches, assuming a linear and stationary system without any assumption on the underlying structures and processes [86]. Resolving the deconvolution equations necessitates the knowledge of at least two measurements: an input function, and either a residual measurement (i.e. the amount of tracer remaining in the system) or an output measurement (i.e. the amount of tracer leaving the system). In

particular, dynamic perfusion imaging grants access to spatially-distributed measurements of the residual tissue function.

The resolution process aims at estimating the system's impulse-response function, which is theoretically independant on the input, and because no assumption is made on the structure of the system, no assumption is made on the shape of the impulse-response function or on the unit of the measurements. Additionally, the impulse-response function can be seen as the probability distribution of the contrast particles transit times [87]. Parameters describing the systemic response of the vascular system can therefore be derived from the impulse-response function estimated by deconvolution.

In 1962, Zierler [178] established the relevance of the impulse response to assess indicator-dilution curves. He deeply investigated the theoretical aspects of indicator-dilution theory, the conditions for its validity, and the consequences when they are not respected, including when a sudden injection is not truly instantaneous. This section established the theoretical basis for deconvolution of indicator-dilution curves. In another section addressing the impact of recirculation, he established the role of the Laplace transform when solving convolution integrals, as found in his theoretical framework.

In 1966, Coulam et al. [26] proposed deconvolution to estimate the impulse response of coronary and renal circulatory systems, as well as the global circulatory transfer function, in a canine study with one dog. Because a perfect impulse injection is not achievable in practice, the transfer function cannot be estimated directly from the downstream time-concentration curve. Therefore bolus injections of indocyanine green dye were performed in a pulmonary artery and blood was sampled at various downstream sites. Deconvolution of the downstream curves by the upstream curve was performed in the frequency domain by simple division of the Fourier coefficients, and the inverse transform was applied to obtain the transfer function in the time domain. The accuracy of the estimation was assessed both visually and numerically, through time-domain convolution of the estimated transfer function with the upstream curve, yielding an estimate of the downstream curve. Using simulations, the role of the number of harmonics present in the upstream curves was investigated. Indeed, for low numbers of harmonics, oscillations could occur in the transfer function, yielding inaccurate estimation. The authors suggest intra-ventricular injection would

alleviate this issue, as the upstream curve would contain more harmonics.

In 1970, Maseri et al. [94] used deconvolution to estimate the impulse response of the pulmonary circulatory system. Two tracers were injected simultaneously, the first one in the pulmonary artery, and the second one in the left ventricle. Both tracers were sampled at the same site, at the aortic root, yielding two time-concentration curves. The authors used Laplace transforms to demonstrate that deconvolving the first time-concentration curve by the second one yields the impulse response of the pulmonary circulatory system, independently of the systemic recirculation of the tracers. The deconvolution was performed using numerically without any curve fitting, despite the reported instability of the solution. In order to limit this instability, the experiments were adapted consequently. Visual checking was used to assess the accuracy of the estimation, and manual correction was performed when necessary. Biases induced by correction of recirculation through mono-exponential interpolation of the wash-out were reported in case of early recirculation.

A popular matrix-based deconvolution technique was proposed by Valentinuzzi and Montaldo Volachec [152] as a technical note in 1975. The method relies on the matrix formulation of the convolution process, however the set of derived linear equations is solved successively, therefore avoiding matrix inversion which is known to be an ill-conditioned problem. Authors acknowledge the sensitivity of the technique to noise, and warn about the impact of imperfect noise filtering on the estimation process. The role of the sampling interval is also discussed, the authors reveal that increasing it can only improve estimation accuracy up to a point, but demonstrated that increasing it too much could actually increase the estimation error.

In 1976, a deconvolution method said to be insensitive to noise, recirculation, and impulse response shape was proposed by Knopp et al. [75] to assess the impulse response of the coronary bed. The method was tested in a canine study with intra-ventricular injection dye injection, and simultaneous blood sampling at the aortic root and in the coronary sinus. The technique first models the impulse response as a weighted sum of delayed spread functions with unit area, which allowed predetermination of the convolved curves and alleviated the signal periodicity condition, and then iteratively minimized the fit error using a gradient descent algorithm. Impulse functions were first investigated, however spread func-

tions were chosen to reduce the computational load while making the estimation more robust and ensuring similar quality of fit. Experiments reveal right-skewed impulse responses with prolonged tails, suggesting non-monoexponential downslopes expected using classical unimodal functions, i.e. lagged-normal, gamma-variate, lognormal. The authors compared their estimates of mean and standard deviation of transit times to the estimates from previous studies, performed by the same group, but focused on other vascular structures, i.e. lungs [74], descending aorta [12], and femoral artery [11]. Despite the reported parametric overlap, authors observed a rise of the relative variation of transit times correlated with the complexity of the vascular structures, which they justified by reminding that different pathways have different mean transit times and flows.

As soon as 1973, Gamel et al. [48] published a review of the various pitfalls affecting the deconvolution process when estimating vascular impulse responses from indicator-dilution curves. The impact of noise on the estimation of the impulse response by the direct method was first demonstrated on simulated data, establishing the necessity of either using an appropriate noise filtering technique, enforcing some predetermined form to the impulse response, or applying some kind of regularization to the estimation process in order to avoid oscillations and negative values. Six estimation methods enforcing either of the above mentioned strategies were then investigated regarding various considerations. The impact of the data starting point was investigated, especially in the output curve which is usually widely spread and delayed. The authors report poor impulse response estimation in case of noisy time-varying data, despite the accuracy of the reconvolved curves. Then the impact of the numerical approximation which is a consequence discretization process was investigated, while trapezoidal integration exhibited lower error than rectangular integration, both methods proved extremely sensitive to noise.

Additionally, in 1984 Lassen [85] warned about the inability to estimate the blood flow unless the shape of the impulse response is accurately known prior to deconvolution. He said this was necessary in order to accurately determin the height of the initial bolus. And while this is not the object of his letter, he also warned about the lack of direct relations between blood flow and the various semi-quantitative parameters proposed in the litterature.

### 2.2.2 Nuclear medicine

Following the development of renography based on gamma-camera acquisitions by Short et al. [135], Kenny et al. [67] used a deconvolution technique first presented in [47], based on the Laplace transform, in an attempt to make the estimation of the kidney function independent on the spread of the bolus when it enters the kidney, and assessed it in a clinical study. The approach accounts for both the establishment of an equilibrium of the tracer in the extravascular space, spread of the bolus during its passage through the kidney, and the removal of the tracer from blood by the kidney assuming bi-exponential clearance in the cardiac measurements. The impulse response of the kidney vascular network was estimated from the Laplace-derived formula established in the paper, involving the renal time-activity curve, its derivative, its integral and various constants to be estimated. Because scintigraphy is a projection imaging technique, the background activity was subtracted using the regions between the two kidneys to obtain the activity as specific to the kidney as possible. This was encouraged by the similarity of the activity curves in this region with those of the nephrectomy sites observed in fifteen kidney-ablated subjects. Authors were able to distinguish healthy kidneys from those affected by various diseases, indeed all affected kidneys exhibited longer minimum, mean, and maximum transit times, and a wider transit time distribution. Additionally, they were able to distinguish between the various studied diseases using the same criteria. Appledorn [2] responded to the publication and expressed his disagreement regarding the formulation of the clearance function, arguing that the input to the renal system depends on the negative time derivative of the cardiac curve. He explained his reasoning mathematically, assuming a two-compartment model previously presented in the litterature [30], and proposed a correction for the renal input function.

Diffey et al. [34] proposed the use of the matrix-based deconvolution method, first generically introduced by Valentinuzzi and Montaldo Volachec [152], to quantify the impulse responses of the renal parenchyma and renal pelvis to a bolus injection of  $^{99m}\text{Tc}$ -DTPA. They used the iterative data-bounding technique prior to deconvolution for noise removal, the technique is detailed in [33]. Non-renal activity is assumed qualitatively similar to arterial activity, thus the correction is simply applied by setting the first term of the impulse response

equal to the second one. The impulse response of the renal parenchyma was obtained by deconvoluting the parenchymal curve by the arterial curve. The impulse response of the renal pelvis was obtained by deconvoluting the pelvic curve by the parenchymal curve. Accounting for the regional variations of tracer retention enabled the authors to differentiate between patients with and without pelvic obstruction, and proved to be an efficient tool to assess the renal function. Authors regret that the spatial resolution of the gamma-camera did not enable to distinguish between cortical and medullary structures.

In 1979, a Fourier-based deconvolution technique was proposed by Alderson et al. [1] to quantify left-to-right cardiac shunts from time-activity curves from scintigraphy following bolus injection of  $[^{99m}\text{Tc}]$ pertechnetate in a canine study. The shunt quantification technique used the gamma-fitting technique first presented by Maltz and Treves [93], and was preceded by either low-pass filtering in the frequency domain, or smoothing of the deconvolved curves in the time domain, in order to reduce the high frequency components, and thus the oscillations observed in the obtained impulse responses. The ability of the technique to estimate the impulse response in case of either prolonged or fragmented bolus was investigated. The technique was able to significantly improve the accuracy of the shunt estimation in case of prolonged bolus, and while time-domain smoothing improve the accuracy of the estimates, frequency domain filtering proved more efficient. However none of the techniques yielded satisfactory results in case of fragmented bolus.

### 2.2.3 X-rays

In 1982, Axel [8] proposed a deconvolution technique to estimate the mean transit time of contrast-enhanced X-ray computed tomography acquired in the brain, where iodinated tracers do not diffuse in the extravascular space. Because the only considered parameter under investigation is the mean transit time, the authors consider the shape of the impulse response unimportant, with only a measure of its width being required. Authors demonstrates this by estimating the impulse response as an exponential function, a Fermi function and a step function. The Fermi and the step functions yielded similar estimations of the mean transit time, however the exponential function yielded lower values of the parameter. Additionally, the Fermi and step function achieved slightly better fits than the exponential

function, but the difference was not found significant. The method previously presented in [7], was used as a reference. The mean transit time was defined as the difference of the first moments of the tissular and vasclar curves following gamma-variate fitting. The mean transit time estimated using this method seem to best agree with the mean transit time values obtained using the exponential impulse response. The author assumes that the impulse response function in most tissues are likely to have a squared shape with rounded corner, which the Fermi function can easily approximate. They comment on the insensitivity of the method to noise compared to transform-based methods, as well as recirculation without needing curve fitting and extrapolation.

In 1992, Yeung et al. [174] presented a single photon absorptiometry method to quantify arterial concentration of iodinated contrast agents using blood sampling, and investigated it through both preclinical and clinical experiments. A deconvolution method was used for the quantification, it was proposed by the research group the same year, however while the paper was submitted it seems it has never been published. The only given details are that it uses a non-negative least square algorithm [89] to ensure that only physiologically relevant positive values can occur in the impulse response function, and that estimated function must be smooth. In 1999, Cenic et al. [24] reused the deconvolution method to quantify dynamic perfusion computed-tomography following bolus injection of iopamidol in white rabbits. Three regions of interest were defined in the brain, i.e. two in the parietal regions, and one in the basal ganglia. Multiple arteries were present in the image, i.e. ear arteries, postcommunicating arteries, and internal carotid arteries. In order to limit the impact of partial volume effects, the chosen artery was the one with the largest cross section seen in the image which resulted in the highest peak average intensity, typically an ear artery. Additionally, partial volume effects were corrected by first fitting a gaussian curve to the non-contrast profile of the artery to obtain its standard deviation. This parameter was used to estimate a partial volume scaling factor, using a formula resulting from phantom experiments of tubes with known inner diameters and tracer concentrations. Finally the arterial intensities were divided by this factor to correct for partial volume effect. Non-contrast scan intensities were subtracted from the average curves in the three regions of interest, as well as from the average arterial curve. Deconvolution allowed the estimation of regional cerebral blood flow, cere-

bral blood volume, and mean transit time. For comparison purposes, the regional cerebral blood flow was also estimated using microspheres measurements, which was considered the ground truth. The authors report good agreement of the measured regional cerebral blood flow as they obtained a slope close to unity in a linear regression analysis, and correlation between measurements was good but far from perfect ( $r = 0.837$ ). When repeated studies were performed, i.e. in five of the six cats included in the study due to sudden death of the sixth rabbit, no significant differences were found between the parameters from the various acquisitions, however the computed-tomography estimates of regional blood flow were ten percent more variable than with the microspheres.

Wintermark et al. [168] compared the results of two deconvolution methods to quantify perfusion computed-tomography exams, using stable xenon computed-tomography as a reference. The first deconvolution is performed using a commercial software, known as *CT Perfusion* (GE Medical Systems). The software basically uses an improvement of the method proposed by Cenic et al. [24], allowing processing of pixel-by-pixel parametric maps with improved stability, by means of a singular value decomposition enforcing noise filtering by thresholding of the singular values. Additionally, the computation time is considerably reduced using this method, which makes it usable in clinical routine. The second method uses a least squares minimization technique with improved stability, taking advantage of prior rank determination through QR decomposition with pivoting, i.e. decomposition of the matrix of shifted observations as the product of an orthogonal matrix, an upper triangular matrix, and a permutation matrix [53]. The authors report a good agreement between the reference method and both the commercial package and the presented method estimates of cerebral blood flow compared to the reference method ( $R^2 = 0.79$  and  $0.67$  respectively), as well as between the two investigated deconvolution methods ( $R^2 = 0.72$ ). However, the methods were shown to differ in terms of spatial filtering of the parametric maps, as well as in the detection thresholds of vessels. Indeed, regions with arterial branches are filtered away using the commercial software, while they exhibit a higher cerebral blood flow using the improved least squares method. Note that these regions with branches are neither visible in the reference method.

Eastwood et al. [37] used the commercial perfusion quantification software presented

above to quantify brain perfusion in patients with acute stroke. Hoeffner et al. [62] provided a review of the technique, as well as the various applications, and limitations of this quantification software. The larger anterior artery was used as an arterial input function, and the superior sagittal sinus was used as a venous outflow function. The authors report significant differences between the healthy and affected hemispheres in either of the three parameters derived from the deconvolution of signals, i.e. cerebral blood flow, cerebral blood volume, and mean transit time. They also observed significant differences between low-enhancement and normal-enhancement regions for cerebral blood flow and cerebral blood volume. Additionally, inter and intra observer variation were investigated and showed good agreement between and within observers.

Cuenod et al. [28] proposed a deconvolution-based method for the quantification of perfusion in metastasis bearing rat livers using contrast-enhanced computed tomography accounting for both arterial and portal supplies, with bolus injection of iobitridol, a iodinated contrast-agent. Because the arterial and portal components are totally mixed in the sinusoidal capillaries, the system assumes a common impulse response for both components shaped as a Weibul function, however the two inputs are weighted. This technique allows the estimation of the hepatic blood flow, which can be separated in two components, yielding the arterial and portal blood flows, and the tissue blood volume. The mean transit time of the contrast agent was also estimated from the impulse response of the system. Additionally, the complementary weights of the two blood supplies allow the estimation of a parameters called the hepatic perfusion index, which is the ratio of the arterial blood flow to the total blood flow. The perfusion of micro and macro metastases were compared to normal liver tissue using the above cited parameters, and significant differences were found in mean transit time, total hepatic blood flow, and portal blood flow for both types of metastases, but also in hepatic perfusion index and the tissue blood volume for macro metastases. The theoretical aspects of the method were presented in more details in [29]. This other study actually investigates the use of two contrast agent, a classical iodinated contrast agent that diffuses in the extravascular space, i.e. iobitridol, and a macromolecular iodinated contrast agent that mostly remains in the intravascular space with little capillary leakage, i.e. carboxyl dextran. The authors report larger estimates of the mean transit time using the macromolecular

contrast agent. Moreover, when comparing hepatic perfusion indices in normal liver tissue with metastatic tissue, the observed much larger values in the metastasis, a large reduction in hepatic blood flow, as well as lower tissue blood volume. The method proved robust to recirculation, which alleviates the necessity for gamma-variate fitting to get rid of recirculation. This is particularly important in the liver, for arterial and portal components partially overlap.

Kudo et al. [82] investigated variants of the singular value decomposition deconvolution method, developed for delay-insensitive deconvolution of magnetic resonance data, and their sensitivity to the tracer time delay. The authors compared regional blood flow, regional blood volume, and mean transit time estimates of the standard singular value decomposition algorithm, to the estimates of a delay-insensitive block-circulant deconvolution method introduced by Wu et al. [171], as well as a delay-corrected deconvolution method proposed by Ibaraki et al. [63]. The three methods were investigated on synthetic datasets varying the tracer delay in the left hemisphere. The block-circulant approach was the most insensitive to tracer delay while the standard method was the most sensitive, and the delay-corrected method yielded intermediate results.

#### 2.2.4 Magnetic resonance

Rosen et al. [131] proposed a review of the contrast agents usable for perfusion imaging using magnetic resonance, depending on the property involved, i.e. relaxivity or susceptibility. He also addressed the perfusion quantification techniques for contrast-enhanced magnetic resonance data, often inspired by the advances in the other perfusion imaging modalities. The main goal the authors want to reach is the estimation of tissue blood flow, and they rely on the central blood volume principle established by Stewart [137], which defines tissue blood flow as the ratio of the tissue blood volume to the mean transit time. They recommended estimating the mean transit time through deconvolution, suggesting the use of Fourier-based methods, and proposed the tissue blood volume as the ratio of the areas under the tissular and arterial curves, as proposed by Lassen et al. [87] for indicator-dilution theory, and Axel [7] for perfusion computed-tomography imaging.

Rempp et al. [127] investigated susceptibility Gd-DTPA2-enhanced magnetic resonance

imaging to quantify cerebral perfusion in a clinical study with twelve healthy patients with intact blood-brain barrier. A dual FLASH sequence was used, allowing interleaved acquisition in two parallel sections, one being the section of interest, the other one containing the feeding arteries. The arterial input function was estimated directly in the imaging plane, either in the carotid or in the vertebral arteries, and the segmentation was performed on pixel-by-pixel maps of semi-quantitative parameters, i.e. the full width at half maximum, peak intensity, and time to peak intensity. More precisely, adaptive thresholding was first performed on the full width at half maximum and peak intensity maps, and only pixels with peak intensities over 75% of the maximum intensity in the image were retained. The authors defined the regional cerebral blood volume as the ratio of the area under the curve in the tissue of interest to the area under the arterial input function, as suggested by indicator-dilution theory, but corrected the estimate for both brain tissue density and hematocrit variations from arteries to smaller blood vessels. Fourier deconvolution enforcing noise filtering by means of a Weiner filter was used to estimate the impulse response of the tissue of interest. Then the mean transit time was estimated as the ratio of the area under the impulse response to its height. Regional cerebral blood volume and blood flow were estimated in both gray and white matter for every patient. The authors report an overall decrease of both perfusion parameters with age, and suggest this explains the large standard deviations of their estimates.

Wilke et al. [167] used a low-order vascular transport operator, presented in [72], to model the vascular impulse response using magnetic resonance imaging with bolus injection of an intravascular contrast agent, i.e. polylysine-Gd-DTPA. They compared their perfusion estimates in the myocardium of dogs, with and without induced coronary stenosis, to the perfusion parameters obtained using radiolabelled microspheres. Contrast signal intensities were normalized according to the pre-contrast values, as well as from the signal intensities observed in an oil phantom placed under the chest of the dogs. The vascular transport operator accounts for the pure delay of the contrast agent, but also for the dispersion of the bolus by means of a fourth-order linear differential operator, resulting from the combination of two attenuated second-order operators in series. The model is therefore parameterized by two parameters only, i.e. the mean transit time of the impulse response, and the relative

dispersion which is defined as the ratio of the standard deviation of the impulse response to its mean transit time. The model is fitted using a fast iterative derivative-free approach presented in [25], which performs non-linear least-squares fitting without making assumptions on the data variance through data weighting. Despite imperfect registration between magnetic resonance estimates and tissue analysis for quantification of microspheres, good agreement between the measurements was reported regarding both myocardial blood volume and myocardial blood flow. Myocardial segments that were hypoperfused because of coronary stenosis were accurately identified using the proposed method.

Østergaard et al. [113] reviewed the various deconvolution approaches which had already been applied for the quantification of perfusion using contrast-enhanced imaging using simulated magnetic resonance data, especially in the case of cerebral imaging where the tracers remain intravascular thanks to the blood-brain barrier. The models are divided between model-based and model-free approaches, the former referring to a one-compartment model with exponential impulse response [41], the latter referring to either transform approaches through the Fourier method [26], algebraic approaches through a matrix-based method [152] with an additional regularization term enforcing decreasing impulse response, or SVD approaches through a classical method with filtering of components which singular values are close to zero [34]. The weight of the regularization term in the algebraic method, as well as the thresholding value for the SVD approach were determined empirically, and chosen as the values that yielded the most accurate impulse responses and cerebral blood flow estimates on twelve representative simulated cases. Multiple factors and their impact on the regional cerebral blood flow estimates were investigated in this simulation study, i.e. noise, vascular structure, cerebral blood flow, cerebral blood volume, and time-delay. Expectedly, the model-based approach was not able to correctly estimate cerebral blood flow when the vascular structure used for simulation did not match the one-compartment model assumption. The Fourier method proved sensitive to the cerebral blood flow, indeed the estimation error was negatively correlated with the simulated value, but also to the simulated vascular structure. The regularized algebraic approach proved to overestimate blood flow for a low cerebral blood volume (3%), and to yield more accurate estimates for higher cerebral blood volume (4.5%), the authors therefore concluded on the sensitivity of the method to

cerebral blood volume. However the authors discuss the possible role of the regularization weight in these variations, as modifying the cerebral blood volume effectively modifies the signal to noise ratio, which does could then differ from the conditions for which the weight was optimized. While the opposite behaviour seems to be observable in the SVD estimates, the authors considered that the bias in the estimation of cerebral blood flow was insensitive to cerebral blood volume. Additionally, when a time delay was added to the simulated curve, the SVD greatly underestimated cerebral blood flow, in particular for large simulated flow values, emphasizing the need for delay correction prior to the estimation process. Model-free approaches were able to estimate cerebral blood flow accurately, however they generally failed to accurately match the shape of the impulse response function. Globally, all approaches were less precise in case of shorter mean transit time values, which the authors justified as a consequence of the arterial input function varying slowly compared to the mean transit time, which determines the time-scale of the impulse response to be estimated.

The second part of the study [112] confronts the models assessed through simulations to experimental contrast-enhanced magnetic resonance data acquired in six healthy subjects, as well as in four clinically relevant cases, following automatic bolus injection of paramagnetic contrast-agents, i.e. Dy-DTPA-BMA, and Gd-DTPA respectively. An additional model-based approach was introduced in the experimental part of the study, i.e. the decreasing part of a Gaussian was proposed as an ad-hoc intermediate between the exponential (one-compartment model) and the square (plug-flow model) impulse responses. All image sequences were filtered using a  $3 \times 3$  averaging kernel prior to deconvolution. The arterial input function was estimated in pixels located around the middle cerebral artery. The time-concentrations curves used for quantification were not converted in actual units, instead a constant hematocrit throughout the brain was assumed, and white matter was used as a reference. Additionally, because time-delays tended bias the estimation of blood flow in the simulation study discussed above, the influence of this parameter was investigated in multiple slices by comparing the estimation of the arterial input function along the middle central artery. This study revealed very little dispersion and delay along major arteries, and the authors mainly attribute this delay to the delay between the acquisition of the different slices. They however suggested that appropriate time correction should be applied when quan-

tifying multiple slices using a common arterial input function estimated in a single slice. However, some cases exhibited time-delays in regions supplied by other arteries, in particular the cerebellum, and in the occipital region which are mainly supplied by the posterior cerebral artery. For all approaches the cerebral blood flow was defined as the maximum of the impulse response curve, and the cerebral blood volume as its area under the curve. In healthy patients, the exponential and SVD approaches yielded very similar parametric maps. The regularized algebraic approach yielded very high flow in the grey matter which can be explained by the high cerebral blood volume in this tissue. The Fourier approach yielded poor contrast between the grey and white matters, confirming the sensitivity of the method to the cerebral blood volume and vascular structure. Strong differences, i.e. almost 2-fold, were observed between the cerebral blood flows estimated using the exponential and Gaussian models, indeed a better agreement was found between the SVD and exponential approaches. Moreover, the fit quality was considerably lower using the Gaussian model, suggesting that the exponential model is a better approximation to model cerebral impulse response.

Inspired by the work of Axel [8] for quantification of perfusion computed-tomography, Jerosch-Herold et al. [64] proposed a Fermi function to model the myocardial impulse response in an attempt to quantify the myocardial perfusion reserve from the first pass of a bolus of Gd-DTPA imaged using a multislice magnetic resonance imaging technique. Interestingly, the convolution operation was performed as a product in the frequency domain, following Fourier transform, but the non-linear least-square fitting was performed in the time-domain, following inverse Fourier transform of the convolved functions. Since two measurements are necessary to estimate myocardial perfusion reserve, two magnetic resonance sequences were acquired to assess this parameter in nine patients with suspected microvascular disease. The first acquisition was performed at rest, and the second was performed during adenosine-induced maximum hyperemia. Fermi-based deconvolution was then performed for both exams, using the left ventricle blood pool as an input function. The myocardial blood flow was defined as the maximum value of the Fermi function, i.e. initial value, and the myocardial blood reserve was obtained as the ratio of the hyperemic blood flow to the basal blood flow. The coronary flow reserve estimated in the left anterior coro-

nary artery using intracoronary Doppler ultrasound was used as a gold standard. Good agreement was found between the reference measurement and the perfusion reserve estimated in the left anterior coronary artery region ( $r = 0.84$ ) with a regression slope close to the unit but with high uncertainty ( $0.98 \pm 0.24$ ). Moreover, even if the data is not presented, agreement between the perfusion in the left anterior coronary artery region and the perfusion reserve averaged over the entire myocardium is reported. They also assessed the ability of the method to estimate blood flow reserve from synthetic data, resulting from random solutions of the multiple-pathway perfusion model described in [81] with simulated uniform random noise. The authors report excellent correlation between the simulated and estimated values ( $r = 0.98$ ) with a regression slope close to the unit ( $1.04 \pm 0.029$ ). However, accounting for capillary permeability responsible for the leakage of contrast agent in the interstitial space in the simulation process, i.e. varying the permeability surface area product, had a direct impact on the simulated curves, but induced a variation of less than ten percent in the estimates of the myocardial perfusion reserve. The impact of varying upstream bolus dispersion, capillary permeability, blood volume, blood flow, sampling frequency, and injection speed on the estimated parameters was also investigated.

### 2.2.5 Ultrasound

In 2004, Mischi et al. [105] proposed a semi-quantitative method to assess pulmonary blood volume in cardiac contrast-enhanced exams. The semi quantitative aspects of the methods are discussed in details in Section 2.1.5. However, prior to being fitted by either the local density random walk or first passage time models, the time-intensity curves were deconvolved using a Wiener filter to correct for the non-instantaneous bolus injection. Because the bolus was injected using an automatic system, the arterial input function was not estimated from image measurements in this study, instead it was modeled as a 0.8 second rectangle function corresponding to the settings of the electronic injector. The ability of the Wiener filter to accurately recover the original simulated time-intensity curve from noise-corrupted convolved curves was assessed.

In 2005, Mischi et al. [106] used the same deconvolution method, but this time applied it to the estimation the impulse response of a vascular system located between two measure-

ment sites. In particular, the goal of the study was to propose an accurate measurement of the forward ejection fraction, even in case of leakage through the mitral valve, hence the use of a contrast-enhanced imaging modality, but avoiding the invasive intra-ventricular injection and replacing it by intravenous injection. To meet this goal, the authors propose estimating the impulse response from the attenuation-corrected time-intensity curve measured in the left ventricle, assuming a one-compartment model, and using the signal measured in the left atrium as an input function. After estimation of the noisy left-ventricular impulse response by the Wiener filter deconvolution, an exponential curve resulting from the one-compartment model assumption was fitted to its downslope, from which the forward ejection fraction can be derived. The accuracy and precision of the deconvolution method was assessed through simulations with varying signal to noise ratio and forward ejection fraction, and good agreement between the simulated and estimated values of both blood volume ( $R^2 = 0.99$ ) obtained using the methodology previously described in [105] (see Section 2.1.5). Contrast-enhanced ultrasound data were acquired in twenty patients following the injection of a small quantity of microbubbles, therefore limiting commonly observed saturation artifacts. The forward ejection fraction was estimated with and without deconvolution of the left-ventricular time-intensity curves, and the results were compared to the ejection fraction estimated using an established bi-plane echocardiographic method [20]. The results without deconvolution clearly underestimated the ejection fraction as measure by the reference method, despite a seemingly good correlation of the two measurements. However, using the deconvolution-based method an excellent agreement of the estimates is reported, indeed the correlation is high ( $R^2 = 0.93$ ) with a mean bias of 1.6%, and a standard deviation of 8%, demonstrating the feasibility of the method.

Gauthier et al. [49] used a deconvolution method based on singular value decomposition, but enforcing Tikhonov regularization to reduce the rapid oscillations in the impulse response function, and finally the impulse response is fitted by the explicit model by Elie et al. [38] presented in Section 2.1.5. The blood flow and the blood volume were then derived from the model fitted to the estimated impulse response, and were respectively defined as the peak value, and the area under the curve. The additional regularization term was weighted, and the determination of this weighting parameter was determined using the

L-curve method described in [57]. The reproducibility of the method was assessed through both in vitro and in vivo experiments, and was compared to the semi-quantitative parameters extracted from the time-intensity curve fitted with the same explicit model, without deconvolution. The in vitro experiments consisted in five acquisition following bolus injection of microbubbles in phantom composed of a feeding pipe and three intertwined pipes, injecting two different volumes of contrast agent. The absolute parameters tend to be slightly less variable than the semi-quantitative parameters of the other method, however no statistical tests were reported, and neither were the estimated parameter values, forbidding the validation of this quantification method by comparison to the in vitro experimental parameters. In vivo, three consecutive acquisitions were performed in five tumor-bearing mice, using an arterial input function estimated directly from the imaging plane in a feeding vessel that was previously detected using Power Doppler imaging. Once again, only the variability of the parameters was reported, the estimated values were not reported, and no statistical analysis was performed.

Jirik et al. [65] proposed a contrast-enhanced ultrasound acquisition scheme referred to as bolus-and-burst for it combines bolus injection and destruction-replenishment, as well as a blind deconvolution method, specific to their custom acquisition scheme, for simultaneous estimation of the arterial input function and the tissue impulse response. As the name suggests, the acquisition is divided in two main parts. The first part consists of a classical low mechanical index image acquisition to image the passage of a bolus of microbubbles injected intravenously. Then, at the end of the bolus-phase, when the concentration of contrast agent in the tissue decays rather slowly, a sequence of high mechanical index pulses are sent to disrupt the circulating microbubbles. The second part is another classical low mechanical index acquisition to image the replenishment of contrast agent in the tissue. A blind deconvolution algorithm is then applied to the average time-intensity curve in the tissue of interest. The quantification is divided in two parts as well. First a rough estimation of the tissue impulse response is performed from the destruction-replenishment curve using [156], i.e. a quantitative formulation of the monoexponential model proposed by Wei et al. [160]. This initial impulse response estimate is then used to roughly estimate the arterial input function by deconvolution of the bolus-phase. In the second part, the arterial input function and the tissue

impulse response are refined by multichannel deconvolution, considering the two parts of the acquisition are independent measurement with a common impulse response. To ensure physiologically relevant and smooth estimation of the arterial input function, a positivity constraint as well as a Tikhonov regularization are enforced. The authors investigated several techniques to address the problem of absolute quantification, and retained the use of a population-based scaling constant resulting from previous acquisitions in feeding arteries with lower contrast agent doses, as proposed by Taxt et al. [141] for magnetic resonance imaging. The sensitivity of the method to the number of pixels in the regions of interest was compared to the burst-replenishment method in terms of mean transit time.

## 2.3 Compartmental models

### 2.3.1 Generalities

The major assumption underlying compartmental modeling is that the tissue under investigation consists of three well-mixed subcompartments: a vascular space, an interstitial space, and a cellular space. Compartmental models estimate the vascular impulse response of a tissue making assumptions on its shape, depending on the characteristics of the tissue, as well as the characteristics of the contrast agent, i.e. flow limitation, membrane limitation, transport mechanism, binding, excretion, metabolism [50]. The exchanges of tracer between the compartments are modeled using differential equations, establishing the relations between the concentration of tracer in each compartment in terms of physiological parameters, i.e. blood flow rates, tissue volumes, transfer constants. Resolving the differential equations yields explicit parametric formulations for the vascular impulse response, allowing direct estimation of the physiological parameters. The explicit formulation of the impulse response function improves the stability of the estimation by reducing the number of degrees of freedom.

Early use of compartmental models to fit indicator-dilution curves was based on the Fick's principle that relates the blood flow to the arterial and venous measurements [69, 70]. Kety and Schmidt [70] derived a method to estimate cerebral blood flow from arterial and

venous blood sampling during inhalation of nitrous oxide, and assessed it in a clinical experiment with eleven subjects. The method corrected for the rise of the time-concentration curve using a fixed ratio of the amplitude of the monoexponential model fitted to the decay phase. Following these developments, the authors proposed a one-compartment model based on the same principle to assess fractional blood flow and fractional blood volume assuming a perfectly diffusible tracer [68].

In 1953, Pappenheimer [114] addressed the subject of the passage of molecules through capillary walls and proposed a method for the quantification of capillary permeability using a two-compartment model assuming free diffusion of the tracer based on Fick's law.

Renkin [128] studied capillary permeability to  $K^{42}$  in skeletal muscles using another diffusion model based on Fick's law. The authors used the permeability surface product as a combined parameter of the model, and established its correspondance to the maximum capillary clearance possible for a given substance assuming an infinite flow. However they proposed a method to quantify the clearance at any flow rate assuming the permeability surface product is known. They explained the variations of the estimated permeability surface product by hemodynamic factors, i.e. arteriovenous shunting, inhomogeneous flow distribution, flow-dependant perfusion network.

Crone [27] developped the indicator diffusion method that relates the capillary permeability to blood flow, capillary surface area, and initial extraction which corresponds to the fractional reduction of the arterial concentration, however litterature values for the two first parameters were used and only the initial extraction was estimated. The authors performed blood sampling experiments in dogs with injection of Evan's blue dye or a combination of insulin and sucrose to study the capillary permeability of these substances in multiple tissues, i.e. brain, kidney, liver, lung, hind limb.

### 2.3.2 Nuclear medicine

Gjedde [52] used a formula from Crone [27], and the previous developments of the group presented in [51], to derive two integral methods to estimate rate constants of glucose from blood to brain tissues in rat experiments. The methods consider the exchanges between the capillary and extracellular space, as well as the metabolic pools reflecting consumption of

glucose by brain cells. The first method estimated the initial rate constant as the difference of the total amount of tracer in the brain and the amount of plasma in brain twenty seconds after injection, normalized by the area under the arterial curve up to twenty seconds. The second method exploited dynamic measurements to derive a graphical method, allowing the conjoint estimation of initial rate constant, and plasma volume, respectively as the slope, and intercept in the linear regression analysis of the ratio of the total amount of tracer in the brain to the arterial concentration, and the ratio of the total amount of tracer that passed in the artery to the arterial concentration. Their experiments led them to the conclusion that the two methods estimated two different transfer rates, reflecting at least two transport mechanisms, i.e. a high affinity system with low capacity, and a low affinity system with high capacity.

Similarly, Patlak et al. [116] proposed a graphical analysis method in 1983 to estimate transfer constants across the blood-brain barrier for irreversible tracers. The method is able to estimate the influx rate in any membrane system composed of at least one region with reversible exchanges without metabolism where the tracer rapidly equilibrates with the plasma and one region with irreversible exchanges. The methods consists in plotting the ratio of the curve in the tissue of interest to the plasmatic curve vs. the ratio of the integral of the plasmatic curve to the plasmatic curve, and fitting a affine model to the linear portion of the resulting curve that corresponds to the steady-state of the system. The slope of the fitted linear model yields the influx rate from plasma to tissue, while the intercept yields an upper bound to the reversible plus plasmatic fractional volumes.

Patlak and Blasberg [115] then generalized the method to analyze time-intensity curves using a reversible reference tissue instead of the arterial measurement, yielding an estimate of the ratio of the influx rate of the tissue to the sum of the reversible and plasmatic fractional volumes. They also addressed cases when tracer binding is incomplete in the irreversible compartment, for both arterial and reference measurements, and presented specific applications of the method.

In 1990, Logan et al. [91] proposed a graphical analysis method to analyze the kinetics of reversible tracers, binding reversibly to receptors or enzyme, and applied it to estimate the parameters of the three-compartment model to characterize the binding of a radiola-

beled cocaine complex in a positron emission tomography study. This is an extension of the method proposed by Gjedde [52] to account for rapid binding and unbinding of the tracer where the graphical analysis is performed similarly. In terms of two-compartment model, the distribution volume can be derived from the slope of the linear portion of the plot. In terms of three-compartment model, an additional measurement is necessary to determine the ratio of binding to unbinding rate from the ratio of the slopes in a receptor tissue to a non-receptor tissue assuming the plasmatic volume is negligible.

The authors later extended the graphical analysis method to estimate distribution volume ratios, defined as the ratio of the distribution volume of a tracer in a receptor tissue to a receptor-free tissue. The method allows the estimation of the distribution volume ratio from studies without arterial blood sampling, using only the curves extracted from the image in two regions. The direct distribution volume ratio estimation using the proposed method was compared to the ratio of the distribution volumes in the two tissues obtained using blood sampling data in a positron emission tomography study with injection of <sup>11</sup>C-labelled raclopride or d-threo- $\alpha$ -methylphenidate. The method requires the knowledge of the average tissue to blood rate constant, as well as the determination of the initial time at which the slope should be estimated, which can be obtained from baseline experiments requiring blood sampling for calibration.

In case of noisy data, the linear formulation of the compartment model can yield underestimated distribution volume estimates because the error are cumulative in the integral terms [45]. Logan et al. [92] proposed a strategy to remove the bias in the graphical analysis method, using the generalized linear least-squares algorithm proposed by Feng et al. [46] to determine the distribution volume directly for one-compartment models or as a smoothing technique prior to graphical analysis for more complex model structures.

In 1984, Hawkins et al. [59] used a two compartments model based on the equation of the graphical analysis with a vascular component, however they directly estimated the parameters of the model using a non-linear least-squares algorithm to fit the model, after resolution of the differential equations that relates the curve in the tissue of interest to the arterial measurement. The non-linear resolution of the equations yields a convolution formulation assuming a decaying monoexponential tissue impulse response function. The method

was used to estimate influx and outflux rate constants, as well as the blood volume fraction from which estimates of the regional cerebral blood volume corrected for the differences in hematocrit were derived, and compared it to direct measurements obtained using a method previously described in [120].

Ziegler et al. [177] compared a dual-input and a single-input compartmental model and their ability to quantify blood flow in dog liver using dynamic positron emission tomography data following injection of a bolus of  $^{15}\text{O}$ -labelled water. On the one hand, the dual-input model accounts for the arterial and portal supplies of the liver using direct measurements resulting from blood sampling. On the other hand, in the single-input model the determination of the portal supply is part of the fitting procedure, and is derived from the arterial measurement resulting from blood sampling by considering a gut compartment, based on a one-compartment model, which distribution volume was fixed and derived from post-mortem experiments in dogs. Additionally the models correct for time-delays and dispersion using the method presented in [99]. Both models make the assumption that the blood supplies diffuse instantaneously from vasculature to the liver tissue, and that the volume of distribution of the tracer is the same for arterial and portal blood. The volume of distribution in the liver was fixed during the estimation process of both model, however the authors report high sensitivity of blood flow, dispersion and fit accuracy to the chosen value. The single-input model additionally enforces a fixed ratio of gut tissue to liver tissue volume. Poor agreement of the blood flow estimates of the dual-input and single-input models was found with microsphere measurements, however the single-input model performed slightly better.

In 1984, Blomqvist [16] proposed a linear formulation of a three-compartment model presented by Raichle et al. [125] obtained by rearranging and integrating twice the second-order differential equations relating the arterial concentration to the tissue concentration. The method was used to derive functional maps from dynamic positron emission tomography data of tracers marked with  $^{11}\text{C}$ . The three-compartment model was composed of a vascular compartment, and two extravascular compartments, one representing the extravascular space exchanging with the plasma, where the tracer is unmetabolized, and the other representing the metabolized compartment. The authors estimated the tracer transfer rate

constants from blood to tissue and from tissue to blood, as well as its metabolizing rate, by solving the system of equation using standard linear least-squares methods. The proposed linear estimation method was compared to the non-linear estimation of the three-compartment model using clinical positron emission tomography data, and good agreement were found between the estimates of the two methods, especially for blood to tissue transfer rate, and for the cerebral metabolic rate for glucose utilization, a composite index which definition can be found in [126].

Gunn et al. [54] reviewed the compartmental models used for quantification of dynamic positron emission tomography data, whether assessing perfusion, metabolism or ligand binding. This theoretical study investigates both models using arterial input functions and models using reference tissues, as well as reversible and irreversible tracers, regardless of the number of compartments involved. General solutions for the impulse response are given in the form of sum of weighted exponential functions, which weight and rate constant are to be determined. The authors revealed that all the micro parameters of a perfusion model cannot be estimated individually, instead one should interpret the macro parameters that the authors defined in terms of the micro parameters, as the estimation of the latter is generally more stable. Additionally, investigating models using a reference tissue region they showed that the macro parameters are expressed relatively to the reference region, and proposed a correction for the bias in graphical estimation methods when the contribution of blood in the reference and studied tissues cannot be neglected.

Watabe et al. [159] also proposed a review of compartmental models for quantification of dynamic positron emission tomography data, especially addressing the models for the quantification of binding tracers. The classical model counts four compartments, i.e. an arterial compartment exchanging with a free compartment, that exchange itself with a specific binding compartment, and a non-specific binding compartment. The specific binding compartment is generally the compartment of interest when studying binding tracers. If the non-specific binding compartment is in equilibrium with the free compartment, then these compartment can be merged, reducing the number of parameters by two. Similarly, the simple one-compartment model, that only considers the exchanges between plasma and tissue through two rate constant parameters, can be used in flow limiting conditions, i.e. when a

quick equilibrium is reached between the free compartment and the binding compartment, or when using non-binding intravascular tracers. It was first proposed by Kety and Schmidt [69] in 1948 to quantify blood flow using  $^{15}\text{O}$  labelled water as a tracer.

### 2.3.3 X-rays

Yeung et al. [175] used a two-compartment model to quantify the blood-to-brain transfer constant of iopadimol, as well as plasmatic blood volume, using dynamic X-ray computed tomography in a clinical study of brain tumors. The two compartments correspond to the cerebral plasma space and the extravascular extracellular space, exchanging tracer with each other through the blood brain barrier assuming permeability limiting conditions. The arterial measurements resulted from blood sampling measurements in a radial artery. The clinical experiments revealed the ability of the estimated parameters to differentiate between healthy white and gray matter, tumor tissue, and metastatic tissue. Indeed, higher values of both parameters were found in tumors and metastasis. Additionally, parametric maps of blood to brain transfer constant and plasmatic blood volume were derived from the dynamic perfusion images, revealing the tumor functional heterogeneity.

Tsushima [150] used a graphical analysis technique based on the work of Patlak et al. [116] to estimate the fractional blood volume and the contrast clearance rate per unit volume of tissue which is closely related to glomerular filtration, using perfusion X-ray computed tomography of human kidney following the intravenous injection of a bolus of iodinated contrast agent. The authors reported a negative correlation of the patient age with the fractional clearance rate, but not with the fractional blood volume despite a tendency to decrease with age. A linear relation was found between X-ray computed tomography estimates and the creatinine clearance rate obtained from urine sampling, which was the clinical reference method to estimate the glomerular filtration rate.

Harvey et al. [58] used the same method to estimate the contrast clearance rate and the fractional blood volume of various tumor types in an attempt to assess tumor response to radiotherapy. Acquisition were performed before treatment for baseline, then early and late response exams were acquired one or two, and six to twelve weeks after treatment, respectively. Authors were able to reveal an increase in the clearance rate as well as in the

fractional blood volume in the early response exams, indicating an hyperemic response to radiotherapy. Later exams revealed a decrease in parameter values compared to the early response, but still exhibited larger values compared to the baseline experiments.

Materne et al. [96] used a dual-input compartmental model, similar to the model proposed by Ziegler et al. [177] for positron emission tomography, to characterize liver perfusion from dynamic contrast-enhanced X-ray computed tomography experiments accounting for both arterial and portal blood supplies. The proposed method accounted for time-delays, but not for dispersion as originally proposed by Ziegler et al. [177]. The arterial and portal curves were extracted directly from the image, which was not possible with positron emission tomography data due to the poor spatial resolution of the imaging modality. Two models were actually considered, in the first one only the liver tissue component was considered, and in the second one the measured kinetic was considered a linear combination of the tissular, arterial, and portal components. Hepatic, arterial, and portal perfusion indices were derived from the estimated model parameters. The perfusion obtained with the first approach exhibited a strong correlation with microsphere measurements, which was not true for the second approach. The reproducibility of the first approach was then investigated in a clinical experiment with healthy patients, and good inter- and intra-observer agreement was reported.

### 2.3.4 Magnetic resonance

In 1999, Tofts et al. [149] introduced compartmental models for the quantification of perfusion parameters using diffusible tracers in dynamic contrast-enhanced magnetic resonance imaging, as well as a set of standardized notations for these parameters. The authors adapted the methods developed for quantification of positron emission tomography using an arterial input function [27, 68, 128] to magnetic resonance imaging assuming the contribution of intravascular tracer to signal intensity can be ignored. They then derived a generalized model parameterized by the transfer constant from plasma to tissue noted  $K_{trans}$ , the extravascular extracellular space volume fraction noted  $V_e$ , and defined the rate constant as the ratio of these two parameters, noted  $k_{ep}$ . The transfer constant is equivalent to the permeability surface area product under permeability-limited conditions, to blood flow under

flow-limited conditions, and to extraction ratio under mixed conditions. They also showed that the rate constant parameter is the decay rate of the exponential impulse response by solving the first-order differential equation of the generalized model. This paper became a standard in the field of perfusion imaging, in particular for magnetic resonance imaging, for it introduced a set of clear and general notations that can be used to model the kinetics of any diffusible tracers.

Murase [109] proposed a linear formulation of the generalized kinetic model presented by Tofts et al. [149], additionally accounting for the vascular component of the signal. The main difference with the non-linear formulation originates in the resolution of the first-order differential equation, which the author performed by integrating both sides of the differential equation. The tracer concentration in the tissue of interest is defined as the linear combination of the integral of the arterial measurement, the integral of the tissue measurement, and the arterial measurement itself, respectively weighted by the sum of the blood to tissue transfer constant and product of the tissue to blood transfer constant with the volume fraction of blood in the tissue, the tissue to blood transfer constant, and the volume fraction of blood in the tissue. The non-linear and linear resolution methods were compared through simulations in terms of accuracy and precision of the estimates, but also in terms of sensitivity to the sampling frequency. The linear method was extensively faster, and more accurate in low to moderate noise conditions, and less sensitive to the sampling interval. Additionally, the linear resolution method does not require initial values for the parameters, making the estimation method more robust.

Balvay et al. [9] investigated the sensitivity of two compartmental models for quantification of contrast-enhanced magnetic resonance imaging to the duration of the acquisition using a new criteria to assess the quality of fit of the models in a preclinical study in mice with human prostatic tumors implants subcutaneously. A one-compartment model accounting for tissue perfusion only, and a two-compartment model accounting for both perfusion and permeability were fitted non-linearly to the mean enhancement curve in the tumor region using an image-based plasma measurement from the heart left ventricle. The one-compartment model was not able to accurately fit the full-length mean enhancement curve in the tumor region and yielded biased tissue blood flow and fractional blood vol-

ume, but it was able to accurately fit shorter curves where permeability can be neglected and yielded parameter estimates comparable to those of the two-compartment model for full-length data.

In 1998, Kovar et al. [77] proposed a compartmental model using the tracer kinetic in a reference tissue, such as a muscle, as well as literature values of perfusion rate, extraction fraction, and extracellular volume in the chosen reference tissue to estimate the vascular input function. They then used the estimated input function to estimate the product of the perfusion rate and the extraction fraction in the tissue of interest. The equations of the model were derived from the differential form of the model proposed by Kety [68]. The method was investigated in a preclinical magnetic resonance study of rats with implanted mammary and prostate tumors to assess the distribution of a diffusible paramagnetic tracer.

Later, Yankeelov et al. [173] proposed a method similar to that of Kovar et al. [77], they however derived their equations from the integral form of the model proposed by Kety [68] and used the standardized notations of Tofts et al. [149]. This formulation avoids the estimation of the arterial input function entirely, and literature values of the transfer constant from plasma to tissue and the distribution volume of the tracer in the reference tissue to directly derive estimates of these parameters in the tissue of interest. The model was investigated through simulations to reveal the sensitivity of the model parameters to noise and to falsy literature reference values. The distribution volume parameter proved robust to noise using the proposed method, however the transfer constant from blood to tissue decreased with rising noise amplitude. The authors also discussed the possibility to avoid the use of literature values characterizing the reference tissue by defining relative parameters as the ratio of a parameter in the tissue of interest to its value in the reference tissue.

Faraneh and Yankeelov [42] proposed a modification of the model presented by Yankeelov et al. [173] to account for the intravascular tracer contribution to signal intensity in either or both of the studied and reference tissues. Given literature values of the vascular parameters characterizing the reference tissue, the arterial input function was estimated using two different formula depending on whether the vascular component was considered. The estimated arterial input function was then used to estimate the perfusion parameters of the studied tissue assuming a two-compartment model, with or without a vascular compart-

ment, and the linear formulation of the model introduced by Murase [109]. Simulations were conducted incorporating the vascular term, and the accuracy and precision of the parameters estimated using the modified reference region model were assessed using the model accounting for intravascular tracer in both the studied and reference tissues as a gold standard. The simulations revealed that accounting for the vascular term in both the studied and reference tissues made the estimation exponentially dependent on the noise amplitude, although accounting for the fractional plasma volume in the studied tissue only yielded inaccurate estimation of all parameters. The effect of the sampling frequency on the accuracy of the vascular parameter estimation revealed complex behavior. The authors gave recommendations on whether the vascular term should be incorporated in the model depending on the information that can be found in the litterature about the expected range of vascular volumes in the studied and reference tissues, as well as on the ability of the sampling frequency to capture the vascular peak in the reference tissue kinetic.

Cárdenas-Rodríguez et al. [23] derived a linear formulation of the reference region model when the contribution of vascular tracer to signal intensity can be neglected in both the studied and reference tissues, as proposed by Yankeelov et al. [173]. The linear formulation is obtained by integrating both sides of the equation derived by Yankeelov et al. [173] instead of solving it by part. The concentration of tracer in the tissue of interest is expressed as the linear combination of the tracer kinetic in the reference tissue, of its integral, and of the integral of the kinetic in the tissue of interest. The weights of this linear model are respectively the relative blood to tissue transfer constant, the ratio of the transfer constant in the tissue of interest to the fractional distribution volume, and the rate constant in the tissue of interest. These weights can therefore be estimated using a linear least-square fitting algorithm. The authors compared the linear and non-linear estimation methods through simulation experiments, and studied the accuracy and the precision of the estimates, as well as the sensitivity of the parameters to the sampling frequency, the noise amplitude, the values of the parameters, and the shape of the arterial input function used to simulate the studied and reference kinetics. Expectedly, in addition to alleviate the need for initialization values, the linear resolution method proved more accurate, especially for low sampling frequencies and high noise amplitudes.

### 2.3.5 Ultrasound

To our knowledge, no proper compartmental approach had been proposed prior to the method proposed in [35] and in Chapter 5 of this document.

Recently, a compartmental model was used to characterize contrast-enhanced ultrasound data by Rizzo et al. [130]. However the method is based on a gamma-variate model of the circulating bubbles with the addition of an irreversible compartment representing a fraction of microbubbles that can get trapped in complex vasculature. This compartment is modeled by the addition of the integral of the fitted gamma-variate curve to the model, and the weight of this term must be estimated. The model was fitted at the pixel level using a variational Bayes estimator which priors were derived from the non-linear fit of the same model at the regional level. The authors reported a better fit in half of the pixel using the model with the irreversible compartment compared to a simple gamma-variate model in a cohort of 99 subjects suffering from arthritis. They designed an automatic algorithm to determine which model should be used according to the data. The fraction of trapped microbubbles also improved classification of patients with rheumatoid and non-rheumatoid arthritis.

## 2.4 Discussion

From an experimental standpoint, the pioneering studies reviewed in this chapter suffer from major limitations which can be explained by the simultaneous development of the imaging technology, contrast agents, and quantification approaches.

Many of these studies used preliminary ultrasound contrast agents, known to be unstable and irregular in size, yielding poor resistance to injection and ultrasound pulses, as well as inconsistencies of the ultrasound signal. All these characteristics made the quantification process of early studies extremely difficult.

Additionally, early contrast-enhanced imaging techniques were not contrast specific and exhibited low sensitivity, especially in the capillaries. Moreover, contrast-enhanced ultrasound data was often acquired using a high mechanical index, causing the disruption of a large number of microbubbles. Intermittent, or transient, imaging accounted for the disruptive nature of the high mechanical index but intrinsically forbids real-time perfusion imaging.

While microbubbles increased the sensitivity of Doppler techniques, allowing visualization of small and deep vessels, it fails to image the capillaries, and was generally of poor help to characterize moving structures. Real-time non-destructive contrast-specific ultrasound imaging only arose with the development of pulse inversion sequences using low mechanical index in the late 1990s.

Most quantification approaches developed for contrast-enhanced ultrasound rely on indicator-dilution theory. One of the main assumption underlying indicator-dilution theory is that the mass of the indicator is conserved throughout the experiment. In vitro studies usually approximatively respect this condition when low mechanical index imaging is used, this is why these experiments are often extremely conclusive, and yield perfusion parameters in good agreement with the ground truth. However, *in vivo*, in addition to the natural and induced disruption, circulating microbubbles are partially filtrated through the lungs and liver, the mass conservation principle is therefore not respected.

Model-free quantification was common in early studies, it is however inherently sensitive to noise, especially as contrast-enhanced ultrasound time-intensity curves are corrupted by a multiplicative noise. Therefore quantifying perfusion using parameters dependant on the peak-intensity is extremely unreliable, as it corresponds to the highest noise amplitude. In pioneering cardiac studies, sampling frequencies were low and did not allow accurate characterization of the high-frequency wash-in resulting from bolus injection, therefore numerous studies focused on contrast-agent wash-out.

Following methodological and computational developments, model-based quantification was proposed to fit time-intensity curves, and allowed the estimation of many semi-quantitative parameters. While physical explanations were found for some explicit models, most studies merely used the models for noise filtering, correction of recirculation and time interpolation. Indeed, semi-quantitative parameters were estimated from fitted curves, then blood flow and blood volume estimates were derived from indicator dilution theory.

Whether extracted directly from the time-intensity curve or from the modeled curve, semi-quantitative parameters are inherently sensitive to experimental conditions. For instance, area under the curve, peak-intensity or even wash-in and wash-out rates, are directly related to the injected dose, moreover time parameters such as the wash-in and wash-out

times, the time to peak-intensity or the mean transit time of the contrast agent are influenced by the site, speed and duration of the injection.

In addition, physiological parameters such as heart rate or even blood pressure can affect the kinetic or the ultrasound response of the microbubbles, and therefore affect the time-intensity curves. Because semi-quantitative parameters are directly extracted from the time-intensity curve, they suffer from physiological inter-exam variations too. This is also true for the replenishment of tissues following disruptive pulses in the case of infusion injection.

Because of the sensitivity of the semi-quantitative parameters to both experimental and physiological conditions, and because indicator-dilution theory is hardly applicable to contrast-enhanced ultrasound as discussed above, one should consider the derived parameters as relative indicators of perfusion, but certainly not as absolute parameters.

Deconvolution approaches estimate the response of a tissue to an instantaneous injection of tracer using an arterial input measurement, a tissue measurement, and none or little a priori on the shape of the estimated impulse tissue response. Deconvolution methods based on the matrix formulation rely on matrix inversion, which is known to be an ill-conditioned problem. Iterative algorithms were proposed to estimate the tissue impulse response without inverting the matrix, however they are extremely sensitive to noise as they are prone to cumulative error. Unconstrained or poorly constrained deconvolution can sometimes yield impulse responses with negative values, which is not physiologically possible. Constrained and regularized deconvolution were proposed to estimate positive, decreasing and smooth impulse response functions, but still few assumptions are made on the shape of the tissue response.

The shape of the estimated curves can be extremely heterogeneous depending on the estimation method and constraints, and extracting parameters can be difficult. To reduce the sensitivity of the deconvolution to noise and to limit oscillations of the tissue response, noise filtering techniques can be enforced rather simply in Fourier or singular value decomposition or by direct filtering of the time-intensity curve, but even small filtering errors can yield imprecise estimates.

Compartmental modeling roughly consist in a model-based deconvolution with strong a priori on the shape of the tissue impulse response and a reduced number of physiologically

relevant parameters. The small number of degrees of freedom restricts the shape of the input function convolved with the tissue impulse respons to a limited set of possible curves, making the estimation process less sensitive to noise. Linear formulations of these models can alleviate the need for initialization, but also make the estimation process more robust to noise, yielding stable estimates with fewer or sparser samples as discussed in Chapter 7.

An arterial measurement is required for some semi-quantitative approaches, by almost all deconvolution approaches, and by most compartmental models. Accurate arterial measurement allows the normalization of the tissue measurement and the estimation of perfusion parameters that are independant of the injection.

Arterial measurement can be performed through blood sampling, this technique is especially popular in the fields of nuclear medicine and radiology as continuous radioactivity measurements apparatus have been extensively developed and commercialized. Nonetheless, patient needs to be catheterized and this procedure remains invasive.

Image-based arterial measurements are extremely unreliable regardless of the imaging modality. Indeed the aorta is not always present in the field of view and a large artery feeding the tissue of interest can be hard to identify, especially in two-dimensional data. Additionally, partial volume effect, attenuation and saturation artifacts can affect the measured signal intensity. Indeed, in most modalities a trade-off must be made between space and time resolution, and the small size of the artery combined to the high speed of a bolus in an artery makes the estimation of the arterial input function extremely difficult. In contrast-enhanced ultrasound the noise is multiplicative, which makes the high-intensity arterial measurements highly unreliable.

A healthy reference tissue can be chosen in the image to normalize the perfusion parameters in the tissue interest by their value in the reference region. The reference region should be chosen in a large, homogeneous and well perfused tissue to limit partial volume effet and saturation artifacts in addition to reducing the noise in the reference tissue enhancement curve.

Direct estimation of relative perfusion parameters can also be obtained using compartmental modeling, alleviating the need for an arterial measurement. The relative perfusion quantification methods were generally formulated with a single enhancement curve to char-

acterize, even though they were often applied later to the region or even pixel level.

Whether fitting an explicit model to a single tissue curve for noise filtering or estimating quantitative parameters using a compartmental model using multiples enhancement curves, one should consider time-delay parameters. Indeed, time-delay parameters are often overlooked in the litterature, however they play a crucial role in the estimation of perfusion parameters as fitting a model without a time-delay parameter or prior delay correction can induce a bias in the estimation. A few methods were presented as delay-insensitive, some other methods actually include time-delay parameters in their equations, and commercial softwares certainly correct for delay, but to our knowledge no study reported on the absolute or relative values of such parameters, or exploited parametric maps revealing the timeline of the bolus arrival in the studied tissue.

# Afterword

The development of quantification methods often came along with the development of the imaging modality itself. Semi-quantitative approaches are the most intuitive approaches, they are generally used to characterize perfusion data in the early stage of the imaging technique, they are however subject to inter-exam physiological and experimental changes. Then physiological parameters are often derived from semi-quantitative parameters characterizing the tracer kinetic in the tissue of interest and in an artery, they however suffer from the same limitations as semi-quantitative parameters, but are also affected by the difficulty of estimating the arterial curve.

Ultrasound contrast agents are not anymore in their early development stages, on the contrary they reached a point where their behavior is well understood and where they can be used routinely for some clinical applications. While the ultrasound imaging technique is not new at all, it was using analog signal processing for a long period of time. It however reached a turning point with the development of numerical ultrasound scanners, exploiting the development of high-end graphical hardware which allows parallel computing to allow complex real-time signal processing. This turning point suggest future development of the imaging technique, in particular with the joint development of ultrafast plane wave imaging and three-dimensional ultrasound probes.

Regarding contrast-enhanced ultrasound, which is the core modality addressed in this thesis, semi-quantitative approaches are by far the most commonly used approaches. Indeed, many manufacturers of ultrasound scanners and contrast-agent implemented these techniques in commercial softwares, which explains their popularity in clinical application. A few approaches relying on deconvolution were also proposed for characterization of contrast-enhanced ultrasound exams, but compartmental modeling remains extremely rare in the

ultrasound litterature. This can be explained by the dependance of the majority of these techniques on the ability to perform an accurate arterial measurement. However accurate measurement is not always possible as arterial regions are usually small and exhibit high tracer concentration, making the estimated curve subject to saturation and partial volume effects. Finding an artery can be especially tricky in two-dimensional data, and even more limiting when attempting to compare two or more exams. Indeed, imaging the exact same plane is extremely difficult even for experienced radiologists, especially in the case of evolving tissues like growing tumors or when monitoring the effect of a treatment. The impact of the arterial function on the parameters of a one-compartment model for quantification of contrast-enhanced ultrasound data will be investigated in Chapter 3.

When an arterial input function cannot be estimated, or at least not accurately, another tissue present in the image can be used as a reference for comparison purposes. Just like the absolute values, the relative or normalized perfusion parameters can be used to perform relative comparison of the tissues observable in a single exam. However, parameter normalization allows comparison of the same tissue observed in different exams, using the reference tissue as a basis for comparison, and assuming the reference tissue did not change between the two exams. The reproducibility of relative approaches will be investigated in the following part of the thesis.

## Bibliography

- [1] P O Alderson, K H Douglass, K G Mendenhall, V A Guadiani, D C Watson, J M Links, and H N Wagner. Deconvolution analysis in radionuclide quantitation of left-to-right cardiac shunts. *Journal of nuclear medicine : official publication, Society of Nuclear Medicine*, 20(6):502–506, June 1979. [39](#)
- [2] C Appledorn. Deconvolution analysis of the scintillation camera renogram. *The British journal of radiology*, 50(591):234–235, 1977. [38](#)
- [3] Marcel Arditi, Peter J A Frinking, Xiang Zhou, and Nicolas G Rognin. A new formalism for the quantification of tissue perfusion by the destruction-replenishment method in contrast ultrasound imaging. *IEEE Transactions on Ultrasonics, Ferroelectrics and Frequency Control*, 53(6):1118–1129, June 2006. [33](#)
- [4] W F Armstrong, T M Mueller, E L Kinney, E G Tickner, J C Dillon, and H Feigenbaum. Assessment of myocardial perfusion abnormalities with contrast-enhanced two-dimensional echocardiography. *Circulation*, 66(1):166–173, July 1982. [20](#)
- [5] S Aronson, J G Wiencek, S B Feinstein, P A Heidenreich, J G Zaroff, R Walker, and M F Roizen. Assessment of renal blood flow with contrast ultrasonography. *Anesthesia & Analgesia*, 76(5):964–970, May 1993. [22](#)
- [6] Michalakis Averkiou, Marios Lampaskis, Konstantina Kyriakopoulou, Dimosthenis Skarlos, Georgios Klouvas, Costas Strouthos, and Edward Leen. Quantification of Tumor Microvascularity with Respiratory Gated Contrast Enhanced Ultrasound for Monitoring Therapy. *Ultrasound in Medicine & Biology*, 36(1):68–77, January 2010. [31](#)
- [7] L Axel. Cerebral blood flow determination by rapid-sequence computed tomography: theoretical analysis. *Radiology*, 137(3):679–686, 1980. [40](#), [43](#)
- [8] L Axel. Tissue mean transit time from dynamic computed tomography by a simple deconvolution technique. *Investigative Radiology*, 18(1):94–99, December 1982. [39](#), [47](#)

- [9] Daniel Balvay, Frédérique Frouin, Guillaume Calmon, Bertrand Bessoud, Edmond Kahn, Nathalie Siauve, Olivier Clément, and Charles A Cuenod. New criteria for assessing fit quality in dynamic contrast-enhanced T1-weighted MRI for perfusion and permeability imaging. *Magnetic Resonance in Medicine*, 54(4):868–877, 2005. [59](#)
- [10] D M Band, R A Linton, T K O'Brien, M M Jonas, and N W Linton. The shape of indicator dilution curves used for cardiac output measurement in man. *The Journal of Physiology*, 498(1):225–229, January 1997. [25](#)
- [11] J B Bassingthwaigte. Plasma indicator dispersion in arteries of the human leg. *Circulation research*, 19(2):332–346, 1966. [37](#)
- [12] J B Bassingthwaigte and F H Ackerman. Mathematical linearity of circulatory transport. *Journal of applied physiology*, 22(5):879–888, May 1967. [37](#)
- [13] A Baur, A Stäbler, R Bartl, R Lamerz, J Scheidler, and M Reiser. MRI gadolinium enhancement of bone marrow: age-related changes in normals and in diffuse neoplastic infiltration. *Skeletal radiology*, 26(7):414–418, July 1997. [18](#)
- [14] H Bleeker, K Shung, and J Barnhart. On the application of ultrasonic contrast agents for blood flowmetry and assessment of cardiac perfusion. *Journal of ultrasound in medicine : official journal of the American Institute of Ultrasound in Medicine*, 9(8):461–471, August 1990. [21](#), [22](#)
- [15] Martin J K Blomley, Richard Coulden, Peter Dawson, Martti Kormano, Pamela Donlan, Cecile Bufkin, and Martin J Lipton. Liver Perfusion Studied with Ultrafast CT. *Journal of Computer Assisted Tomography*, 19(3):424–433, May 1995. [14](#), [15](#)
- [16] G Blomqvist. On the construction of functional maps in positron emission tomography. *Journal of Cerebral Blood Flow & Metabolism*, 4(4):629–632, December 1984. [55](#)
- [17] J M Bogaard, J R Jansen, E A von Reth, A Versprille, and M E Wise. Random walk type models for indicator-dilution studies: comparison of a local density random walk and

- a first passage times distribution. *Cardiovascular research*, 20(11):789–796, November 1986. 28
- [18] William Bommer, James Neef, Alexander Neumann, Lynn Weinert, Garrett Lee, Dean T Mason, and Anthony N DeMaria. Indicator-dilution curves obtained by photometric analysis of two-dimension echo-contrast studies. *American Journal of Cardiology*, 41(2):370, February 1978. 19
- [19] R C Brasch, H J Weinmann, and G E Wesbey. Contrast-enhanced NMR imaging: animal studies using gadolinium-DTPA complex. *AJR. American journal of roentgenology*, 142(3):625–630, March 1984. 16
- [20] Walter C Brogan III, D Brent Glamann, Richard A Lange, and L David Hillis. Comparison of single and biplane ventriculography for determination of left ventricular volume and ejection fraction. *The American Journal of Cardiology*, 69(12):1079–1082, April 1992. 49
- [21] P N Burns, S R Wilson, and D H Simpson. Pulse inversion imaging of liver blood flow: improved method for characterizing focal masses with microbubble contrast. *Investigative Radiology*, 35(1):58–71, January 2000. 32
- [22] B D Butler and B A Hills. The lung as a filter for microbubbles. *Journal of applied physiology: respiratory, environmental and exercise physiology*, 47(3):537–543, September 1979. 19
- [23] Julio Cárdenas-Rodríguez, Christine M Howison, and Mark D Pagel. A linear algorithm of the reference region model for DCE-MRI is robust and relaxes requirements for temporal resolution. *Magnetic resonance imaging*, 31(4):497–507, May 2013. 61
- [24] A Cenic, D G Nabavi, R A Craen, A W Gelb, and T Y Lee. Dynamic CT measurement of cerebral blood flow: a validation study. *AJNR. American journal of neuroradiology*, 20(1):63–73, January 1999. 40, 41
- [25] I S Chan, A A Goldstein, and J B Bassingthwaighte. SENSOP: a derivative-free solver

- for nonlinear least squares with sensitivity scaling. *Annals of Biomedical Engineering*, 21(6):621–631, November 1993. [45](#)
- [26] C M Coulam, H R Warner, E H Wood, and J B Bassingthwaigte. A transfer function analysis of coronary and renal circulation calculated from upstream and downstream indicator-dilution curves. *Circulation research*, 19(5):879–890, November 1966. [35, 45](#)
- [27] Christian Crone. The Permeability of Capillaries in Various Organs as Determined by Use of the ‘Indicator Diffusion’ Method. *Acta Physiologica*, 58(4):292–305, August 1963. [52, 58](#)
- [28] C Cuenod, I Leconte, N Siauve, A Resten, C Dromain, B Poulet, Frédérique Frouin, O Clément, and G Frija. Early changes in liver perfusion caused by occult metastases in rats: detection with quantitative CT. *Radiology*, 218(2):556–561, February 2001. [42](#)
- [29] Charles A Cuenod, Isabelle Leconte, Nathalie Siauve, Frédérique Frouin, Clarisse Dromain, Olivier Clément, and Guy Frija. Deconvolution Technique for Measuring Tissue Perfusion by Dynamic CT. *Academic Radiology*, 9(1):S205–S211, January 2002. [42](#)
- [30] J A DeGrazia, P O Scheibe, P E Jackson, Z J Lucas, W R Fair, J M Vogel, and L J Blumin. Clinical applications of a kinetic model of hippurate distribution and renal clearance. *Journal of nuclear medicine : official publication, Society of Nuclear Medicine*, 15(2): 102–114, February 1974. [38](#)
- [31] Anthony N DeMaria, William Bommer, Lily George, Alexander Neumann, Lynn Weinert, and Dean T Mason. Combined peripheral venous injection and cross-sectional echocardiography in the evaluation of cardiac disease. *American Journal of Cardiology*, 41(2):370, February 1978. [20](#)
- [32] C F Dietrich, Michalakis Averkiou, J-M Correas, N Lassau, E Leen, and F Piscaglia. An EFSUMB introduction into Dynamic Contrast-Enhanced Ultrasound (DCE-US) for quantification of tumour perfusion. In *Ultraschall in der Medizin (Stuttgart, Germany : 1980)*, pages 344–351. Innere Medizin 2, Caritas-Krankenhaus, Bad Mergentheim. Christoph.Dietrich@ckbm.de, © Georg Thieme Verlag KG, August 2012. [14](#)

- [33] B L Diffey and J R Corfield. Data-bounding technique in discrete deconvolution. *Medical & biological engineering*, 14(4):478–478, 1976. [38](#)
- [34] B L Diffey, F M Hall, and J R Corfield. The 99mTc-DTPA dynamic renal scan with deconvolution analysis. *Journal of nuclear medicine : official publication, Society of Nuclear Medicine*, 17(5):352–355, May 1976. [38, 45](#)
- [35] Maxime Doury, Alexandre Dizeux, Alain De Cesare, Olivier Lucidarme, S Lori Bridal, and Frédérique Frouin. Regularized linear resolution of a one-compartment model to improve the reproducibility of perfusion parameters in CEUS. In *2016 IEEE International Ultrasonics Symposium (IUS*, pages 1–4. IEEE, 2016. [62](#)
- [36] P E Dugdale and K A Miles. Hepatic metastases: the value of quantitative assessment of contrast enhancement on computed tomography. *European journal of radiology*, 30(3):206–213, June 1999. [15](#)
- [37] James D Eastwood, Michael H Lev, Tarek Azhari, Ting-Yim Lee, Daniel P Barboriak, David M Delong, Clemens Fitzek, Michael Herzau, Max Wintermark, Reto Meuli, David Brazier, and James M Provenzale. CT perfusion scanning with deconvolution analysis: pilot study in patients with acute middle cerebral artery stroke. *Radiology*, 222(1):227–236, January 2002. [41](#)
- [38] N Elie, N Lassau, P Peronneau, and V Rouffiac. Method and system for quantification of tumoral vascularization. US Patent Office, September 2014. [27, 49](#)
- [39] R Erlemann, M F Reiser, P E Peters, P Vasallo, B Nommensen, C R Kusnierz-Glaz, J Ritter, and A Roessner. Musculoskeletal neoplasms: static and dynamic Gd-DTPA-enhanced MR imaging. *Radiology*, 171(3):767–773, June 1989. [14, 17, 18](#)
- [40] Jens Eyding, Christos Krogias, Wilko Wilkening, Saskia Meves, Helmut Ermert, and Thomas Postert. Parameters of cerebral perfusion in phase-inversion harmonic imaging (PIHI) ultrasound examinations. *Ultrasound in Medicine & Biology*, 29(10):1379–1385, October 2003. [26, 27](#)

- [41] M J Faddy and J A Jacquez. Compartmental Analysis in Biology and Medicine, 2nd edition. *Biometrics*, 43(4):1028, December 1987. [45](#)
- [42] A Z Faranesh and Thomas E Yankeelov. Incorporating a vascular term into a reference region model for the analysis of DCE-MRI data: a simulation study. *Physics in medicine and biology*, 2008. [60](#)
- [43] S B Feinstein, F J Ten Cate, W Zwehl, K Ong, G Maurer, C Tei, P M Shah, S Meerbaum, and E Corday. Two-dimensional contrast echocardiography. I. In vitro development and quantitative analysis of echo contrast agents. *Journal of the American College of Cardiology*, 3(1):14–20, January 1984. [20](#)
- [44] R Felix, W Schörner, M Laniado, H P Niendorf, C Claussen, W Fiegler, and U Speck. Brain tumors: MR imaging with gadolinium-DTPA. *Radiology*, 156(3):681–688, September 1985. [16](#)
- [45] D Feng, Z Wang, and S C Huang. A study on statistically reliable and computationally efficient algorithms for generating local cerebral blood flow parametric images with positron emission tomography. *IEEE Transactions on Medical Imaging*, 12(2):182–188, 1993. [54](#)
- [46] D Feng, S C Huang, and Z Z Wang. An unbiased parametric imaging algorithm for nonuniformly sampled biomedical system parameter estimation. *IEEE Transactions on Medical Imaging*, 15(4):512–518, 1996. [54](#)
- [47] J S Fleming and B A Goddard. A technique for the deconvolution of the renogram. *Physics in medicine and biology*, 19(4):546–549, July 1974. [38](#)
- [48] J Gamel, W F Rousseau, C R Katholi, and E Mesel. Pitfalls in digital computation of the impulse response of vascular beds from indicator-dilution curves. *Circulation research*, 32(4):516–523, April 1973. [37](#)
- [49] Marianne Gauthier, Farid Tabarout, Ingrid Leguerney, Mélanie Polrot, Stéphanie Pitre, Pierre Peronneau, and Nathalie Lassau. Assessment of quantitative perfusion parameters by dynamic contrast-enhanced sonography using a deconvolution

- method: an in vitro and in vivo study. *Journal of ultrasound in medicine : official journal of the American Institute of Ultrasound in Medicine*, 31(4):595–608, April 2012. 49
- [50] L E Gerlowski and R K Jain. Physiologically based pharmacokinetic modeling: principles and applications. *Journal of pharmaceutical sciences*, 72(10):1103–1127, October 1983. 51
- [51] A Gjedde, A J HANSEN, and E SIEMKOWICZ. Rapid simultaneous determination of regional blood flow and blood-brain glucose transfer in brain of rat. *Acta Physiologica*, 108(4):321–330, April 1980. 52
- [52] Albert Gjedde. High- and Low-Affinity Transport of D-Glucose from Blood to Brain. *Journal of Neurochemistry*, 36(4):1463–1471, April 1981. 52, 54
- [53] Gene H Golub and Charles Van Loan. *Matrix computations; 3rd ed.* Johns Hopkins Univ., Baltimore, MD, 1996. 41
- [54] R N Gunn, S R Gunn, and V J Cunningham. Positron emission tomography compartmental models. *Journal of Cerebral Blood Flow & Metabolism*, 21(6):635–652, June 2001. 56
- [55] Donald J Hagler, Abdul J Tajik, James B Seward, and Erik L Ritman. Videodensitometric Quantitation of Left-to-Right Shunts with Contrast Echocardiography. In *Contrast Echocardiography*, pages 298–303. Springer Netherlands, Dordrecht, 1982. 20
- [56] W F Hamilton, John Walker Moore, J M Kinsman, and R G Spurling. STUDIES ON THE CIRCULATION. *American Journal of Physiology – Legacy Content*, 99(3):534–551, February 1932. 19, 29
- [57] P C Hansen. Analysis of discrete ill-posed problems by means of the L-curve. *SIAM review*, 34(4):561–580, 1992. 50
- [58] C Harvey, A Dooher, J Morgan, M Blomley, and P Dawson. Imaging of tumour therapy responses by dynamic CT. *European journal of radiology*, 30(3):221–226, June 1999. 57

- [59] R A Hawkins, M E Phelps, S C Huang, J A Wapenski, P D Grimm, R G Parker, G Juillard, and P Greenberg. A kinetic evaluation of blood-brain barrier permeability in human brain tumors with [68Ga]EDTA and positron computed tomography. *Journal of Cerebral Blood Flow & Metabolism*, 4(4):507–515, December 1984. [54](#)
- [60] P A Heidenreich, J G Wiencek, J G Zaroff, S Aronson, L J Segil, P V Harper, and S B Feinstein. In vitro calculation of flow by use of contrast ultrasonography. *Journal of the American Society of Echocardiography*, 6(1):51–61, January 1993. [22](#)
- [61] A J Hilson, M N Maisey, C B Brown, C S Ogg, and M S Bewick. Dynamic renal transplant imaging with Tc-99m DTPA (Sn) supplemented by a transplant perfusion index in the management of renal transplants. *Journal of nuclear medicine : official publication, Society of Nuclear Medicine*, 19(9):994–1000, September 1978. [14](#)
- [62] Ellen G Hoeffner, Ian Case, Rajan Jain, Sachin K Gujar, Gaurang V Shah, John P Deveikis, Ruth C Carlos, B Gregory Thompson, Mark R Harrigan, and Suresh K Mukherji. Cerebral Perfusion CT: Technique and Clinical Applications. *Radiology*, 231(3):632–644, June 2004. [42](#)
- [63] Masanobu Ibaraki, Eku Shimosegawa, Hideto Toyoshima, Kazuhiro Takahashi, Shuichi Miura, and Iwao Kanno. Tracer delay correction of cerebral blood flow with dynamic susceptibility contrast-enhanced MRI. *Journal of Cerebral Blood Flow & Metabolism*, 25(3):378–390, March 2005. [43](#)
- [64] Michael Jerosch-Herold, Norbert Wilke, Arthur E Stillman, and Robert F Wilson. Magnetic resonance quantification of the myocardial perfusion reserve with a Fermi function model for constrained deconvolution. *Medical physics*, 25(1):73–84, June 1998. [47](#)
- [65] Radovan Jirik, Kim Nylund, Odd H Gilja, Martin Mezl, Vratislav Harabis, Radim Kolar, Michal Standara, and Torfinn Taxt. Ultrasound perfusion analysis combining bolus-tracking and burst-replenishment. *IEEE Transactions on Ultrasonics, Ferroelectrics and Frequency Control*, 60(2):310–319, February 2013. [50](#)

- [66] Sanjiv Kaul, Paul Kelly, Jonathan D Oliner, William P Glasheen, Mark W Keller, and Denny D Watson. Assessment of regional myocardial blood flow with myocardial contrast two-dimensional echocardiography. *Journal of the American College of Cardiology*, 13(2):468–482, February 1989. [24](#)
- [67] R W Kenny, D M Ackery, J S Fleming, B A Goddard, and R W Grant. Deconvolution analysis of the scintillation camera renogram. *The British journal of radiology*, 48(570):481–486, June 1975. [38](#)
- [68] Seymour S Kety. The theory and applications of the exchange of inert gas at the lungs and tissues. *Pharmacological reviews*, 3(1):1–41, March 1951. [52](#), [58](#), [60](#)
- [69] Seymour S Kety and C F Schmidt. The nitrous oxide method for the quantitative determination of cerebral blood flow in man: theory, procedure and normal values. *Journal of Clinical Investigation*, 27(4):476–483, 1948. [51](#), [57](#)
- [70] Seymour S Kety and Carl F Schmidt. The Quantitative Determination of Cerebral Blood Flow in Man by the Use of Nitrous Oxide in Low Concentrations. *The American Journal of the Medical Sciences*, 208(6):809, 1944. [51](#)
- [71] Grete Mørk Kindberg, Helge Tolleshaug, Norbert Roos, and Tore Skotland. Hepatic clearance of Sonazoid perfluorobutane microbubbles by Kupffer cells does not reduce the ability of liver to phagocytose or degrade albumin microspheres. *Cell and tissue research*, 312(1):49–54, 2003. [19](#)
- [72] R B King, A Deussen, G M Raymond, and J B Bassingthwaighte. A vascular transport operator. *American Journal of Physiology – Legacy Content*, 265(6 Pt 2):H2196–208, December 1993. [44](#)
- [73] E Klotz and M König. Perfusion measurements of the brain: using dynamic CT for the quantitative assessment of cerebral ischemia in acute stroke. *European journal of radiology*, 30(3):170–184, June 1999. [16](#)
- [74] T J Knopp and J B Bassingthwaighte. Effect of flow on transpulmonary circulatory transport functions. *Journal of applied physiology*, 27(1):36–43, July 1969. [37](#)

- [75] T J Knopp, W A Dobbs, J F Greenleaf, and J B Bassingthwaite. Transcoronary intravascular transport functions obtained via a stable deconvolution technique. *Annals of Biomedical Engineering*, 4(1):44–59, March 1976. [36](#)
- [76] M Koenig, E Klotz, B Luka, D J Venderink, J F Spittler, and L Heuser. Perfusion CT of the brain: diagnostic approach for early detection of ischemic stroke. *Radiology*, 209(1):85–93, October 1998. [14, 16](#)
- [77] D A Kovar, M Lewis, and G S Karczmar. A new method for imaging perfusion and contrast extraction fraction: input functions derived from reference tissues. *Journal of Magnetic Resonance Imaging*, 8(5):1126–1134, September 1998. [60](#)
- [78] Martin Krix, Fabian Kiessling, Nabeel Farhan, Kerstin Schmidt, Johannes Hoffend, and Stefan Delorme. A multivessel model describing replenishment kinetics of ultrasound contrast agent for quantification of tissue perfusion. *Ultrasound in Medicine & Biology*, 29(10):1421–1430, October 2003. [32](#)
- [79] Martin Krix, Fabian Kiessling, Silvia Vosseler, Isabel Kiessling, Martin Le-Huu, Norbert E Fusenig, and Stefan Delorme. Comparison of intermittent-bolus contrast imaging with conventional power Doppler sonography: quantification of tumour perfusion in small animals. *Ultrasound in Medicine & Biology*, 29(8):1093–1103, August 2003. [33](#)
- [80] Christos Krogias, Thomas Postert, Saskia Meves, Wilko Wilkening, Horst Przuntek, and Jens Eyding. Semiquantitative analysis of ultrasonic cerebral perfusion imaging. *Ultrasound in Medicine & Biology*, 31(8):1007–1012, August 2005. [27](#)
- [81] K Kroll, N Wilke, M Jerosch-Herold, Y Wang, Y Zhang, R J Bache, and J B Bassingthwaite. Modeling regional myocardial flows from residue functions of an intravascular indicator. *American Journal of Physiology - Heart and Circulatory Physiology*, 271(4):H1643–H1655, October 1996. [48](#)
- [82] Kohsuke Kudo, Makoto Sasaki, Kuniaki Ogasawara, Satoshi Terae, Shigeru Ehara, and Hiroki Shirato. Difference in Tracer Delay–induced Effect among Deconvolution Al-

- gorithms in CT Perfusion Analysis: Quantitative Evaluation with Digital Phantoms. *Radiology*, 251(1):241–249, April 2009. [43](#)
- [83] M P J Kuenen, M Mischi, and H Wijkstra. Contrast-Ultrasound Diffusion Imaging for Localization of Prostate Cancer. *IEEE Transactions on Medical Imaging*, 30(8):1493–1502, July 2011. [30](#)
- [84] Marios Lampaskis and Michalakis Averkiou. Investigation of the relationship of non-linear backscattered ultrasound intensity with microbubble concentration at low MI. *Ultrasound in Medicine & Biology*, 36(2):306–312, February 2010. [19](#)
- [85] N A Lassen. Cerebral transit of an intravascular tracer may allow measurement of regional blood volume but not regional blood flow. *Journal of Cerebral Blood Flow & Metabolism*, 4(4):633–634, December 1984. [37](#)
- [86] Niels A Lassen, William Perl, and lassen. Summary of Black-Box Analysis. In *Tracer kinetic methods in medical physiology*, pages 1–11. 1979. [34](#)
- [87] Niels A Lassen, William Perl, and lassen. Volume/Flow or Mass/Flux Ratio (Mean Transit Time): Bolus Injection. In *Tracer kinetic methods in medical physiology*, pages 1–26. 1979. [35, 43](#)
- [88] Sonia Lavisse, Pascale Lejeune, Valérie Rouffiac, Nicolas Elie, Estelle Bribes, Brigitte Demers, Patricia Vrignaud, Marie-Christine Bissery, Aude Brûlé, Serge Koscielny, Pierre Peronneau, and Nathalie Lassau. Early quantitative evaluation of a tumor vasculature disruptive agent AVE8062 using dynamic contrast-enhanced ultrasonography. *Investigative Radiology*, 43(2):100–111, February 2008. [27](#)
- [89] Charles L Lawson and Richard J Hanson. *Solving Least Squares Problems*. SIAM, December 1995. [40](#)
- [90] R A F Linton, N W F Linton, and D M Band. A new method of analysing indicator dilution curves. *Cardiovascular research*, 30(6):930–938, December 1995. [25](#)

- [91] J Logan, J S Fowler, N D Volkow, A P Wolf, S L Dewey, D J Schlyer, R R MacGregor, R Hitzemann, B Bendriem, and S J Gately. Graphical analysis of reversible radioligand binding from time-activity measurements applied to [N-11C-methyl]-(-)-cocaine PET studies in human subjects. *Journal of Cerebral Blood Flow & Metabolism*, 10(5):740–747, September 1990. [53](#)
- [92] J Logan, J S Fowler, N D Volkow, Y S Ding, G J Wang, and D L Alexoff. A strategy for removing the bias in the graphical analysis method. *Journal of Cerebral Blood Flow & Metabolism*, 21(3):307–320, March 2001. [54](#)
- [93] David L Maltz and S Treves. Quantitative Radionuclide Angiocardiography. *Circulation*, 47(5):1049–1056, May 1973. [39](#)
- [94] A Maseri, P Caldini, S Permutt, and K L Zierler. Frequency Function of Transit Times through Dog Pulmonary Circulation. *Circulation research*, 26(5):527–543, 1970. [36](#)
- [95] H Masugata, B Peters, S Lafitte, G M Strachan, K Ohmori, and A N DeMaria. Quantitative assessment of myocardial perfusion during graded coronary stenosis by real-time myocardial contrast echo refilling curves. *Journal of the American College of Cardiology*, 37(1):262–269, January 2001. [32](#)
- [96] R Materne, B E Van Beers, A M Smith, I Leconte, J Jamart, J P Dehoux, A Keyeux, and Y Horsmans. Non-invasive quantification of liver perfusion with dynamic computed tomography and a dual-input one-compartmental model. *Clinical science (London, England : 1979)*, 99(6):517–525, December 2000. [58](#)
- [97] R S Meltzer, J Roelandt, O L Bastiaans, L Piérard, P W Serruys, and C T Lancée. Video-densitometric processing of contrast two-dimensional echocardiographic data. *Ultrasound in Medicine & Biology*, 8(5):509–514, 1982. [20](#)
- [98] Richard S Meltzer, E Glen Tickner, and Richard L Popp. Why do the lungs clear ultrasonic contrast? *Ultrasound in Medicine & Biology*, 6(3):267–269, January 1980. [19](#)
- [99] E Meyer. Simultaneous correction for tracer arrival delay and dispersion in CBF measurements by the H<sub>2</sub>15O autoradiographic method and dynamic PET. *Journal of nu-*

- clear medicine : official publication, Society of Nuclear Medicine*, 30(6):1069–1078, June 1989. 55
- [100] K A Miles. Measurement of tissue perfusion by dynamic computed tomography. *The British journal of radiology*, 64(761):409–412, May 1991. 14, 15
- [101] K A Miles. Functional computed tomography in oncology. *European Journal of Cancer*, 38(16):2079–2084, November 2002. 15
- [102] K A Miles, M Hayball, and A K Dixon. Colour perfusion imaging: a new application of computed tomography. *The Lancet*, 337(8742):643–645, March 1991. 14, 15
- [103] K A Miles, M P Hayball, and A K Dixon. Functional images of hepatic perfusion obtained with dynamic CT. *Radiology*, 188(2):405–411, August 1993. 14, 15
- [104] K A Miles, M P Hayball, and A K Dixon. Measurement of human pancreatic perfusion using dynamic computed tomography with perfusion imaging. *The British journal of radiology*, 68(809):471–475, May 1995. 15
- [105] M Mischi, T A Kalker, and E H Korsten. Contrast echocardiography for pulmonary blood volume quantification. *IEEE Transactions on Ultrasonics, Ferroelectrics and Frequency Control*, 51(9):1137–1147, September 2004. 28, 29, 48, 49
- [106] M Mischi, A H M Jansen, A A C M Kalker, and H H M Korsten. Identification of ultrasound contrast agent dilution systems for ejection fraction measurements. *IEEE Transactions on Ultrasonics, Ferroelectrics and Frequency Control*, 52(3):410–420, March 2005. 48
- [107] M Mischi, J A den Boer, and H H M Korsten. On the physical and stochastic representation of an indicator dilution curve as a gamma variate. *Physiological Measurement*, 29(3):281–294, March 2008. 29
- [108] Massimo Mischi, Ton Kalker, and Erik Korsten. Videodensitometric Methods for Cardiac Output Measurements. *EURASIP Journal on Advances in Signal Processing*, 2003(5):862083–489, December 2003. 28

- [109] Kenya Murase. Efficient method for calculating kinetic parameters using T1-weighted dynamic contrast-enhanced magnetic resonance imaging. *Magnetic Resonance in Medicine*, 51(4):858–862, 2004. [59](#), [61](#)
- [110] J V Nally, H S Clarke, J P Windham, G P Grecos, M L Gross, and W J Potvin. Technetium-99m DTPA renal flow studies in Goldblatt hypertension. *Journal of nuclear medicine : official publication, Society of Nuclear Medicine*, 26(8):917–924, August 1985. [14](#), [15](#)
- [111] David Norman, Edwin A Stevens, S Douglas Wing, Victor Levin, and Thomas H Newton. Quantitative Aspects of Contrast Enhancement in Cranial Computed Tomography. *Radiology*, 129(3):683–688, December 1978. [14](#)
- [112] Leif Østergaard, Alma Gregory Sorensen, Kenneth K Kwong, Robert M Weisskoff, Carsten Gyldensted, and Bruce R Rosen. High resolution measurement of cerebral blood flow using intravascular tracer bolus passages. Part II: Experimental comparison and preliminary results. *Magnetic Resonance in Medicine*, 36(5):726–736, November 1996. [46](#)
- [113] Leif Østergaard, Robert M Weisskoff, David A Chesler, Carsten Gyldensted, and Bruce R Rosen. High resolution measurement of cerebral blood flow using intravascular tracer bolus passages. Part I: Mathematical approach and statistical analysis. *Magnetic Resonance in Medicine*, 36(5):715–725, November 1996. [45](#)
- [114] J R Pappenheimer. Passage of molecules through capillary walls. *Physiological Reviews*, 33(3):387–423, June 1953. [52](#)
- [115] C S Patlak and R G Blasberg. Graphical evaluation of blood-to-brain transfer constants from multiple-time uptake data. Generalizations. *Journal of Cerebral Blood Flow & Metabolism*, 5(4):584–590, December 1985. [53](#)
- [116] Clifford S Patlak, Ronald G Blasberg, and Joseph D Fenstermacher. Graphical Evaluation of Blood-to-Brain Transfer Constants from Multiple-Time Uptake Data. *Journal of Cerebral Blood Flow & Metabolism*, 3(1):1–7, March 1983. [53](#), [57](#)

- [117] A M Peters, J Brown, G G Hartnell, M J Myers, C Haskell, and J P Lavender. Non-invasive measurement of renal blood flow with  $^{99m}\text{Tc}$  DTPA: comparison with radiolabelled microspheres. *Cardiovascular research*, 21(11):830–834, November 1987. [14](#), [15](#)
- [118] A M Peters, R D GUNASEKERA, B L HENDERSON, J Brown, J P Lavender, M DE SOUZA, J M ASH, and D L GILDAY. Noninvasive measurement of blood flow and extraction fraction. *Nuclear Medicine Communications*, 8(10):823–837, October 1987. [14](#), [15](#)
- [119] Holger Pettersson, N Ackerman, J Kaude, R E Googe, A A Mancuso, K N Scott, R H Hackett, D A Hager, and S Caballero. Gadolinium-DTPA Enhancement of Experimental Soft Tissue Carcinoma and Hemorrhage in Magnetic Resonance Imaging. *Acta* ..., 28(1):75–78, January 1987. [14](#), [17](#)
- [120] M E Phelps, S C Huang, E J Hoffman, and D E Kuhl. Validation of tomographic measurement of cerebral blood volume with C-11-labeled carboxyhemoglobin. *Journal of nuclear medicine : official publication, Society of Nuclear Medicine*, 20(4):328–334, April 1979. [55](#)
- [121] T Postert, P Hoppe, J Federlein, S Helbeck, H Ermert, H Przuntek, T Büttner, and W Wilkening. Contrast agent specific imaging modes for the ultrasonic assessment of parenchymal cerebral echo contrast enhancement. *Journal of Cerebral Blood Flow & Metabolism*, 20(12):1709–1716, December 2000. [26](#)
- [122] T C Potdevin, J B Fowlkes, A P Moskalik, and P L Carson. Analysis of refill curve shape in ultrasound contrast agent studies. *Medical physics*, 31(3):623–632, March 2004. [33](#)
- [123] Titaina C U Potdevin, J Brian Fowlkes, Aaron P Moskalik, and Paul L Carson. Refill model of rabbit kidney vasculature. *Ultrasound in Medicine & Biology*, 32(9):1331–1338, September 2006. [33](#)
- [124] Emilio Quaia, Aldo Nocentini, and Lucio Torelli. Assessment of a new mathematical model for the computation of numerical parameters related to renal cortical blood

- flow and fractional blood volume by contrast-enhanced ultrasound. *Ultrasound in Medicine & Biology*, 35(4):616–627, April 2009. [34](#)
- [125] M E Raichle, K B Larson, M E Phelps, R L Grubb, M J Welch, and M M Ter-Pogossian. In vivo measurement of brain glucose transport and metabolism employing glucose-<sup>11</sup>C. *American Journal of Physiology – Legacy Content*, 228(6):1936–1948, June 1975. [55](#)
- [126] M Reivich, A Alavi, A Wolf, J H Greenberg, J Fowler, D Christman, R MacGregor, S C Jones, J London, C Shiue, and Y Yonekura. Use of 2-Deoxy-D[1-<sup>11</sup>C]Glucose for the Determination of Local Cerebral Glucose Metabolism in Humans: Variation within and between Subjects. *Journal of Cerebral Blood Flow & Metabolism*, 2(3):307–319, 1982. [56](#)
- [127] K A Rempp, G Brix, F Wenz, C R Becker, F Gückel, and W J Lorenz. Quantification of regional cerebral blood flow and volume with dynamic susceptibility contrast-enhanced MR imaging. *Radiology*, 193(3):637–641, December 1994. [43](#)
- [128] E M Renkin. Transport of potassium-42 from blood to tissue in isolated mammalian skeletal muscles. *American Journal of Physiology – Legacy Content*, 197:1205–1210, December 1959. [52](#), [58](#)
- [129] D Revel, R C Brasch, H Paajanen, W Rosenau, W Grodd, B Engelstad, P Fox, and J Winkelhake. Gd-DTPA contrast enhancement and tissue differentiation in MR imaging of experimental breast carcinoma. *Radiology*, 158(2):319–323, February 1986. [17](#)
- [130] Gaia Rizzo, Matteo Tonietto, Marco Castellaro, Bernd Raffeiner, Alessandro Coran, Ugo Fiocco, Roberto Stramare, and Enrico Grisan. Bayesian Quantification of Contrast-Enhanced Ultrasound Images With Adaptive Inclusion of an Irreversible Component. *IEEE Transactions on Medical Imaging*, 36(4):1027–1036, December 2016. [62](#)

- [131] Bruce R Rosen, John W Belliveau, James M Vevea, and Thomas J Brady. Perfusion imaging with NMR contrast agents. *Magnetic Resonance in Medicine*, 14(2):249–265, May 1990. [43](#)
- [132] T Schlosser, C Pohl, C Veltmann, S Lohmaier, J Goenechea, A Ehlgren, J Köster, D Bimmel, S Kuntz-Hehner, H Becher, and K Tiemann. Feasibility of the flash-replenishment concept in renal tissue: which parameters affect the assessment of the contrast replenishment? *Ultrasound in Medicine & Biology*, 27(7):937–944, July 2001. [32](#)
- [133] K Q Schwarz, G P Bezante, X Chen, J G Mottley, and R Schlieff. Volumetric arterial flow quantification using echo contrast. An in vitro comparison of three ultrasonic intensity methods: radio frequency, video and Doppler. *Ultrasound in Medicine & Biology*, 19(6):447–460, 1993. [23](#)
- [134] C W Sheppard and L J Savage. The random walk problem in relation to the physiology of circulatory mixing. In *Physical Review*, pages 489–490. AMERICAN PHYSICAL SOC ONE PHYSICS ELLIPSE, COLLEGE PK, MD 20740-3844 USA, 1951. [28](#)
- [135] M D Short, H I Glass, G D Chisholm, P Vernon, and D J Silvester. Gamma-camera renography using <sup>123</sup>I-hippuran. *The British journal of radiology*, 46(544):289–294, April 1973. [38](#)
- [136] D H Simpson and P N Burns. Pulse inversion Doppler: a new method for detecting nonlinear echoes from microbubble contrast agents. *Ultrasonics Symposium*, 1997. [32](#)
- [137] G N Stewart. Researches on the Circulation Time and on the Influences which affect it. *The Journal of Physiology*, 22(3):159–183, November 1897. [13, 19, 29, 43](#)
- [138] T Stolnikow. *Die Aichung des Blutetromes in der Aorta des Hundes.* Arch f Anat u Physiol, 1886. [13](#)
- [139] R W Stow and P S Hetzel. An empirical formula for indicator-dilution curves as obtained in human beings. *Journal of applied physiology*, 7(2):161–167, September 1954. [25](#)

- [140] Ukihide Tateishi, Hiroshi Nishihara, Satoshi Watanabe, Toshiaki Morikawa, Kazuhiko Abe, and Kazuo Miyasaka. Tumor Angiogenesis and Dynamic CT in Lung Adenocarcinoma: Radiologic–Pathologic Correlation. *Journal of Computer Assisted Tomography*, 25(1):23–27, January 2001. [15](#)
- [141] Torfinn Taxt, Radovan Jirik, Cecilie Brekke Rygh, Renate Grüner, Michal Bartos, Erling Andersen, Fitz-Roy Curry, and Rolf K Reed. Single-channel blind estimation of arterial input function and tissue impulse response in DCE-MRI. *Biomedical Engineering*, 59(4):1012–1021, March 2012. [51](#)
- [142] C Tei, T Sakamaki, P M Shah, S Meerbaum, K Shimoura, S Kondo, and E Corday. Myocardial contrast echocardiography: a reproducible technique of myocardial opacification for identifying regional perfusion deficits. *Circulation*, 67(3):585–593, March 1983. [20](#)
- [143] F J Ten Cate, J K Drury, S Meerbaum, J Noordsy, S Feinstein, P M Shah, and E Corday. Myocardial contrast two-dimensional echocardiography: experimental examination at different coronary flow levels. *Journal of the American College of Cardiology*, 3(5):1219–1226, May 1984. [20](#)
- [144] F J Ten Cate, J H Cornel, P W Serruys, W B Vletter, J Roelandt, and W H Mitterreiner. Quantitative assessment of myocardial blood flow by contrast two-dimensional echocardiography: initial clinical observations. *American journal of physiologic imaging*, 2(2):56–60, 1987. [21](#)
- [145] K Tiemann, T Schlosser, C Pohl, D Bimmel, G Wietasch, A Hoeft, J Likungu, C Vahlhaus, S Kuntz, N C Nanda, H Becher, and B Lüderitz. Are microbubbles free flowing tracers through the Myocardium? Comparison of indicator-dilution curves obtained from dye dilution and echo contrast using harmonic power Doppler imaging. *Echocardiography (Mount Kisco, N.Y.)*, 17(1):17–27, January 2000. [25](#)
- [146] Klaus Tiemann, Harald Becher, Dieter Bimmel, Reinhard Schlieff, and Navin C Nanda. Stimulated Acoustic Emission Nonbackscatter Contrast Effect of Microbubbles Seen

- with Harmonic Power Doppler Imaging. *Echocardiography (Mount Kisco, N.Y.)*, 14(1): 65–70, January 1997. [25](#)
- [147] Klaus Tiemann, Stefan Lohmeier, Stefanie Kuntz, Jörg Köster, Christoph Pohl, Peter Burns, Thomas R, Navin C Nanda, Berndt Lüderitz, and Harald Becher. Real-Time Contrast Echo Assessment of Myocardial Perfusion at Low Emission Power: First Experimental and Clinical Results Using Power Pulse Inversion Imaging. *Echocardiography (Mount Kisco, N.Y.)*, 16(8):799–809, November 1999. [32](#)
- [148] R Tigerstedt. *Bestimmung der von dem linken Herzen herausgetriebenen Blutmenge*. Skand. Arch. f. Physiol, 1891. [13](#)
- [149] Paul S Tofts, Gunnar Brix, David L Buckley, Jeffrey L Evelhoch, Elizabeth Henderson, Michael V Knopp, Henrik B Larsson, Ting-Yim Lee, Nina A Mayr, Geoffrey J Parker, Ruediger E Port, June Taylor, and Robert M Weisskoff. Estimating kinetic parameters from dynamic contrast-enhanced T(1)-weighted MRI of a diffusible tracer: standardized quantities and symbols. *Journal of Magnetic Resonance Imaging*, 10(3):223–232, 1999. [58](#), [59](#), [60](#)
- [150] Y Tsushima. Functional CT of the kidney. *European journal of radiology*, 30(3):191–197, June 1999. [57](#)
- [151] Yoshito Tsushima, Martin J K Blomley, Shoichi Kusano, and Keigo Endo. The Portal Component of Hepatic Perfusion Measured by Dynamic CT (An Indicator of Hepatic Parenchymal Damage). *Digestive Diseases and Sciences*, 44(8):1632–1638, 1999. [15](#)
- [152] M E Valentinuzzi and E M Montaldo Volachec. Discrete deconvolution. *Medical & biological engineering*, 13(1):123–125, January 1975. [36](#), [38](#), [45](#)
- [153] Byron F Vandenberg, Robert Kieso, Karen Fox-Eastham, William Chilian, and Richard E Kerber. Quantitation of myocardial perfusion by contrast echocardiography: Analysis of contrast gray level appearance variables and intracyclic variability. *Journal of the American College of Cardiology*, 13(1):200–206, January 1989. [21](#)

- [154] K L Verstraete, Y De Deene, H Roels, A Dierick, D Uyttendaele, and M Kunnen. Benign and malignant musculoskeletal lesions: dynamic contrast-enhanced MR imaging-parametric "first-pass" images depict tissue vascularization and perfusion. *Radiology*, 192(3):835–843, September 1994. [18](#)
- [155] C Vierordt. Die Erscheinungen und Gesetze der Stromgeschwindigkeiten des Blutes: Nach Versuchen, 1858. [13](#)
- [156] Rolf Vogel, Andreas Indermühle, Jessica Reinhardt, Pascal Meier, Patrick T Siegrist, Mehdi Namdar, Philipp A Kaufmann, and Christian Seiler. The quantification of absolute myocardial perfusion in humans by contrast echocardiography: algorithm and validation. *Journal of the American College of Cardiology*, 45(5):754–762, March 2005. [50](#)
- [157] A W Volkmann. *Die Hämodynamik*. 1850. [13](#)
- [158] D Walley and C W Sheppard. Basic Principles of the Tracer Method. *Biometrika*, 51(1/2):294, June 1964. [28](#)
- [159] Hiroshi Watabe, Yoko Ikoma, Yuichi Kimura, Mika Naganawa, and Miho Shidahara. PET kinetic analysis-compartmental model. *Annals of nuclear medicine*, 20(9):583–588, November 2006. [56](#)
- [160] Kevin Wei, Ananda R Jayaweera, Soroosh Firoozan, Andre Linka, Danny M Skyba, and Sanjiv Kaul. Quantification of Myocardial Blood Flow With Ultrasound-Induced Destruction of Microbubbles Administered as a Constant Venous Infusion. *Circulation*, 97(5):473–483, February 1998. [31](#), [32](#), [50](#)
- [161] Kevin Wei, Elizabeth Le, Jian-Ping Bin, Matthew Coggins, Jerrel Thorpe, and Sanjiv Kaul. Quantification of renal blood flow with contrast-enhanced ultrasound. *Journal of the American College of Cardiology*, 37(4):1135–1140, March 2001. [32](#)
- [162] H J Weinmann, R C Brasch, W R Press, and G E Wesbey. Characteristics of gadolinium-DTPA complex: a potential NMR contrast agent. *AJR. American journal of roentgenology*, 142(3):619–624, March 1984. [16](#)

- [163] G E Wesbey, C B Higgins, M T McNamara, B L Engelstad, M J Lipton, R Sievers, R L Ehman, J Lovin, and R C Brasch. Effect of gadolinium-DTPA on the magnetic relaxation times of normal and infarcted myocardium. *Radiology*, 153(1):165–169, October 1984. [16](#)
- [164] J G Wiencek, S B Feinstein, R Walker, and S Aronson. Pitfalls in quantitative contrast echocardiography: the steps to quantitation of perfusion. *Journal of the American Society of Echocardiography*, 6(4):395–416, July 1993. [24](#)
- [165] W Wijns, P W Serruys, J H Reiber, M van den Brand, M L Simoons, C J Kooijman, K Balakumaran, and P G Hugenholtz. Quantitative angiography of the left anterior descending coronary artery: correlations with pressure gradient and results of exercise thallium scintigraphy. *Circulation*, 71(2):273–279, February 1985. [21](#)
- [166] N Wilke, C Simm, J Zhang, J Ellermann, X Ya, H Merkle, G Path, H Lüdemann, R J Bache, and K Uğurbil. Contrast-enhanced first pass myocardial perfusion imaging: correlation between myocardial blood flow in dogs at rest and during hyperemia. *Magnetic Resonance in Medicine*, 29(4):485–497, April 1993. [18](#)
- [167] Norbert Wilke, Keith Kroll, Hellmut Merkle, Ying Wang, Yukata Ishibashi, Ya Xu, Jiani Zhang, Michael Jerosch-Herold, Andreas Muhler, Arthur E Stillman, James B Bassingthwaigte, Robert Bache, and Kamil Ugurbil. Regional myocardial blood volume and flow: First-pass MR imaging with polylysine-Gd-DTPA. *Journal of Magnetic Resonance Imaging*, 5(2):227–237, March 1995. [44](#)
- [168] M Wintermark, J P Thiran, P Maeder, P Schnyder, and R Meuli. Simultaneous measurement of regional cerebral blood flow by perfusion CT and stable xenon CT: a validation study. *AJNR. American journal of neuroradiology*, 22(5):905–914, May 2001. [41](#)
- [169] M E Wise. The geometry of log-normal and related distributions and an application to tracer-dilution curves. *Statistica Neerlandica*, 20(1):119–142, March 1966. [25](#)

- [170] M E Wise. Tracer dilution curves in cardiology and random walk and lognormal distributions. *Acta physiologica et pharmacologica Neerlandica*, 14(2):175–204, 1966. [28](#)
- [171] Ona Wu, Leif Østergaard, Robert M Weisskoff, Thomas Benner, Bruce R Rosen, and A Gregory Sorensen. Tracer arrival timing-insensitive technique for estimating flow in MR perfusion-weighted imaging using singular value decomposition with a block-circulant deconvolution matrix. *Magnetic Resonance in Medicine*, 50(1):164–174, July 2003. [43](#)
- [172] Kyosuke Yanagisawa, Fuminori Moriyasu, Takeo Miyahara, Miyata Yuki, and Hiroko Iijima. Phagocytosis of ultrasound contrast agent microbubbles by Kupffer cells. *Ultrasound in Medicine & Biology*, 33(2):318–325, February 2007. [19](#)
- [173] Thomas E Yankeelov, Jeffrey J Luci, Martin Lepage, Rui Li, Laura Debusk, P Charles Lin, Ronald R Price, and John C Gore. Quantitative pharmacokinetic analysis of DCE-MRI data without an arterial input function: a reference region model. *Magnetic resonance imaging*, 23(4):519–529, May 2005. [60, 61](#)
- [174] W T Yeung, T Y Lee, R F Del Maestro, R Kozak, J D Bennett, and T Brown. An absorptiometry method for the determination of arterial blood concentration of injected iodinated contrast agent. *Physics in medicine and biology*, 37(9):1741–1758, September 1992. [40](#)
- [175] W T Yeung, T Y Lee, R F Del Maestro, R Kozak, and T Brown. In vivo CT measurement of blood-brain transfer constant of iopamidol in human brain tumors. *Journal of neuro-oncology*, 14(2):177–187, October 1992. [57](#)
- [176] M Zhang and M Kono. Solitary pulmonary nodules: evaluation of blood flow patterns with dynamic CT. *Radiology*, 205(2):471–478, November 1997. [15](#)
- [177] Sibylle I Ziegler, Uwe Haberkorn, Helen Byrne, Garrison Tong, Rudolph Schosser, Heiner Krieter, Stefan Kaja, Jens A Richolt, Adriaan A Lammertsma, and Patricia Price. Measurement of liver blood flow using oxygen-15 labelled water and dynamic

- positron emission tomography: Limitations of model description. *European Journal of Nuclear Medicine*, 23(2):169–177, February 1996. [55](#), [58](#)
- [178] Kenneth L Zierler. Theoretical Basis of Indicator-Dilution Methods For Measuring Flow and Volume. *Circulation research*, 10(3):393–407, March 1962. [35](#)



## **Part II**

**Reproducibility of the existing methods  
and the relations between them**



# Foreword

In the second part of this thesis, we perform an in-depth investigation of three major perfusion quantification techniques. The techniques investigated are a semi-quantitative method using the log-normal distribution, a one-compartment model using an arterial measurement, and a one-compartment model using a reference tissue. The first two methods yield absolute parameters while the third directly yields relative parameters. Relative parameters were derived from the absolute parameters using their value inside a reference tissue. In an attempt to reveal the spatial functional heterogeneity of tumors while ensuring reasonable signal-to-noise ratio in the time-intensity curves, the models were fitted to regional time-intensity curves resulting from the cutout of the perfused tumor area.

Our group previously proposed a multiplicative noise model to reflect the characteristics of noise in ultrasound data. The multiplicative noise model was not used in this study however, as it was unable to accurately fit the regional data despite using the least-square estimates as initialization values. Instead, we used a non-linear least-square estimation method to fit all models.

The log-normal model is commonly used in the litterature to fit perfusion curves, and in particular contrast-enhanced ultrasound data. It is mainly used to filter out the noise of the time-intensity curves, and semi-quantitative parameters are usually derived from the fitted curve, e.g. the area under the curve, the peak enhancement, or the wash-in rate. Our research group used the log-normal model to fit the global mean time-intensity curve inside the perfused area of tumors. The author of this study revealed the poor reproducibility of the global semi-quantitative parameters despite the improvement resulting from the use of an automatic injection setup, which was also used in Chapter 3.

Compartmental modeling performs a normalization of the studied time-intensity curve

by the input of the system through deconvolution, theoretically making parameters independant on the characteristics of the tracer injection, i.e. quantity, duration. Compartmental approaches were primarily developed for nuclear medicine imaging techniques, they were then extended to other perfusion imaging modalities, in particular to contrast-enhanced magnetic resonance imaging. The one-compartment model is the most basic form of compartmental model, and is particularly designed for intravascular tracers like ultrasound contrast agents. However no reference of this model applied to contrast-enhanced ultrasound data was found in the litterature. The method allows the estimation of absolute perfusion parameters, i.e. tissue blood flow, and tissue blood volume. However, as discussed in Chapter 2, arterial measurements are subject to artifacts, and are in fact not always possible.

To alleviate the need for arterial measurements, relative methods making use of a reference tissue instead were developed, allowing direct estimation of relative perfusion parameters. These relative parameters are closely related to the absolute parameters, except they are normalized according to the reference tissue. The tissue interest can be selected in a large and homogeneous region free of large blood vessels, reducing the influence of noise, saturation, and partial volumes.

The reproducibility of the regional parameters estimated using the two absolute methods and the three relative methods was investigated through test-retest experiments in order to limit the inter-exam changes to their minimum. Additionally, the impact of accounting for the time taken by the tracer to arrive in the tissue on the reproducibility of the estimated perfusion parameter was studied. The experimental setup and the results are reported in Chapter 3 which is the content of an article published in *Physics in Medicine and Biology*. In Chapter 4, we propose an extention of this work establishing the relations between the parameters of the three models mentioned above, first theoretically, and then experimentally through a correlation study. The references cited in these two chapters are pooled together and presented at the end of this part of the thesis.

# **Chapter 3**

## **Quantification of tumor perfusion using DCE-US: impact of mathematical modeling**

### **3.1 Abstract**

Dynamic Contrast Enhanced Ultrasound has been proposed to monitor tumor therapy, in complement to volume measurements. To assess the variability of perfusion parameters in ideal conditions, four consecutive test-retest studies were acquired in a tumor model of mouse, using controlled injections. The impact of mathematical modeling on parameter variability was then investigated. Coefficients of variation (CV) of tissue blood volume (BV) and tissue blood flow (BF) based-parameters were estimated inside 32 sub-regions of the tumors, comparing the log-normal (LN) model with a one-compartment model fed by an arterial input function (AIF) and improved by the introduction of a time delay parameter. Relative perfusion parameters were also estimated by normalization of the LN parameters and normalization of the one-compartment parameters estimated with the AIF, using a reference tissue (RT) region. A direct estimation ( $rRT_d$ ) of relative parameters based on the one-compartment model without using the AIF was also obtained by using the kinetics inside the RT region. Results on test-retest studies show that absolute regional parameters

have high CV, whatever the approach, with median values of about 30% for BV, and 40% for BF. The positive impact of normalization was established, showing a coherent estimation of relative parameters, with reduced CV (about 20% for BV and 30% for BF using the rRTd approach). These values were significantly lower ( $p < 0.05$ ) when compared to CV of absolute parameters. The rRTd approach provided the smallest CV and should be preferred for estimating relative perfusion parameters.

## 3.2 Introduction

Reliable quantification of tumor perfusion is a challenging objective in order to establish cancer diagnosis and to monitor therapy. Tumor perfusion can be assessed through various imaging modalities, including PET, Dynamic Contrast Enhanced (DCE) MR, CT, and ultrasound (DCE-US).

Compared to DCE-MRI, DCE-CT and PET, the main advantages of DCE-US are its real-time, non-ionizing, and cost-effective characteristics. Moreover, as micro-bubbles do not diffuse in the extra-vascular space, DCE-US studies reflect only the tissue vasculature. Different acquisition protocols are available including bolus and destruction-replenishment during infusion [24]. The present work focuses on bolus injections, since this acquisition mode is the most widely used [2].

It is currently recommended for bolus DCE-US studies to estimate semi-quantitative parameters using explicit models, such as the Log-Normal model [17]. However, it was shown that these semi-quantitative parameters were sensitive to various factors [18]: scanner-related (e.g. frequency, mechanical index, dynamic range, focal length), patient-related (e.g. blood pressure, tissue motion, physiological interaction), and bubble-related (e.g. bubble type, concentration, preparation, injection) factors. The quantification of bolus DCE-US studies thus remains a major challenge.

In an attempt to make quantification of tissue perfusion less sensitive to external factors, quantitative approaches based on indicator dilution theory and commonly used for PET, DCE-MRI or DCE-CT exams [14, 19, 23] could be applied to DCE-US data. These methods estimate tissue blood volume and tissue blood flow parameters by performing a specific de-

convolution of the tissue time-intensity curve inside the tumor by an Arterial Input Function (AIF) measured in the imaging plane. Similarly to what was done in above cited imaging modalities, a compartmental approach was recently proposed for DCE-US [4]. Precisely, a one-compartment model was proposed since the contrast agent remains in the blood. This approach defines a set of admissible curves for the transfer function (mono-exponential functions), and the estimation of parameters is then regularized intrinsically. It can thus be distinguished from blind deconvolutions, as recently proposed in DCE-US [5, 10]. Indeed, these approaches require establishing strong constraints on the transfer functions, due to their large number of unknown parameters.

The present study aimed at comparing different modeling approaches and at studying the reproducibility of perfusion parameters in test-retest measurements on a mouse tumor model, acquired using controlled injections [3]. Three absolute modeling approaches including a Log-Normal model and a one-compartment model without and with a time delay were first compared. In a second time, relative perfusion parameters were defined by normalizing the values obtained in the tumor with values obtained in a reference tissue region, and five relative derived models were studied.

## 3.3 Materials

### 3.3.1 Animals

Murine Lewis Lung Carcinoma (3LL) were used. Tumor fragments (20-40 mm<sup>3</sup>) were implanted subcutaneously 20 days prior to the experiment in the right flank of four Balb/C mice. All experiments were conducted in accordance with the institutional guidelines and the recommendations for the care and use of laboratory animals.

Prior to imaging, animals were individually placed in an induction chamber, where anesthesia was induced with 4% isoflurane in air with delivery rate of 1 L/min. Anesthesia was maintained with 2% isoflurane in air delivered by a face mask with the same delivery rate. The temperature of the animal was regulated using a thermostatic heating plate (Minerve, Esternay, France). Each mouse was secured in position with surgical tape so that the oper-

ator could not inadvertently reposition it during the procedure.

### 3.3.2 Image acquisition

Dynamic contrast-enhanced US sequences were acquired using a 15L8W transducer and a Sequoia 512 US system (Acuson, Siemens, Mountain View, CA, USA) with constant mechanical index (0.1), dynamic range (80 dB), and time gain compensation settings. The imaging plane was selected as the largest cross-section of the tumor and the probe was fixed to a support in the selected position.

A bolus of 50  $\mu$ L of SonoVue (Bracco Suisse SA, Geneva, Switzerland) diluted to 20% was injected at a rate of 4.5 mL/min using a controlled injection system to improve acquisition reproducibility [3]. This diluted concentration was proposed to reduce attenuation artifacts. Each acquisition consisted of a 4 minute dual-mode recording, including B-Mode and Contrast Pulse Sequencing (CPS) images, using a frame rate of 3 Hz during the first 30 seconds (including the wash-in phase and the beginning of the wash-out phase), and 1 Hz for the remaining time. Four consecutive (test-retest) studies were acquired for each mouse without any modification in the setup. Fifteen minute breaks were observed between acquisitions to ensure the destruction of all circulating micro-bubbles.

### 3.3.3 Data pre-processing

Linear echo-power kinetics were extracted from log-compressed video data using a validated home-made software calibrated using dose-ranging data [16]. Both probe and animal motion were assumed negligible for the selected sequences.

Tumors were segmented on the B-mode acquisition and necrotic zones were excluded as previously described [3]. In order to further reveal spatial heterogeneity inside the tumor, a regional analysis of the tumor area was performed. Dividing the non-necrotic tumor region into 32 sub-regions according to 4 radial layers and 8 angular sectors (Figure 3-1) provided a good compromise between showing heterogeneity while preserving the signal to noise ratio of the time-intensity curves and the spatial matching of the sub-regions between the four test-retest studies.

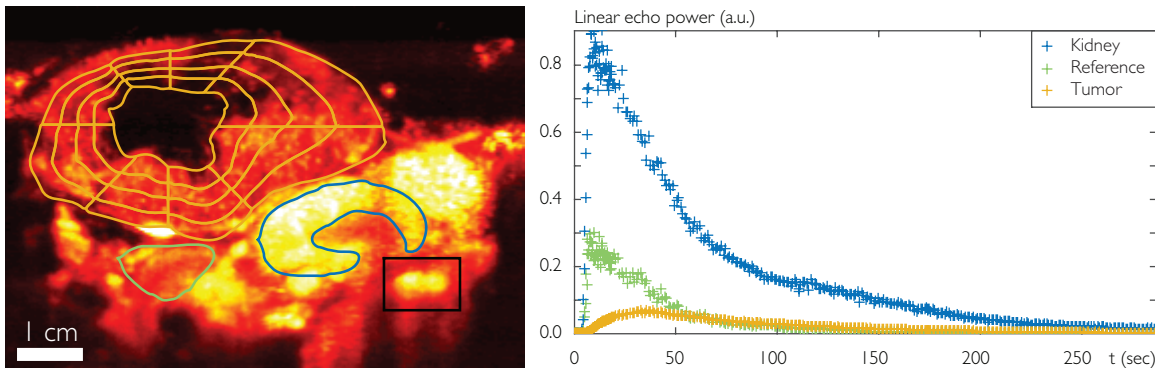


**Figure 3-1:** Illustration of the data pre-processing steps. Left: The contours of the tumor and its necrotic core have been overlaid on a contrast enhanced image (in ochre color). The perfused tumor area was divided into 4 radial layers and 8 angular sectors. A reference tissue region (in green color) and a renal cortex region (in blue color) were also delineated. Right: Mean kinetics associated with the non-necrotic part of the tumor, the reference tissue, and the renal cortex.

## 3.4 Methods

### 3.4.1 Quantification of tumor perfusion

Table 3.1 summarizes the main features of the eight methods tested, three absolute and five relative, for tumor perfusion quantification. Some methods require the definition of an arterial region in order to estimate the AIF, its estimation is presented in section 3.4.1. Relative quantification methods require the selection of a reference tissue region (labeled with subscript R). This region was segmented in order to define a homogeneous area, while being large enough in order to reduce noise influence on the subsequent analysis (Figure 3-1).

For all methods, quantitative parameters were derived by the minimization of the root-mean-square error between the time-intensity curve inside the tumor,  $C_T(t)$ , and the corresponding fitted curve, using an interior-point algorithm (MATLAB, MathWorks, Natick, MA, USA). To make the comparison between models easier, we focused on volume-based, flow-based, and time delays parameters.

Acronym	Model Name	Input data AIF/RT	Eq.	Parameters
<b>aLN</b>	Log-Normal	No/No	(3.1)	$AUC, WIR, \Delta$
<b>aAIF</b>	One-Compartment	Yes/No	(3.2)	$V, F$
<b>aAIFd</b>	One-Compartment with delay	Yes/No	(3.2)	$V, F, d$
<b>rLN</b>	Relative Log-Normal	No/Yes	(3.1,6.5)	$rAUC, rWIR, D$
<b>rAIF</b>	Relative One-Compartment	Yes/Yes	(3.2,3.4)	$rV_{AIF}, rF_{AIF}$
<b>rAIFd</b>	Relative One-Compartment with delay	Yes/Yes	(3.2,3.4)	$rV_{AIF}, rF_{AIF}, D_{AIF}$
<b>rRT</b>	Relative Reference Tissue	No/Yes	(7.6,3.6)	$rV_{RT}, rF_{RT}$
<b>rRTd</b>	Relative Reference Tissue with delay	No/Yes	(7.6,3.6)	$rV_{RT}, rF_{RT}, D_{RT}$

**Table 3.1:** Synthesis of the different models tested. The first three models propose absolute quantification. The last five models propose relative quantification.

### Absolute Log-normal model: aLN [17].

The kinetics  $C_T(t)$  is fitted according to the equation (3.1):

$$\begin{aligned} C_T(t) &= \frac{AUC_T}{\sqrt{2\pi}\sigma_T(t-\Delta_T)} \exp\left(-\frac{[\ln(t-\Delta_T)-\mu_T]^2}{2\sigma_T^2}\right) \text{ if } t > \Delta_T, \\ &= 0 \text{ otherwise,} \end{aligned} \quad (3.1)$$

where  $AUC_T$  is the area under the  $C_T$  curve,  $\mu_T$  and  $\sigma_T$  are the expectation and standard deviation of the distribution  $C_T(\tau)/AUC_T$  when substituting  $\ln(t-\Delta_T)$  with  $\tau$ , and  $\Delta_T$  represents the time shift between the start of the acquisition and the arrival of the contrast agent in the tumor. As the area under the curve  $AUC_T$  is related to the tissue blood volume [20] and the wash-in rate  $WIR_T$  (derived from  $AUC_T$ ,  $\mu_T$  and  $\sigma_T$ ) is related to the tissue blood flow [2], these two parameters were estimated in addition to  $\Delta_T$  in the remaining analysis.

### One-Compartment model with an Arterial Input Function: aAIF and aAIFd

[7]. The mathematical expression of  $C_T(t)$  is given by equation (3.2):

$$\begin{aligned} C_T(t) &= F_T \int_0^{t-d_T} C_A(\tau) \exp^{-\frac{F_T}{V_T}(t-d_T-\tau)} d\tau \quad \text{if } t \geq d_T, \\ &= 0 \text{ otherwise,} \end{aligned} \quad (3.2)$$

where  $C_A(t)$  is the kinetics inside the feeding artery (the AIF),  $V_T$  the tissue blood volume (in %),  $F_T$  the tissue blood flow (in  $s^{-1}$ ), and  $d_T$  (in s) the time-delay of the contrast agent from the feeding artery to the tumor. When it is neglected ( $d_T = 0$ ), the model is noted **aAIF**. When it is estimated in addition to  $V_T$  and  $F_T$ , the model is noted **aAIFd**.

To estimate the AIF, a bounding box surrounding arterial vessels was first defined according to anatomical considerations and high values of enhancement (see Figure 3-1). Peak Enhancement ( $PE$ ) and Time To Peak ( $TTP$ ) parametric maps were then computed for each pixel of the bounding box. The maximal value of  $PE$  ( $PE_{max}$ ) and the minimal value of  $TTP$  ( $TTP_{min}$ ) were extracted. Pixels verifying  $PE/PE_{max} \geq rPE^*$  and  $TTP - TTP_{min} \leq \Delta TTP^*$  were considered as part of the artery region (Figure 3-2), where  $rPE^*$  and  $\Delta TTP^*$  are empirically chosen cut-off values, equal to 50% and 3 s, unless specified differently. The AIF,  $C_A(t)$ , was computed as the geometric mean of the kinetics inside the artery region and modeled using the LN model (3.1).

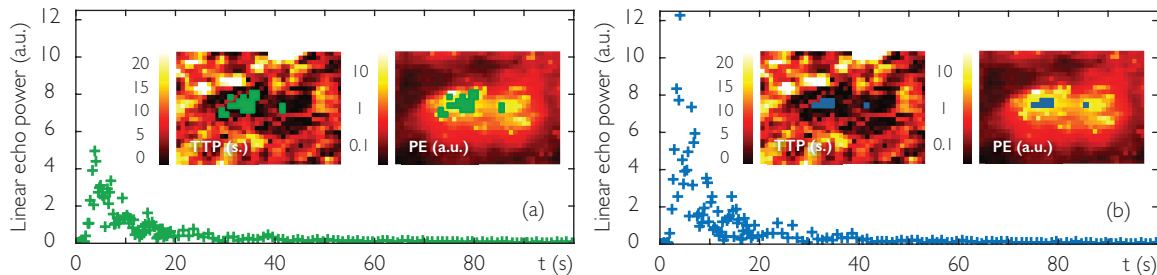


**Figure 3-2:** Automated detection of the AIF: parametric maps  $TTP$  and  $PE$  inside the artery region; segmentation results and associated AIF with: (a)  $rPE^* = 50\%$  and  $\Delta TTP^* = 3$  s (in green color); (b)  $rPE^* = 70\%$  and  $\Delta TTP^* = 2.5$  s (in blue color).

### Relative Log-Normal model: rLN.

This model estimates three relative parameters: the relative area under the curve  $rAUC$ , the relative wash-in rate  $rWIR$ , and the time delay between the arrival of the contrast in the tumor and the reference tissue  $D_{T-R}$  according to equation (6.5):

$$rAUC = \frac{AUC_T}{AUC_R}, \quad rWIR = \frac{WIR_T}{WIR_R}, \quad \text{and} \quad D_{LN}^{T-R} = \Delta_T - \Delta_R, \quad (3.3)$$

where  $(AUC_T, WIR_T, \Delta_T)$  and  $(AUC_R, WIR_R, \Delta_R)$  are the absolute LN parameters estimated in the tumor and in the reference tissue respectively using equation (3.1).

### Relative One-Compartment model with an Arterial Input Function: rAIF and rAIFd.

This model estimates three parameters: the relative blood volume  $rV_{AIF}$ , the relative blood flow  $rF_{AIF}$  and the time delay between the arrival of the contrast in the tumor and the reference tissue  $D_{AIF}^{T-R}$  according to equation (3.4):

$$rV_{AIF} = \frac{V_T}{V_R}, \quad rF_{AIF} = \frac{F_T}{F_R}, \quad \text{and} \quad D_{AIF}^{T-R} = d_T - d_R, \quad (3.4)$$

where  $(V_T, F_T, d_T)$  and  $(V_R, F_R, d_R)$  are the perfusion parameters estimated in the tumor and in the reference tissue respectively using the AIF according to equation (3.2). This method is referred to as **rAIF** when  $D_{AIF}^{T-R}$  is set to zero and **rAIFd** otherwise.

### Relative One-Compartment model using the Reference Tissue kinetics: rRT and rRTd

[15, 25]. This model estimates three parameters: the relative blood volume  $rV_{RT}$ , the relative blood flow  $rF_{RT}$  and the time delay between the arrival of the contrast in the tumor and the reference tissue  $D_{RT}^{T-R}$ , the subscript  $RT$  being used for distinguishing this approach from the previous one (section 3.4.1). Assuming that the tumor and the reference region have a common AIF, the kinetics  $C_R(t)$  and  $C_T(t)$  can be described by equation (3.2). When replacing  $C_A(t)$  by its expression as a function of  $C_R(t)$  in equation (3.2),  $C_T(t)$  can then be described by equation (5):

$$\begin{aligned} C_T(t) &= rF_{RT} \left[ C_R(t - D_{RT}^{T-R}) \right. \\ &\quad \left. + (k_R - k_T) \int_{d_R}^{t-D_{RT}^{T-R}} C_R(\tau) e^{-k_T(t-D_{RT}^{T-R}-\tau)} d\tau \right] \quad \text{if } t \geq d_T, \\ &= 0 \text{ otherwise,} \end{aligned} \quad (3.5)$$

where  $k_R = F_R/V_R$  and  $k_T = F_T/V_T$ . The parameter  $k_R$  was chosen as the mean value of the  $k_R$  values estimated with the relative AIF approach (**rAIFd**) and was set to 0.15. The parameters  $rF_{RT}$ ,  $k_T$  and  $D_{RT}^{T-R}$  were estimated by solving equation (7.6). The parameter  $rV_{RT}$

was then deduced using equation (3.6):

$$rV_{RT} = \frac{V_T}{V_R} = \frac{F_T}{k_T} \frac{k_R}{F_R} = rF_{RT} \frac{k_R}{k_T}. \quad (3.6)$$

The method is referred to as **rRT** when  $D_{RT}^{T-R}$  is set to zero and **rRTd** otherwise.

### 3.4.2 Data analysis

For each model, the quantitative assessment of the fit was achieved using the normalized root mean square error (*NRMSE*), and the fraction of information that is modeled (*FMI*), as defined in [1]. The *NRMSE* was defined by:

$$NRMSE = \frac{\sqrt{\frac{1}{nt} \sum_{t=1}^{nt} (C_{fit}(t) - C(t))^2}}{\max_t(C(t)) - \min_t(C(t))}, \quad (3.7)$$

where  $C$  and  $C_{fit}$  are the observed and fitted kinetics and  $nt$  is the total number of frames. A good fit corresponds to *NRMSE* close to 0 and *FMI* close to 100%. For each sub-region, results for which  $FMI < 90\%$  were judged as poor quality fits.

In order to assess the reproducibility of the parameters  $\theta^{hl}$  of the mouse  $m_l$  ( $l$  from 1 to 4) in the sub-region  $s_h$  ( $h$  from 1 to 32), coefficients of variation  $CV^{hl}$  were estimated using the four test-retest studies, as follows:

$$CV^{hl} = \frac{\sqrt{\frac{1}{4} \sum_{k=1}^4 (\theta^{hl}(k) - \mu^{hl})^2}}{\mu^{hl}}, \text{ where } \mu^{hl} = \frac{1}{4} \sum_{k=1}^4 \theta^{hl}(k), \quad (3.8)$$

$\theta^{hl}(k)$  being the parameter  $\theta^{hl}$  estimated for the  $k$ th test-retest study (with  $k$  from 1 to 4). As parameters  $\theta^{hl}(k)$  corresponding to poor quality fits were removed, missing values were replaced using multivariate imputation according to the R package {mice}, 'Multivariate Imputation by Chained Equations' [21], in order to compute  $CV^{hl}$  using four values systematically.

Statistical tests were performed to compare goodness of fit criteria and coefficients of variation between the different models, using the R package {coin}, 'Conditional Inference Procedures in a Permutation Test Framework' [9]. They were considered as significant when

Model	All data		$FMI > 90\%$		
	NRMSE	FMI	NRMSE	FMI	N
<b>aLN</b>	5.75 [4.70-7.41]	99.4 [98.5-99.8]	5.63 [4.62-7.00]	99.4 [98.8-99.8]	28
<b>aAIF</b>	9.95*† [6.03-24.2]	94.7*† [45.2-98.3]	6.72° [5.12-9.20]	97.8° [95.5-98.9]	212
<b>aAIFd</b>	6.21 [4.71-8.43]	98.7* [97.3-99.4]	6.04 [4.66-8.20]	98.8* [97.6-99.4]	19
<b>rRT</b>	7.72*‡ [5.83-9.85]	97.6*‡ [94.9-98.7]	7.45*‡ [5.71-9.34]	97.8*‡ [95.6-98.8]	56
<b>rRTd</b>	6.32 [4.91-8.21]	98.7* [97.2-99.4]	6.18 [4.85-8.00]	98.8* [97.6-99.4]	19

**Table 3.2:** Median [first-third quartiles] values of  $NMRSE$  and  $FMI$  (in %) obtained for the different models.  $N$  is the number of sub-regions where  $FMI < 90\%$ . Significant differences between **aLN** and any other model are indicated by \*. In addition, significant differences between **aAIF** (resp. **rRT**) and **aAIFd** (resp. **rRTd**) are indicated by † (resp. ‡). The symbol ° indicates that comparisons were not reported due to the high number of missing data.

p values were less than 0.05. As all the tests were conducted on paired data, when goodness of fit criteria were removed (due to poor quality fits), they were replaced with imputed data. The non-parametric Friedman test with post-hoc analysis (Tukey's HSD test) was chosen for dealing with multiple comparisons.

## 3.5 Results

### 3.5.1 Model comparison through quality of fit criteria

Table 3.2 shows the quartile values of the quality of fit criteria ( $NMRSE$  and  $FMI$ ), which are computed for the 512 ( $4 \times 4 \times 32$ ) tumor sub-regions for the five models: **aLN**, **aAIF**, **aAIFd**, **rRT**, and **rRTd**. Since the  $NMRSE$  and  $FMI$  criteria obtained by the three relative methods **rLN**, **rAIF** and **rAIFd** are identical to those obtained by **aLN**, **aAIF** and **aAIFd**, these results are not reported in Table 3.2. Additionally, quartile values are provided for the  $N$  sub-regions verifying  $FMI > 90\%$ . Due to the large portion of missing data for the **aAIF** model when considering only good fits (the number of excluded regions,  $N$ , being equal to 212), results of hypothesis testing were not presented for that specific case. The **aLN** model shows slightly better quality criteria than the other models (these differences are significant for  $FMI$  in all cases, and significant for  $NRMSE$  in case of **aAIF** and **rRT** models). The introduction of the time delay parameter (**aAIFd**, **rAIFd** and **rRTd** models)

significantly improved the modeling quality, according to both criteria. Furthermore, the number of cases for which  $FMI < 90\%$  was largely reduced when taking into account the time delays. For these reasons, results obtained without time delays (**aAIF**, **rAIF** and **rRT**) were not further reported.

### 3.5.2 Model comparison through coefficients of variation

All mean values and standard deviations of the perfusion parameters are given for each mouse in Appendix, in Table 3.4. Figure 3-3 illustrates for one specific mouse ( $m_1$ ) the comparison between the parameters estimated by the different models. It shows a high correlation between the volume-based parameters:  $AUC$ ,  $rAUC$ ,  $V$ ,  $rV_{AIF}$ , and  $rV_{RT}$  as well as a high correlation between the flow-based parameters:  $WIR$ ,  $rWIR$ ,  $F$ ,  $rF_{AIF}$ , and  $rF_{RT}$ . This figure shows also that there is a large range of values for each parameter within one tumor, demonstrating that perfusion parameters inside the different sub-regions of the tumor are far from being similar. Finally, it proves that the slopes may be quite different from one study to another, and that the use of relative parameters contributes to largely reduce the differences between the test-retest studies, the estimation of  $rF_{AIF}$  being less robust than the estimation of  $rWIR$  or  $rF_{RT}$  for this specific example. Table 3.3 illustrates the influence of the AIF choice on the estimation of volume, flow, and time delay parameters. On this specific exam, two AIF were generated, the first one ( $AIF_1$ ) with thresholds  $rPE^* = 50\%$  and  $\Delta TTP^* = 3$  s, the second one ( $AIF_2$ ) with thresholds  $rPE^* = 70\%$  and  $\Delta TTP^* = 2.5$  s (as shown in Figure 3-2). The variations were very large for  $V$  and  $F$  parameters, while they remained moderate for  $rF_{AIF}$  and time delays, and very low for  $rV_{AIF}$ .

	$V$ (%)	$rV_{AIF}$ (%)	$F$ ( $10^{-3} \text{ s}^{-1}$ )	$rF_{AIF}$ (%)	$d_T$ (s)	$D_{AIF}^{T-R}$ (s)
$AIF_1$	$8.02 \pm 3.89$	$84.5 \pm 40.9$	$6.54 \pm 5.37$	$8.83 \pm 7.24$	$2.4 \pm 3.4$	$1.4 \pm 3.4$
$AIF_2$	$4.65 \pm 2.25$	$85.2 \pm 41.3$	$3.20 \pm 2.61$	$10.1 \pm 8.21$	$2.0 \pm 3.3$	$1.6 \pm 3.3$

**Table 3.3:** Mean  $\pm$  standard deviation of the parameters estimated with the **aAIFd** and **rAIFd** models, using two different sets of cut-offs to generate the AIF functions.

Finally, Figure 5-2 shows the distributions of the coefficients of variation of volume-based and flow-based parameters, computed according to equation (3.8). Relative volume

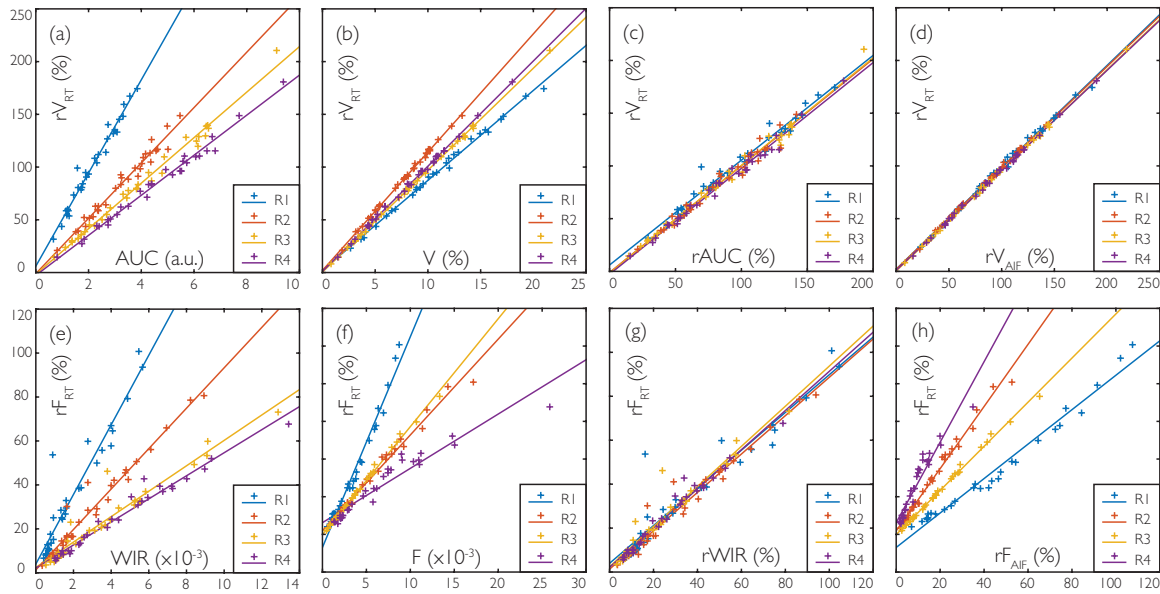


**Figure 3-3:** Comparison of the volume-based and flow-based parameters obtained for the four test-retest exams ( $R_1$ ,  $R_2$ ,  $R_3$ , and  $R_4$ ) of the mouse  $m_1$ : linear regressions between (a)  $rV_{RT}$  and  $AUC$  (a.u.), (b)  $rV_{RT}$  and  $V$ , (c)  $rV_{RT}$  and  $rAUC$ , (d)  $rV_{RT}$  and  $rV_{AIF}$ , (e)  $rF_{RT}$  and  $WIR$ , (f)  $rF_{RT}$  and  $F$ , (g)  $rF_{RT}$  and  $rWIR$ , (h)  $rF_{RT}$  and  $rF_{AIF}$ .

parameters ( $rAUC$ ,  $rV_{AIF}$ , and  $rV_{RT}$ ) have significantly lower CV than absolute volume parameters ( $AUC$  and  $V$ ). No significant difference was found when comparing  $WIR$ ,  $F$ , and  $rWIR$ , but the CV of these parameters are significantly higher than those of  $rF_{AIF}$  and  $rF_{RT}$ . Numerical values of these mean CV are given for each mouse in Appendix, in Table 3.5.

## 3.6 Discussion

Using a test-retest study with a controlled bolus injection, it was possible to assess the variability of DCE-US perfusion parameters. To reduce this variability, the interest of estimating relative parameters, which necessitates the definition of a reference tissue region, was practically demonstrated. Our study also shows the importance of choosing an appropriate method for the estimation of the parameters, because estimation methods have an impact on parameter variability. Thus the reference tissue approach (**rRTd**) can be recommended, since it is the most robust method when considering the volume-based and the flow-based parameters simultaneously.

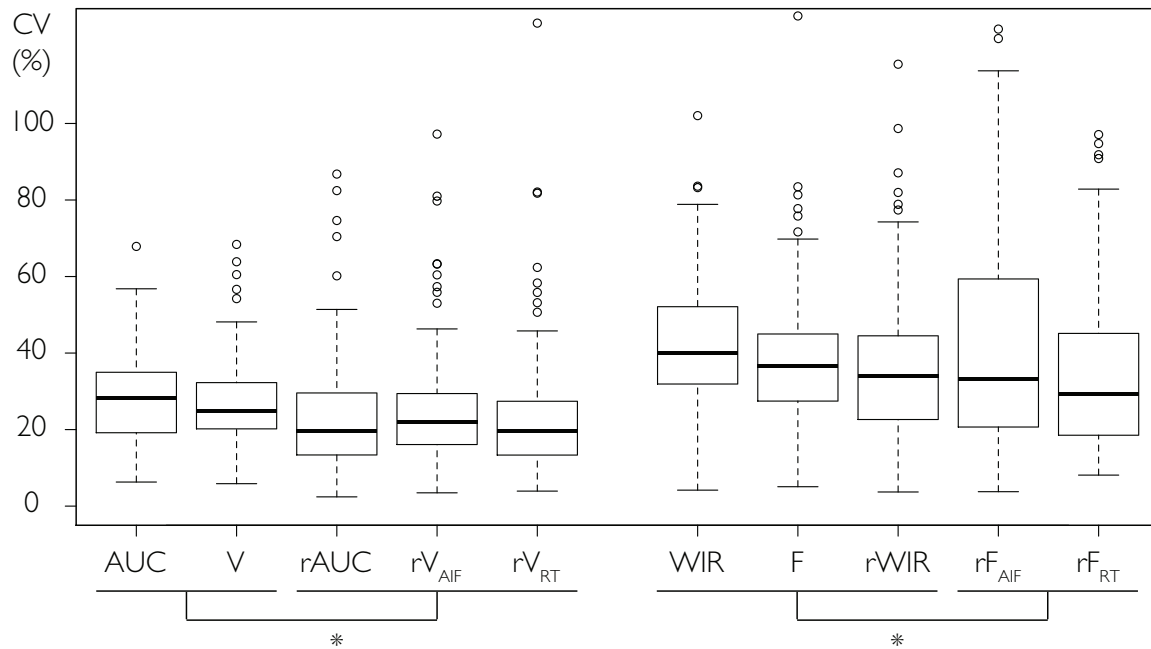


**Figure 3-4:** Boxplot showing the coefficients of variation of blood volume parameters (left) and blood flow parameters (right) estimated with the **aLN**, **rLN**, **aAIFd**, **rAIFd**, and **rRTd** models. For each box, the bold line represents the median value, the bottom and top lines the first and third quartiles. Dotted lines extend to the most extreme data points which are less than 1.5 times the interquartile range. Outlier points are displayed with empty circles. Two groups of parameters were built (horizontal lines below the parameter names) such that there were no significant intra-group differences while there were statistically significant inter-group differences (marked by \*).

The recommendations of the EFSUMB for DCE-US quantification in oncology suggest to estimate parameters such as *AUC* and *WIR* from explicitly defined models, e.g. using the **aLN** model. To reduce the variability of the estimated parameters, Dizeux et al. proposed a controlled injection system [3]. However, the present study shows that the differences between two consecutive exams are still not negligible for a regional analysis. Since in PET and DCE-MRI, deconvolution approaches and compartmental models have proved their efficiency to make parameters more robust to inter-exam changes, we decided to test some of these approaches. The most commonly used methods require the estimation of an arterial input function. Deconvolution approaches were recently proposed to quantify tissue perfusion in DCE-US [5]. These approaches estimate the transfer function of the system (depending on a large number of parameters), and to avoid aberrant solutions, this estima-

tion needs to be regularized. Following this idea, the one-compartment model with time delay is a deconvolution depending on three parameters only. When the time delay is set to 0, (**aAIF** model), we have shown that the quality of fit is worse than the one obtained when using the explicit **aLN** model. When introducing a time delay parameter, an option that is unfortunately generally overlooked [11], a much more accurate fit of regional tumor kinetics was obtained. Indeed, the quality of fit using **aLN** (depending on four parameters) and this **aAIFd** model was equivalent in terms of *NRMSE*.

Our study shows the crucial role of the AIF estimation in the variability of the perfusion parameters (see Table 3.3). When focusing the field of view in the main plane of the tumor, it can be difficult to estimate the AIF robustly (see Figure 3-2). Indeed, AIF measurements in small vessels can be affected by partial volume effects, yielding underestimation of the signal intensity. Thus coefficients of variation deduced from the **aAIFd** model can be high. Note that some problems could also occur in larger vessels, including non-linearities between concentration and measured signal, and attenuation artifacts [13].

The use of relative parameters was suggested to overcome the difficulties of estimating the AIF for a compartmental model in DCE-MRI [25]. Clinical studies have reported the interest of estimating normalized perfusion parameters in DCE-US [6, 8, 12]. Using systematically three models (**rLN**, **rAIFd**, **rRTd**), our study reinforces the interest of estimating relative parameters. The choice of a reference tissue region is less critical than the segmentation of an artery. Indeed, a larger structure can be used, reducing segmentation errors and the impact of partial volume effect. Furthermore, as the contrast concentration is lower, the quantification errors due to non-linearity are reduced. Kidney regions were initially tested but finally excluded because of the overlap of cortical, proximal tubular and distal tubular compartments. Muscular regions that could be delineated on the four exams were finally chosen.

Recirculation is a major problem when dealing with modeling techniques adapted to first-pass studies. However, its quantitative impact is reduced in DCE-US when compared to other modalities since the destruction of microbubbles, in the lungs in particular, makes the number of microbubbles much smaller in the second pass (and following) than it is in the first pass. We deliberately did not try to model the recirculation, when we chose the **aLN**

model to fit tumor kinetics or when we first fit the AIF using the **aLN** model. In addition, using simulated data, we showed that the practical impact on parameters estimation when neglecting the recirculation was limited, especially for relative parameters, since the coefficients of variation between parameters estimated with and without simulating the recirculation effect were less than the ones estimated through the test-retest studies (this recirculation effect was about 5% on CV values with the **rRTd** approach).

The use of normalized parameters induced a significant reduction of coefficients of variation in our test-retest study. Furthermore, estimating relative volume and flow parameters using equation (7.6), which eliminates the need for an AIF, is more robust than using the AIF directly. It should also be noted that the small 3D displacements occurring between the four test-retest studies can partly explain the CV, due to the imperfect spatial alignment between sub-regions from one exam to the following one.

Figure 3-3 reveals strong correlations between the different parameters computed inside a same sub-region, and a large variation of these parameters according to the tumor sub-regions. Thus, whatever the model used, all the flow-based or volume-based parameters can reveal spatial tumor heterogeneity. However, when it comes to the comparison of longitudinal exams, it is crucial to have comparable parameter values. Thus, the estimation of relative parameters seem to be the most powerful solution, provided that the reference tissue characteristics are not modified between exams. Some interesting results have been recently shown [22] for a longitudinal study using a 3D DCE-US approach. Compared with the 2D approach, the 3D approach enables assessment of the whole tumor and should be preferred for tumor monitoring.

## 3.7 Conclusion

This study aimed at proposing valuable modeling of DCE-US studies to estimate reliable perfusion parameters in a murine model of tumor. First, it was shown that a one-compartment model based on an AIF, and completed by the estimation of a time-delay parameter, could fit kinetics as closely as the explicit log-normal model. Second, a comprehensive comparison of the parameters estimated by different approaches was proposed, showing high correla-

tions between the volume-based and flow-based parameters respectively estimated. Based on test-retest studies with controlled injections, a large variability (up to 40%) of regional perfusion parameters was established due to the inherent variations of experimental and physiological conditions for the log-normal modeling and to the difficulties in estimating a correct AIF in the image field of view for the compartmental approach. To reduce this variability, the use of relative values of these regional perfusion parameters was proposed, requiring in all cases the delineation of a reference tissue region. To estimate these relative parameters, the reference tissue model proved to be the most reliable computing approach. Thus we recommend the use of this model to estimate reliable relative perfusion parameters.

### 3.8 Acknowledgments

The authors are grateful to the anonymous reviewers for their valuable comments on the paper. This work was funded by the Fondation pour la Recherche Médicale through the Bio-ingénierie pour la Santé research grant DBS2013lI28436. Research was also supported by the Institut Universitaire d'Ingénierie en Santé, Sorbonne Université, Projet OCSCC 2014/2016. Experiments were performed on a platform of France Life Imaging partly funded by the grant ANR-11-INBS-0006 associated within the Plateforme Imagerie du Vivant. All the animals were house kept at Centre d'Explorations Fonctionnelles of Centre de Recherche des Cordeliers, Agreement A75-06-12.

## Appendix

This appendix gives the numerical results that were obtained for each mouse ( $m_1$ ,  $m_2$ ,  $m_3$ , and  $m_4$ ), including mean values and standard deviations of regional parameters (Table 3.4) and coefficients of variation of these parameters (Table 3.5).

	Absolute parameters		Relative parameters		
	AUC (a.u.)	V (%)	rAUC (%)	rV <sub>AIF</sub> (%)	rV <sub>RT</sub> (%)
$m_1$	$3.47 \pm 1.82$	$8.61 \pm 4.31$	$87.2 \pm 37.9$	$87.6 \pm 41.5$	$85.9 \pm 41.2$
$m_2$	$5.97 \pm 2.08$	$17.6 \pm 6.60$	$11.2 \pm 3.19$	$18.1 \pm 6.25$	$13.2 \pm 3.51$
$m_3$	$6.74 \pm 3.51$	$12.9 \pm 6.40$	$144 \pm 81.3$	$131 \pm 73.0$	$132 \pm 75.2$
$m_4$	$7.90 \pm 4.23$	$21.2 \pm 11.6$	$57.9 \pm 30.6$	$62.3 \pm 33.1$	$59.4 \pm 31.6$
	WIR (a.u. s <sup>-1</sup> )	F (s <sup>-1</sup> )	rWIR (%)	rF <sub>AIF</sub> (%)	rF <sub>RT</sub> (%)
$m_1$	$3.30 \pm 2.66$	$4.94 \pm 4.07$	$29.7 \pm 23.4$	$21.9 \pm 21.9$	$27.0 \pm 20.3$
$m_2$	$4.70 \pm 3.03$	$6.49 \pm 3.45$	$17.7 \pm 10.2$	$17.2 \pm 8.34$	$16.1 \pm 11.0$
$m_3$	$4.88 \pm 4.19$	$3.64 \pm 2.90$	$32.9 \pm 28.6$	$36.4 \pm 27.7$	$25.1 \pm 21.0$
$m_4$	$6.63 \pm 5.30$	$5.21 \pm 3.59$	$23.7 \pm 19.0$	$26.4 \pm 18.2$	$18.0 \pm 13.6$
Delay	$\Delta$ (s)	$d$ (s)	$D_{LN}^{T-R}$ (s)	$D_{AIF}^{T-R}$ (s)	$D_{RT}^{T-R}$ (s)
$m_1$	$5.5 \pm 3.4$	$3.2 \pm 4.1$	$-1.9 \pm 3.4$	$2.7 \pm 4.2$	$3.9 \pm 4.7$
$m_2$	$2.8 \pm 2.5$	$5.7 \pm 4.7$	$0.7 \pm 2.4$	$4.2 \pm 4.5$	$5.3 \pm 4.0$
$m_3$	$3.2 \pm 2.8$	$7.4 \pm 5.6$	$0.4 \pm 3.1$	$3.6 \pm 5.5$	$4.4 \pm 5.8$
$m_4$	$4.4 \pm 2.4$	$7.0 \pm 4.6$	$-0.8 \pm 2.3$	$5.9 \pm 4.5$	$5.6 \pm 4.7$

**Table 3.4:** Mean  $\pm$  standard deviation of the volume, flow and delay parameters estimated in the different sub-regions of the tumor, for the four test-retest exams, after multiple imputation of missing values due to poor fit quality. Values of WIR and F are multiplied by 1000.

	Absolute parameters		Relative parameters		
	CV <sub>AUC</sub>	CV <sub>V</sub>	CV <sub>rAUC</sub>	CV <sub>rV<sub>AIF</sub></sub>	CV <sub>rV<sub>RT</sub></sub>
$m_1$	$34.7 \pm 10.6$	$30.2 \pm 17.1$	$22.4 \pm 14.4$	$24.6 \pm 17.5$	$24.7 \pm 17.3$
$m_2$	$26.2 \pm 6.83$	$26.7 \pm 9.85$	$15.0 \pm 6.51$	$21.8 \pm 9.99$	$15.3 \pm 7.01$
$m_3$	$31.0 \pm 12.3$	$26.6 \pm 10.9$	$37.2 \pm 16.8$	$35.2 \pm 17.8$	$35.2 \pm 18.7$
$m_4$	$20.7 \pm 10.6$	$23.3 \pm 9.93$	$18.8 \pm 8.68$	$19.0 \pm 7.61$	$17.8 \pm 8.17$
	CV <sub>WIR</sub>	CV <sub>F</sub>	CV <sub>rWIR</sub>	CV <sub>rF<sub>AIF</sub></sub>	CV <sub>rF<sub>RT</sub></sub>
$m_1$	$42.4 \pm 12.4$	$35.4 \pm 12.5$	$33.4 \pm 14.9$	$75.5 \pm 19.9$	$29.6 \pm 13.2$
$m_2$	$44.4 \pm 11.0$	$34.4 \pm 7.23$	$27.4 \pm 10.9$	$23.4 \pm 9.94$	$33.1 \pm 18.7$
$m_3$	$45.3 \pm 18.5$	$46.9 \pm 17.7$	$50.9 \pm 17.7$	$36.8 \pm 16.6$	$38.3 \pm 21.3$
$m_4$	$34.9 \pm 18.9$	$33.3 \pm 17.3$	$38.3 \pm 21.2$	$27.1 \pm 13.7$	$29.4 \pm 15.8$

**Table 3.5:** Mean  $\pm$  standard deviation of the coefficients of variation (CV), expressed in percentage, of volume and flow parameters estimated for each sub-region after multiple imputation of missing values due to poor fit quality. CV were not computed for time delays, since their values can be either positive or negative.



# Chapter 4

## Relations between perfusion parameters: theoretical and experimental considerations

### 4.1 Introduction

This chapter is an extension of the work presented in Chapter 3, and relies on the same experimental data, mathematical models, and notations. It aims at establishing the relations between the semi-quantitative perfusion parameters commonly derived from the Log-Normal model, but also between these parameters and the quantitative parameters of the one-compartment model. The relations between parameters were first established theoretically, and then experimentally through correlation studies.

### 4.2 Theory

This section gives the analytic expressions of *AUC*, *PE*, *TTP*, *MTT*, *WIR*, *WOR*, and *TD* parameters for the Log-Normal model, **aLN** (Table 4.1), and for the one-compartment model, **aAIFd** (Table 4.2). The equations of the models are given in Section 3.4.1 of Chapter 3.

*AUC* was defined as the infinite integral of the function, *PE* as the value taken by the

function where its derivative is null,  $TTP$  the time where the function derivative is null,  $MTT$  as the expected value of the function normalized by its  $AUC$ , the  $WIR$  and  $WOR$  as the derivative of the function where its second order derivative is null, and  $TD$  as the time-delay of the function.

$AUC$	$A$
$TTP$	$e^{\mu - \sigma^2}$
$PE$	$A \frac{e^{\frac{\sigma^2}{2} - \mu}}{\sigma \sqrt{2\pi}}$
$MTT$	$e^{\mu + \frac{\sigma^2}{2}}$
$WIR$	$\frac{A}{\sigma \sqrt{2\pi}} \left( \frac{y}{\sigma^2} - 1 \right) e^{2y - 2\mu - \frac{y^2}{2\sigma^2}}$ , where $y = \frac{3\sigma^2 + \sigma \sqrt{\sigma^2 + 4}}{2}$
$WOR$	$\frac{A}{\sigma \sqrt{2\pi}} \left( 1 - \frac{z}{\sigma^2} \right) e^{2z - 2\mu - \frac{z^2}{2\sigma^2}}$ , where $z = \frac{3\sigma^2 - \sigma \sqrt{\sigma^2 + 4}}{2}$
$TD$	$\Delta_T$

**Table 4.1:** Analytic expressions of perfusion parameters using the **aLN** model, WOR being the absolute value of the maximum negative slope.

### 4.3 Data Analysis

Coefficients of determination  $R_{\theta_i, \theta_j}^2$  were estimated from the least-squares linear regression between the 32 regional estimates of parameters  $\theta_i^h$  and  $\theta_j^h$ , one estimate per sub-region  $s_h$ ). These coefficients were computed independently for each of the 16 DCE-US studies (4 mice  $m_l \times 4$  test-retest studies  $R_k$ ). A linear regression was also computed between sets of 512 parameters (the 32 sub-regions of the 16 studies were polled together) to assess the consistency of the relationships between parameters.

### 4.4 Results

The heatmaps shown in Figure 4-1 correspond to  $R^2$  coefficients from the linear regressions between pairs of parameters. Figure 4-1 (a) shows the  $R^2$  coefficients between all pairs of parameters derived from the **aLN** model. It reveals strong linear relationships between some

AIF	$K\delta(t)$	$Krect_a(t)$	$C_A(t)$
$AUC$	$KV_T$	$KV_T$	$V_T \int_0^{+\infty} C_A(\tau) d\tau$
$TPP$	0	$a$	$\{t_P \mid C_T(t_P - d_T) = V_T C_A(t_P)\}$
$PE$	$KF_T$	$\frac{KV_T}{a} \left(1 - e^{-\frac{aF_T}{V_T}}\right)$	$F_T e^{-\frac{F_T}{V_T} t_P} \int_0^{t_P} C_A(\tau) e^{\frac{F_T}{V_T} \tau} d\tau$
$MTT$	$\frac{V_T}{F_T}$	$\frac{V_T}{F_T} + \frac{a}{2}$	$\frac{V_T}{F_T} + MTT_{C_A}$
$WIR$	$\infty$	$\frac{KF_T}{a}$	$\frac{F_T(C_A(t_I) - \frac{1}{V_T} C_T(t_I - d_T))}{\{t_I \mid \frac{dC_T}{dt}(t_I - d_T) = V_T \frac{dC_A}{dt}(t_I), \frac{dC_A}{dt}(t_I) > 0\}}$
$WOR$	$\frac{KF_T^2}{V_T}$	$\frac{KF_T}{a} \left(1 - e^{-\frac{aF_T}{V_T}}\right)$	$\frac{F_T(C_A(t_O) - \frac{1}{V_T} C_T(t_O - d_T))}{\{t_O \mid \frac{dC_T}{dt}(t_O - d_T) = V_T \frac{dC_A}{dt}(t_O), \frac{dC_A}{dt}(t_O) < 0\}}$
$TD$	$d_T$	$d_T$	$d_T$

**Table 4.2:** Analytic expressions of perfusion parameters using a one-compartment model (**aAIFd**) and assuming three different shapes of AIF: impulse function ( $\delta$ ), rectangle function of width  $a$  and height  $1/a$ ,  $rect_a(t)$ , and general case  $C_A(t)$ . In the first two cases,  $K$  stands for the injected concentration. In the general case,  $MTT_{C_A}$  stands for the mean transit time of  $C_A(t)$ .

AIF	$K\delta(t)$	$Krect_a(t)$	$C_A(t)$
$rAUC$	$\frac{V_T}{V_R}$	$\frac{V_T}{V_R}$	$\frac{V_T}{V_R}$
$rWIR$	-	$\frac{F_T}{F_R}$	$\frac{F_T(C_A(t_{I,T}) - \frac{1}{V_T} C_T(t_{I,T} - d_T))}{F_R(C_A(t_{I,R}) - \frac{1}{V_R} C_R(t_{I,R} - d_R))}$ $\{t_{I,T} \mid \frac{dC_T}{dt}(t_{I,T} - d_T) = V_T \frac{dC_A}{dt}(t_{I,T}), \frac{dC_A}{dt}(t_{I,T}) > 0\}$ $\{t_{I,R} \mid \frac{dC_R}{dt}(t_{I,R} - d_R) = V_R \frac{dC_A}{dt}(t_{I,R}), \frac{dC_A}{dt}(t_{I,R}) > 0\}$
$rTD$	$d_T - d_R$	$d_T - d_R$	$d_T - d_R$

**Table 4.3:** Analytic expressions of the relative perfusion parameters using a relative one-compartment model (**rAIFd**) and assuming three different shapes of AIF: impulse function ( $\delta$ ), rectangle function of width  $a$  and height  $1/a$ ,  $rect_a(t)$ , and general case  $C_A(t)$ . In the first two cases,  $K$  stands for the injected concentration.

of the parameters, especially  $AUC$  and  $PE$ ,  $PE$  and  $WIR$ ,  $WIR$  and  $WOR$ . The formal non-linear relationships between these parameters (expressed in Table 4.1) generate high linear links and thus information redundancy. For that reason we further focused on three derived parameters:  $AUC$ , which is related to tissue blood volume  $V$ , according to the analytic expressions given in Table 4.2,  $WIR$ , which is mainly related to tissue blood flow  $F$ , and

the delay parameter  $\Delta$ . This theoretical identification is confirmed experimentally by Figure 4-1 (b) which shows strong linear relationships between volume (first 3 rows/columns) and flow parameters (middle 3 rows/columns). For instance, the linear regressions between  $AUC$ ,  $V$  and  $rV_{RT}$  yielded  $R^2$  values greater than 0.95. The same trend is observed for  $WIR$ ,  $F$  and  $rF_{RT}$ . The correlations between volume parameters and flow parameters are medium ( $R^2 < 0.50$ ). Finally for the time parameters (last 3 rows/columns), there is a high correlation between  $d$  and  $D$  but there is no correlation between  $\Delta$  and the other time delays ( $R^2 < 0.15$ ).

Figure 4-1 (c) and Figure 4-1 (d) show the trends observed on flow and volume parameters when pooling parameters issued from all the exams. There is a very high correlation between the relative volume parameters  $rAUC$ ,  $rV_{AIF}$ , and  $rV_{RT}$  and a high correlation between the relative flow parameters  $rWIR$ ,  $rF_{AIF}$ , and  $rF_{RT}$ . Correlations are poor ( $R^2 < 0.20$ ) between absolute and relative volume parameters, and medium between absolute and relative flow parameters ( $R^2 < 0.55$ ). Since the intra-exam correlations between volume (resp. flow) parameters are high, the correlation over pooled data reflects the inter-exam consistency of linear regression slopes: it is much higher for relative volumes (or flows) than for absolute volumes (or flows). Figure 3-3 from Chapter 3 illustrates this trend for one specific mouse ( $m_1$ ).

## 4.5 Discussion

The equations in Table 4.1 were used in Chapter 3, and later in this thesis, to analytically derive the perfusion parameter values from the fitted Log-Normal model, therefore avoiding numerical approximations.

Interestingly, Figure 4-1 reveals strong correlations between the parameters estimated for the different sub-regions, and a large variation of these parameters according to the tumoral sub-regions. Thus all the parameters can be used to assess spatial tumor heterogeneity. But when it comes to the comparison of longitudinal exams, it is crucial to have comparable parameter values. Thus, relative parameters seem to be the most powerful solution, provided that the reference tissue characteristics are not modified between exams.

## 4.6 Conclusion

A comprehensive comparison of the parameters estimated by different approaches was proposed, showing high correlations between the volume-based and flow-based parameters respectively estimated.

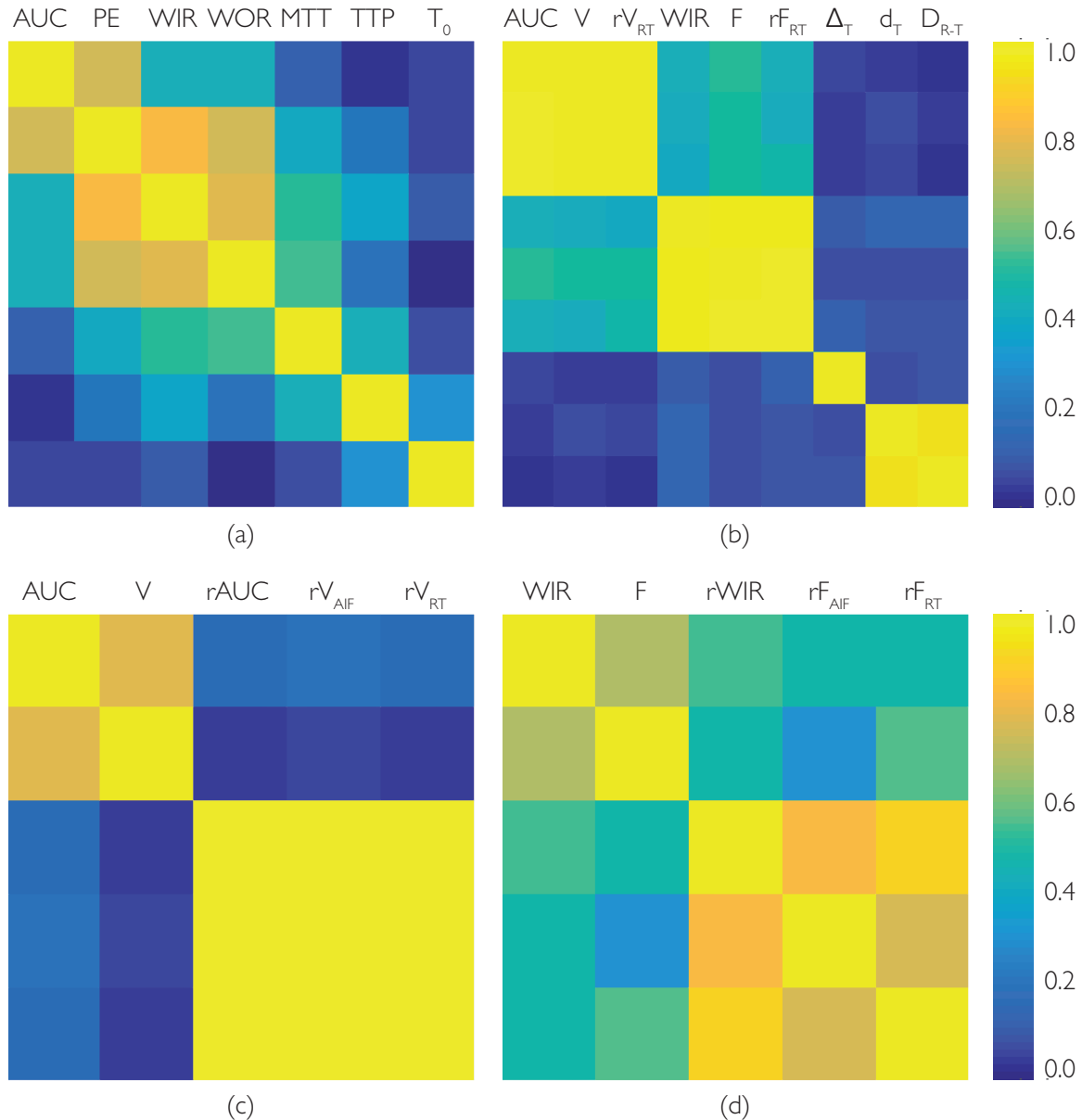


**Figure 4-1:** (a-b) Median (of 16 values) coefficient of determination ( $R^2$ ) of the least-squares linear regression between pairs of parameters  $\theta_i, \theta_j$  computed for the 32 sub-regions of one exam: (a) parameters derived from the **aLN** approach; (b) volume (AUC, V and  $rV_{RT}$ ), flow (WIR, F and  $rF_{RT}$ ) and time delay ( $\Delta_T$ ,  $d_t$  and  $D_{RT}$ ) parameters respectively computed with **aLN**, **aAIFd** and **RTd** models. (c-d) Coefficients of determination ( $R^2$ ) of the least-squares linear regression computed when pooling the 512 sub-regions together: (c)  $R^2$  between pairs of volume parameters computed with **aLN**, **aAIFd**, **rLN**, **rAIFd** and **RTd** models, (d)  $R^2$  between pairs of flow parameters computed with **aLN**, **aAIFd**, **rLN**, **rAIFd** and **RTd** models.

# Afterword

The analytical expression of the area under the curve reveals its straightforward relation with the fractional blood volume. This semi-quantitative parameter is proportional to the physiological parameter, and can be used for relative comparison of tissues observed in a single exam. Furthermore, using the normalized area under the curve successfully corrects for the inter-exam variations, and therefore makes the comparison more robust.

The relation of the wash-in rate with the tissue blood flow is more complex, and while the normalized parameter is analitically and empirically proportional to the normalized blood flow, the slope of the relation varies from one experiment to another. This explains the weaker improvement observed in terms of reproducibility for the normalized wash-in rate compared to the absolute value.

This study reveals the sensitivity of the arterial measurement to segmentation. Indeed, arterial regions exhibiting both small areas and high signal intensities, small changes in the segmentation can result in large changes in the mean arterial curve. In addition, a log-normal model was fitted to the arterial curve for noise-filtering prior to quantification. Given the noise level in those high intensity regions, the fitted curve is likely biased. Absolute perfusion parameters were strongly affected by varyiation of the segmented artery region, however relative parameters exhibited a better agreement.

This formulation of the reference tissue model introduces an unidentifiable parameter, i.e. the rate constant in the reference tissue. In this study, this parameter was given the mean value obtained with the one-compartment model using the arterial measurement. And while the estimated parameters are most likely biased depending on the discrepancy of the fixed parameter value with its actual value, direct estimation of relative perfusion parameters was the most robust approach in our study. In the next part of this thesis, a linear

formulation of the reference tissue model is presented to address this issue, along with a regularized estimation scheme to improve parameter reproducibility and comparability.

## Bibliography

- [1] Daniel Balvay, Frédérique Frouin, Guillaume Calmon, Bertrand Bessoud, Edmond Kahn, Nathalie Siauve, Olivier Clément, and Charles A Cuenod. New criteria for assessing fit quality in dynamic contrast-enhanced T1-weighted MRI for perfusion and permeability imaging. *Magn Reson Med*, 54(4):868–877, 2005. [105](#)
- [2] C F Dietrich, Michalakis Averkiou, J-M Correas, N Lassau, E Leen, and F Piscaglia. An EFSUMB introduction into Dynamic Contrast-Enhanced Ultrasound (DCE-US) for quantification of tumour perfusion. *Ultraschall Med*, 33(4):344–351, August 2012. [98](#), [102](#)
- [3] Alexandre Dizeux, Thomas Payen, Guillaume Barrois, Delphine Le Guillou-Buffello, and S Lori Bridal. Reproducibility of Contrast-Enhanced Ultrasound in mice with controlled injection. *Mol Imaging Biol*, 18(5):651–658, October 2016. [99](#), [100](#), [109](#)
- [4] Maxime Doury, Alexandre Dizeux, Alain De Cesare, Olivier Lucidarme, S Lori Bridal, and Frédérique Frouin. Comparison of the reproducibility of perfusion parameters obtained in CEUS studies with three modeling approaches. In *Proc IEEE Int Symp Biomed Imaging*, Prague, February 2016. [99](#)
- [5] Marianne Gauthier, Farid Tabarout, Ingrid Leguerney, Mélanie Polrot, Stéphanie Pitre, Pierre Peronneau, and Nathalie Lassau. Assessment of quantitative perfusion parameters by dynamic contrast-enhanced sonography using a deconvolution method: an in vitro and in vivo study. *J Ultrasound Med*, 31(4):595–608, April 2012. [99](#), [109](#)
- [6] Aymeric Guibal, Laurent Taillade, Sébastien Mulé, Eva Comperat, Yasmina Badachi, Jean Louis Golmard, Delphine Le Guillou-Buffello, Olivier Rixe, S Lori Bridal, and Olivier Lucidarme. Noninvasive contrast-enhanced US quantitative assessment of tumor microcirculation in a murine model: effect of discontinuing anti-VEGF therapy. *Radiology*, 254(2):420–429, February 2010. [110](#)
- [7] R N Gunn, S R Gunn, and V J Cunningham. Positron emission tomography compartmental models. *J Cereb Blood Flow Metab*, 21(6):635–652, 2001. [102](#)

- [8] C Hoeffel, S Mulé, L Huwart, Frédérique Frouin, J P Jais, O Helenon, and J-M Correas. Renal blood flow quantification in pigs using contrast-enhanced ultrasound: an ex vivo study. *Ultraschall Med*, 31(4):363–369, April 2010. [110](#)
- [9] T Hothorn, K Hornik, MA van de Wiel, and A Zeileis. Implementing a Class of Permutation Tests: The coin Package. *Journal of Statistical Software*, 28(8):1–23, 2008. [105](#)
- [10] Radovan Jirík, Karel Soucek, Martin Mezl, Michal Bartos, Eva Drazanova, Frantisek Drafi, Lucie Grossova, Jiří Kratochvíla, Ondřej Macicák, Kim Nylund, Aleš Hampl, Odd Helge Gilja, Torfinn Taxt, and Zenon Starcuk. Blind deconvolution in dynamic contrast-enhanced MRI and ultrasound. *Conf Proc IEEE Eng Med Biol Soc*, 2014:4276–4279, 2014. [99](#)
- [11] Kohsuke Kudo, Makoto Sasaki, Kuniaki Ogasawara, Satoshi Terae, Shigeru Ehara, and Hiroki Shirato. Difference in tracer delay-induced effect among deconvolution algorithms in CT perfusion analysis: quantitative evaluation with digital phantoms. *Radiology*, 251(1):241–249, April 2009. [110](#)
- [12] Thibaud Lefort, Frank Pilleul, Sébastien Mulé, S Lori Bridal, Frédérique Frouin, Catherine Lombard-Bohas, Thomas Walter, Olivier Lucidarme, and Aymeric Guibal. Correlation and agreement between contrast-enhanced ultrasonography and perfusion computed tomography for assessment of liver metastases from endocrine tumors: normalization enhances correlation. *Ultrasound Med Biol*, 38(6):953–961, June 2012. [110](#)
- [13] Sébastien Mulé, Alain de Cesare, Olivier Lucidarme, Frédérique Frouin, and Alain Herment. Regularized Estimation of Contrast Agent Attenuation for Improvement of Microbubble Imaging in Small Animal Studies. *Ultrasound Med Biol*, 34(6):938–948, 2008. [110](#)
- [14] J P B O'Connor, A Jackson, G J M Parker, and G C Jayson. DCE-MRI biomarkers in the clinical evaluation of antiangiogenic and vascular disrupting agents. *Br J Cancer*, 96(2):189–195, January 2007. [98](#)

- [15] Clifford S Patlak, Ronald G Blasberg, and Joseph D Fenstermacher. Graphical evaluation of blood-to-brain transfer constants from multiple-time uptake data. *J Cereb Blood Flow Metab*, 3(1):1–7, March 1983. [104](#)
- [16] Thomas Payen, Alain Coron, Michele Lamuraglia, Delphine Le Guillou-Buffello, Emmanuel Gaud, Marcel Ardit, Olivier Lucidarme, and S Lori Bridal. Echo-Power estimation from log-compressed video data in dynamic contrast-enhanced ultrasound imaging. *Ultrasound Med Biol*, 39(10):1826–1837, October 2013. [100](#)
- [17] Costas Strouthos, Marios Lampaskis, Vassilis Sboros, Alan McNeilly, and Michalakis Averkiou. Indicator dilution models for the quantification of microvascular blood flow with bolus administration of ultrasound contrast agents. *IEEE Trans Ultrason Ferroelectr Freq Control*, 57(6):1296–1310, June 2010. [98](#), [102](#)
- [18] M X Tang, H Mulvana, T Gauthier, A K P Lim, D O Cosgrove, R J Eckersley, and E Stride. Quantitative contrast-enhanced ultrasound imaging: a review of sources of variability. *Interface Focus*, 1(4):520–539, June 2011. [98](#)
- [19] Paul S Tofts, Gunnar Brix, David L Buckley, Jeffrey L Evelhoch, Elizabeth Henderson, Michael V Knopp, Henrik B Larsson, Ting-Yim Lee, Nina A Mayr, Geoffrey J Parker, Ruediger E Port, June Taylor, and Robert M Weisskoff. Estimating kinetic parameters from dynamic contrast-enhanced T(1)-weighted MRI of a diffusable tracer: standardized quantities and symbols. *J Magn Reson Imaging*, 10(3):223–232, 1999. [98](#)
- [20] A Tudorica, H Fang Li, F Hospod, E Delucia-Deranja, W Huang, CS Patlak, and GC Newman. Cerebral blood volume measurements by rapid contrast infusion and T2\*-weighted echo planar MRI. *Magn Reson Med*, 47(6):1145–1157, June 2002. [102](#)
- [21] Stef van Buuren and Karin Groothuis-Oudshoorn. mice: Multivariate Imputation by Chained Equations in R. *J Stat Softw*, 45(1):1–67, December 2011. [105](#)
- [22] Huaijun Wang, Dimitre Hristov, Jiale Qin, Lu Tian, and Jürgen K Willmann. Three-dimensional dynamic Contrast-enhanced US imaging for early antiangiogenic treat-

ment assessment in a mouse colon cancer model. *Radiology*, 277(2):424–434, November 2015. [111](#)

[23] Suparna Bonthala Wedam, Jennifer A Low, Sherry X Yang, Catherine K Chow, Peter Choyke, David Danforth, Stephen M Hewitt, Arlene Berman, Seth M Steinberg, David J Liewehr, Jonathan Plehn, Arpi Doshi, Dave Thomasson, Nicole McCarthy, Hartmut Koeppen, Mark Sherman, JoAnne Zujewski, Kevin Camphausen, Helen Chen, and Sandra M Swain. Antiangiogenic and antitumor effects of bevacizumab in patients with inflammatory and locally advanced breast cancer. *J Clin Oncol*, 24(5):769–777, February 2006. [98](#)

[24] K Wei, A R Jayaweera, S Firoozan, A Linka, D M Skyba, and S Kaul. Quantification of myocardial blood flow with ultrasound-induced destruction of microbubbles administered as a constant venous infusion. *Circulation*, 97(5):473–483, February 1998. [98](#)

[25] Thomas E Yankeelov, Jeffrey J Luci, Martin Lepage, Rui Li, Laura Debusk, P Charles Lin, Ronald R Price, and John C Gore. Quantitative pharmacokinetic analysis of DCE-MRI data without an arterial input function: a reference region model. *Magn Reson Imaging*, 23(4):519–529, May 2005. [104](#), [110](#)

## **Part III**

# **Proposition and assessment of a new quantification method**



# Foreword

Chapter 3 revealed the superior reproducibility of the relative perfusion parameters estimated by the reference tissue model. However, as discussed in the afterword of the second part of this thesis, the formulation of the reference tissue model used in this study requires a fixed value of parameter  $k_R$ , i.e. the rate constant characterizing the time-intensity curve in the reference tissue. In the third and last part of this thesis, we propose a linear formulation of the reference tissue model alleviating the need for a fixed value of  $k_R$ , and assess it using both experimental and simulated data.

Using the linear formulation for regional analysis, a value of  $k_R$  should be estimated for each region. Such discrepancies in the values of  $k_R$  can affect the value of the other perfusion parameters. This issue is further discussed in Chapter 5, where a regularized estimation method ensuring a single value of  $k_R$  is estimated per exam. The reproducibility of the linear resolution method and of the proposed regularized method are assessed using the same test-retest experiments as presented in Chapter 3, and compared to the absolute and normalized parameters of the Log-Normal model, i.e.  $AUC$ ,  $rAUC$ ,  $WIR$ ,  $rWIR$ . This work was published in the proceedings of the *IEEE International Ultrasonics Symposium* (IUS) [10].

The reviewers of [10] raised an interesting question regarding the impact of recirculation on the perfusion parameters estimated in our contrast-enhanced ultrasound test-retest study. Chapter 6 address this issue in depth and study the impact of recirculating microbubbles on the accuracy and precision of the perfusion parameters through a simulation study. A simple recirculation model was used, it was however able to reflect the various passes of the bolus, as well as its dispersion and attenuation. An intuitive approach to avoid recirculation consist in fitting the model to the portion of data acquired before recirculation occurs, thus a classical and a cropped version of the Log-Normal model were assessed. Oppositely,

compartmental models are build to account for recirculation. The robustness of the linear reference tissue model and of its regularized version to recirculation was assessed. This work has been submitted to *Innovation and Research in BioMedical Engineering* (IRBM).

Chapter 7 formally presents the linear and regularized estimation methods to solve the reference tissue model. Indeed, getting into details was not possible in [11] because of the limited space available in the proceedings template. This is however not the core of this work, which aims at evaluating the sensitivity of perfusion parameters to varying data characteristics, and analysis choices. In particular, the impact of acquisition duration, acquisition frequency, noise amplitude, number of regions, as well as the characteristics of the reference tissue were investigated. In order to provide a ground truth, synthetic data based on preclinical experiments was generated using a one-compartment model.

# **Chapter 5**

## **Regularized Linear Resolution of a One-Compartment Model to Improve the Reproducibility of Perfusion Parameters in CEUS**

### **5.1 Abstract**

Contrast-enhanced ultrasound (CEUS) has been proposed to monitor tumor therapy, in complement to size measurements. Estimating reliable perfusion parameters from CEUS studies is essential in order to propose adapted therapy options according to the parameter values. The variability of these parameters was assessed in an ideal case of consecutive test-retest CEUS studies, in a mouse tumor model. The impact of mathematical modeling on parameter variability was investigated on these data. Four models were compared in 32 tumor sub-regions : the log-normal model (LN), the relative LN model (rLN) where parameters of LN are normalized by the parameters estimated inside a reference tissue (RT) region, a linear resolution of a one-compartment model based on the RT (rLin), a modified version of rLin implementing regularization (rLinReg) to ensure coherent results between the different sub-regions of the tumor. Results show that LN model had highest coefficients

of variation. The positive impact of normalization using RT (rLN) was established, showing reduced coefficients of variation. The rLin approach showed large variations especially for flow parameters. Its regularization version, rLinReg, greatly improved parameter reproducibility while providing coherent results between the sub-regions. In conclusion, the rLinReg approach provided the smallest coefficients of variations and should be preferred for estimating perfusion parameters in CEUS.

## 5.2 Introduction

Reliable quantification of tumor perfusion is a challenging, yet necessary, milestone to reach in order to efficiently monitor tumor growth and treatment efficiency. Contrast-enhanced ultrasound (CEUS) is a non-invasive tool allowing real-time quantitative vascular imaging: for every sampling time and every pixel in the image, the linearized signal intensity is proportional to the concentration of contrast agent for low concentrations.

Recommendations for the quantification of CEUS studies rely on explicit modeling of time-intensity curves (TICs), e.g. using a log-normal model [8]. Then, semi-quantitative parameters are usually derived directly from the modeled TIC, e.g. area under the curve (AUC) and wash-in rate (WIR). These parameters are directly affected by inter-exam changes occurring either in physiology, e.g. heart rate, blood pressure, or in experimental conditions, e.g. injected quantity, or injection speed [21]. Controlled injections and compartmental modeling have been proposed to reduce this variability [12]. To overcome the issues related to the estimation of a correct arterial input function, the use of a reference tissue (RT) region (e.g. [7]) has been successfully tested [12]. In the present study, a linear formulation of the one-compartment model is presented and evaluated. This formulation allows the evaluation of an otherwise unidentifiable parameter, characterizing the RT region, which value had to be set arbitrarily to 0.15. To prove the interest of this new approach, the coefficients of variation of perfusion parameters estimated at a regional scale were compared using four different approaches: 1) the log-normal model (LN), 2) the relative LN model (rLN), where parameters are normalized by the (LN) parameters estimated inside the RT region, 3) a linear resolution of the one-compartment model based on the RT region (rLin), 4) a modified

version of **rLin** implementing regularization (**rLinReg**) to ensure a coherent estimation of the ratio between blood flow and blood volume in the RT region when taking into account the different sub-regions in the tumor.

## 5.3 Materials

### 5.3.1 Animals

All experiments were conducted in accordance with the institutional guidelines and the recommendations for the care and use of laboratory animals. They were based on a murine model of Lewis Lung Carcinoma (3LL). Tumor fragments (20-40 mm<sup>3</sup>) were implanted 20 days prior to the CEUS acquisitions in the right flank of Balb/C mice. Anesthesia was maintained during the whole acquisition through a face mask delivering 2% isoflurane in air delivered at a 1 L/min rate.

### 5.3.2 Image acquisition

Tumors were imaged in their largest cross-section plane, mice motion was limited using surgical tape securing animal position during and between acquisitions. A controlled injection system was used to inject, at a rate of 4.5 mL/min, a 50 µL bolus of SonoVue (Bracco Suisse SA, Geneva, Switzerland) diluted to 20%. Meanwhile, dynamic contrast-enhanced US sequences were acquired using a 15L8W transducer coupled to a Sequoia 512 US system (Acuson, Siemens, Mountain View, CA, USA) in dual-mode, i.e. anatomical B-Mode along with Contrast Pulse Sequencing (CPS) images. Mechanical index was set to 0.1, dynamic range to 80 dB, and time gain compensation was applied. The frame rate was set to 3 Hz during the first 30 seconds (including the wash-in phase and the beginning of the wash-out phase), and 1 Hz for the remaining time.

For the four mice in the study, four consecutive (test-retest) data-sets were acquired without any modification in the setup. Fifteen minute breaks were observed between acquisitions to ensure the disruption of previously injected micro-bubbles.

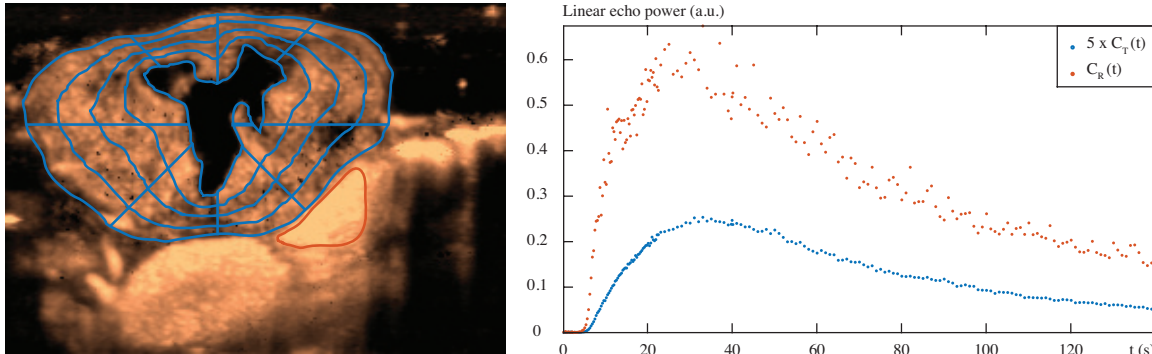


**Figure 5-1:** Illustration of the data pre-processing steps. Left: The contours of the perfused tumor area have been overlaid on a contrast-enhanced image (in blue color). This area was automatically divided into 4 radial layers and 8 angular sectors as shown by the spiderweb patterns. A RT region (in orange color) was also delineated. Right: Mean TICs associated with the perfused area of the tumor, and the RT.

## 5.4 Methods

### 5.4.1 Data pre-processing

Linear echo-power TICs were calibrated from log-compressed video data using a laboratory-made software. Both probe and animal motion were assumed negligible for the selected sequences.

Tumors (hereafter labeled with subscript T) were segmented on the B-Mode images and the non-perfused areas were removed for data analysis. In order to preserve the signal-to-noise-ratio (SNR) of the TICs while revealing the spatial heterogeneity of the tumor, a regional analysis of the tumor area was performed. The perfused tumor region was divided into  $N_T = 32$  sub-regions according to 4 radial layers and 8 angular sectors (Figure 5-1). Then mean regional TICs  $C_T^i(t)$ , for  $i = 1, \dots, N_T$  were computed. As three of the four quantification methods require the selection of a RT region, for each mouse, this RT region (hereafter labeled with subscript R) was chosen to be easily identifiable on the different test-retest studies. A muscular region close to the kidney was generally selected, the renal cortex being excluded from the RT region due to the complexity of perfusion patterns observed inside this structure.

Finally for each sub-region, a time delay parameter,  $D_i$ , representing the time of arrival

of the contrast agent in the considered region, was estimated as follows:

$$D_i = \max_t \frac{d^2}{dt^2} (C_T^i * W * W), \quad (5.1)$$

where  $W$  is an average filter with a fixed width empirically set to 2.0 seconds. Using this specific time delay, all regional TICs were registered in time for subsequent analysis.

### 5.4.2 Definition of the four models

#### Log-Normal model (LN)

This method based on the log-normal distribution was recommended by the EFSUMB for quantification of tumor perfusion in clinical studies [8]. The TIC inside the  $i^{th}$  region of the tumor,  $C_T^i(t)$ , is fitted according to equation (5.2):

$$\begin{aligned} C_T^i(t) &= \frac{A_T^i}{\sqrt{2\pi}\sigma_T^i t} \exp\left(-\frac{[\ln(t)-\mu_T^i]^2}{2\sigma_T^{i^2}}\right) \text{ if } t \geq 0, \\ &= 0 \text{ otherwise.} \end{aligned} \quad (5.2)$$

Regional parameters  $A_T^i$ ,  $\mu_T^i$ , and  $\sigma_T^i$  were estimated for each sub-region. Semi-quantitative parameters are then derived from the model, including  $AUC^i$  and  $WIR^i$ . These parameters depend, in a non-linear way, on the parameters of the LN model,  $A^i$ ,  $\mu^i$ , and  $\sigma^i$ . Relations have been established, both analytically and experimentally, between parameters derived from the LN model and physiological parameters, showing  $AUC^i$  is related to blood volume, and  $WIR^i$  to blood flow [12].

#### Normalized log-normal model (rLN)

Regional relative parameters:  $rAUC^i$  and  $rWIR^i$  were derived from the parameters estimated with the (LN) model in the tumor sub-regions ( $AUC_T^i$ ,  $WIR_T^i$ ) and those estimated in the RT region ( $AUC_R$ ,  $WIR_R$ ). They were defined as follows:

$$\begin{cases} rAUC^i = AUC_T^i / AUC_R, \\ rWIR^i = WIR_T^i / WIR_R. \end{cases} \quad (5.3)$$

### Simple one-compartment model (rLin)

The resolution of the one-compartment model follows the graphical analysis technique introduced by Patlak et al. for the quantification of irreversible tracers in PET. The method, based on compartmental modeling, estimates blood-related physiological parameters by means of linear regression, assuming the arterial input function (AIF) is known [19]. This linear approach is generalized to reversible tracers [16]. These approaches have also been adapted to relax the need for blood sampling or AIF measurement and the kinetics inside a RT region was then used (see for instance [7]). This resolution was adapted to CEUS data, considering the ultrasound contrast agent is strictly intra-vascular. Considering a one-compartment model to describe flow exchanges inside the tissue, the following equations can be written for each sub-region,  $i = 1, \dots, N_T$ :

$$\frac{dC_T^i(t)}{dt} = F_T^i \cdot C_A(t) - \frac{F_T^i}{V_T^i} C_T^i(t). \quad (5.4)$$

In (5.4)  $C_A(t)$  represents the arterial input function feeding the tissue, while  $V_T^i$  stands for the fractional blood volume, and  $F_T^i$  for the blood flow in the sub-region  $i$ .

Considering jointly the TIC inside the RT region and the TICs in the tumor, and assuming a common feeding input for the RT region and the tumor, we have the following set of equations:

$$\begin{cases} \frac{dC_R(t)}{dt} = F_R \cdot C_A(t) - \frac{F_R}{V_R} C_R(t), \\ \frac{dC_T^i(t)}{dt} = F_T^i \cdot C_A(t) - \frac{F_T^i}{V_T^i} C_T^i(t), \forall i. \end{cases} \quad (5.5)$$

Rearranging the first equation,  $C_A(t)$  can be isolated and expressed as a function of  $C_R(t)$ , and then replaced by its new expression in the  $N_T$  following equations, yielding the next system:

$$\begin{cases} C_A(t) = \frac{1}{F_R} \frac{dC_R(t)}{dt} + \frac{1}{V_R} C_R(t), \\ \frac{dC_T^i(t)}{dt} = \frac{F_T^i}{F_R} \frac{dC_R(t)}{dt} + \frac{F_T^i}{V_R} C_R(t) - \frac{F_T^i}{V_T^i} C_T^i(t). \end{cases} \quad (5.6)$$

After integration over time (from 0 to  $t$ ), and definition of the parameters  $rF^i = F_T^i/F_R$ ,  $rV^i = V_T^i/V_R$ , and  $k_T^i = F_T^i/V_T^i$ , the last equations of the system become:

$$C_T^i(t) = rF^i C_R(t) + rV^i k_T^i \int_0^t C_R(\tau) d\tau - k_T^i \int_0^t C_T^i(\tau) d\tau. \quad (5.7)$$

For each sub-region  $i$ , a sub-system of  $N$  linear equations (6.7) is computed, obtained for  $N$  successive values of  $t$ .  $N$  is the total number of dynamic frames. Solving this sub-system of  $N$  linear equations, the parameters  $rF^i$ ,  $rV^i$ , and  $k_T^i$  can thus be estimated in the least-squares sense. Using this approach, the  $N_T$  linear equations corresponding to the different sub-regions are thus solved independently.

### Regularization of the one-compartment model (**rLinReg**)

Using the previously described **rLin** model,  $N_T$  different values of  $k_R = F_R/V_R$  can be derived, using the estimation of  $rF^i$ ,  $rV^i$ , and  $k_T^i$  and the relation between the four parameters:

$$k_R = \frac{F_R}{F_T} \frac{F_T^i}{V_T^i} \frac{V_T^i}{V_R} = \frac{rV^i \cdot k_T^i}{rF^i} \quad \text{for } i = 1, \dots, N_T. \quad (5.8)$$

As the  $k_R$  values do not depend on sub-region  $i$ , the simple estimation proposed by **rLin** can introduce some inconsistencies  $k_R$  and possible biases in some  $rF^i$ ,  $rV^i$ , and  $k_T^i$  values. To solve this issue, and consider one single value for  $k_R$  (whatever the number of sub-regions in the tumor), the regularized approach solves the system of equations (Eq. 6.7), under the following constraints:

$$\frac{rV^i \cdot k_T^i}{rF^i} = K, \quad \forall i = 1, \dots, N_T, \quad (5.9)$$

where  $K$  is a constant (equal to  $k_R$ ). The system is solved globally for the  $N_T$  sub-regions. Briefly, the value of  $k_R$  is successively modified, thus providing a unique least-squares solution for the  $3N_T$  parameters ( $rF^i$ ,  $rV^i$ , and  $k_T^i$ ), until the optimization of the fit for the whole set of  $N_T$  sub-regions.

#### 5.4.3 Data analysis

For each model, a vector ( $\Theta$ ) of  $M$  perfusion parameters ( $\theta_m$ ) was estimated in each tumor sub-region ( $i = 1, \dots, 32$ ) of each mouse ( $j = 1, \dots, 4$ ) for each repeated acquisition ( $k = 1, \dots, 4$ ), providing 512 results of curve fitting,  $\Theta_k^{ij}$ , per model. The fit quality was assessed quantitatively, using the fraction of modeled information,  $FMI$ , according to [1].

The reproducibility of the perfusion parameters was then deduced for each sub-region of

each mouse by computing coefficients of variation  $CV(\theta_m)^{ij}$  defined for the four repeated studies, as the ratio between the standard deviation and the mean value  $\mu_m^{ij}$  of the parameter  $(\theta_m)_k^{ij}$ :

$$CV(\theta_m)^{ij} = \frac{\sqrt{\frac{1}{4}\sum_{k=1}^4((\theta_m)_k^{ij} - \mu_m^{ij})^2}}{\mu_m^{ij}}. \quad (5.10)$$

Parameters corresponding to poor quality fits ( $FMI > 90\%$ ) were replaced using multivariate imputation by chained equations with the R module {mice} [24]. This strategy was defined to compute the CV using four values systematically.

Statistical tests were finally applied to compare the CV of the parameters estimated using the four models. Significant differences in the CV distributions were assessed using the Friedman test and the associated post-hoc analysis for multiple comparisons. Distribution means were considered as significantly different when p-values were less than 0.05.

## 5.5 Results

Model	LN	rLN	rLin	rLinReg
<i>FMI</i>	99.3%	99.3%	98.8%	98.1%
<i>N<sub>rem</sub></i>	28	28	1	39

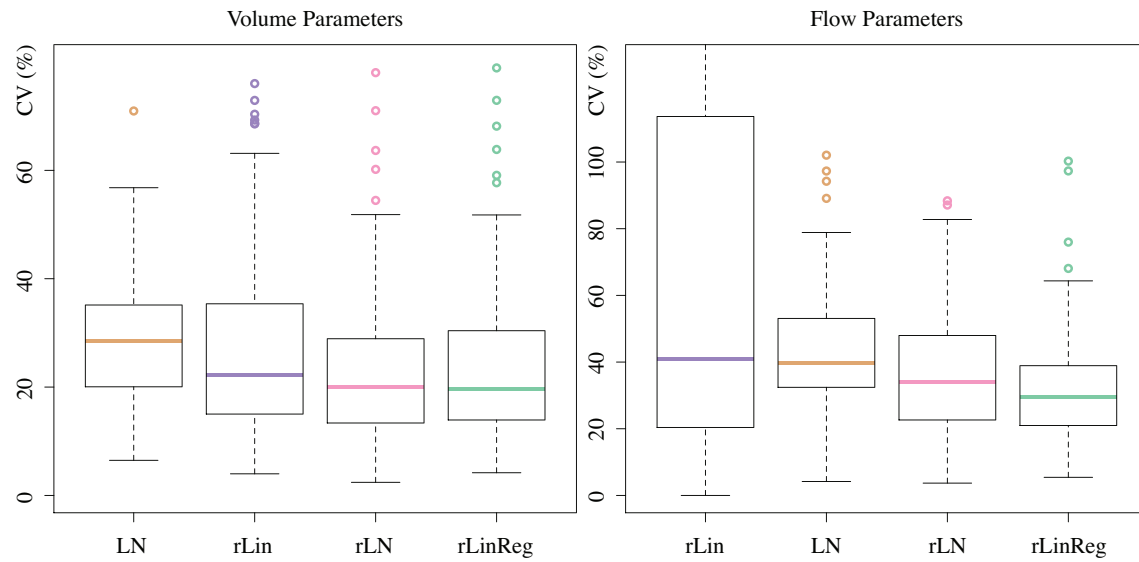
**Table 5.1:** Median values of *FMI* obtained for the four models and number of sub-regions  $N_{rem}$ , out of 512, for which  $FMI < 90\%$ .

Table 5.1 shows the median values of the FMI obtained for the four models and the number of regions excluded from further statistical analysis because of bad fit quality.

Figure 5-2 displays a boxplot of the 128 coefficients of variation of blood volume parameters and blood flow parameters obtained for the four models **LN**, **rLN**, **rLin**, and **rLinReg**.

The p-values obtained after the post-hoc analysis of the Friedman test are shown in Table 5.2, significant differences in parameter distributions are emphasized in bold.

In terms of blood volume parameters, the **LN** model is the most variable with a median value of the coefficient of variation (CV) equal to 28.5%. Using the **rLin** model, the median CV tends to be lower (22.2%), however the difference is not statistically significant. Models



**Figure 5-2:** Boxplot showing the CV of blood volume (left) and blood flow (right) estimated with the LN, rLN, rLin, and rLinReg models.

	Volume parameters			Flow parameters		
	rLinReg	rLin	rLN	rLinReg	rLin	rLN
LN	<b>0.001</b>	0.1	<b>0.003</b>	$7 \times 10^{-6}$	0.96	0.74
rLN	0.995	0.73		$5 \times 10^{-4}$	0.49	
rLin	0.52			$8 \times 10^{-7}$		

**Table 5.2:** p-values obtained in the post-hoc analysis of the Friedman test. Significant results ( $p < 0.05$ ) in bold.

**rLN** and **rLinReg** yield significantly more reproducible blood volume parameters than **LN**, with median CV values of 20.0% and 19.7%, respectively. For the blood flow parameters, models **rLin** and **LN** appear to be the most variable parameters with medians of CV equal to 40.8% and 39.6%, respectively. The **rLN** model tends to yield lower CV, with a median value of 34.1%. Finally the mean CV of blood flow using the **rLinReg** model is equal to 29.4%. It is significantly lower than the CV of blood flow obtained with the three other models.

## 5.6 Discussion

The number of sub-regions was chosen to reveal some spatial heterogeneity in the vascular network of the tumor, while ensuring regions were large enough to guarantee reasonable signal to noise ratios in regional TICs. Increasing the number of regions would reveal spatial heterogeneity more finely, at the expense of the accuracy of the estimates.

Both physiological and experimental variations get in the way of accurate quantification and exam comparison, affecting blood circulation, as well as measurements accuracy [21]. The semi-quantitative parameters of the **LN** model, recommended for tumor quantification, were found highly sensitive to inter-exam changes in our study and resulted in the least reproducible parameters.

When compared to the **LN** model, the normalized version, the **rLN** model reduces the variability of parameters. If the reduction of variability for blood flow parameters was not statistically significant, it was significant for blood volume parameters. Thus normalization using a RT region has a real potential to improve exam comparison.

Similarly to the **rLN** approach, the **rLin** model uses the RT region, but in addition, it assumes a one-compartment model to describe contrast exchanges between large vessels and micro-vascular areas in tissue. The first resolution method, which was tested in the present study and proposes to estimate three unknown parameters per sub-region, yields highly variable parameters, especially in terms of blood flow. However, the median CV of blood volume was reduced when compared to *AUC* CV, estimated with the **LN** model. This method was implemented in a naive way, resulting in inconsistent values of parameter  $k_R$  in the different tumor sub-regions.

The **rLinReg** model was built to overcome these inconsistencies, ensuring a single value of  $k_R$ . Enforcing a common value of  $k_R$  in sub-regions comes down to impose a fixed ratio between the first and second terms of Eq. 6.7. The number of degrees of freedom was thus reduced. The combined use of normalization through a RT region and regularization respects the compartmental modeling paradigm while yielding the most reproducible parameters in our study.

## 5.7 Conclusion

Using the LN model, derived parameters have high coefficients of variation. The positive impact of normalization using a reference tissue region on parameter reproducibility was established. The **rLinReg** approach takes into account the different sub-regions involved in the quantification, yielding a single value of parameter  $k_R$  common to all tumor sub-regions. In addition, this spatial regularization significantly reduces coefficients of variations of the blood flow parameter and should therefore be preferred to estimate spatially-distributed perfusion parameters.



# Chapter 6

## Impact of Recirculation in Dynamic Contrast-Enhanced Ultrasound: a Simulation Study

### 6.1 Abstract

*Objectives* The impact of recirculation on the quantification of perfusion is often neglected. It can however introduce a bias or some variability in the estimation of perfusion parameters and thus hamper comparison between exams. *Methods* Time-intensity curves (TICs) were simulated using a one-compartment model fed by an arterial input function (AIF). A simple model was developed to simulate recirculation in the AIF. Using AIF with and without recirculation, and sets of regional perfusion parameters, TICs corresponding to different tissue regions were simulated by convolution of the AIFs with the transfer function associated to each region. 150 simulations for each of the 10 noise levels were then computed. For each simulated study, six quantification methods based on either Log-Normal modeling or relative compartmental modeling were tested. Variations of the conventional Log-Normal model were also investigated, including using parameters estimated in a reference tissue for normalization purposes, and fitting only the first phase of the TIC to avoid recirculation. *Results* The impact of recirculation varies according to the quantification method. Restricting

parameter estimation to the first samples of the TICs, before recirculation occurs, appears to be the worst strategy. Errors are largely minimized when using a reference tissue to establish relative parameters. The most robust approach is the compartmental modeling based on a reference tissue and applied to multiple regions with a regularization constraint. *Conclusion* This simulation study demonstrates the influence of recirculation on the estimation of perfusion parameters. To reduce the impact of this unavoidable effect, the quantification method based on compartmental modeling and using a reference tissue appear to be the most reliable strategy.

## 6.2 Introduction

With the advent of contrast agents, perfusion imaging has been developed for different medical imaging modalities, including PET, CT, MRI, and more recently ultrasound. Perfusion parameters including regional tissue blood volume and tissue blood flow are functional indices which can help in the diagnosis of some vascular abnormalities, such as ischemia. Vascular modification in tumors is also a key application of perfusion imaging and can be used in order to assess tumor diagnosis or tumor monitoring [8].

A widely used approach to estimate perfusion parameters relies on bolus injections of contrast agent and dynamic recording of frames. However the quantification of signal and the estimation of perfusion parameters through mathematical modeling remains a hard task and has generated a lot of research work [23]. An accurate and robust estimation of perfusion parameters is of course crucial to compare perfusion imaging exams meaningfully. This is primordial in order to allow inter-subject exams or to perform monitoring. Among the different mathematical models that have been proposed in contrast-enhanced ultrasound (CEUS) studies, little attention has been devoted to compartmental modeling, despite its wide use in PET or MRI studies. Indeed, explicit modeling using for instance a Log-Normal function is often recommended to analyze dynamic data [8, 20]. Of course different reasons can explain this restricted use of the compartmental approach; among them the difficulty in estimating a correct arterial input function in dynamic ultrasound images can be cited. To get rid of this difficulty which occurs also while using other imaging techniques, some

authors in PET imaging and more recently in MRI have proposed to use a reference tissue in order to define relative perfusion parameters [6, 26], defined as the ratio between the perfusion parameters in the tissue of interest and the perfusion parameters defined in the reference tissue. Our group has recently shown the practical interest of this approach in a test-retest protocol applied to a murine tumor model [9, 11].

As no absolute gold-standard exist for preclinical or clinical studies, simulations can be used to assess the performance of different models and compare them. Of course, as it is quite complex to reproduce *in silico* the complexity of *in vivo*, the extrapolation of simulations to real cases should be done very carefully. However they can be used to focus on one specific trait and to quantify its impact. In the present study, the studied trait was recirculation, since this process is often overlooked when quantifying CEUS exams. This is especially true in small animals, where recirculation occurs quickly and can overlap with the first pass of the bolus of micro-bubbles in tissues, affecting the time-intensity curves (TICs) used for quantification.

For the present study, a one-compartmental model was assumed to be representative of the underlying physiology that is observable at a regional scale. Different values of perfusion parameters (tissue blood flow, tissue blood volume and time-delays) were simulated in order to better apprehend the spatial heterogeneity that can be observed inside a tumor. The values of these parameters were derived from results obtained in a preclinical study in order to be coherent with practical observations. In addition to recirculation, the impact of signal to noise ratio was studied. For the modelling approach, two versions of the Log-Normal model (absolute and relative), and two versions of the relative one-compartment model (one based on a single region, one taking advantage from the existence of multiple regions) were considered. In addition, in order to limit the impact of recirculation while estimating perfusion parameters with the Log-Normal model, a simple and popular strategy was tested which consists in using the first samples of TICs, i.e. samples acquired before recirculation occurs [18]. These six perfusion quantification methods were fitted to simulated TICs to study the precision and the accuracy of the estimated perfusion parameters.

## 6.3 Theory

### 6.3.1 One-compartment vascular model

Consider  $N$  vascularized tissue regions  $T_i$ ,  $i = 1, \dots, N$  in a spatial domain, each region being an homogeneous compartment fed by the same arterial input function (AIF),  $C_A$ . This mono-compartmental hypothesis is realistic since the distribution of microbubbles is restricted to the vascular space [13]. Each tissue TIC,  $C_{T_i}$ , is characterized by a tissue blood volume  $V_i$ , and a tissue blood flow  $F_i$ . Since introducing a time-delay parameter in this model was shown to improve the quality of fit in tumor tissues [11], a parameter  $D_i$  reflecting the transit time of the contrast agent from the feeding artery to the tissue was also considered. The mathematical relationship between the tissue TIC and the TIC in its feeding artery is given by equation 7.1:

$$C_{T_i} = C_A * h_{F_i, V_i, D_i} \quad (6.1)$$

where  $h_{F_i, V_i, D_i}(t) = F_i \cdot e^{-\frac{F_i}{V_i}(t-D_i)} \forall t \leq D_i, 0 \text{ else}$ , represents the transfer function of the  $i^{th}$  tissue region.

### 6.3.2 Simplified recirculation model

After injection in a vein, the bolus of microbubbles travels through the lungs and heart chambers before being distributed in the whole body through the arterial system. After this first pass in the tissues, microbubbles return to the venous system for another circulation loop. During each loop, the bolus is attenuated by the natural disruption of microbubbles, and their filtration through the lungs and the liver. Additionally, the bolus length spreads in time because of the inhomogeneous path length of the individual microbubbles [5].

An AIF with recirculation,  $C_{Aw}$ , can therefore be approximated by a sum of consecutive passes of the bolus in the region of interest (equation 6.2):

$$C_{Aw}(t) = C_{Al}(t) + \sum_{r=1}^{N_R} R_r(t), \quad (6.2)$$

where  $C_{Al}(t)$  is the TIC of the first pass of the bolus,  $R_r(t)$  is the TIC of the  $r^{th}$  recirculation,

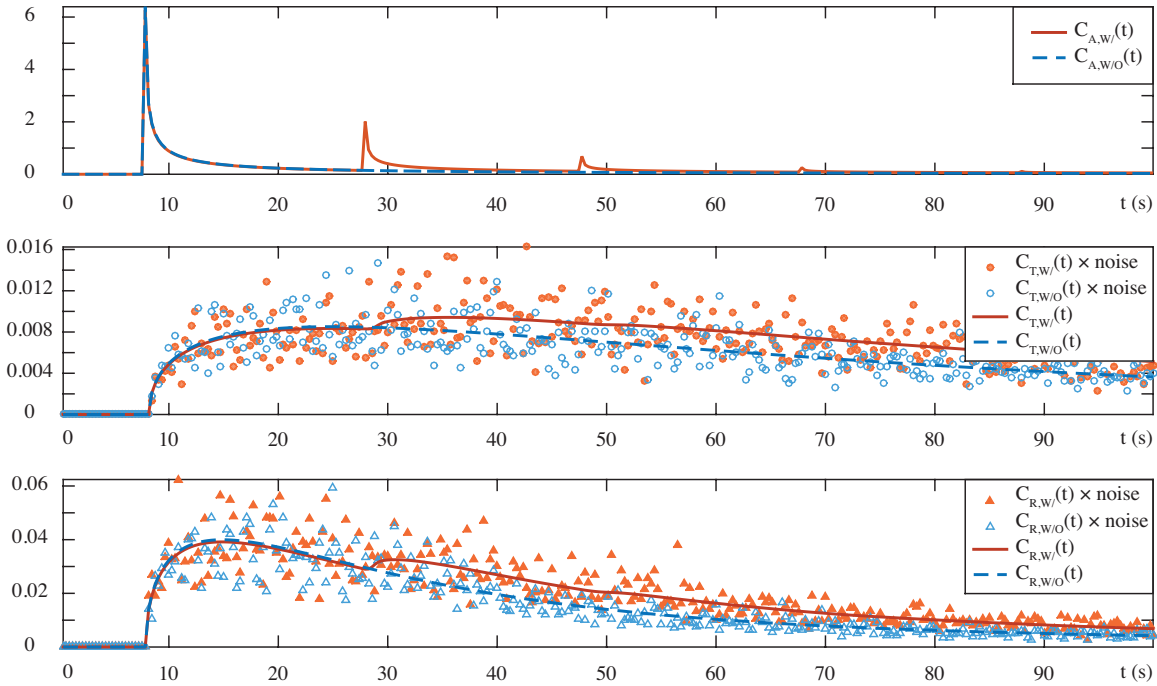


**Figure 6-1:** Simulated TICs with (orange) and without recirculation (blue) corresponding to noise-free AIF (top), examples of noise-free and noisy TICs in the fourth tissue region (middle) and in the reference tissue (bottom). The first hundred seconds are displayed here.

and  $N_R$  is the number of recirculation loops which are taken into account. The TIC,  $C_{A1}(t)$ , thus represents the AIF without recirculation.

To go further in the simulation process, a simplified recirculation model was defined, assuming a constant recirculation period  $\gamma$ , a constant recirculation fraction  $\beta$  (the fraction of microbubbles remaining from the previous bolus pass taking into account bubble disruption and filtration), a constant spread factor  $\alpha$  through the different recirculation loops, and an exponential spread and decay of the signal. The  $r^{\text{th}}$  recirculation TIC,  $R_r(t)$ , was simulated by equation 6.3:

$$R_r(t - r\gamma) = \frac{\beta^r}{\alpha^r} C_{A1} \left( \frac{t}{\alpha^r} \right) \quad (6.3)$$

Examples of AIF with and without recirculation are shown in Figure 6-1 (first row). For the present study,  $C_{A1}(t)$  is represented by a log-normal function,  $C_{Aw}(t)$  is computed using  $\alpha = 2$ ,  $\beta = 30\%$ ,  $\gamma = 20$  s and  $N_R = 7$ . TICs were simulated for a total duration of 165 s with a frame rate of 3 Hz.

### 6.3.3 Noise model

A multiplicative noise model following a gamma distribution [2] while constraining the mean intensity to be 1 (unit mean). Indeed, a unit mean distribution for a multiplicative noise is the equivalent of a zero-centered distribution for additive noise. A gamma distribution is defined by two parameters: its shape parameter  $\kappa$ , and its scale parameter  $\theta$ . Enforcing a unit mean is equivalent to set  $\theta = 1/\kappa$ , the noise distribution  $p(\nu)$  is then defined by Eq. 6.4:

$$p(\nu) = \frac{1}{\Gamma(\kappa)} \kappa^\kappa \nu^{\kappa-1} e^{-\nu\kappa}, \forall \nu \geq 0. \quad (6.4)$$

The parameter  $\kappa$  controls the sharpness of the noise distribution, and is related to the standard deviation of the noise distribution by  $\sigma = 1/\sqrt{\kappa}$ .

### 6.3.4 Perfusion quantification methods

Six perfusion quantification methods ( $M_1 - M_6$ ) were tested and compared. Among them, four relative approaches ( $M_3 - M_6$ ) making use of an in-plane reference tissue (R) were proposed to make parameters more robust to inter-exam changes (due to unavoidable experimental or physiological varying conditions). Furthermore, the last method ( $M_6$ ) takes advantage of the multiple regions that can be defined inside an image.

#### Methods $M_1$ and $M_2$ - Log-Normal model (LN)

The Log-normal function is an explicit model that depends on four parameters, it is frequently used to fit TICs, in particular from dynamic contrast-enhanced ultrasound studies [20]. From this model, the area under the curve  $AUC_i$ , which is proportional to the tissue blood volume (see Appendix for proof) and  $\tau_i$  a time parameter reflecting the delay between the beginning of the acquisition and the arrival of the first microbubbles in the tissue of interest are directly estimated. In addition, the wash-in rate ( $WIR_i$ ), that is the maximal slope of the uptake part of the TIC, a parameter related to the tissue blood flow (see Appendix for proof), is commonly derived. Appendix shows the analytical expression of the  $AUC$  and  $WIR$  parameters, using the conventional expression of the Log-Normal model. For the first

method ( $M_1$ ), all the time samples are analyzed while for the second model ( $M_2$ ), the analysis is restricted to the first pass of the bolus, which roughly corresponds to the wash-in phase.

### Methods $M_3$ and $M_4$ - relative Log-Normal model (rLN)

The relative Log-Normal models propose the comparison of the LN model parameters estimated in the tissue region  $i$  ( $AUC_i$ ,  $WIR_i$ , and  $\tau_i$ ) with the corresponding values estimated in the reference tissue  $R$  ( $AUC_R$ ,  $WIR_R$ , and  $\tau_R$ ), following equation 6.5:

$$rAUC_i = \frac{AUC_i}{AUC_R}, rWIR_i = \frac{WIR_i}{WIR_R}, \Delta = \tau_i - \tau_R. \quad (6.5)$$

For the method  $M_3$ , all the time samples are analyzed while for the method  $M_4$ , the analysis is restricted to the first pass of the bolus.

### Methods $M_5$ - relative one-compartment model (rLin)

The model M5 is derived from the one-compartment model presented in Section 6.3.1. It was proposed to take into account the multiple cases for which the estimation of the AIF is tricky, see for instance [11]. It assumes that the tissue region and the reference tissue are parallel single compartments, fed by a common AIF. Writing equation (7.1) respectively for  $C_{T_i}$  and  $C_R$ , and rearranging them, a convolution equation that is independent of the AIF can be deduced. Four related perfusion parameters [11], defined by Eq. 6.6, can then be estimated as a linear function:

$$rF_i = F_i/F_R, rV_i = V_i/V_R, k_i = F_i/V_i, \delta_i = D_i - D_R. \quad (6.6)$$

When the time delay  $\delta_i$  is estimated (defined as the inflexion point after temporal filtering), the convolution equation can be written as follows:

$$W_i(t) = rF_i \cdot X(t) + rV_i \cdot k_i \cdot Y(t) - k_i \cdot Z_i(t), \forall t \geq \delta_i. \quad (6.7)$$

with  $W_i(t) = C_{T_i}(t - \delta_i)$ ,  $X(t) = C_R(t - \delta_R)$ ,  $Y(t) = \int_0^t C_R(\tau - \delta_R) d\tau$ , and  $Z_i(t) = \int_0^t C_{T_i}(\tau - \delta_i) d\tau$ .

The three parameters  $rF_i$ ,  $rV_i$ , and  $k_i$  can thus be estimated using a linear regression which

minimizes the least-squares error. For that reason the method  $M_5$  is noted rLin. It was introduced in [9] following Patlak's approach [19].

### **Method $M_6$ - Regularized relative one compartment model (rReg)**

This approach was proposed in [9] to overcome the limitations of the rLin model when it is applied to  $N$  ( $N$  being more than one) tissue regions. Indeed, the estimation of  $N$  values of  $rF_i$ ,  $rV_i$ , and  $k_i$  provides  $N$  potentially different values of  $k_R = F_R/V_R$ , since  $k_R = \frac{F_R}{F_T} \frac{F_T^i}{V_T^i} \frac{V_T^i}{V_R} = \frac{rV_i \cdot k_i}{rF_i}$ . The discrepancy of the values of  $k_R$  can be overcome by forcing this parameter to have the same value across the different regions, i.e. forcing a common ratio between  $rV^i \cdot k_T^i$  and  $rF^i$  across all tissue regions. In summary, an iterative estimation method was proposed, each iteration being conducted in two steps : first a value for  $k_R = \frac{rV_i \cdot k_i}{rF_i}$  is chosen, then the  $3N$  values  $rF_i$ ,  $rV_i$ , and  $k_i$  are estimated by applying  $N$  linear optimization processes under constraints, this two-step procedure being repeated in order to minimize a global error term defined as the sum of the  $N$  errors of the  $N$  fittings. As compartmental approaches take into account recirculation inherently, the truncature approach defined for Log-Normal based models was not tested for models  $M_5$  and  $M_6$ .

## **6.4 Experimental design**

### **6.4.1 Simulations**

Simulations were derived from the small animal experiments described in [11]. For that study, the tumor area was divided into 32 regions ( $N = 32$ ) and a reference tissue were considered, yielding 33 TICs. For the present study, two sets of 33 TICs were generated, using two different arterial input functions:  $C_{A1}(t)$ , based on a log-normal model, and  $C_{Aw}(t)$ , directly derived from  $C_{A1}(t)$  according to equation (6.2) to simulate recirculation (Figure 6-1). Reference perfusion parameters  $F_i$ ,  $V_i$ ,  $D_i$ ,  $V_R$ ,  $F_R$ , and  $D_R$ , displayed on Figure 6-2, were chosen according to values estimated on an experimental dataset. The  $(N + 1)$  TICs  $C_{T_i}$  and  $C_R(t)$  were simply derived using equations (7.1) and (6.4). Fig. 6-1 shows two examples of such simulated TICs. For each configuration (without and with recirculation), noise-free

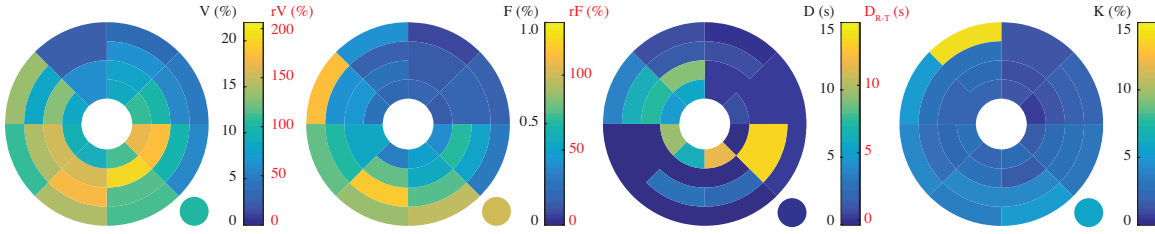


**Figure 6-2:** Bull's-eyes representation of the perfusion parameters used to simulate the 32 regional TICs,  $C_{T_i}$  (large circle), and the reference TIC,  $C_R$  (bottom right disk). From left to right: tissue blood volume ( $V$ ), tissue blood flow ( $F$ ), time-delay ( $D$ ), and rate constant ( $K$ ). The scale displayed in red color shows relative parameters:  $rV$ ,  $rF$ ,  $\delta$  as defined by Eq. (6.6).

and noisy TICs were simulated (see Figure 6-1). Ten noise levels with  $\sigma$  varying from 0.05 to 0.5 were defined and in each case, 150 realizations were considered. A Log-Normal model was fitted to each simulated noise-free  $C_{T_i}$  TIC (generated using  $C_{A1}(t)$ ), yielding reference values for  $AUC_i$ ,  $WIR_i$  and  $\tau_i$ .

#### 6.4.2 Data analysis

For each simulated TIC  $C_{hi}^{nj}(t)$ , associated with configuration  $h$  (for  $h = 1$ , the AIF is  $C_{A1}(t)$ , for  $h = 2$  the AIF is  $C_{Aw}(t)$ ), region  $i$  ( $i = 1, \dots, 32$ ), noise level  $n$  ( $n = 0, \dots, 10$ ) and realization  $j$  ( $j = 1, \dots, 150$ ), the different perfusion parameters  $\Theta_{hi}^{nj}(M_m)$  were estimated using the six methods ( $M_m$ ,  $m = 1, \dots, 6$ ) presented in Section 6.3.4. As the methods  $M_2$  and  $M_4$  were defined to be less sensitive to recirculation, the LN model was fitted to the 20 first seconds following the time-delay estimated for each TIC, since  $\gamma = 20$  seconds was the recirculation period used for simulation.

For parameters related to the tissue blood flow or to the tissue blood volume, the relative estimation error, expressed in %, was defined as follows:

$$E_{hi}^{nj}(M_m) = \frac{\Theta_{hi}^{nj}(M_m) - \Lambda_i(M_m)}{\Lambda_i(M_m)} \quad (6.8)$$

where  $\Lambda_i(M_m)$  is the reference value of the perfusion parameter estimated in the  $i^{th}$  tissue region using method  $M_m$ . For time-delay parameters the absolute estimation error was

defined in seconds as:

$$E_{hi}^{nj}(M_m) = \Theta_{hi}^{nj}(M_m) - \Lambda_i(M_m), \quad (6.9)$$

## 6.5 Results

Fig. 6-3 shows statistical results related to the perfusion parameters estimated inside one specific region ( $i = 4$ ) using the six models ( $M_m$ ) described in section 6.3.4,  $\Theta_{h4}^n(M_m)$ . Indeed, the simulated values  $\Lambda_4(M_m)$  and the median, first, and third quartile values over the 150 simulations of parameters are represented as a function of the noise level (indice  $n$ , proxied by  $\sigma$ ). These results are displayed for simulations without ( $h = 1$ ) and with recirculation ( $h = 2$ ).

In complement to Fig. 6-3, Fig. 6-4, 6-5, and 6-6 display bull's-eye representations of the median estimation errors in the 32 regions for an intermediate noise level ( $\sigma = 0.25$ ,  $n = 6$ ),  $E_{hi}^6(M_m)$ , for the six quantification methods and the two conditions of recirculation.

### 6.5.1 Model $M_1$

When focusing on data without recirculation, the LN model (model  $M_1$ ) is robust, it estimates accurate values of  $AUC_i$  and  $WIR_i$ , whatever the level of noise. In particular, the intermediate noise level yields relevant estimates in all tissue regions. The time delay seems to be the less robust parameter but does not impact the reliability of the other parameters. When introducing the recirculation model, the estimation of  $AUC_i$  ( $E \geq 25\%$ ), and in a less extent the estimation of  $WIR_i$  ( $E \leq 15\%$ ) are biased, but the bias does not vary with noise. As for the estimation of time-delays, behaviors similar to the LN model without recirculation can be observed.

### 6.5.2 Model $M_2$

When using the LN model restricted to the wash-in phase (model  $M_2$ ), both  $AUC_i$  and  $WIR_i$  parameters are respectively largely under and over estimated, whatever the configuration, i.e. without and with recirculation. Some disparities exist between regional parameters: the

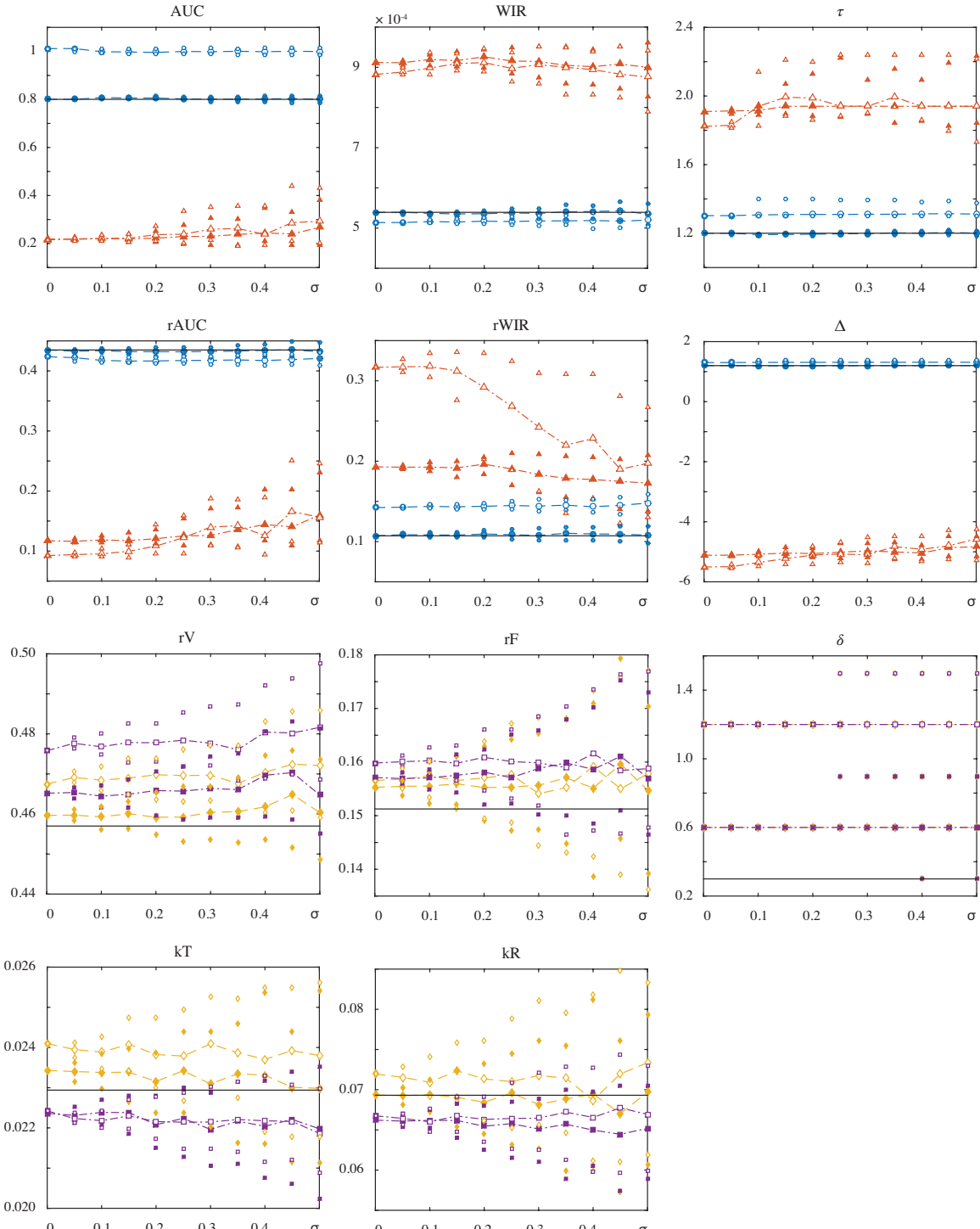


**Figure 6-3:** Median values (large symbols), first and third quartiles (small symbols) of parameters estimated for the fourth tissue region  $C_{T_4}$  (outer ring, upper halve, right octant). First column: tissue blood volume related parameters, second column: tissue blood flow related parameters, third column: time-delay related parameters, fourth row: rate constants in the tissue region and reference tissue. Constant lines in black represent simulated values, blue lines the estimation corresponding to the LN model, red lines the estimation corresponding to the LN model restricted to wash-in phase. Yellow color stands for rLin model, while purple color stands for rReg model. For all of the cases, filled symbols correspond to the configuration without recirculation, while empty symbols correspond to the configura-

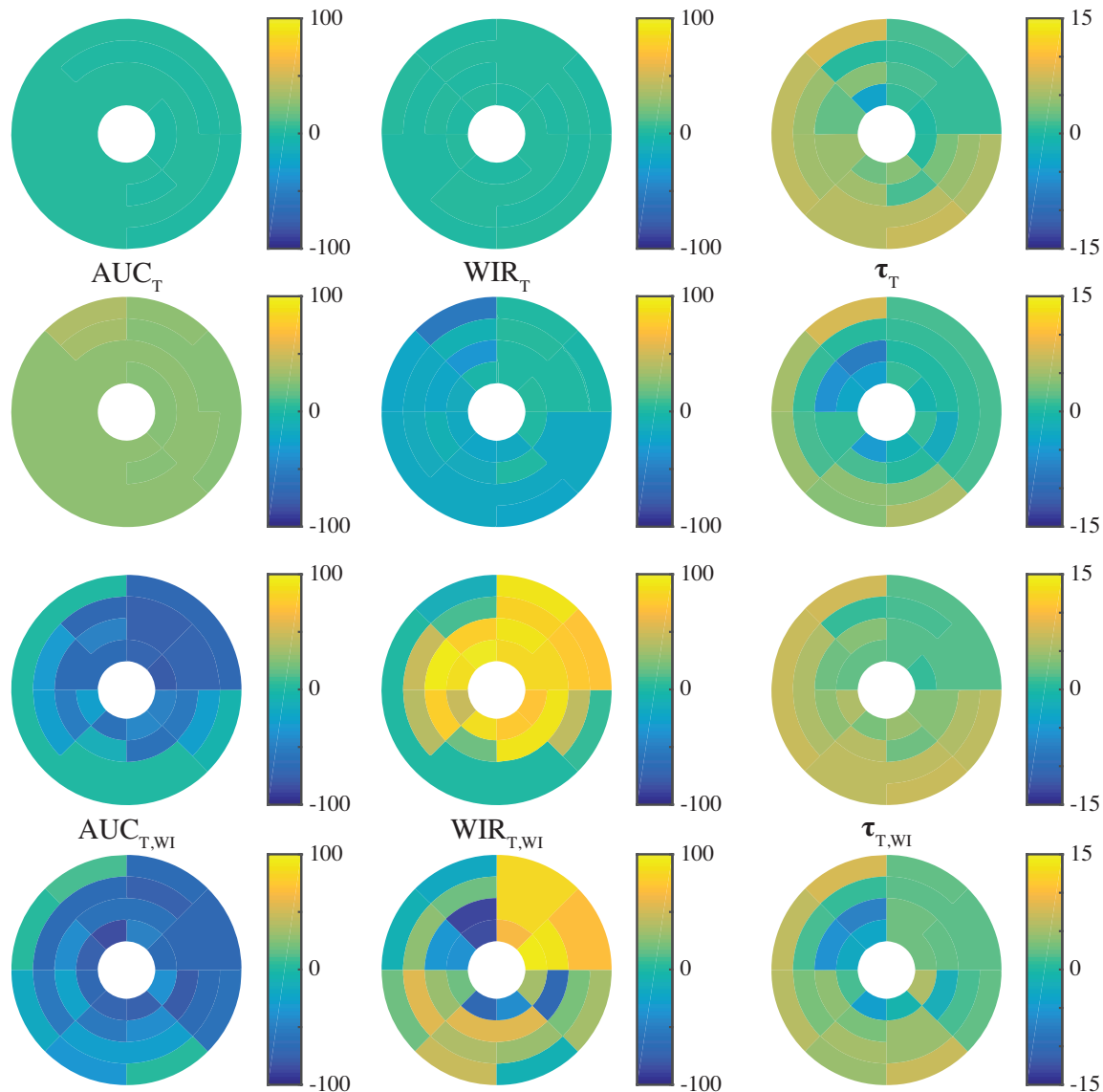


**Figure 6-4:** Bull's-eyes of the median estimation errors obtained by the LN model at the intermediate noise level. From left to right: estimation errors corresponding to tissue blood volume, tissue blood flow, time delay. From top to bottom:  $M_1$  without recirculation,  $M_1$  with recirculation,  $M_2$  without recirculation,  $M_2$  with recirculation.

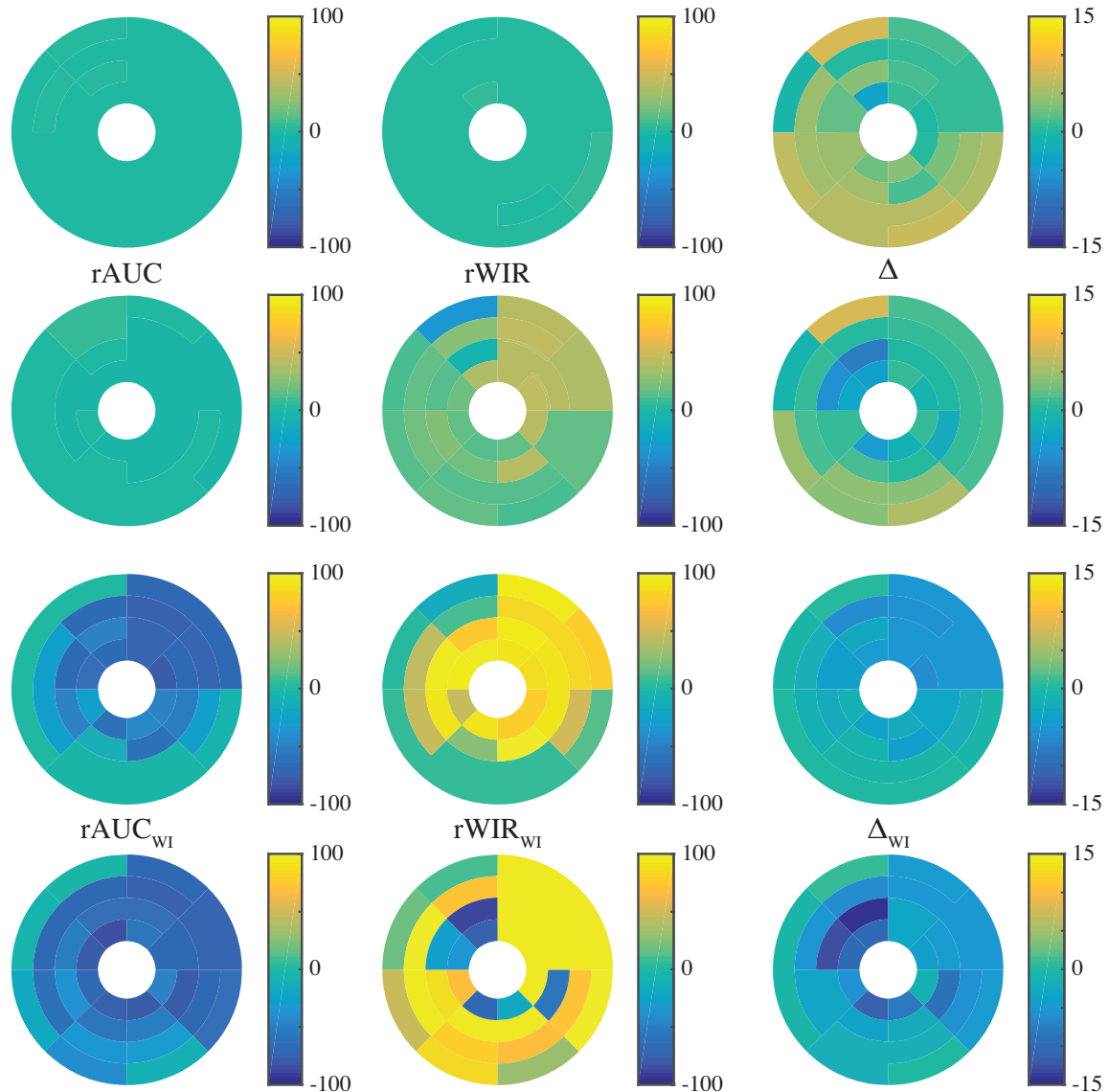


**Figure 6-5:** Bull's-eyes of the median estimation errors obtained by the rLN model at the intermediate noise level. From left to right: errors corresponding to tissue blood volume, tissue blood flow, time delay. From top to bottom:  $M_3$  without recirculation,  $M_3$  with recirculation,  $M_4$  without recirculation,  $M_4$  with recirculation.

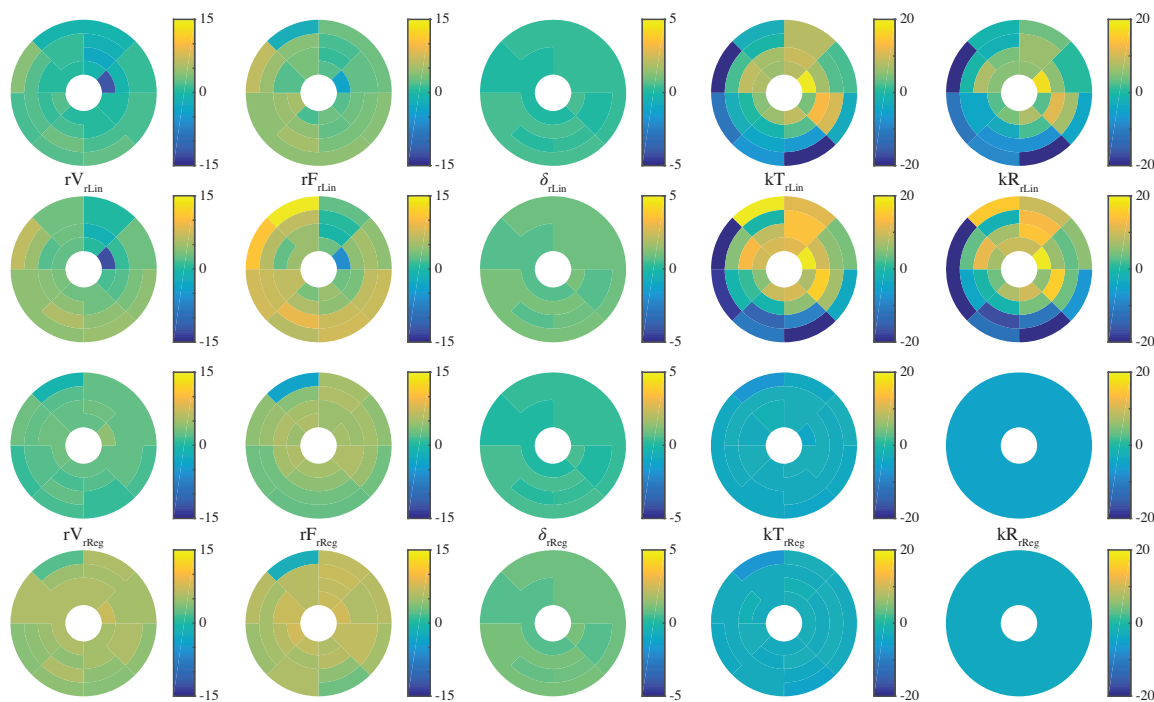


**Figure 6-6:** Bull's-eyes of the median estimation errors obtained by the  $rLin$  and  $rReg$  models at the intermediate noise level. From left to right: errors corresponding to tissue blood volume, tissue blood flow, time delay, rate constant in tissue regions, rate constant in the reference tissue deduced from the different estimations inside tissue regions. From top to bottom:  $M_5$  without recirculation,  $M_5$  with recirculation,  $M_6$  without recirculation,  $M_6$  with recirculation.

smallest values of tissue blood flow or tissue blood volume tend to provide larger relative estimation errors.

### 6.5.3 Model $M_3$

As expected, the rLN model (model  $M_3$ ) for data without recirculation is robust, and provides accurate values of  $rAUC_i$  and  $rWIR_i$ , whatever the level of noise and for the intermediate noise level, and the estimation is relevant in all regions. As could be anticipated, introducing recirculation, the estimation of  $rAUC_i$  was rather accurate but the estimation of  $rWIR_i$  was biased (bias invariant with noise), especially for smaller values of simulated tissue blood flow.

### 6.5.4 Model $M_4$

When using the rLN model restricted to the wash-in phase (model  $M_4$ ), both  $rAUC_i$  and  $rWIR_i$  parameters were respectively largely under and over estimated, whatever the configuration: without and with recirculation. Results show similar trends to those observed when using the LN model restricted to the wash-in phase (model  $M_2$ ).

### 6.5.5 Model $M_5$

The rLin model (model  $M_5$ ) accurately estimates relative tissue blood volume and relative tissue blood flow parameters, exhibiting small biases, but the precision depends on the noise level. The estimation of time delays parameters appears to be robust. Biases are larger when taking into account studies with recirculation, but remain in most cases moderate ( $E \leq 15\%$ ). Considering rate constants, some heterogeneity in estimated  $k_R$  values was found. This confirms our assumption, since no constraints are applied to this specific values. Moreover, related errors appear in the estimates of  $k_{T_i}$ .

### 6.5.6 Model $M_6$

Compared with the model  $M_5$ , results using model  $M_6$  are improved. By construction, a constant value of  $k_R$  is estimated for all the subregions (slightly underestimated in the case shown in Figure 6-6), and consequently the relative error in the estimation of  $k_{T_i}$  is highly homogeneous across tissue regions and almost constant. Indeed the largest median relative error on  $k_{T_i}$  is observed for the highest value of simulated  $k_{T_i}$ . The rReg model estimates relative blood flow parameters and relative blood tissue parameters, with median relative errors generally less than 5% without recirculation for the intermediate noise level (see Fig. 6-6). Of course, recirculation yields higher estimation errors, nevertheless they remain below 7% in most cases and appear to be more homogeneous across the 32 subregions than the estimates of model  $M_5$ .

## 6.6 Discussion

This study aimed at comparing the behavior of different models suitable for quantification of perfusion in contrast-enhanced ultrasound studies. Our whole analysis was based on simulated studies in order to have an irrefutable gold standard and to compare the different methods in terms of precision and accuracy. The model describing contrast displacement relies on a one-compartment model, that has proved to be valid to describe contrast enhancement in a murine tumor model [11]. In order to introduce some variations in the tissue blood flows, tissue blood volumes and time-delays, reflecting the regional heterogeneity among tissue regions, as observable with ultrasound.  $N$  regions inside the simulated tissue of interest were introduced, each one being characterized by its set of perfusion parameters. In addition an arterial input function was first simulated using a single Log-Normal function, then approximated by a sum of modified Log-Normal functions to mimic recirculation. Although the deformation of the first-pass is quite simplistic, this approach enables us to consider two configurations: one idealized configuration without recirculation and one configuration closer to physiological conditions introducing recirculation. Finally different signal to noise conditions were simulated using a multiplicative noise model, as opposed to an additive Gaussian model, reflecting conditions encountered in contrast-enhanced ul-

trasound. Using 150 noisy simulations for each condition guarantees a representative set of possibilities, allowing generalization of the results, as well as enabling the study of the precision of the estimations.

The use of median and quartile operators to assess the estimation errors was necessary to reduce the impact of outliers, which were mostly found in the estimates of the rLin model. Using relative estimation errors (as opposed to absolute estimation errors) for tissue blood flows and tissue blood volumes related parameters allows easy comparison of the errors obtained for parameters with different simulated values.

As expected, results of this study exhibit lower precision of the estimated parameters with decreasing signal to noise ratio. Interestingly, most of the methods are not strongly affected by the signal to noise ratio in terms of accuracy (reflected by the median error on parameters). In addition, perfusion parameters were found less accurate when estimated with recirculation, compared to the estimates without recirculation.

The Log-Normal model, when applied to the whole duration of the study is robust to noise. However this model is subject to recirculation error. To get rid of this dependency, a naive approach consists in limiting the estimation of Log-Normal model to the first samples of the TIC (before recirculation occurs). However this solution appears to be unstable, providing estimates with huge discrepancies when compared to simulated parameters and also showing a large dependency to noise. This naive approach should therefore be absolutely avoided when dealing with dynamic perfusion data. Indeed results are not accurate for both configurations, i.e. with or without recirculation. Thus the present simulation study also emphasizes the need for acquisitions with sufficiently long durations in order a reliably estimate perfusion parameters, and in particular when relying on the Log-Normal model for quantification.

The use of a reference tissue to normalize perfusion parameters was already recommended following a test-retest study that was conducted on dynamic contrast-enhanced ultrasound acquisitions performed on small animals [11]. Normalization was also proposed by a clinical study in order to enable the comparison of perfusion parameters estimated using contrast-enhanced ultrasound data and contrast-enhanced computerized tomography [15]. The present simulation study confirms the interest of normalization when looking at the

accuracy and the precision of estimated parameters. Despite the use of the division operator that could be impacted by noise issues, normalized parameters are more accurate than “absolute” parameters when introducing recirculation in simulated TICs. As recirculation is physiological and cannot be suppressed experimentally, our results emphasize the need to address this question when dealing with real data.

Comparing the estimation of relative parameters using the rLN model, it appears that the  $rAUC$  parameter is more precise than the  $rWIR$  parameter. This experimental result is in concordance with the theory, as detailed in the appendix section of this paper. The differences which are observed between the estimated and simulated values of  $rAUC$  in case of recirculation can partly be explained by the fitting of a Log-Normal model to the reference tissue prior to quantification. This step is useful to reduce the impact of noise but slightly inaccurate to represent TICs with recirculation, the use of a model-free noise-filtering technique should be investigated. To summarize it is important to note that in case of recirculation, the  $rAUC$  is more representative of the simulated parameters than  $AUC$ .

The linear resolution of the relative one-compartment approach (method  $M_5$ ) was introduced to process contrast-enhanced ultrasound studies in [9]. It ensures the fitting error reaches its global minimum, as opposed to the non-linear approach used in [11]. Furthermore, linear resolution significantly reduces computing-time. Some aberrant values of perfusion parameters can however be found since parameters were not bounded during the estimation process. As indicated in the theory section, applying this method independently to multiple regions yields multiple values of  $k_R$ , this effect was also shown in Figure 6-3 and Figure 6-6. Method  $M_6$  simply enforces a single value of  $k_R$  should be estimated across tissue regions. As a consequence, the approach yields spatially regularized estimates of  $k_T$ , slightly biased. As expected, the impact of recirculation on estimates of models  $M_5$  and  $M_6$  is rather low, however not negligible. This effect could be partly explained by the approximation of the TIC inside the reference tissue by the Log-Normal model which does not account for recirculation. This prior modeling was performed in order to reduce the impact of noise on the relative perfusion parameters. The median relative errors on these parameters are all less than 7%, even in presence of recirculation, which is acceptable. This is illustrated in Figure 6-6 for an intermediate noise level.

The estimation of absolute values of perfusion parameters is possible, at least theoretically. It would however require an accurate estimation of the arterial input function. Its proper estimation from image data is a large research question which is not fully solved, even considering other perfusion imaging modalities such as MRI or PET. Some problems are inherent to ultrasound data, ranging from the calibration of signal intensity according to the amount of injected contrast agent, to issues resulting from the 2D nature of data. Additionally, the estimation of such a function in small vessels, surrounding a tumor for instance, is subject to partial volume effects, along with small displacements effects. Therefore, when quantifying CEUS data, we recommend using relative parameters, i.e. parameters normalized according to a reference tissue. Indeed, the chosen reference tissue should be accessible and rather homogeneous. However the robustness of the rLin and rReg models to the choice of the reference tissue remains to be fully investigated.

## 6.7 Conclusion

This study was designed to investigate the impact of recirculation on the quantification of contrast-enhanced ultrasound exams, by means of simulations based on experimental data. Fitting a Log-Normal model on the first pass of the bolus implies a reduction of the number of points used to fit the model and yields unstable estimates, especially on noisy data. This solution is thus inappropriate. Modeling methods such as compartmental modeling, that account for recirculation intrinsically, are indeed the most robust to recirculation. Making use of a reference tissue, the estimation of relative parameters appears to be robust. Taking advantage of the multiple regions, and enforcing estimation of a single rate constant characterizing the reference tissue, provides stable estimates, especially when comparing parameter estimates across regions. This approach is therefore recommended because of its reduced sensitivity to recirculation, and better homogeneity of the estimates inside the considered field of view.

## Appendix

Taking into account the generic expression of the Log-Normal model:

$$\frac{A}{\sqrt{2\pi}\sigma(t-\tau)} \exp\left(-\frac{[\ln(t-\tau) - \mu]^2}{2\sigma^2}\right)$$

and considering the formal definitions of the area under the curve and of the wash-in rate, it can be deduced:

$$\begin{aligned} AUC &= A \\ WIR &= \frac{A}{\sigma\sqrt{2\pi}} \left( \frac{y}{\sigma^2} - 1 \right) e^{2y-2\mu-\frac{y^2}{2\sigma^2}} \\ \text{with } y &= \frac{3\sigma^2 + \sigma\sqrt{\sigma^2 + 4}}{2} \end{aligned}$$

These equations were directly used to compute the *AUC* and *WIR* parameters from a Log-Normal approximation.

*AUC* and *WIR* can also be derived when considering a one-compartment vascular model, their expression is computed for two cases in the following table: one simplified case assuming that  $C_A(t)$  follows a gate function and the general case. In addition relative parameters  $rAUC$  and  $rWIR$  are formally computed when considering a reference tissue. Using the gate function for  $C_A(t)$  shows a strong equivalence between *AUC* and tissue blood volume  $V$ , but also between *WIR* and tissue blood flow  $F$ . Thus, for that case,  $rAUC = rV$  and  $rWIR = rF$ . Using the general shape for  $C_A(t)$  shows that *AUC* is strictly proportional to  $V$ , and that  $rAUC = rV$ . Furthermore, *WIR* is related to  $F$ , but  $rWIR$  is not strictly identical to  $rF$ , since a corrective factor  $\rho$  is introduced. This factor depends of the time of inflexion (denoted  $t_I$ ) of each TIC and explains why the  $rWIR$  is generally not strictly equivalent to  $rF$ .

AIF	$Krect_a(t)$	$C_A(t)$
$AUC$	$KV_T$	$V_T \int_0^{+\infty} C_A(\tau) d\tau$
$WIR$	$\frac{KF_T}{a}$	$\begin{aligned} & F_T \left( C_A(t_I) - \frac{1}{V_T} C_T(t_I - D_T) \right) \\ & \{ t_I \mid \frac{dC_T}{dt}(t_I - D_T) = V_T \frac{dC_A}{dt}(t_I), \\ & \quad \frac{dC_A}{dt}(t_I) > 0 \} \end{aligned}$
$rAUC$	$rV$	$rV$
$rWIR$	$rF$	$\rho \cdot rF$

**Table 6.1:** Analytic expressions of perfusion parameters using a one-compartment model and assuming two different shapes of AIF: rectangle function of width  $a$  and height  $1/a$ ,  $rect_a(t)$ , and general case  $C_A(t)$ . In the first case,  $K$  stands for the injected concentration.



# **Chapter 7**

## **Error Sources Affecting Relative Quantification of CEUS**

### **7.1 Introduction**

In Chapter 5 we studied the impact of inter-exam changes on perfusion parameters estimated from CEUS data, whether occurring at the experimental or physiological level. Additionally, a simulation study addressing the issue of recirculation in CEUS quantification was presented in Chapter 6. In these studies we showed the superiority of the one-compartment reference tissue model in terms of reproducibility. In particular, the linear formulation of this model and its regularized version yielded the most reproducible and robust perfusion parameters among the investigated methods. In this Chapter we investigate other potential sources of error affecting quantification using these two models through a series of simulation experiment with varying factors, and by assessing the accuracy and precision of the estimated perfusion parameters. These include data intrinsic characteristics, i.e. noise level, exam duration, sampling time; as well as quantification strategy, i.e. analysis scale, estimation method, reference tissue selection.

## 7.2 Theory

### 7.2.1 Simulation models

In this section, the two models employed to simulate synthetic noisy CEUS data are presented. First, the one vascular compartment model was used to generate noiseless time-intensity curves (TICs), with known physiology-related perfusion parameters. Then, because of the multiplicative nature of the noise in ultrasound data, a parametric multiplicative noise model was used to corrupt the simulated noiseless TICs.

#### One vascular compartment model (OVC)

A vascularized tissue is considered an homogeneous compartment fed by an artery. The vascular compartment is parameterized by tissue blood volume  $V$ , and tissue blood flow  $F$ , since the distribution of microbubbles is restricted to the vascular space [12, 14]. An additional time-delay parameter  $D$ , reflecting the transit time of the contrast agent from the feeding artery to the tissue of interest, was used to fit data more accurately, thus avoiding biasing the estimation of vascular parameter. The mathematical expression of this model is given by equation (7.1):

$$\begin{aligned}\dot{C}(t - D) &= F \cdot C_A(t) - \frac{F}{V} \cdot C(t - D), \quad \forall t \geq D, \\ &= 0 \text{ otherwise.}\end{aligned}\tag{7.1}$$

where  $C_A$  is the AIF,  $C$  is the modeled TIC, and  $\dot{C}$  is the time derivative of  $C$ .

Given the AIF  $C_A(t)$  and the TIC in a region of interest  $C(t)$ , three perfusion parameters can be estimated by least-squares fitting:  $V$ ,  $F$ , and  $D$ . Inversely, given an AIF  $C_A(t)$ , and the set of three perfusion parameters  $V$ ,  $F$ , and  $D$ , the associated TIC  $C(t)$  can be simulated.

#### Multiplicative noise model

A multiplicative noise model following a gamma distribution enforcing unit mean was used, inspired by Barrois et al., i.e.  $\text{mean}_v p(v) = 1$ , where  $p(v)$  is the gamma distribution [3]. A unit mean distribution for a multiplicative noise ensures no bias in introduced by the noise

model: it is the equivalent of a centered distribution for additive noise.

The gamma distribution is traditionally parameterized by two parameters: the shape parameter  $k$ , and the scale parameter  $\theta$ . However, enforcing a unit mean is equivalent to set  $\theta = 1/k$ , the noise distribution  $p(v)$  can therefore be parameterized by a single parameter,  $k$ , as

$$p(v) = \frac{1}{\Gamma(k)} k^k v^{k-1} e^{-vk}, \forall v \geq 0. \quad (7.2)$$

The shape parameter  $k$  controls the sharpness of the noise distribution, and is related to the standard deviation by the relation  $\sigma = 1/\sqrt{k}$ , allowing modulation of the noise level in simulated TICs. Fig. 6-1 shows an example of multiplicative random noise on simulated TICs for  $k = 16$ , corresponding to  $\sigma = 0.25$ . Unless specified differently, this value of  $\sigma$  was used as the default standard deviation of the noise distribution and 150 random noise sequences were generated from this distribution.

## 7.2.2 Quantification models

In this section we present relative quantification methods, making use of a reference tissue, derived from the previously described OVC model. The following methods are intended to estimate perfusion parameters from  $N_T$  tissues in a single CEUS exam. The TIC in the  $i^{th}$  tissue of interest is noted  $C_T^i(t)$ , where  $i \in [[1, N_T]]$ , and the TIC in the chosen reference tissue is noted  $C_R(t)$ . All TICs are defined for  $t \in [0, L]$ .

### Relative OVC model (rOVC)

A relative OVC model can be derived from the previously presented OVC model, considering conjointly one tissue of interest with TIC  $C_T^i(t)$ , and one reference tissue with TIC  $C_R(t)$ :

$$\begin{cases} \dot{C}_R(t - D_R) &= F_R \cdot C_A(t) - \frac{F_R}{V_R} \cdot C_R(t - D_R), \quad \forall t \geq D_R, \\ &= 0 \text{ otherwise;} \\ \dot{C}_T^i(t - D_T^i) &= F_T^i \cdot C_A(t) - \frac{F_T^i}{V_T^i} \cdot C_T^i(t - D_T^i), \quad \forall t \geq D_T^i, \\ &= 0 \text{ otherwise.} \end{cases} \quad (7.3)$$

The first equation of the system of equations (7.3) can be rearranged as

$$\begin{aligned} C_A(t) &= \frac{1}{F_R} \cdot \dot{C}_R(t - D_R) + \frac{1}{V_R} \cdot C_R(t - D_R) \quad \forall t \geq D_R, \\ &= 0 \text{ otherwise.} \end{aligned} \quad (7.4)$$

Replacing  $C_A(t)$  in the second equation of system (7.3) by its expression in equation (7.4),  $\dot{C}_T^i(t)$  can be expressed as

$$\begin{aligned} \dot{C}_T^i(t - D_T^i) &= \frac{F_T^i}{F_R} \cdot \dot{C}_R(t - D_R) + \frac{F_T^i}{V_R} \cdot C_R(t - D_R) \\ &\quad - \frac{F_T^i}{V_T^i} \cdot C_{T^i}(t - D_{T^i}), \quad \forall t \geq D_T^i, \\ &= 0 \text{ otherwise.} \end{aligned} \quad (7.5)$$

Defining the relative flow as  $rF^i = V_T^i/V_R$ , the relative volume as  $rV^i = V_T^i/V_R$ , and the rate constant in the  $i^{th}$  tissue of interest as  $k_T^i = F_T^i/V_T^i$ , the previous equation rewrites

$$\begin{aligned} \dot{C}_T^i(t - D_T^i) &= rF^i \cdot \dot{C}_R(t - D_R) + rV^i \cdot k_T^i \cdot C_R(t - D_R) \\ &\quad - k_T^i \cdot C_T^i(t - D_T^i), \quad \forall t \geq D_T^i, \\ &= 0 \text{ otherwise.} \end{aligned} \quad (7.6)$$

Assuming initial concentrations are equal to zero in both tissues,  $\dot{C}_T^i$  in Eq. 7.6 integrates in exponential form [26], yielding

$$\begin{aligned} C_T^i(t - D_T^i) &= rF^i \cdot (k_R - k_T^i) \cdot \int_0^t C_R(\tau - D_R) \cdot e^{-k_T^i \cdot (t - D_R - \tau)} d\tau \\ &\quad + rF^i \cdot C_R(t - D_R) \quad \forall t \geq D_T^i, \\ &= 0 \text{ otherwise,} \end{aligned} \quad (7.7)$$

where  $k_R = F_R/V_R$  is the rate constant in the reference tissue.

The latter equation, however, is not linearly solvable. A non-linear resolution method must therefore be used in order to estimate vascular parameters  $rF^i$ ,  $rV^i$ ,  $k_T^i$ , and  $k_R$  in each of the  $N_T$  tissues of interest.

### Linear resolution of the rOVC model (rLin)

Alternatively, under similar assumptions,  $\dot{C}_T^i$  in Eq. 7.6 can be integrated over time, yielding the following expression of  $C_T^i$  [7]

$$\begin{aligned} C_T^i(t - D_T^i) &= rF^i \cdot C_R(t - D_R) + rV^i \cdot k_T^i \cdot \int_0^t C_R(\tau - D_R) d\tau \\ &\quad - k_T^i \cdot \int_0^t C_T^i(\tau - D_T^i) d\tau, \quad \forall t \geq D_T^i, \\ &= 0 \text{ otherwise.} \end{aligned} \quad (7.8)$$

Assuming time delay parameters  $D_T^i$  and  $D_R$  are known beforehand, TICs can be time-registered, mimicking an ideal case with no delay in bolus arrival. Variables  $x^i(t)$ ,  $y^i(t)$  are time-registered versions of the TIC in the  $i^{th}$  tissue of interest and its integral. They were defined  $\forall t \in [0, L - D_T^i]$ , as

$$\begin{aligned} x^i(t) &= C_T^i(t), \\ y^i(t) &= -\int_0^t C_T^i(\tau) d\tau. \end{aligned} \quad (7.9)$$

Similarly, variables  $u(t)$ ,  $v(t)$  are time-registered versions of the reference TIC and its integral. They were defined  $\forall t \in [0, L - D_R]$ , as

$$\begin{aligned} u(t) &= C_R(t), \\ v(t) &= \int_0^t C_R(\tau) d\tau. \end{aligned} \quad (7.10)$$

Eq. 7.8 can be interpreted as an overly determined linear system of equations [4], i.e. one equation for each time sample  $t$ . It therefore rewrites

$$x^i(t) = a^i \cdot u(t) + b^i \cdot v(t) + c^i \cdot y^i(t) \quad \forall t \geq D_T^i, \quad (7.11)$$

where coefficients  $a^i$ ,  $b^i$ , and  $c^i$  are defined in terms of vascular parameters as

$$a^i = rF^i, \quad b^i = rV^i \cdot k_T^i, \quad c^i = k_T^i. \quad (7.12)$$

The system can be solved using a linear least-squares resolution method, yielding esti-

mates of parameters  $a^i$ ,  $b^i$ , and  $c^i$  by minimization of the squared fit error  $\varepsilon^i$

$$\arg \min_{\{a^i, b^i, c^i\}} \varepsilon^i, \text{ where } \varepsilon^i = \sum_t \left( x^i(t) - a^i \cdot u(t) + b^i \cdot v(t) + c^i \cdot y^i(t) \right)^2. \quad (7.13)$$

Vascular parameters of the **rLin** model can then be derived easily using

$$rF^i = a^i, rV^i = b^i/c^i, \text{ and } k_T^i = c^i. \quad (7.14)$$

The linear resolution of the **rOVC** model will be referred to as **rLin** in the following.

### Regularized linear resolution of the **rOVC** model (**rReg**)

Estimating  $rF^i$ ,  $rV^i$ , and  $k_T^i$  in  $N_T$  tissues using the **rLin** model,  $N_T$  values of parameter  $k_R$  can be derived as a linear combination of the **rLin** model parameters:

$$k_R = \frac{F_R}{F_T} \frac{F_T^i}{V_T^i} \frac{V_T^i}{V_R} = \frac{rV^i \cdot k_T^i}{rF^i} = \frac{b^i}{a^i} \quad (7.15)$$

However, there is but one reference tissue per exam, associated to a single reference TIC  $C_R(t)$ . Since parameter  $k_R$  characterizes the vascular function of a single reference tissue, a unique value should be estimated per exam in order to avoid discrepancies of  $k_R$  values between tissues of interest.

The linear relation between parameters of the **rLin** model provided by Eq. 7.15 can be used as a constraint to ensure the  $N_T$  derived values of  $k_R$  are consistent across tissues. Substituting in Eq. 7.11 yields

$$x^i(t) = a^i \cdot (u(t) + k_R \cdot v(t)) + c^i \cdot y^i(t), \quad (7.16)$$

which rewrites

$$x^i(t) = a^i \cdot w(t) + c^i \cdot y^i(t) \quad (7.17)$$

where  $w(t)$  is a linear combination of variables  $u(t)$  and  $v(t)$ , which were defined in

Eq. 7.10,

$$\begin{aligned} w(t) &= u(t) + k_R \cdot v(t), \\ &= C_R(t - D_R) + k_R \cdot \int_0^t C_R(\tau - D_R) d\tau. \end{aligned} \quad (7.18)$$

Provided a value of parameter  $k_R$ , the  $N_T$  linear system equations defined in Eq. 7.16 are independently solvable using a linear least-squares resolution method, minimizing the squared error,  $e^i$ :

$$\arg \min_{\{a^i, c^i\}} e^i, \text{ where } e^i = \sum_t \left( x^i(t) - [a^i \cdot w(t) + c^i \cdot y^i(t)] \right)^2. \quad (7.19)$$

Since the value of  $k_R$  is unknown, and is necessary to define  $w(t)$ , its value must be determined. We proposed a non-linear optimization scheme that estimates the value of  $k_R$  by minimization of the normalized mean squared error,  $E$ :

$$\arg \min_{k_R} E, \text{ where } E = \sum_i \frac{\sqrt{e^i / N^i}}{|x^i|_\infty}, \quad (7.20)$$

$N^i$  being the number of samples in  $x^i(t)$ , i.e. the number of time samples verifying  $t \in [0, L - D_T^i]$ . Vascular parameters were then derived from the model estimates as

$$rF^i = a^i, rV^i = \frac{k_R \cdot a^i}{c^i}, \text{ and } k_T^i = c^i. \quad (7.21)$$

### Estimation of time-delay parameters

As stated in the presentation of the **rLin** and **rReg** models, time-delay parameters must be known beforehand, and TICs registered in time in order to solve the linear system of equations. The determination method of the time-delay parameter, noted  $D$ , of a generic TIC, noted  $C(t)$ , used the empirical method described below.

$C(t)$  was noise-filtered twice by a moving-average filter of width 2 seconds, yielding  $C_f(t)$ . The time when  $C_f(t)$  reaches 20% of its maximum value is a rough approximation that intentionally overestimates  $D$ , it was noted  $t_{20\%}$ .  $C_f(t)$  was then truncated, conserving only the part where  $t \leq t_{20\%}$ . The derivative of  $C_f(t)$ , noted  $\dot{C}_f(t)$ , was approximated by convolution of the TIC with the central difference operator [25]. Finally, assuming no os-

cillation occurred in the TIC prior to bolus arrival,  $D$  was defined as the time at which the derivative  $\dot{C}_f(t)$  reaches 20% of its value at  $t = t_{20\%}$ :

$$\exists D \in \mathbb{R}^+, D \leq t_{20\%} \wedge \dot{C}_f(D) = 20\% \times \dot{C}_f(t_{20\%}). \quad (7.22)$$

## 7.3 Materials and Methods

### 7.3.1 Simulations of CEUS data

#### Simulation process

Regional perfusion parameters were derived from experimental data fitted with the **OVC** model presented in Section 7.2.1. The arterial input function was estimated in the image using the segmentation method presented in Chapter 3. A log-normal model was fitted to the resulting arterial curve for noise-filtering purposes. Regional enhancement curves were simulated using the same model, along with the estimated model parameters and arterial input function. The perfusion parameters of the **OVC** model used for simulation are presented in Figure 7-1. The associated time-intensity curves simulated for each tumor region, as well as for the reference tissue are displayed in Figure 7-2.

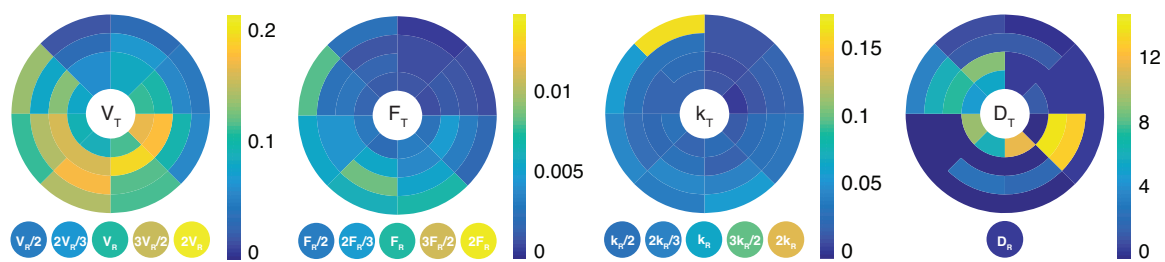


**Figure 7-1:** Absolute perfusion parameters used for simulation with the OVC model, i.e. tissue blood volume,  $V_T$  and  $V_R$ , tissue blood flow,  $F_T$  and  $F_R$ , tissue rate constant,  $k_T$  and  $k_R$ , and time delay,  $D_T$  and  $D_R$ . Bullseye view of the parameters in the 32 tumor regions. The bottom disks represent the parameters used to simulate the reference tissue region, the center disk being the original value used for all experiments. The other disks are, from left to right, the half, two third, three half, and double of the original value, used to study the influence of the reference tissue.

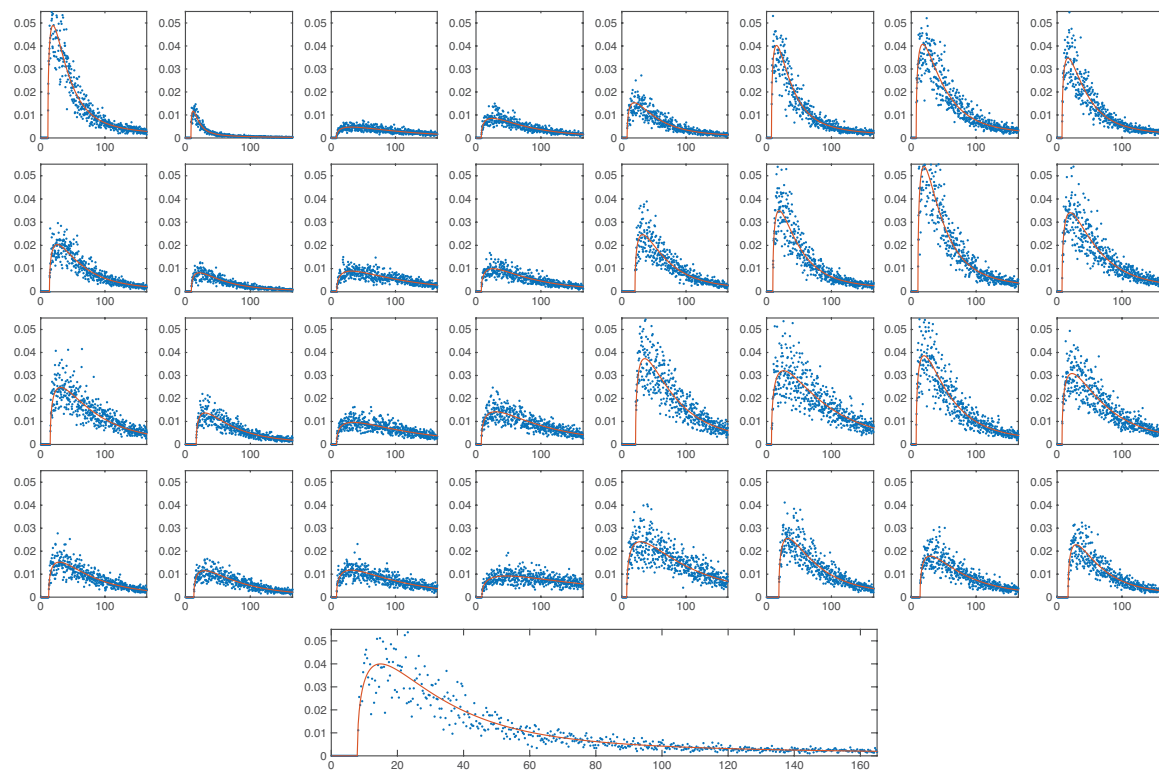


**Figure 7-2:** Time-intensity curves inside of each of the 32 tumor regions (top grid), and in the reference tissue (bottom), simulated using the **OVC**. Each plot shows the simulated noiseless curve (orange line) in the region, i.e.  $\sigma = 0$ , as well as the curve with simulated multiplicative noise (blue dots), i.e.  $\sigma = 0.25$ .

## Varying factors

**Noise level** The influence of noise was investigated by varying parameter  $\sigma$ , i.e. the standard deviation of the multiplicative noise level presented in Section 7.2.1.  $\sigma$  was varied linearly with increments of 0.05 from 0, corresponding to a noiseless conditions, to 0.5, corresponding to high noise conditions. For each noise level, 150 random noise sets following the multiplicative gamma noise model were generated.

**Exam duration** Various exam durations were investigated by varying the number of samples in the simulated data. More precisely, the exam duration was varied from 50 seconds to 165 seconds with 5 seconds increments.

**Sampling period** Simulated noiseless enhancement curves were resampled using varying sampling periods to study the impact of this parameter on the accuracy and precision of the estimation. The sampling period was varied from 0.1 to 1.0 second with 0.1 increments, this range is representative of the acquisition settings that can be found in contrast-enhanced ultrasound studies.

**Reference tissue** The reference tissue can be represented functionally by the parameters of the OVC model, i.e.  $V_R$ ,  $F_R$ , and  $k_R = \frac{F_R}{V_R}$ . The impact of these parameters on the accuracy and the precision of the quantification process using the **rLin** and the **rReg** models was investigated. In particular, the tissue blood volume, the tissue blood flow of the reference tissue were varied by scaling either or both of them by  $\frac{1}{2}$ ,  $\frac{2}{3}$ ,  $\frac{3}{2}$ , 1,  $\frac{1}{2}$ , and 2. Because of the relation between the three parameters, they cannot be varied individually. It is however possible to fix either of the parameters while varying the two others. The disks at the bottom Figure 7-1 shows the various values of the perfusion parameters used to simulate the reference tissue enhancement curve, the center disk being the original value obtained from experimental data.

**Number of regions** Various regional segmentation were performed varying the number of tumor regions as powers of two, ranging from 1 to 32. For each segmentation, the parameters of the OVC model were estimated using the mean enhancement curve in each tumor

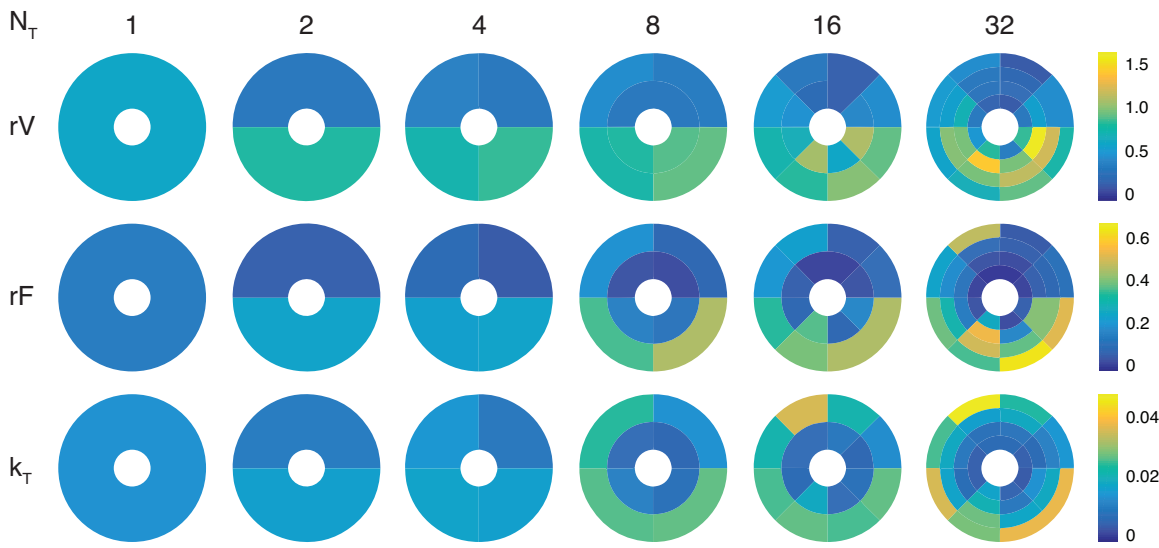


**Figure 7-3:** Relative perfusion parameters used for simulation varying the number of tumor regions  $N_T$  from 1 (left) to 32 (right), i.e. relative tissue blood volume,  $rV$ , relative tissue blood flow,  $rF$ , tissue rate constant,  $k_T$ .

and reference region, as well as an estimate of the arterial input function derived from the image. Figure 7-3 shows the simulated values of the perfusion parameters for the various segmentations with a varying number of regions. The absolute perfusion parameters of the OVC model were used to derive the parameters of the rOVC model using the definitions of Eq. 7.6. The derived parameters were then used as ground truth to evaluate the accuracy of the perfusion parameters estimated using the **rLin** and the **rReg** models.

### 7.3.2 Data analysis

The accuracy and the precision of the parameters estimated using the **rLin** and the **rReg** models were respectively investigated through the median value, and either the standard deviation or the interquartile range, of the relative estimation error over 150 random noise samples. The relative estimation error of parameter  $\theta$ , noted  $rE_\theta$ , is expressed in percent and defined as

$$rE_\theta = 100 \times \frac{\theta_{est} - \theta_{sim}}{\theta_{sim}} \quad (7.23)$$

i.e. the difference between the estimated parameter  $\theta_{est}$  and the simulated parameter  $\theta_{sim}$ , normalized by the simulated value.

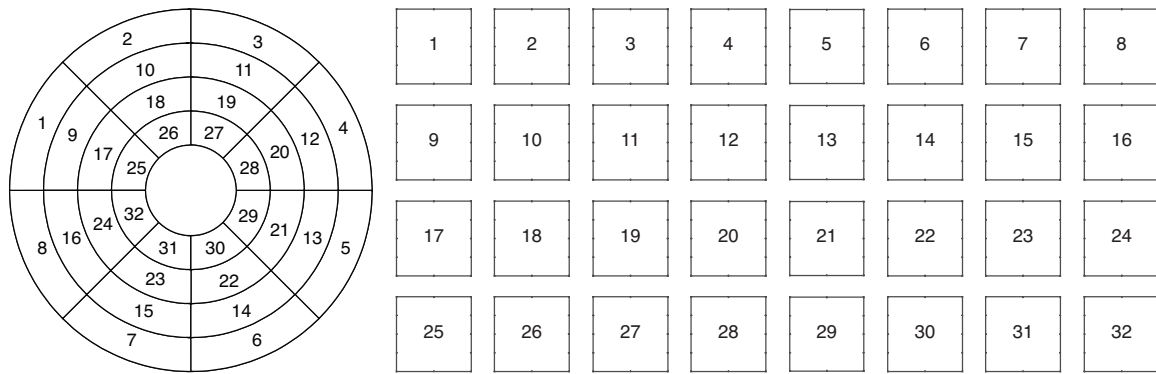


**Figure 7-4:** Correspondance of the regions between bullseye (left) and grid (right) representation.

## 7.4 Results

In this section we present the results of our simulation experiments. Figure 7-4 provides the correspondance between regions, depending on the type of data to be presented. Indeed, color-coded bullseyes were used when a single value had to be represented per region, but grids of plots were used to show the regional results as a function of a simulation parameter, i.e. noise level, exam duration, and sampling period.

**Noise level** Figures 7-5 to 7-8 show the relative estimation error of the relative tissue blood volume (Figure 7-5), relative tissue blood flow (Figure 7-6), and rate constants in the tumor (Figure 7-7) and reference (Figure 7-8) tissues obtained using the **rLin** and **rReg** models, as a function of the noise level simulated in the data, i.e. the standard deviation of the multiplicative noise model.

Expectedly, for the four parameters of both models, the interquartile range of the relative estimation bias increased with the noise level, and no relation was found between the noise level and the median value of the relative estimation error. In terms of relative tissue blood volume (see Figure 7-5), the two models were hardly differentiable. Inside a given region, the median relative estimation error value can be different with a slight advantage for the **rLin** model, but the precision of the estimation is however generally comparable. Additionally, the **rReg** model makes the estimation bias of  $rV$  more consistent across regions. Regarding relative blood flow (see Figure 7-6), the **rLin** model was generally more accurate than the

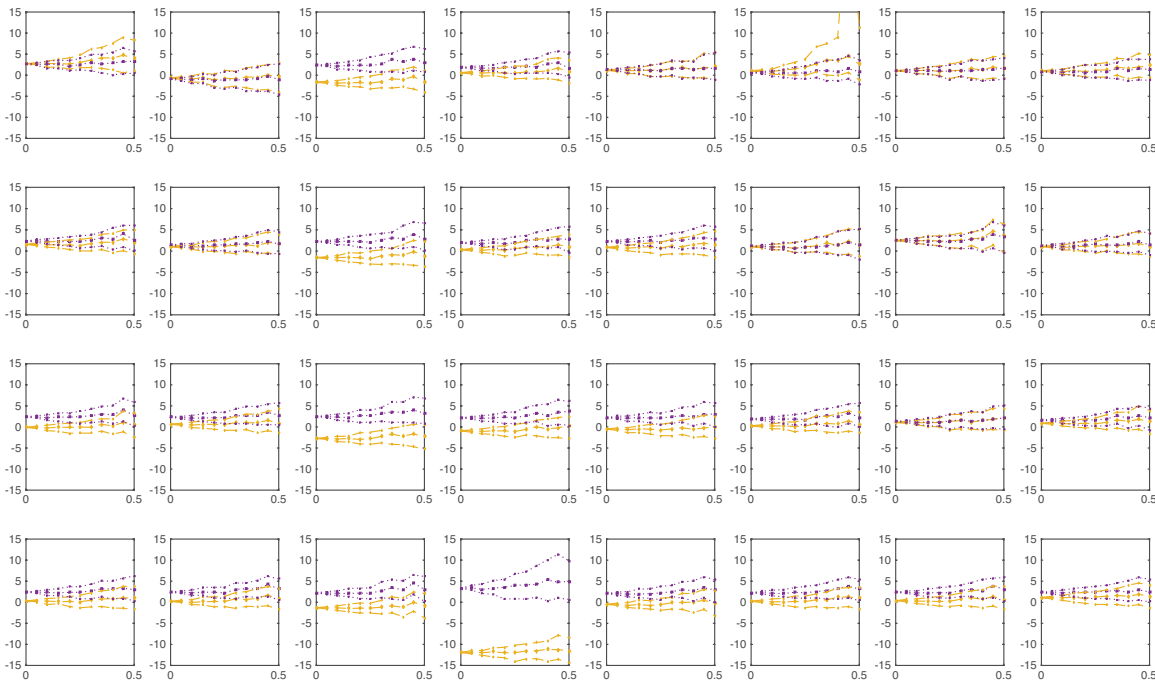


**Figure 7-5:** Median (large symbols) and first and third quartiles (small symbols) of the relative estimation error for the relative blood volume ( $rV$ ) estimated using the **rLin** (yellow diamonds) and **rReg** (purple squares) models, as a function of the noise level.

**rReg** model. However the estimation of  $rF$  was less precise and more sensitive to noise using the **rLin** model. In terms of the rate constant in tumor tissues (see Figure 7-7), the **rReg** model proved both more accurate and more precise than the **rLin** model. Indeed, the **rReg** model exhibited an extremely consistent estimation bias across regions, with an average of -3%, and a lower sensitivity to noise. The **rLin** model on the other hand, yielded estimates of  $k_T$  with highly variable biases, with median biases reaching 40% in one of the regions, and overestimating the parameter in some regions while underestimating it in others. A common value of the rate constant in the reference tissue (see Figure 7-8),  $k_R$ , was estimated for all tumor regions using the **rReg** model. The regularized model underestimated  $k_R$  by 5% in average in our experiments and exhibited a rather low sensitivity to noise. Oppositely, the estimates of the **rLin** model were extremely inconsistent across regions, and were more sensitive to noise in most regions.

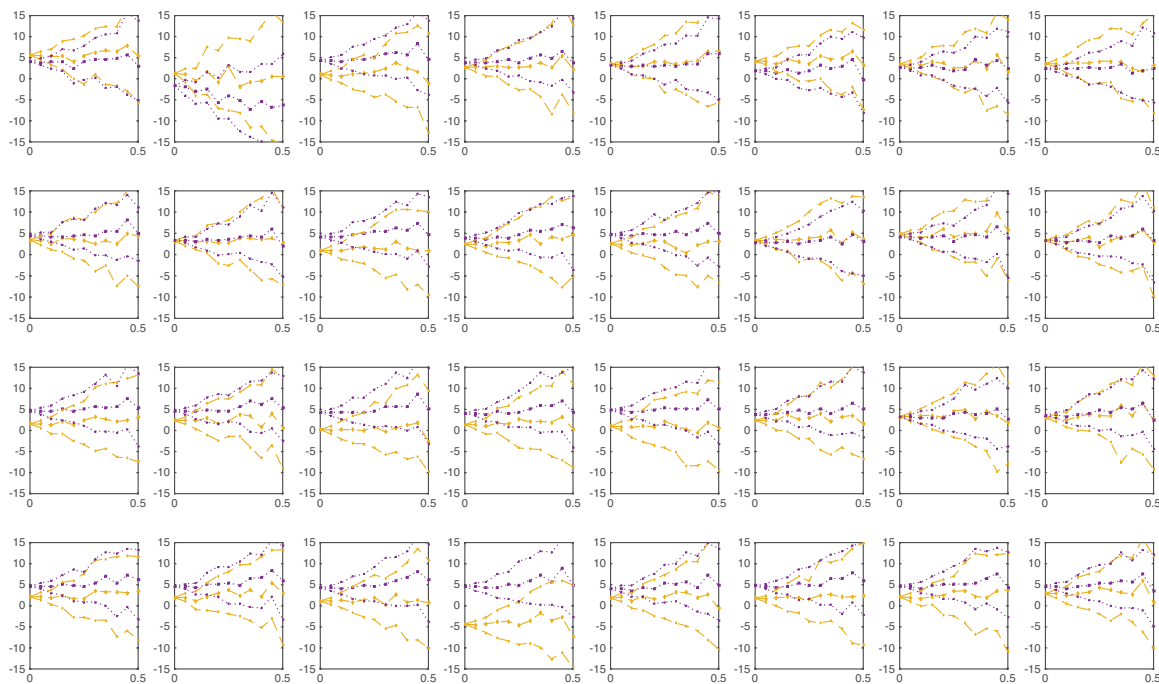


**Figure 7-6:** Median (large symbols) and first and third quartiles (small symbols) of the relative estimation error for the relative blood flow ( $rF$ ) estimated using the **rLin** (yellow diamonds) and **rReg** (purple squares) models, as a function of the noise level.

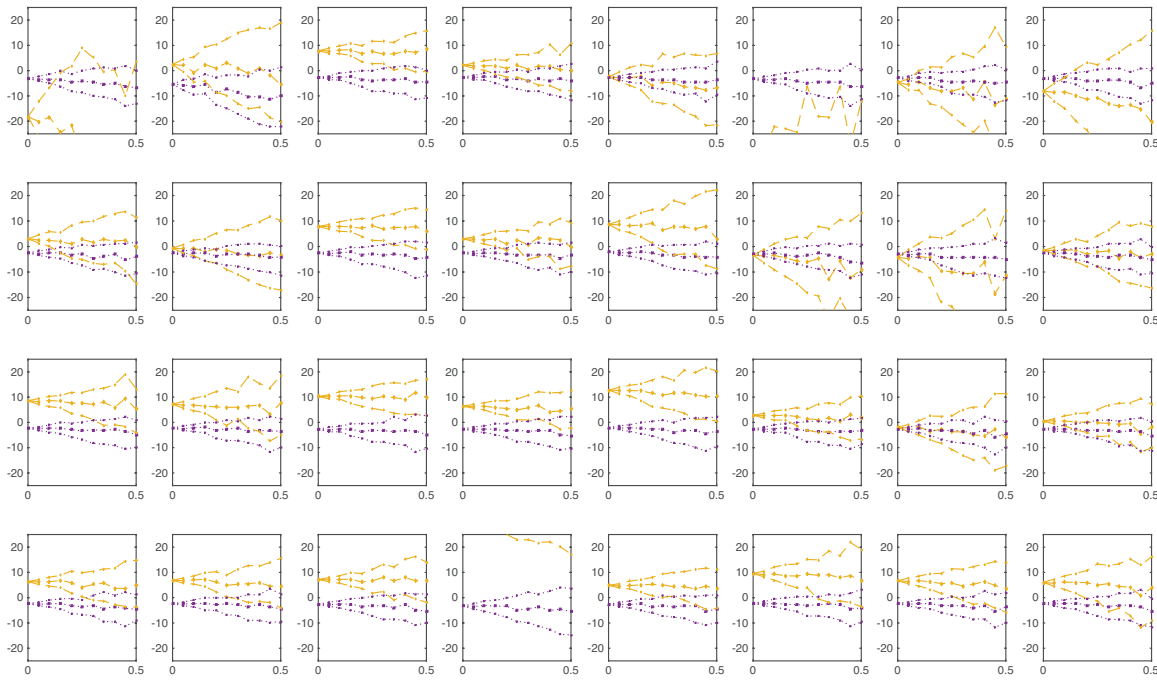


**Figure 7-7:** Median (large symbols) and first and third quartiles (small symbols) of the relative estimation error for the rate constant in the tumor ( $k_T$ ) estimated using the **rLin** (yellow diamonds) and **rReg** (purple squares) models, as a function of the noise level.

**Exam duration** Figures 7-9 to 7-12 show the impact of the exam duration on the relative estimation error of the perfusion parameters of the **rLin** and **rReg** models, i.e. relative tissue blood volume (Figure 7-9), relative tissue blood flow (Figure 7-10), and rate constants in the tumor (Figure 7-11) and in the reference tissue (Figure 7-12). In Figures 7-9 to 7-12, each plot represents a tumor region, i.e. the top row corresponds to the outer rim and the bottom row to the inner rim, the columns correspond to the clockwise ordering of the regions on a rim starting with the left region above the horizontal line.

Regarding relative blood volume (see Figure 7-9), the **rReg** model was able to estimate the parameter accurately, and to reach a steady state with exams as short as 80 seconds. Oppositely, the **rLin** model only yielded accurate estimates using the whole exam duration, i.e. 165 seconds, and at the exception of one region it overall underestimated  $rV$ . Comparably, the relative blood flow (see Figure 7-10) was steadily estimated using the **rReg** model with exams as short as 50 seconds, despite an average overestimation of less than 4%. The estimates of  $rF$  given by the **rLin** were found more sensitive to the duration of the exam,

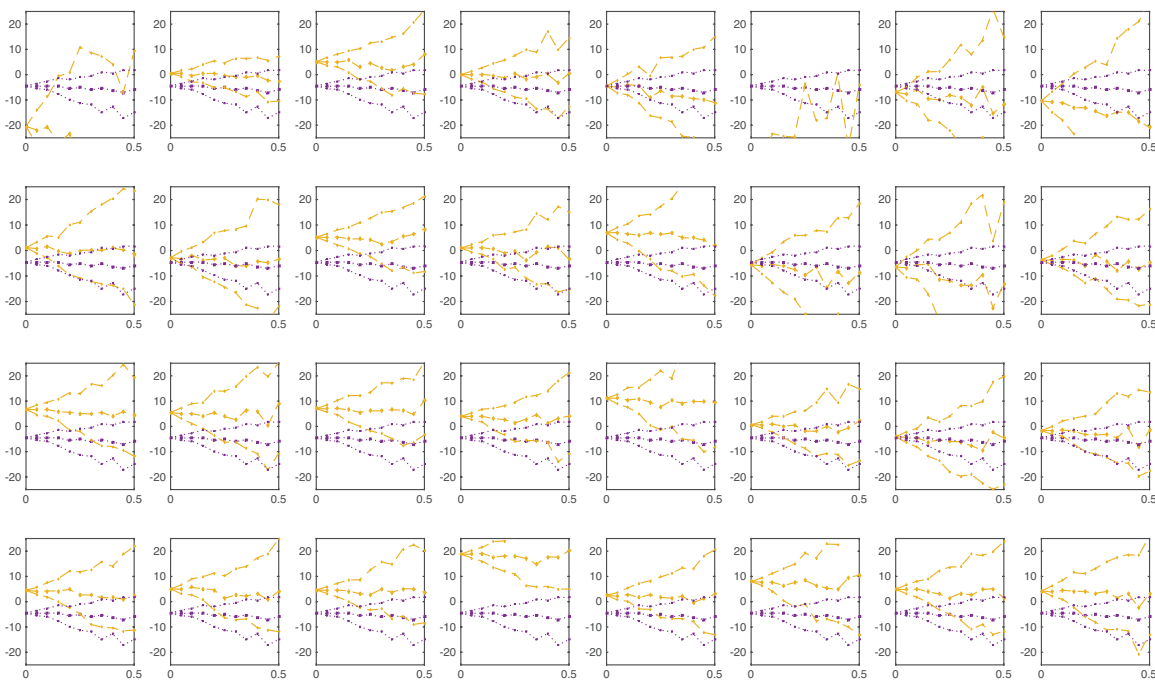


**Figure 7-8:** Median (large symbols) and first and third quartiles (small symbols) of the relative estimation error for the rate constant in the reference tissue ( $k_R$ ) estimated using the **rLin** (yellow diamonds) and **rReg** (purple squares) models, as a function of the noise level.

and generally overestimated  $rF$  for very short exams, the bias decreasing with exam duration. And then, past some duration threshold, which variable from one region to another, the bias increased linearly with the exam duration. Regarding the rate constant in the tumor (see Figure 7-11), the **rLin** model was unable to accurately estimate the parameter for incomplete exams, and exhibited strong biases in short exams, again varying from one exam to another. The **rReg** model was able to steadily and uniformly estimate parameter  $k_T$ , despite the tendency of the median relative estimation error to slightly decrease with the exam duration for exams lasting more than 100 seconds. Moreover, the estimation of  $k_T$  was more precise using the **rReg** model. For both models, the bias in the estimation of  $k_R$ , the rate constant in the reference tissue (see Figure 7-12), was strongly correlated to the bias in the estimation of  $k_T$ .

**Sampling period** Figures 7-13 to 7-16 show the impact of the sampling period on the relative estimation error of the perfusion parameters of the **rLin** and **rReg** models, i.e. relative

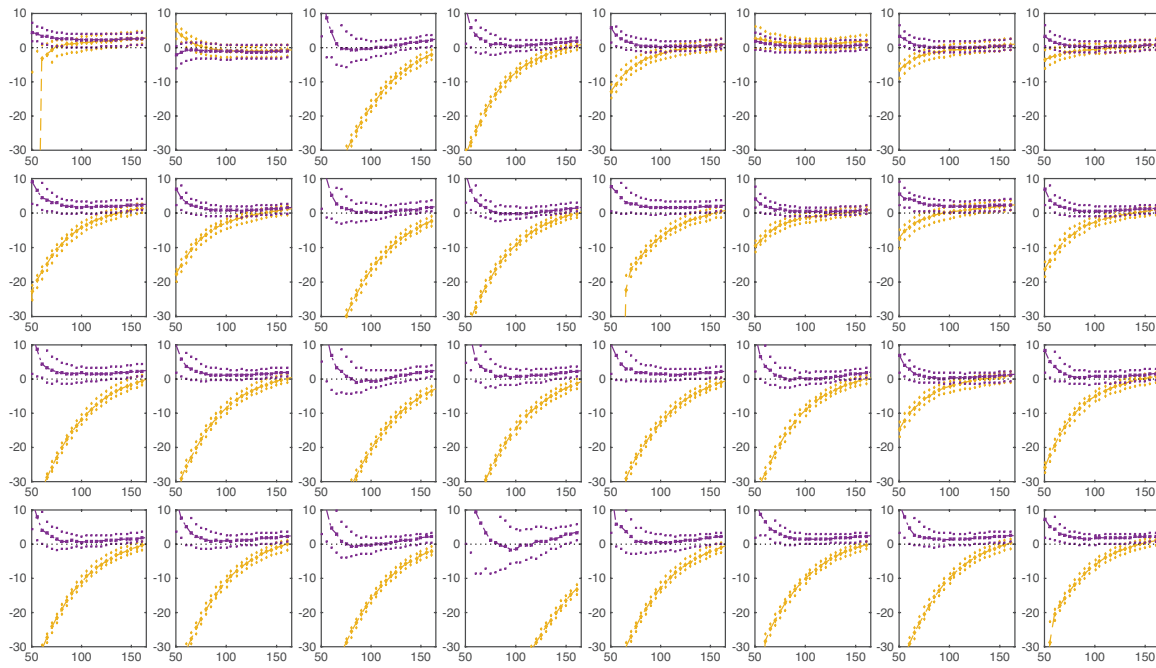


**Figure 7-9:** Median (large symbols) and first and third quartiles (small symbols) of the relative estimation error for the relative blood volume ( $rV$ ) estimated using the **rLin** (yellow diamonds) and **rReg** (purple squares) models, as a function of the exam duration.

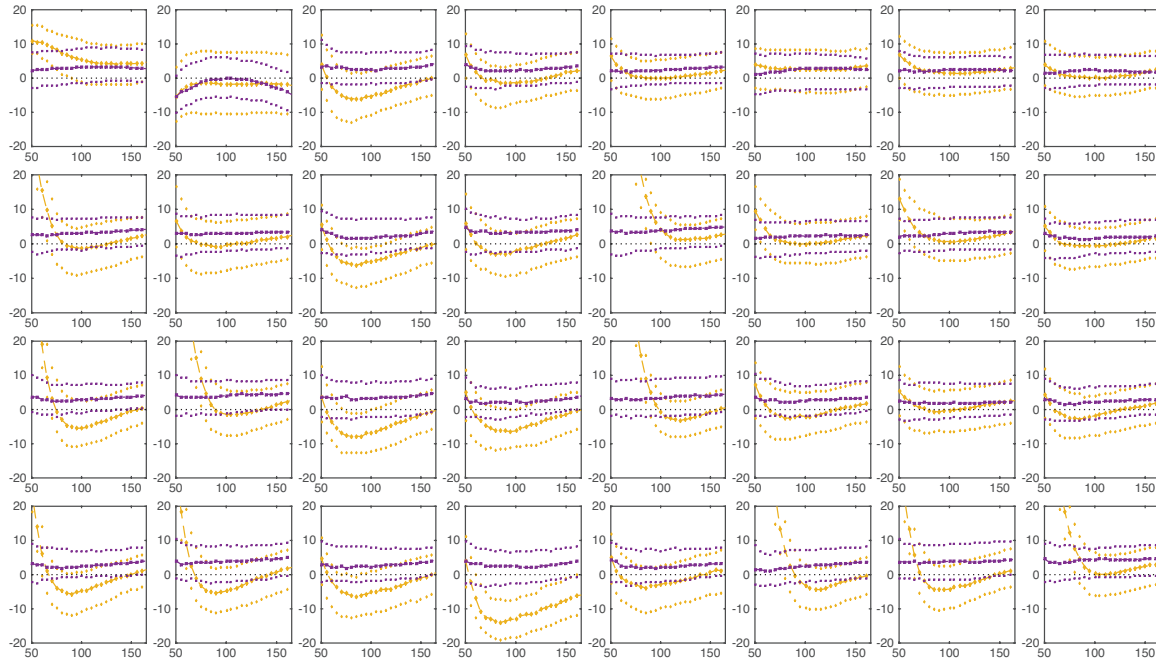


**Figure 7-10:** Median (large symbols) and first and third quartiles (small symbols) of the relative estimation error for the relative blood flow ( $rF$ ) estimated using the **rLin** (yellow diamonds) and **rReg** (purple squares) models, as a function of the exam duration.

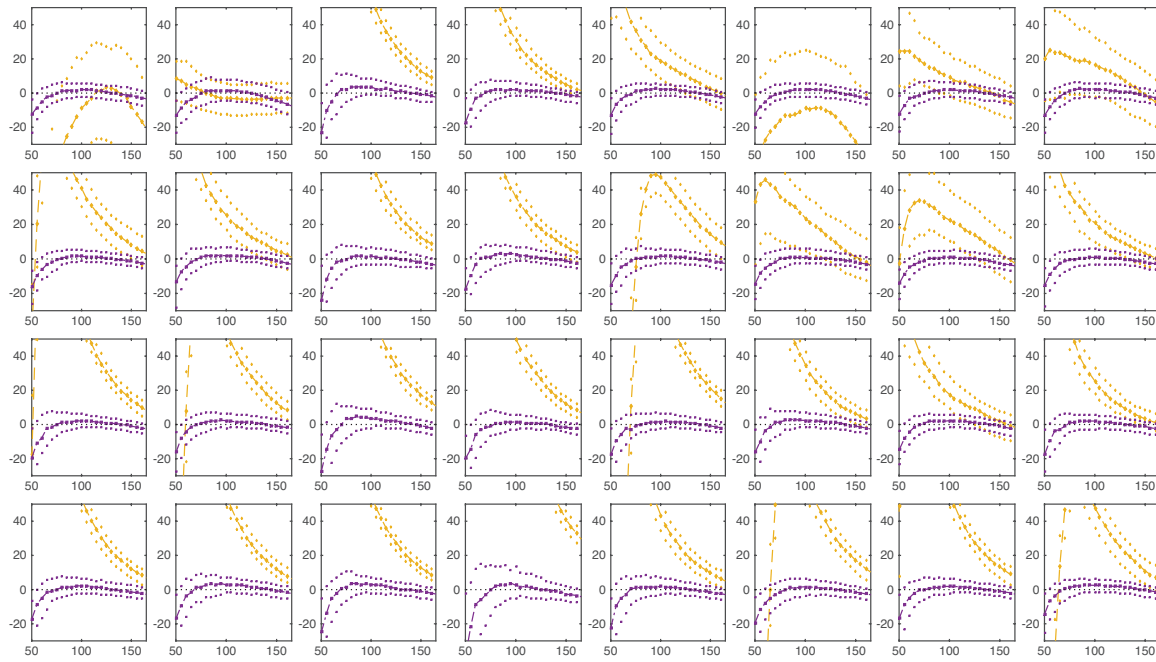


**Figure 7-11:** Median (large symbols) and first and third quartiles (small symbols) of the relative estimation error for the rate constant in the tumor ( $k_T$ ) estimated using the **rLin** (yellow diamonds) and **rReg** (purple squares) models, as a function of the exam duration.

tissue blood volume (Figure 7-13), relative tissue blood flow (Figure 7-14), and rate constants in the tumor (Figure 7-15) and in the reference tissue (Figure 7-16). In Figures 7-13 to 7-16, each plot represents a tumor region, i.e. the top row corresponds to the outer rim and the bottom row to the inner rim, the columns correspond to the clockwise ordering of the regions on a rim starting with the left region above the horizontal line.

Varying the sampling period over the investigated range, i.e. from 0.1 to 1 second, did not have a significant impact on the accuracy of the estimation of the relative tissue blood volume parameter using both the **rLin** and **rReg** models (see Figure 7-13), and only a slight decrease in precision was observed for larger sampling period. Similarly to the varying noise level experiments, the bias in the estimation bias of  $rV$  was more consistent across regions using the **rReg** model, with the median relative estimation errors generally inferior to 4%. The estimates of  $rF$ , the relative tissue blood flow, exhibited a tendency to decrease with increasing sampling period, especially in regions with large simulated  $k_T$  values. While in most regions the estimates of  $rF$  from the **rReg** model get closer to zero for large sampling

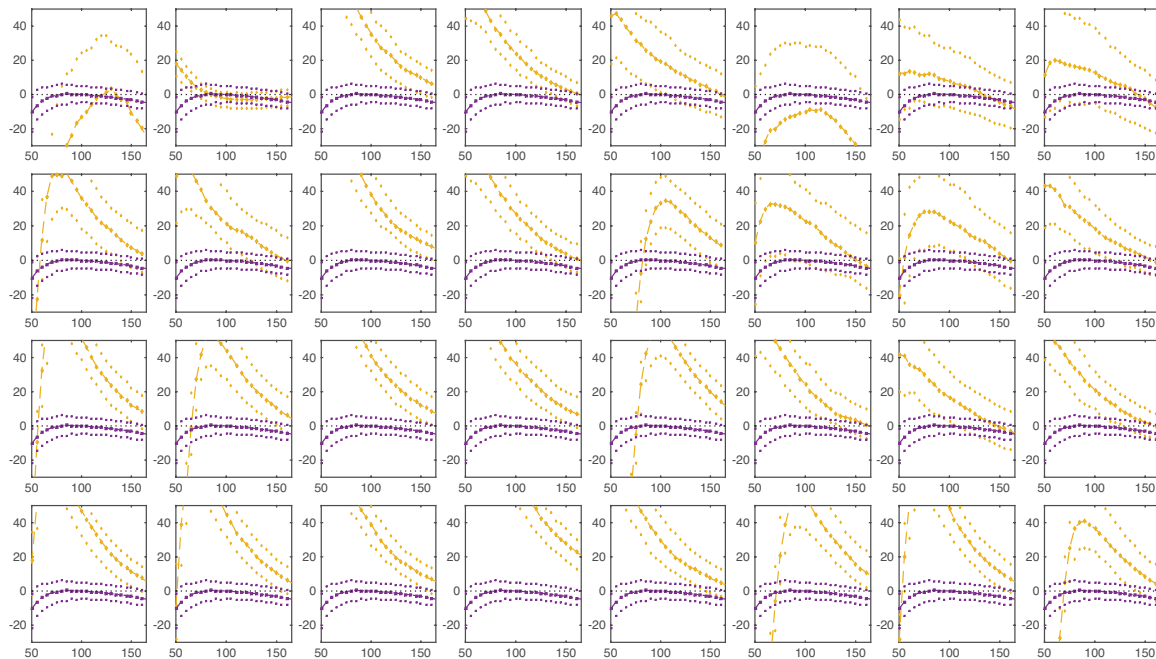


**Figure 7-12:** Median (large symbols) and first and third quartiles (small symbols) of the relative estimation error for the rate constant in the reference tissue ( $k_R$ ) estimated using the **rLin** (yellow diamonds) and **rReg** (purple squares) models, as a function of the exam duration.

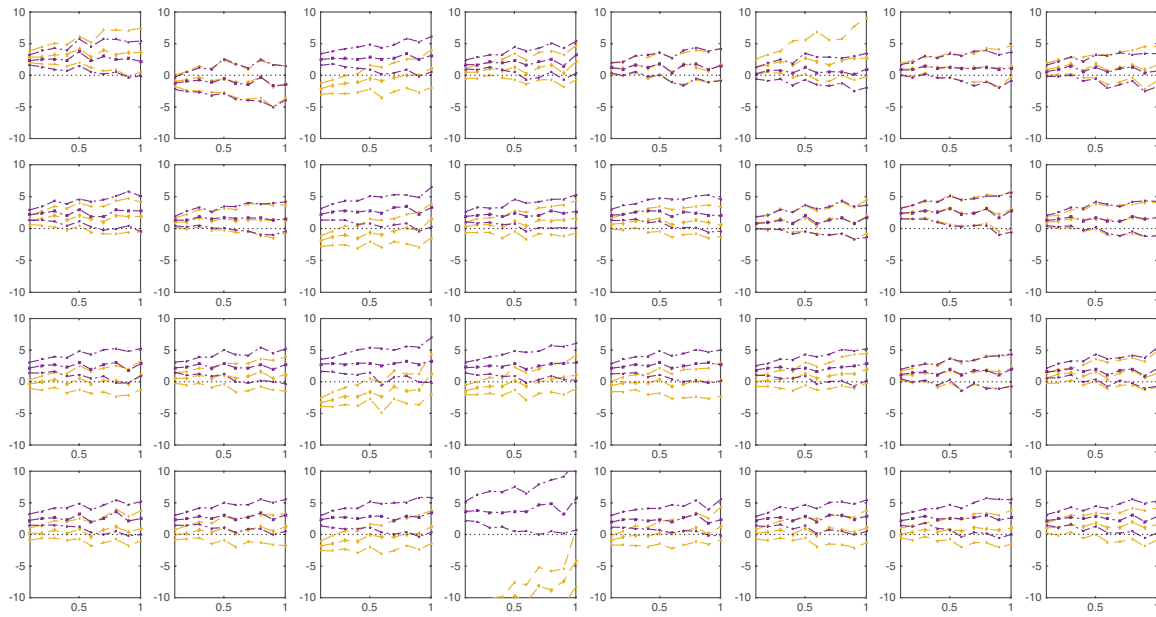


**Figure 7-13:** Median (large symbols) and first and third quartiles (small symbols) of the relative estimation error for the relative tissue blood volume ( $rV$ ) estimated using the **rLin** (yellow diamonds) and **rReg** (purple squares) models, depending on the sampling period used for simulation.

periods, one region underestimated the parameter by more than 20%. The estimates of  $rF$  from the **rLin** model exhibited a similar trend, but in addition they were overall more sensitive to the sampling period in terms of precision, and less consistent across regions. In terms of rate constant in the tumor (see Figure 7-15), the **rReg** model yielded consistent negative biases across regions, and generally yielded more precise estimates than the **rLin** model. For both models, a slight decrease of the estimates of  $k_T$  with the sampling period was observed for both models in most regions, but stronger negative slopes were observed in regions with larger simulated  $k_T$ . The rate constant in the reference tissue was estimated consistently across tumor regions using the **rReg** model (see Figure 7-16), and despite a slight underestimation, the estimation was overall more accurate and precise with this model. Indeed, the estimation of  $k_R$  using the **rLin** model was extremely imprecise in some regions.

**Reference tissue** The effect of varying the characteristics of the reference tissue on the accuracy and precision of the estimation process are displayed in Figures 7-17 to 7-20. In any of these eight Figures, the first line corresponds to fixed values of the tissue blood volume

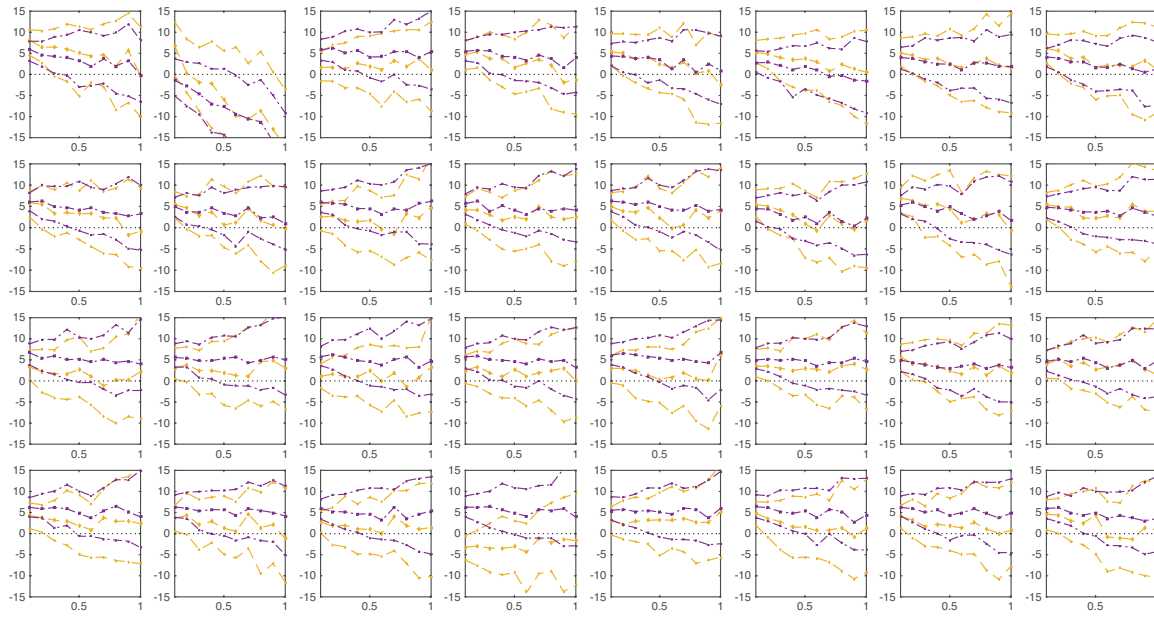


**Figure 7-14:** Median (large symbols) and first and third quartiles (small symbols) of the relative estimation error for the relative tissue blood flow ( $rF$ ) estimated using the **rLin** (yellow diamonds) and **rReg** (purple squares) models, depending on the sampling period used for simulation.

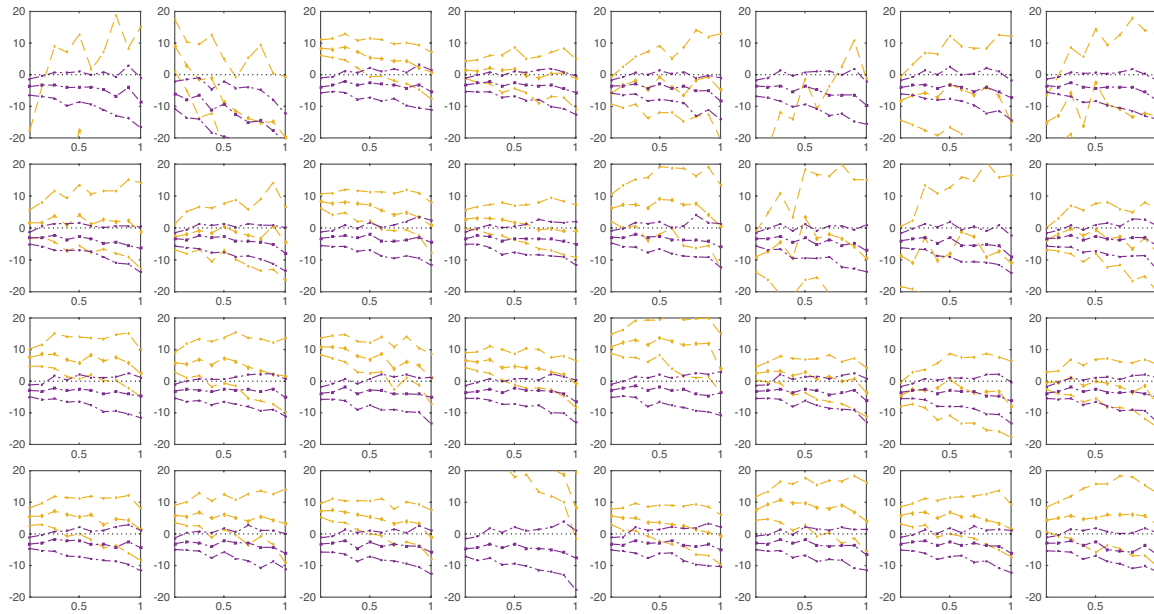


**Figure 7-15:** Median (large symbols) and first and third quartiles (small symbols) of the relative estimation error for the rate constant in the tumor ( $k_T$ ) estimated using the **rLin** (yellow diamonds) and **rReg** (purple squares) models, depending on the sampling period used for simulation.

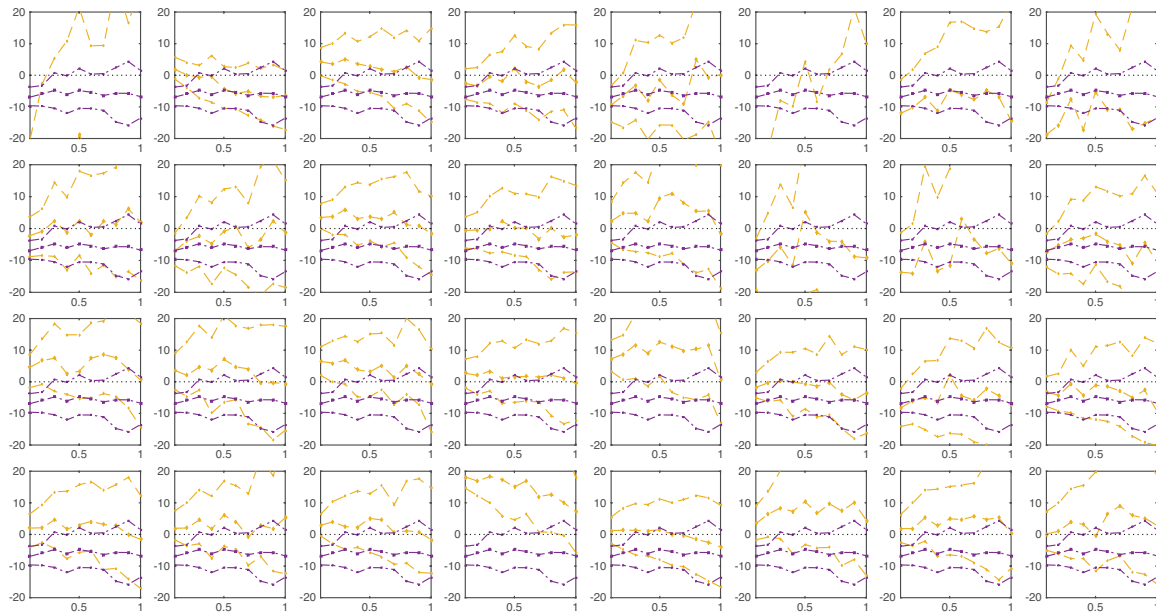


**Figure 7-16:** Median (large symbols) and first and third quartiles (small symbols) of the relative estimation error for the rate constant in the reference tissue ( $k_R$ ) estimated using the **rLin** (yellow diamonds) and **rReg** (purple squares) models, depending on the sampling period used for simulation.

$V_R$  with varying tissue blood flow  $F_R$ , the second line corresponds to fixed values of  $F_R$  with varying  $V_R$ , and the third line correspond to fixed values of  $k_R$  with varying values of both  $V_R$  and  $k_R$ . Each bullseye displays the median relative estimation error in each of the 32 tumor regions for the considered parameter.

The relative tissue blood volume (see Figure 7-17),  $rV$ , estimated using the **rLin** model revealed sensitive to variations of parameter  $k_R$ . Indeed, an increase in  $k_R$  resulted in increased positive or negative biases, along with increased heterogeneity of the bias across regions. Using the **rReg** model reduced the discrepancies across regions compared to the **rLin** model, but varying  $k_R$  one way or the other overestimated the values of  $rV$ . Similarly, the relative blood flow (see Figure 7-18),  $rF$ , estimated using either the **rLin** model or the **rReg** model were sensitive to variations of  $k_R$ . Larger biases were found using the **rReg** model, however larger discrepancies across regions were observed in the estimation biases of the **rLin** model. For both models, regions with large simulated  $k_T$  values were inversely biased, i.e.  $rF$  was underestimated while the other regions were overestimated and oppositely. The

smallest biases in the estimation of  $rF$  were found for two thirds of the original  $k_R$  value. In case of fixed  $k_R$  values, using lower values of both  $F_R$  and  $V_R$  yielded overestimated  $rV$  and  $rF$  values using both models. Regarding the rate constant in the tumor (see Figure 7-19),  $k_T$ , large discrepancies can be observed using the **rLin** model, and they tend to increase with decreasing values of  $k_R$ . Using the **rReg** model, the bias in the estimation of  $k_T$  increased for lower values of  $k_R$ . Additionally, discrepancies across regions are almost inexistant using the **rReg** model, except in regions with large simulated  $k_T$  values, revealing the effect of regularization. Biases close to zero were found in most regions simulating the reference tissue curve using two thirds of the original  $k_R$  value. The rate constant in the reference tissue (see Figure 7-20),  $k_R$ , exhibited behaviors extremely similar to those of  $k_T$ , whether estimated using the **rLin** model or the **rReg** model. In case of fixed  $k_R$  values, using lower values of both  $F_R$  and  $V_R$  yielded underestimated  $kT$  and  $kR$  values using both models.

**Number of regions** The impact of varying the number of regions on the accuracy and precision of the estimates of the **rLin** and **rReg** models is shown in Figures 7-21 to 7-24. Indeed, each figure corresponds to a parameter, and the first line represent the accuracy of the estimation through the median relative estimation error, while the second line represents the precision of the estimation through the standard deviation of the relative estimation error. The relative tissue blood volume  $rV$  (see Figure 7-21) from the **rLin** and **rReg** models were slightly underestimated using both methods, the latter however yielded more homogeneous median biases across regions. The **rLin** model was particularly imprecise in the region exhibiting the larger value of  $k_T$ . For both models, no significant effect of the number of region on the accuracy and precision of the estimates of  $rV$  was observed in our experiments. Using the **rLin** model, increasing the number of region resulted in a lower precision of the regional estimates of  $rF$ , the relative tissue blood flow (see Figure 7-22). The **rReg** model yielded slightly more biased estimates of  $rF$ , but increasing the number of regions included in the analysis increased the precision of the estimation for studies including two or more regions. Overall, the biases in the estimates of  $rF$  from the **rReg** model were more consistent across tumor regions. The rate constant in the tumor  $k_T$  (see Figure 7-23) was globally overestimated using the **rLin** model, except in the region with the largest simulated  $k_T$  value

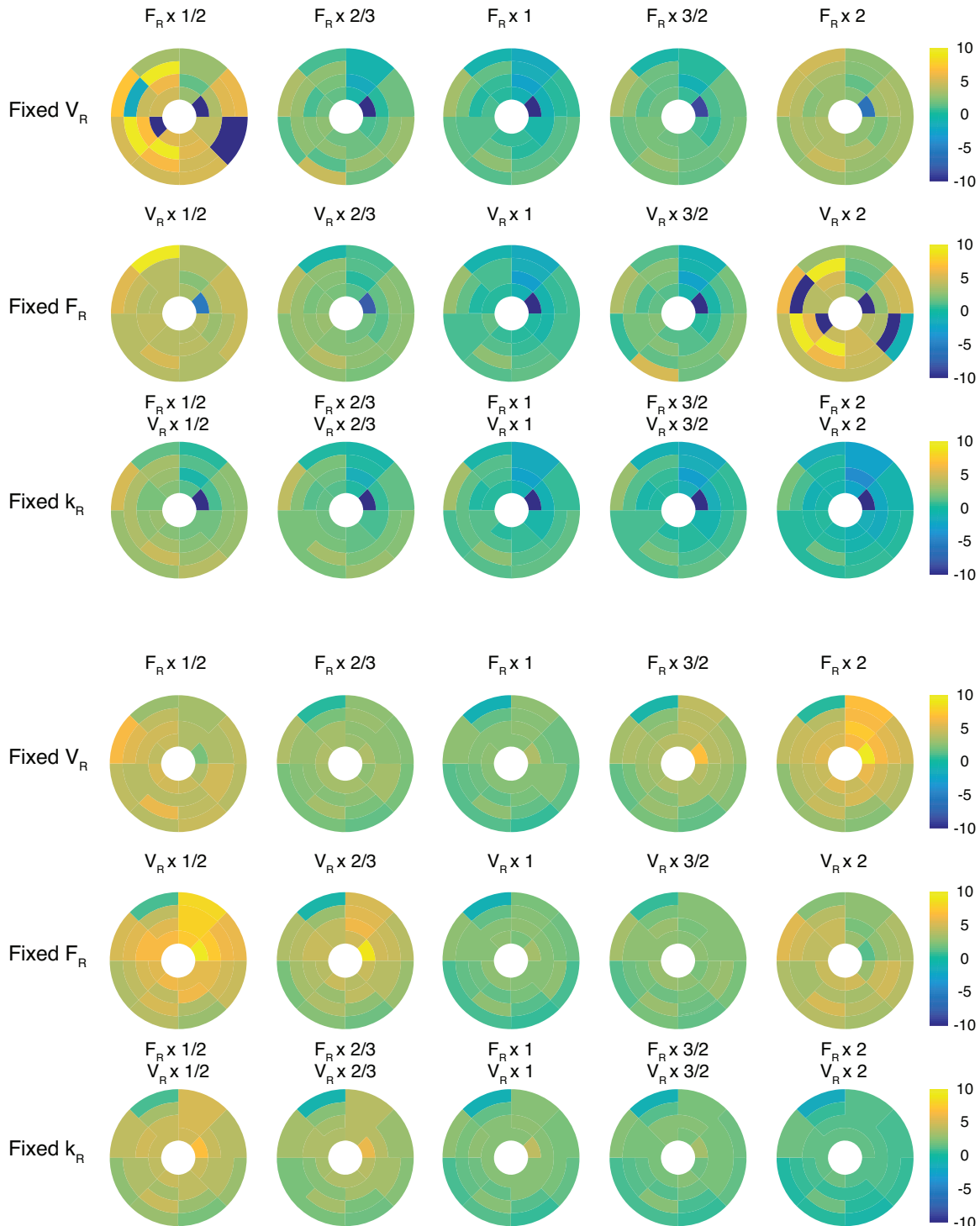


**Figure 7-17:** Bullseyes of the median relative estimation error for the relative tissue blood volume ( $rV$ ) estimated using the **rLin** (top) and **rReg** (bottom) models depending on the characteristics of the reference tissue used for simulation.

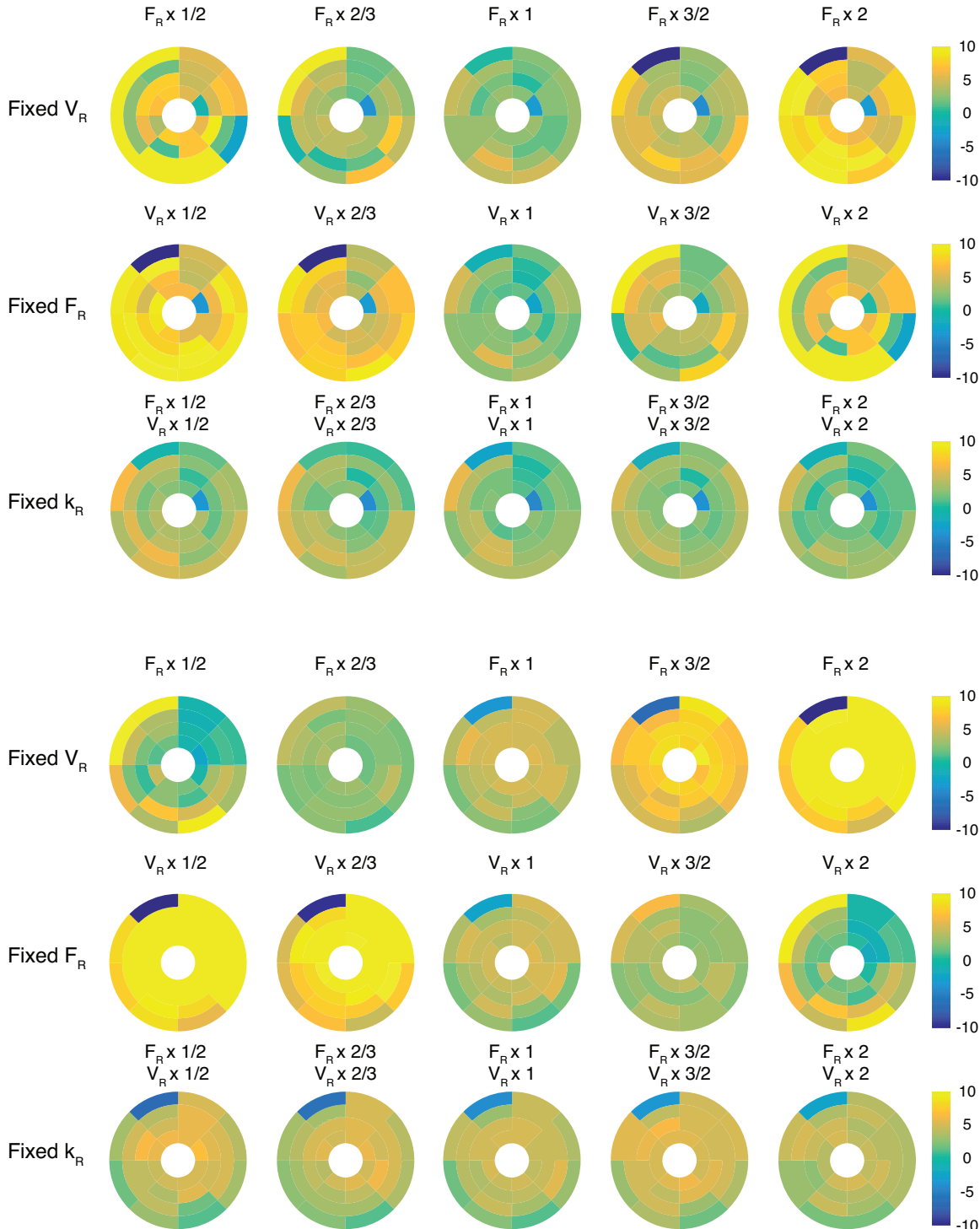


**Figure 7-18:** Bullseyes of the median relative estimation error for the relative tissue blood flow ( $rF$ ) estimated using the **rLin** (top) and **rReg** (bottom) models depending on the characteristics of the reference tissue used for simulation.

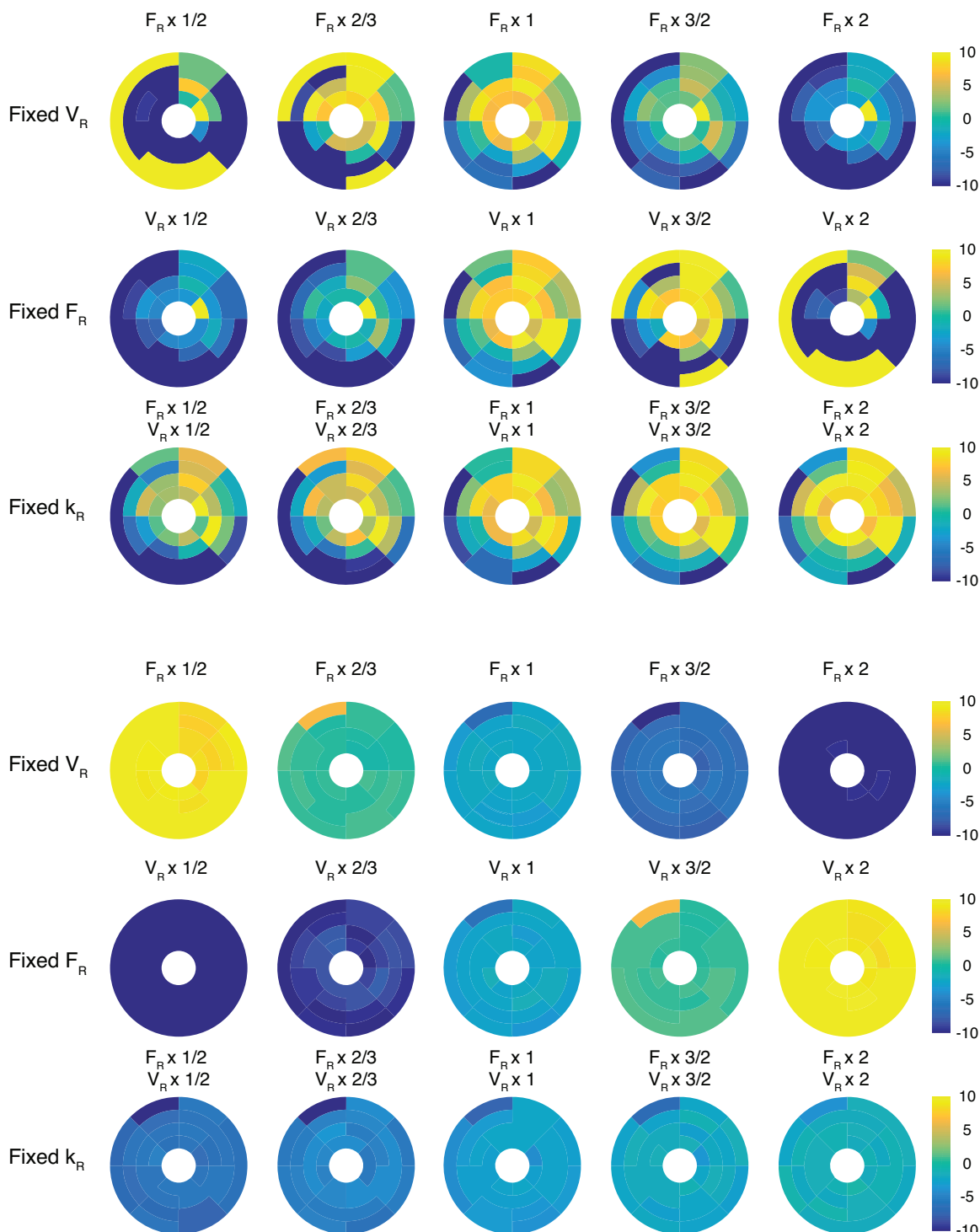


**Figure 7-19:** Bullseyes of the median relative estimation error for the rate constant in the tumor ( $k_T$ ) estimated using the **rLin** (top) and **rReg** (bottom) models depending on the characteristics of the reference tissue used for simulation.

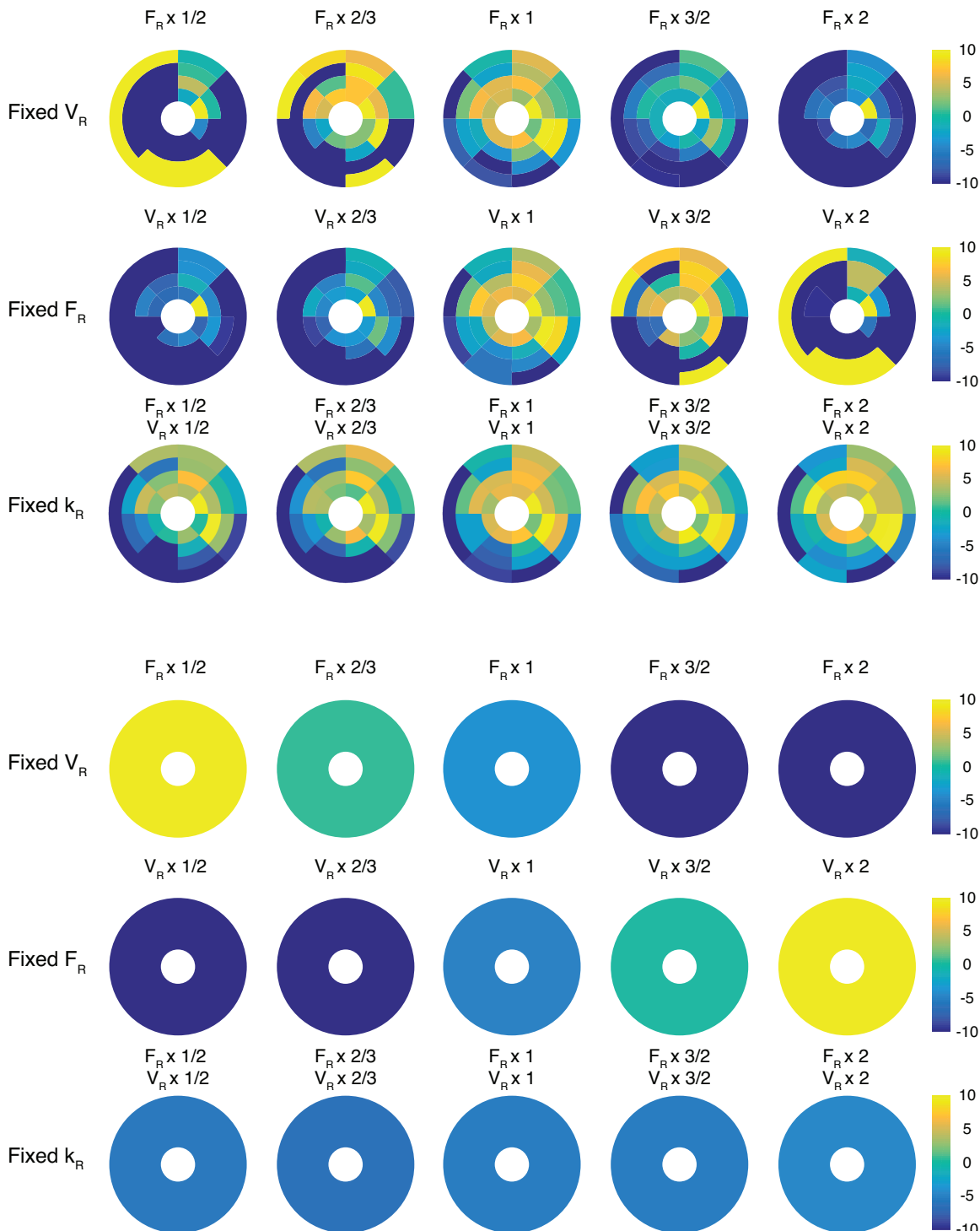


**Figure 7-20:** Bullseyes of the median relative estimation error for the rate constant in the reference tissue ( $k_R$ ) estimated using the **rLin** (top) and **rReg** (bottom) models depending on the characteristics of the reference tissue used for simulation.

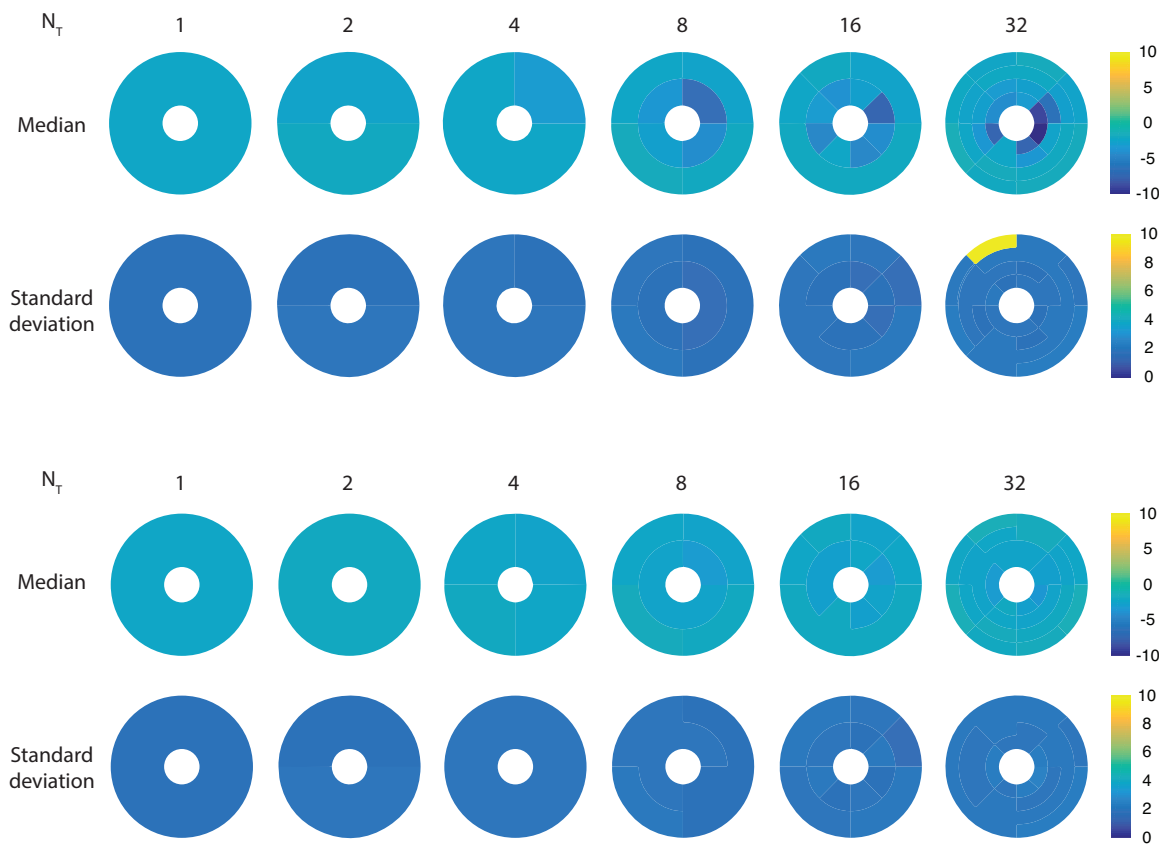


**Figure 7-21:** Bullseyes of the median value and the standard deviation of the relative estimation error for the relative tissue blood volume ( $rV$ ) estimated using the **rLin** (top) and **rReg** (bottom) models depending on the number of regions  $N_T$ .

where it was underestimated. The most imprecise estimation of  $k_T$  with this model were also found in the four regions exhibiting the largest simulated values of  $k_T$ . Using the **rReg** model considerably reduced the median value of the estimation bias for studies including four or more regions, as well as its standard deviation for studies with eight or more regions. Additionally, the estimation is more homogeneous across regions in terms of both accuracy and precision. Regarding  $k_R$ , the rate constant in the reference tissue (see Figure 7-24), the precision and the homogeneity of the estimates from the **rLin** model clearly decreases with the number of regions, while the precision actually increases using the **rReg** model. Increasing the number of regions increased the heterogeneity of the biases in the  $k_R$  estimates of the **rLin** model. The  $k_R$  estimates of the **rReg** model exhibit a slight negative bias, which does not change much when changing the number of regions

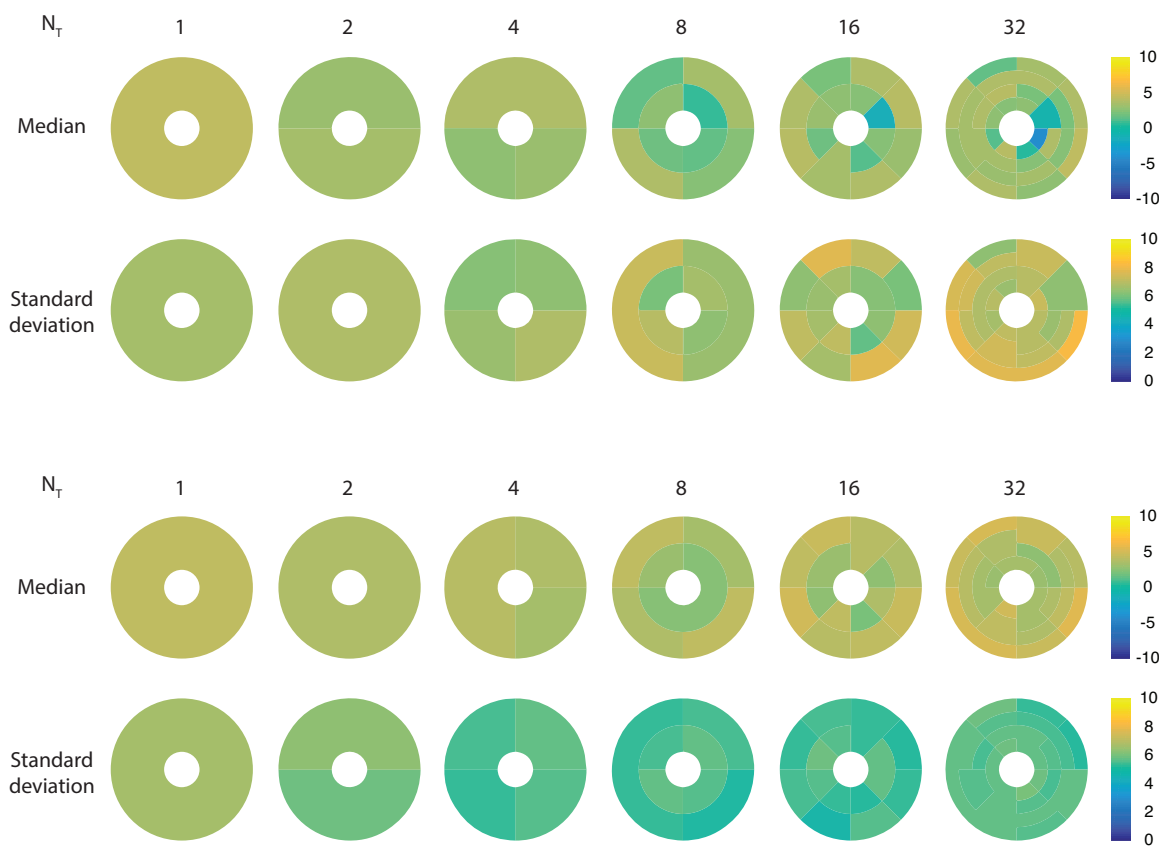


**Figure 7-22:** Bullseyes of the median value and the standard deviation of the relative estimation error for the relative tissue blood flow ( $rF$ ) estimated using the **rLin** (top) and **rReg** (bottom) models depending on the number of regions  $N_T$ .

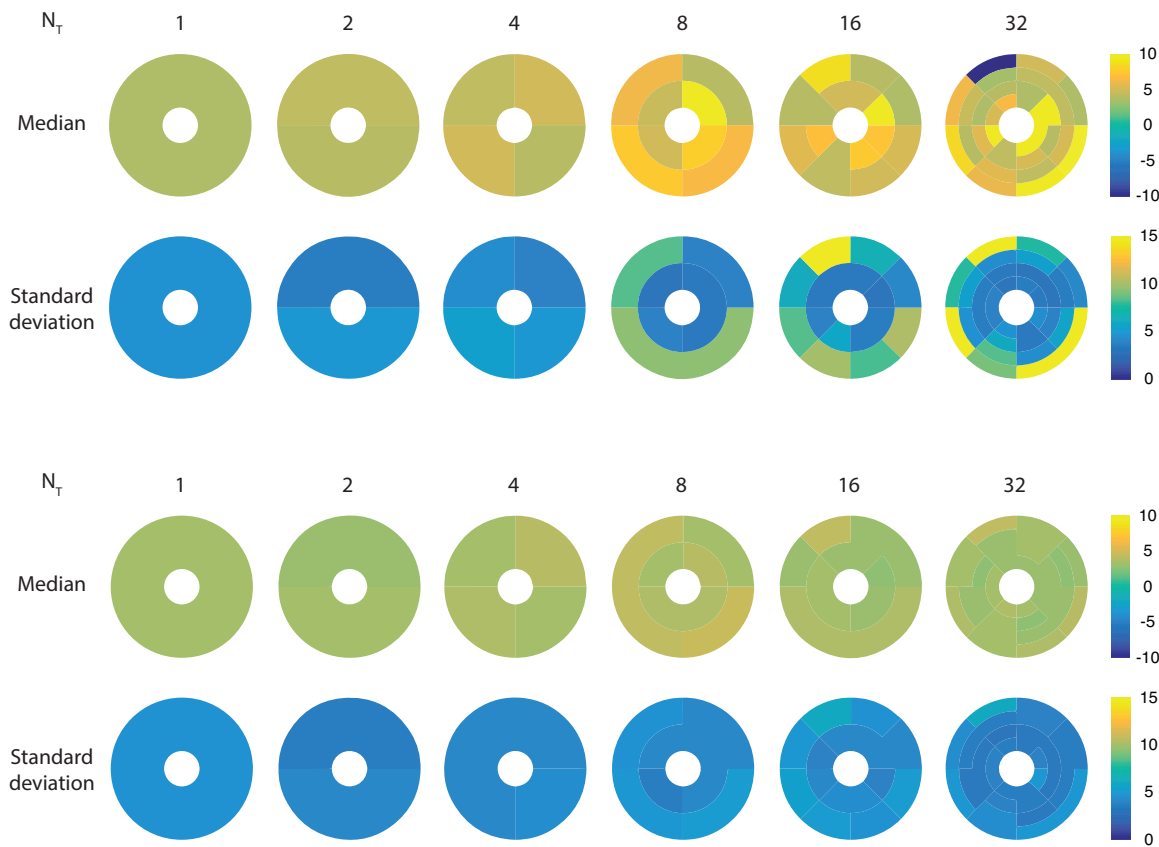


**Figure 7-23:** Bullseyes of the median value and the standard deviation of the relative estimation error for the rate constant in the tumor ( $k_T$ ) estimated using the **rLin** (top) and **rReg** (bottom) models depending on the number of regions  $N_T$ .

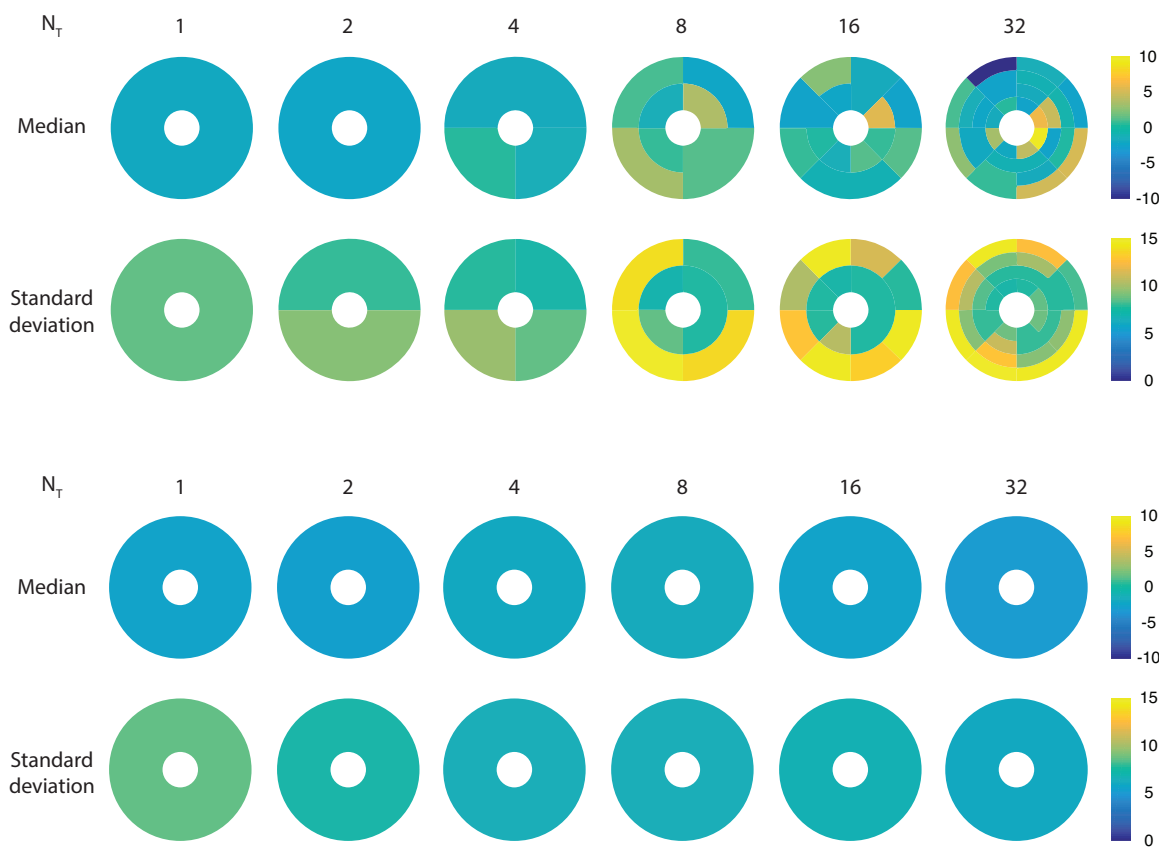


**Figure 7-24:** Bullseyes of the median value and the standard deviation of the relative estimation error for the rate constant in the reference tissue ( $k_R$ ) estimated using the **rLin** (top) and **rReg** (bottom) models depending on the number of regions  $N_T$ .

## 7.5 Discussion

In 2001, Logan et al. [17] investigated strategies to remove the bias in the graphical analysis of positron emission tomography data, which is basically a resolution method for the **OVC** model, i.e. with a known arterial input function, but the study was also extended to the **rOVC** model, i.e. with a reference tissue. The linear formulation of the **rOVC** model, named **rLin** in this study, was assessed through simulation experiments with various noise levels, and various strategies were proposed to reduce the estimation bias of the distribution volume ratio, which is the generalization for the relative tissue blood volume when addressing non-intravascular tracers. We first proposed the **rReg** model in [10] as a new strategy to improve parameter reproducibility in a test-retest preclinical study, and here we investigated the ability of the method to remove the bias in the resolution of the **rOVC** model by taking advantage of the functional heterogeneity among the studied tissues.

Theoretically, the number of regions included in the analysis should not have any impact on the parameters of the **rLin** model as every regional enhancement curve is modeled individually. In practice, increasing the number of regions resulted in even more biased parameters. Nevertheless, varying the number of regions reveals the importance of regularizing parameter  $k_R$  across tumor regions, as implemented by the **rReg** model, by comparison with the **rLin** model. In this study, simulations did not account for the variations of the signal to noise ratio depending on the size of the region. Instead it investigates solely the impact of the number of regions included in the analysis on the accuracy and precision of the estimates depending on whether the approach is regularized for parameter  $k_R$  by keeping the noise level constant regardless of the number of regions.

The regularization greatly improved the homogeneity of the estimation across regions. In some cases the regularization actually induced stronger bias in the estimation, however the biases are more homogeneous across regions, allowing meaningful regional comparison of the perfusion parameters. Moreover, the **rLin** approach was largely outperformed by the **rReg**, especially regarding the estimates of the rate constant parameters,  $k_T$  and  $k_R$ , but also regarding the relative tissue blood volume and flow parameters,  $rV$  and  $rF$ . The regularization also made the estimation more robust to the acquisition settings over the investigated

range, including the exam duration and the sampling period.

Different simulation studies should be conducted to investigate the applicability of the **rReg** models to contrast-enhanced images acquired using other imaging modalities in case of intravascular tracers, or in permeability-limited and flow-limited conditions with diffusing tracers, i.e. when permeability or blood flow is much larger than the other one [22], or when the data only reflects one of the processes [1]. Indeed, the range of investigated parameters should be adapted to the imaging modality of interest, for instance the sampling period and the exam duration are usually longer in other modalities than in ultrasound. Additionally, the multiplicative noise model used for simulation is specific of ultrasound data, and the data was simulated using the **OVC** model to reflect the intravascular characteristics of ultrasound contrast agents.

The rate constant in the tumor,  $k_T$ , appears to be related to the bias in the estimation of perfusion parameters using both models. In particular for the **rReg** model, the region with a simulated  $k_T$  value larger than  $k_R$ , and more generally regions with large  $k_T$  values, yielded estimates of  $k_T$  more biased than the other regions. This phenomenon was investigated by Cárdenas-Rodríguez et al. [7] in a simulation study assessing the ability of the **rLin** model to accurately quantify perfusion in contrast-enhanced magnetic resonance imaging data. Oppositely, regions with large  $k_T$  values yielded accurate estimates of  $rV$ , while regions with small  $k_T$  values yielded more biased estimates of the parameter. Our experiments also reveal that estimation biases can either be positive or negative in a given region, depending on the value of  $k_R$ .

Our study revealed that the choice of the reference tissue plays a crucial role in the accuracy and precision of the perfusion parameters estimated using the **rReg** model, it should therefore be further investigated. Indeed, it is necessary to identify the ideal reference tissue in order to improve the robustness of the estimation. A deeper and finer understanding of the relations between the characteristics of the reference tissue and the estimated perfusion parameters would allow correction of the estimation bias in case the ideal reference tissue does not exist in the image. Our study reveals that halving  $V_R$  or doubling  $F_R$ , which both result in doubling  $k_R$ , has almost the same impact on the estimation bias. Actually, the least biased estimation overall was obtained using two thirds of the original  $k_R$  value,

i.e.  $k_R = \frac{2}{3} \times 0.0693 = 0.0462$ . Additionally, increasing the values of both  $V_R$  and  $F_R$ , while enforcing fixed values of  $k_R$ , increased the accuracy of the estimates of the **rReg** model. This suggests that a well perfused tissue should be preferred, i.e. a tissue with a high tissue blood flow and high tissue blood volume.

## 7.6 Conclusion

A simulation study based on preclinical contrast-enhanced ultrasound experiments was conducted to assess and compare the accuracy and precision of two estimation methods for the **rOVC** model, a one-compartment reference tissue model. The **rLin** model relies on the linear formulation of the **rOVC** model, and estimates perfusion parameters in each region of analysis individually. A limitation of this approach lies in the existence of a perfusion parameter that characterizes the reference tissue, i.e. its rate constant  $k_R$ , which can be derived from the perfusion parameters estimated in each tumor region. However, since the same reference tissue is used to analyse all the regions, this parameter should be homogeneous across the regions of analysis. The **rReg** model is based on the **rLin** model, but it takes advantage of the functional diversity of the regions of analysis, and ensures that the rate constant of the reference tissue is the same across all regions of analysis.

These simulation studies demonstrated the superiority of the **rReg** model in terms of accuracy and precision. The regularization of  $k_R$  also made the biases more homogeneous across regions, making comparison of regional parameters more meaningful. Additionally, the **rReg** model relaxes the requirements for temporal resolution and exam duration, allowing accurate estimation of perfusion parameters in shorter and degraded data. Our experiments suggest that the regularization improve the accuracy and precision of the estimation if at least four regions are included in the analysis. Regarding the number and the size of the regions of analysis, a compromise should be made to reveal the spatial heterogeneity of the tissue, while limiting the noise level to ensure accurate estimation of the perfusion parameters.

Indeed the choice of the reference tissue is crucial as it has a significant impact on the accuracy of the estimation, and should be further investigated. We were however able to

draw some recommendations regarding its selection. The rate constant parameter is critical when selecting the reference tissue, a region exhibiting a rate constant larger than the rate constants in the regions of analysis yielded more accurate parameters in our experiments, however an optimal value of  $k_R$  seems to exist. Furthermore, using a well perfused reference tissue, i.e. a tissue with high tissue blood volume and tissue blood flow, yields more accurate perfusion parameters.



# Afterword

In the third part of this thesis, we proposed and assessed a new quantification model based on the one-compartment reference tissue model that allows simultaneous, robust, and homogeneous estimation of perfusion parameters in multiple regions. The model ensures a single value of the rate constant characterizing the reference tissue is estimated across the various regions of analysis through regularization of the parameter.

In Chapter 5 we first demonstrated the superiority of the approach in terms of parameter reproducibility through preclinical test-retest experiments. Indeed, the regularized model yielded the most reproducible perfusion parameters among the investigated methods. Then, the robustness of the model to recirculation of the contrast agent throughout the course of the acquisition was assessed on simulated data in Chapter 6. This study confirmed the robustness of compartmental models to recirculation, and revealed the sensitivity of semi-quantitative parameters to this physiological phenomenon. Finally, in Chapter 7 we investigated the impact of data characteristics, i.e. noise level, exam duration, and sampling period, as well as analysis strategies, i.e. number of regions, choice of reference tissue. The regularized model proved robust to noise, and relaxed the requirements for temporal resolution and exam duration. Additionally, regularizing the estimation of  $k_R$  made the estimation more homogeneous across regions, allowing meaningful comparison of perfusion parameters between regions. The choice of the reference tissue was proved to affect parameter estimation, and the role of parameter  $k_R$  was revealed. Moreover, we recommend using a large and well perfused tissue as a reference.

## Bibliography

- [1] Daniel Balvay, Frédérique Frouin, Guillaume Calmon, Bertrand Bessoud, Edmond Kahn, Nathalie Siauve, Olivier Clément, and Charles A Cuenod. New criteria for assessing fit quality in dynamic contrast-enhancedT1-weighted MRI for perfusion and permeability imaging. *Magnetic Resonance in Medicine*, 54(4):868–877, 2005. [137](#), [197](#)
- [2] Guillaume Barrois, Alain Coron, Thomas Payen, Alexandre Dizeux, and S Lori Bridal. A Multiplicative Model for Improving Microvascular Flow Estimation in Dynamic Theory and Experimental Validation. *IEEE Trans. Ultrason., Ferroelect., Freq. Contr.*, 60(11):2284–2294, 2013. [148](#)
- [3] Guillaume Barrois, Alain Coron, Thomas Payen, Alexandre Dizeux, and S Lori Bridal. A multiplicative model for improving microvascular flow estimation in dynamic contrast-enhanced ultrasound (DCE-US): theory and experimental validation. *IEEE Transactions on Ultrasonics, Ferroelectrics and Frequency Control*, 60(11):2284–2294, November 2013. [166](#)
- [4] Å Björck. Numerical methods for least squares problems, 1996. [169](#)
- [5] M J Blomley and P Dawson. Bolus dynamics: theoretical and experimental aspects. *Br J Radiol*, 70(832):351–359, April 1997. [146](#)
- [6] Julio Cárdenas-Rodríguez, Christine M Howison, and Mark D Pagel. A linear algorithm of the reference region model for DCE-MRI is robust and relaxes requirements for temporal resolution. *Magn Reson Imaging*, 31(4):497–507, May 2013. [145](#)
- [7] Julio Cárdenas-Rodríguez, Christine M Howison, and Mark D Pagel. A linear algorithm of the reference region model for DCE-MRI is robust and relaxes requirements for temporal resolution. *Magnetic resonance imaging*, 31(4):497–507, May 2013. [132](#), [136](#), [169](#), [197](#)
- [8] C F Dietrich, Michalakis Averkiou, J-M Correas, N Lassau, E Leen, and F Piscaglia. An EFSUMB introduction into Dynamic Contrast-Enhanced Ultrasound (DCE-US) for

- quantification of tumour perfusion. In *Ultraschall in der Medizin (Stuttgart, Germany : 1980)*, pages 344–351. Innere Medizin 2, Caritas-Krankenhaus, Bad Mergentheim. Christoph.Dietrich@ckbm.de, © Georg Thieme Verlag KG, August 2012. [132](#), [135](#), [144](#)
- [9] Maxime Doury, Alexandre Dizeux, Alain De Cesare, Olivier Lucidarme, S Lori Bridal, and Frédérique Frouin. Regularized linear resolution of a one-compartment model to improve the reproducibility of perfusion parameters in CEUS. In *2016 IEEE International Ultrasonics Symposium (IUS)*, pages 1–4. IEEE, 2016. [145](#), [150](#), [160](#)
- [10] Maxime Doury, Alexandre Dizeux, Alain De Cesare, Olivier Lucidarme, S Lori Bridal, and Frédérique Frouin. Regularized linear resolution of a one-compartment model to improve the reproducibility of perfusion parameters in CEUS. In *2016 IEEE International Ultrasonics Symposium (IUS)*, pages 1–4. IEEE, 2016. [129](#), [196](#)
- [11] Maxime Doury, Alexandre Dizeux, Alain De Cesare, Olivier Lucidarme, Claire Pellet-Barakat, S Lori Bridal, and Frédérique Frouin. Quantification of tumor perfusion using dynamic contrast-enhanced ultrasound: impact of mathematical modeling. *Phys Med Biol*, 62(3):1113–1125, February 2017. [130](#), [145](#), [146](#), [149](#), [150](#), [158](#), [159](#), [160](#)
- [12] Maxime Doury, Alexandre Dizeux, Alain De Cesare, Olivier Lucidarme, Claire Pellet-Barakat, S Lori Bridal, and Frédérique Frouin. Quantification of tumor perfusion using dynamic contrast-enhanced ultrasound: impact of mathematical modeling. *Physics in medicine and biology*, 62(3):1113–1125, February 2017. [132](#), [135](#), [166](#)
- [13] R N Gunn, S R Gunn, and V J Cunningham. Positron emission tomography compartmental models. *J Cereb Blood Flow Metab*, 21(6):635–652, June 2001. [146](#)
- [14] R N Gunn, S R Gunn, and V J Cunningham. Positron emission tomography compartmental models. *Journal of Cerebral Blood Flow & Metabolism*, 21(6):635–652, June 2001. [166](#)
- [15] Thibaud Lefort, Frank Pilleul, Sébastien Mulé, S Lori Bridal, Frédérique Frouin, Catherine Lombard-Bohas, Thomas Walter, Olivier Lucidarme, and Aymeric Guibal.

- Correlation and agreement between contrast-enhanced ultrasonography and perfusion computed tomography for assessment of liver metastases from endocrine tumors: normalization enhances correlation. *Ultrasound Med Biol*, 38(6):953–961, 2012. [159](#)
- [16] J Logan, J S Fowler, N D Volkow, A P Wolf, S L Dewey, D J Schlyer, R R MacGregor, R Hitzemann, B Bendriem, and S J Gatley. Graphical analysis of reversible radioligand binding from time-activity measurements applied to [N-<sup>11</sup>C-methyl]-(-)-cocaine PET studies in human subjects. *Journal of Cerebral Blood Flow & Metabolism*, 10(5):740–747, September 1990. [136](#)
- [17] J Logan, J S Fowler, N D Volkow, Y S Ding, G J Wang, and D L Alexoff. A strategy for removing the bias in the graphical analysis method. *Journal of Cerebral Blood Flow & Metabolism*, 21(3):307–320, March 2001. [196](#)
- [18] MR Lowerison, JJ Tse, MN Hague, AF Chambers, DW Holdsworth, and JC Lacefield. Compound speckle model detects anti-angiogenic tumor response in preclinical non-linear contrast-enhanced ultrasonography. *Med Phys*, 44(1):99–111, 2017. [145](#)
- [19] Clifford S Patlak, Ronald G Blasberg, and Joseph D Fenstermacher. Graphical Evaluation of Blood-to-Brain Transfer Constants from Multiple-Time Uptake Data. *Journal of Cerebral Blood Flow & Metabolism*, 3(1):1–7, March 1983. [136](#), [150](#)
- [20] Costas Strouthos, Marios Lampaskis, Vassilis Sboros, Alan McNeilly, and Michalakis Averkiou. Indicator dilution models for the quantification of microvascular blood flow with bolus administration of ultrasound contrast agents. *IEEE Trans Ultrason Ferroelectr Freq Control*, 57(6):1296–1310, June 2010. [144](#), [148](#)
- [21] M X Tang, H Mulvana, T Gauthier, A K P Lim, D O Cosgrove, R J Eckersley, and E Stride. Quantitative contrast-enhanced ultrasound imaging: a review of sources of variability. *Interface Focus*, 1(4):520–539, August 2011. [132](#), [140](#)
- [22] Paul S Tofts, Gunnar Brix, David L Buckley, Jeffrey L Evelhoch, Elizabeth Henderson, Michael V Knopp, Henrik B Larsson, Ting-Yim Lee, Nina A Mayr, Geoffrey J Parker, Ruediger E Port, June Taylor, and Robert M Weisskoff. Estimating kinetic parameters

- from dynamic contrast-enhanced T(1)-weighted MRI of a diffusible tracer: standardized quantities and symbols. *Journal of Magnetic Resonance Imaging*, 10(3):223–232, 1999. [197](#)
- [23] Simona Turco, Hessel Wijkstra, and Massimo Mischi. Mathematical Models of Contrast Transport Kinetics for Cancer Diagnostic Imaging: A Review. *IEEE Reviews in Biomedical Engineering*, 9:121–147, 2016. [144](#)
- [24] Stef van Buuren and Karin Groothuis-Oudshoorn. mice: Multivariate Imputation by Chained Equations in R. *Journal of Statistical Software*, 45(1):1–67, December 2011. [138](#)
- [25] E T Whittaker and G Robinson. The calculus of observations a treatise on numerical mathematics, 2008. [171](#)
- [26] Thomas E Yankeelov, Jeffrey J Luci, Martin Lepage, Rui Li, Laura Debusk, P Charles Lin, Ronald R Price, and John C Gore. Quantitative pharmacokinetic analysis of DCE-MRI data without an arterial input function: a reference region model. *Magn Reson Imaging*, 23(4):519–529, May 2005. [145](#), [168](#)



## **Abbreviations and reference data**